1995

IMPLEMENTATION OF THE HYPERBOLIC CLASS OF TIME-FREQUENCY DISTRIBUTIONS AND REMOVAL OF CROSS TERMS

Sanigepalli Praveenkumar
University of Rhode Island

IMPLEMENTATION OF THE HYPERBOLIC CLASS OF TIME-FREQUENCY DISTRIBUTIONS AND REMOVAL OF CROSS TERMS

BY

PRAVEENKUMAR. V. SANIGEPALLI

A THESIS SUBMITTED IN PARTIAL FULFILLMENT OF THE
REQUIREMENTS FOR THE DEGREE OF
MASTER OF SCIENCE
IN
ELECTRICAL ENGINEERING

UNIVERSITY OF RHODE ISLAND
1995

MASTER OF SCIENCE THESIS

OF

PRAVEENKUMAR. V. SANIGEPALLI

APPROVED:

Thesis Committee

Major Professor

DEAN OF THE GRADUATE SCHOOL

UNIVERSITY OF RHODE ISLAND

1995

Abstract

This thesis proposes new, efficient techniques for implementing some members of the Hyperbolic class of time-frequency distributions (TFD). A new, efficient algorithm is proposed for the Altes-Marinovic Q-distribution. The algorithm is a generalization of the Fast Mellin transform implementation of the Bertrand P_0 distribution. Other TFDs of the Hyperbolic class, which are the smoothed versions of the Altes-Marinovic distribution, are implemented using the Fast Mellin transform to compute the Altes distribution of the signal, which is then appropriately weighted and smoothed using numerical integration and first order linear interpolation techniques.

Also, an extensive analysis of the warping technique proposed by Canfield and Jones is done in this thesis. Canfield and Jones have implemented the data adaptive, radially Gaussian kernel hyperbolic class time-frequency representation. We have used their warping technique but with different kernels to implement various members of the Hyperbolic class like the Pseudo Altes-Marinovic distribution, Smoothed Pseudo Altes-Marinovic distribution, etc. Our implementation has the following approach. The Woodward Ambiguity function of the logarithmically frequency warped signal is calculated to compute the Hyperbolic ambiguity function. The Hyperbolic ambiguity function (HAF) is examined to determine the mapping of the various signal auto and cross components. Many complicated signals map to simple regions in the HAF plane. A suitable kernel is chosen so as to remove the cross terms without distorting the auto terms and is multiplied with the Hyperbolic Ambiguity function. Since HC class kernels can be formulated to be equivalent to (up to a proportionality factor) Cohen's class kernels, all of the useful kernel design strategies thus far developed for Cohen's class TFDs can now be applied straight forwardly to HAF plane kernel design. Then, a two dimensional Fourier transform of the product is

taken. The time frequency localization of the result is corrected to compute the corresponding hyperbolic class time frequency distribution.

This approach is intuitive and often makes kernel design easier for cross term removal. The logarithmic signal spectrum warping and the time frequency localization are implemented using the warpings techniques proposed by Canfield and Jones.

Also, a new Hyperbolic class member is proposed which uses the Multiform tiltable exponential kernel of Costa in the Hyperbolic Ambiguity function domain. This kernel does as well as or better than other Hyperbolic class TFDs in time-frequency scenarios that were considered in this thesis. Various nonstationary signals like Hyperbolic impulses, linear FM chirps, etc. were analyzed. In the case of Hyperbolic impulses, the Hyperbolic class TFRs do remarkably well over the Cohen's class TFRs in terms of time frequency localization and cross term removal.

Finally, the proposed implementation technique for the TFDs of the Hyperbolic class using the Fast Mellin transform and numerical integration is compared with the Canfield/Jones warping technique regarding memory requirements and computational time. The new Altes Q-distribution algorithm, implemented using a Fast Mellin transform, is faster and requires less memory than using the Canfield/Jones algorithm to warp the Wigner distribution. The new smoothed Altes distribution algorithms, which require the Altes algorithm followed by numerical integration, require less memory, but takes more time to compute than the corresponding Canfield/Jones algorithm.

Acknowledgments

I am deeply indebted to Dr. G. Faye Boudreaux-Bartels for guiding me through my thesis. Without her patience, expert advice and understanding, this project would not have been completed. She taught me the importance of setting high standards and goals, and striving to attain them. She was always a constant source of inspiration for me and discussions with her have proved beneficial to me in various aspects of my life.

I would like thank Antonia, Sumit, Ramli and all my other friends for their help, attention, advice in times of need and encouraging me when I really needed it.

I like to thank Drs. Paulo Gonçalvès, D. L. Jones and A. H. Costa for their help on this project.

I like to thank Drs. Leland Jackson, Bala Ravikumar, and E Suryanarayana for agreeing to serve on my committee and for their helpful comments, suggestions and discussions.

Last but not the least, I would like to thank my family for their love, support and encouragement.

Praveenkumar V Sanigepalli

Contents

List of Tables

List of Figures

Chapter 1

Introduction and Overview

Time-frequency representations combine the concepts of time domain and frequency domain by displaying signals over a joint time-frequency plane. For a fixed time, a time-frequency representation shows which frequencies are present whereas for a fixed frequency, it shows the approximate times of occurrence. This contrasts with classical signal theory which treats the time domain and the frequency domain as two distinct worlds. The time domain does not yield immediate information about frequency, whereas the frequency domain (spectrum) does not easily reveal the times at which a given frequency occurs [1].

Time-frequency representations are classified into various classes depending upon their properties. The most prominent among them is Cohen's fixed kernel class, $T_X^{(C)}(t,f)$, whose members are invariant to time-shifts and frequency-shifts [5].

$$T_{S_\tau X}^{(C)}(t,f) = T_X^{(C)}(t-\tau,f) \quad \text{and} \quad T_{M_\nu X}^{(C)}(t,f) = T_X^{(C)}(t,f-\nu) \tag{1.1}$$

Here, the time-shift operator S_τ and the frequency-shift operator M_ν are defined by $(S_\tau X)(f) = e^{-j2\pi\tau f}X(f)$ and $(M_\nu X)(f) = X(f-\nu)$, respectively, where $X(f)$ is the Fourier transform (FT) of the signal $x(t)$. Another class of time-frequency distributions is the Affine class, $T_X^{(A)}(t,f)$, whose members are invariant to time-shifts and time and frequency scalings [5], i.e.,

$$T_{S_\tau X}^{(A)}(t,f) = T_X^{(A)}(t-\tau,f) \quad \text{and} \quad T_{C_a X}^{(A)}(t,f) = T_X^{(A)}(at,\frac{f}{a}), \tag{1.2}$$

with the time-shift operator S_τ defined as before and the time-frequency scaling operator C_a defined as $(C_a X)(t,f) = \sqrt{\frac{1}{a}}X(\frac{f}{a})$, $a > 0$.

Another class of time-frequency distributions, which this thesis seeks to implement, is the Hyperbolic class, $T_X^{(H)}(t,f)$, whose members are invariant to Hyperbolic time-shifts and time and frequency scalings [3], i.e.,

$$T_{C_a X}^{(H)}(t,f) = T_X^{(H)}(at, \frac{f}{a}) \quad \text{and} \quad T_{D_c X}^{(H)}(t,f) = T_X^{(H)}(t - \frac{c}{f}, f), \tag{1.3}$$

with the time-frequency scaling operator C_a defined as before and the hyperbolic time-shift operator D_c defined as $(D_c X)(f) = e^{-j2\pi\tau c \ln \frac{f}{f_r}} X(f)$.

Each member in the Hyperbolic class has a corresponding member in Cohen's class. The implementation of the distributions of the Hyperbolic class is a challenging problem since it involves warped forms of the signal, which are difficult to compute using conventional methods. In the next chapter, an introduction to time-frequency analysis is discussed, with an emphasis on Cohen's class and the Hyperbolic class of time-frequency distributions. The Bertrand unitary P_0 distribution, which is a joint member of the Affine class and the Hyperbolic class, has been implemented recently [6]. This implementation involves the use of the Mellin transform, which reduces the task of implementation to just a few FFTs (Fast Fourier transform) [6]. This implementation, along with the Discrete Mellin transform for signal analysis, will be discussed in the third chapter.

Recently, a way of implementing the members of the Hyperbolic class by using Cohen's class distributions has been suggested by Canfield and Jones [7]. In this technique, the signal is subjected to a *logarithmic frequency warping* and then a Cohen's class time-frequency distribution of the warped signal is computed and finally, the time-frequency localization of the computed distribution is corrected to implement a particular Hyperbolic class time frequency distribution. This implementation will also be discussed in the third chapter.

This thesis proposes to implement the distributions of the Hyperbolic class using the Discrete Mellin transform. For implementing the Discrete Mellin transform, we subject the signal to geometric sampling which makes the problem of interpolation and numerical integration, needed in the implementation of some time-frequency representations of the Hyperbolic class, very complex and challenging. We have implemented the Altes-Marinovic distribution, which is the most well known distribution of the Hyperbolic class, using the Discrete Mellin transform extending the way the

Bertrand unitary P_0 distribution has been implemented by Ovarlez, Bertrand and Bertrand [6]. Also, we have implemented smoothed versions of the Altes-Marinovic distribution which are members of the Hyperbolic class by the following procedure. Initially, the Altes-Marinovic distribution of the signal is calculated. Then, an appropriate window is selected and a slice of the Altes-Marinovic distribution of the window at a particular time is calculated. Let us call the slice of the Altes-Marinovic distribution of the window as the smoothing function. Then, time and frequency remapping of the smoothing function and the Altes-Marinovic distribution of the signal are done, and finally the product of the remapped smoothing function and the Altes-Marinovic distribution of the signal is integrated using numerical integration techniques. The time frequency remapping and the numerical integration techniques require interpolation of the Altes-Marinovic distribution of the signal and the smoothing function at various time and frequency locations. These problems of numerical integration, interpolation and time frequency remapping are quite challenging and complex and the way we have dealt with these problems is discussed in the fourth chapter. Also, in this chapter, various nonstationary signals will be analyzed using various distributions of the Hyperbolic class.

In the field of time-frequency analysis, cross terms or interference terms between components in different time-frequency regions are a recurring problem and these cross terms potentially lead to confusion and misinterpretation. The Woodward or narrowband Ambiguity function [10] of a signal has been extensively studied and utilized in removing these cross terms for distributions in Cohen's class. In the fifth chapter of this thesis, we have used the Canfield and Jones warping technique [7, 8] to implement the Hyperbolic Ambiguity function of a signal. We used the following approach. The Hyperbolic Ambiguity function of the signal is calculated by *logarithmic frequency warping* of the signal and then calculating the Woodward Ambiguity function of the warped signal. Then, the appropriate time frequency distribution kernel is multiplied with Hyperbolic Ambiguity function to remove cross terms. Then, a 2D Fast Fourier transform of the resultant distribution is taken and finally, the time-frequency localization of the computed distribution is corrected to implement a particular Hyperbolic class time frequency distribution. In the case of a Hyperbolic

impulse, the approach of using the Hyperbolic Ambiguity function is advantageous over that of using the Woodward Ambiguity function because a Hyperbolic impulse maps to a straight line in a Hyperbolic Ambiguity function plane which makes the kernel design for cross term removal easy whereas in the Ambiguity function plane, a Hyperbolic impulse maps to a non-linear region which makes the kernel design very challenging and in certain cases impossible. Canfield and Jones have implemented the data adaptive, radially Gaussian kernel in the Hyperbolic Ambiguity function plane. We have used different kernels to implement various members of the Hyperbolic class like the Pseudo Altes-Marinovic distribution, Smoothed Pseudo Altes-Marinovic distribution, etc. Signals like linear FM chirps, Gaussian signals, etc. map to tilted regions at the origin of the Hyperbolic ambiguity function plane making tiltability a desirable feature for a weighting kernel to remove cross terms in the case of a multi-component signal. So, we have proposed a new member of the Hyperbolic class known as the MTEK (Multiform Tiltable Exponential Kernel) Smoothed Altes-Marinovic distribution in the fifth chapter. The MTEK smoothed Altes-Marinovic distribution works does as well as or better than other Hyperbolic class TFDs in cross term removal and auto term preservation in the examples that were considered in this thesis.

In the sixth chapter, the proposed implementation of the Hyperbolic class of TFRs using the Fast Mellin transform (discussed in the fourth chapter) is compared and contrasted in terms of memory requirements, computational time, etc. with the Canfield and Jones warping method. Also, the conclusions and future work will be provided.

Chapter 2

Introduction to Time-Frequency Analysis

2.1 Motivation for Time-Frequency analysis

The fundamental idea of time-frequency distributions is to understand and describe situations where the frequency content of a signal is changing in time [9]. The Fourier transform spectrum allows us to determine the frequencies that existed for the whole duration of a signal but a combined time-frequency analysis allows us to determine which frequencies are present at a particular time. That is the basic aim - to display the frequencies that exist at each instant of time. This kind of analysis is needed in various nonstationary signals like speech signals, sonar signals, bio-acoustical and biological transients.

Let us consider an example which demonstrates the need for a time-frequency distribution. Consider a digital signal $x[n]$, given in Figure 2.1. The signal $x[n]$ consists of three windowed complex sinusoids of normalized frequencies 0.25, 0.05 and 0.15, respectively. The extent of the time support of $x[n]$ (i.e., the region of time support $n \in [n_0, n_1]$ such that $x[n] = 0$ for $n \notin [n_0, n_1]$) is the interval of time indices $n \in [1, 176]$. The extent of the time supports for the first, second and third windowed sinusoids are the intervals [1,48], [65, 112] and [129 176], respectively. The Fourier transform $X(f)$, of the signal, $x(t)$, is given by

$$X(f) = \int_{-\infty}^{\infty} x(t)\, e^{-j2\pi ft} dt. \tag{2.1}$$

The Discrete Fourier transform (DFT), $X[k]$ of the length N, causal, finite duration

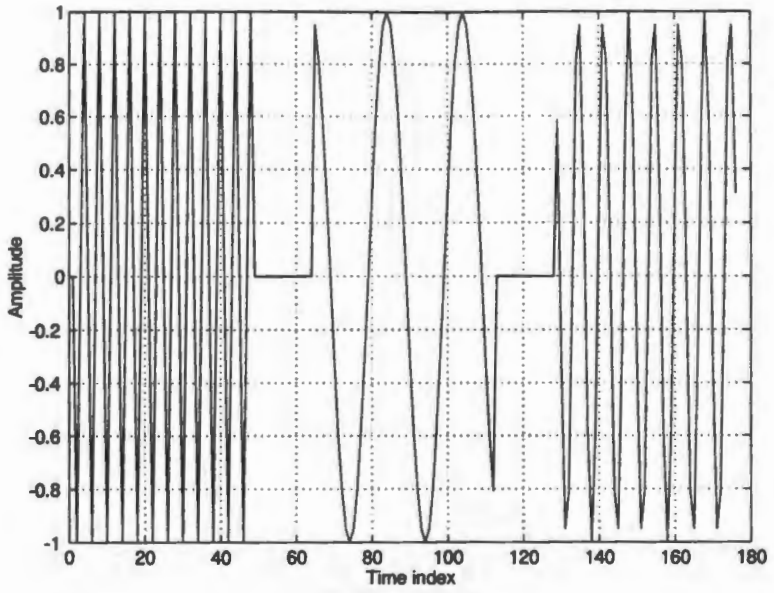

Figure 2.1: Real part of the time domain signal $x[n]$.

signal $x[n]$ is given by

$$X[k] = \sum_{n=0}^{N-1} x[n]\, e^{-j2\pi kn/N}, \tag{2.2}$$

where $k \in [0, N\text{-}1]$. If $x[n] = x(n\Delta T)$, and if $X(f)$ is sufficiently bandlimited, i.e, $|X(f)| = 0$ for $|f| > \frac{1}{2\Delta T}$, then $X[k] = X(\frac{k}{N\Delta T})$. In this thesis, the sampling period $\Delta T = 1$, unless otherwise indicated. The DFT magnitude $|X[k]|$, obtained by computing the Fast Fourier transform (FFT) [10] of the discrete-time signal, $x[n]$, is shown in Figure 2.2. As one can see, the Discrete Fourier transform shows peaks at 0.05, 0.15 and 0.25 in normalized frequency. But, the Discrete Fourier transform magnitude doesn't tell us when those frequencies occurred. The time domain analysis or the frequency domain analysis do not fully describe what is happening. This constitutes the need for time-frequency analysis since a time-frequency plot clearly shows which frequencies exist at a particular time.

An ideal time-frequency representation (TFR) for a signal should be similar to a musical score for a particular musical work. A musical score indicates what notes should be played, how long they should be held, how loudly they should be played and when they should be played. A time-frequency representation should indicate

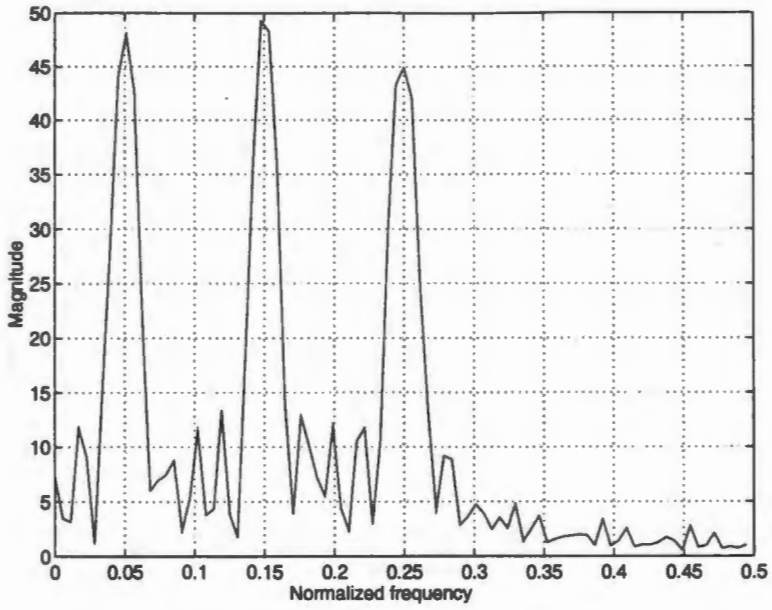

Figure 2.2: $|X[k]|$, the Discrete Fourier transform of $x[n]$.

what frequency components exist, their amplitude and the time intervals over which they exist. These criteria require that a time-frequency representation be plotted over a time-frequency plane. An ideal TFR for the signal $x[n]$ is shown in Fig 2.3.

The ideal TFR shows no uncertainty in the time or the frequency locations of the components of $x[n]$. However, Gabor points out in [11] that, for any signal, the time and frequency resolutions cannot be made arbitrarily precise simultaneously. Let Δt be the r.m.s. time duration for a signal component and let Δf be the r.m.s. frequency duration for the same component. Gabor states in [11] that time duration and frequency duration are related as follows:

$$\Delta t \Delta f \geq \frac{1}{4\pi} \tag{2.3}$$

which is also known as the uncertainty principle or the Heisenburg inequality [9]. This equation implies that there is a trade-off between time resolution and frequency resolution in a realizable TFR [11]. Formula (2.3) has been used to argue that a TFR does not have resolution to pinpoint simultaneously the exact time and frequency of a given signal component [11]. Because an ideal TFR shows no uncertainty in time or frequency, this TFR cannot be realised except for the cases in which it can be

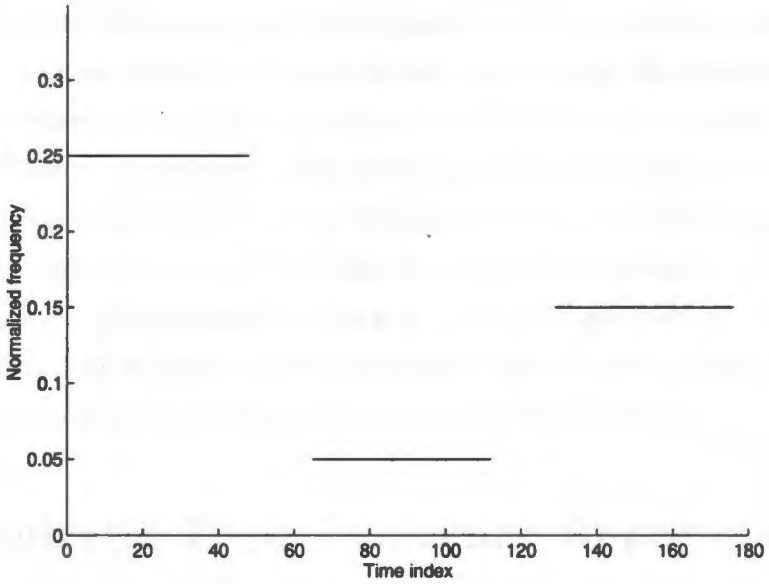

Figure 2.3: Ideal Time Frequency representation of the signal $x[n]$ in Figure 2.1.

generated by inspection.

2.2 Short-time Fourier transform

The short-time Fourier transform (STFT), whose squared magnitude is known as the spectrogram, is a linear time-frequency representation that was first used in 1946 with the invention of the sound spectrogram [12]. Since then, it has been used by many authors to analyze non-stationary signals [13-18]. The basic idea of the STFT is that if you want to know what frequencies exist at a particular time, then take a small segment of the signal around that time and Fourier analyze the small segment. Since the time interval is short compared to the whole signal, this process is called the taking the short-time Fourier transform. The length of the time interval is decided by the choice of the window function $\gamma(t)$ – the phrase "window" indicating that we look at only certain part of the signal[1].

$$\mathrm{STFT}_x^{(\gamma)}(t,f) = \int x(t')\gamma^*(t'-t)e^{-j2\pi ft'}dt'. \tag{2.4}$$

[1]Unless otherwise indicated, the limits of integration are assumed to extend from $-\infty$ to ∞

The STFT assumes that the signal is stationary over the duration of the window. The more compact we make the window in the time domain, the more time resolution is achieved. Similarly, if we choose a compact window in the frequency domain, high frequency resolution is achieved. But one cannot make both time resolution and frequency resolution arbitrarily good. Because of the uncertainty principle, there is an inherent tradeoff between time and frequency resolutions in the STFT for a particular window. This is the drawback of the STFT method, as it results in an unavoidable trade-off in time resolution versus frequency resolution. Some of the bilinear time-frequency representations do not face this problem.

2.3 Quadratic Time-Frequency Representations

Although linearity of a TFR is a desirable property, the quadratic structure of an TFR is an intuitively reasonable assumption when we want to interpret a TFR as a time-frequency energy distribution, since energy is a quadratic signal representation. An "energetic" TFR, $T_X(t,f)$, seeks to combine the concepts of the instantaneous power, $p_X(t) = |x(t)|^2$, and the spectral energy density, $P_X(f) = |X(f)|^2$. Ideally, this energetic representation is expressed by the *marginal properties*,

$$\begin{aligned} \int_f T_X(t,f)df &= p_X(t) = |x(t)|^2, \\ \int_t T_X(t,f)dt &= P_X(f) = |X(f)|^2, \end{aligned} \tag{2.5}$$

which state that the one-dimensional energy densities $p_X(t)$ and $P_X(f)$ are "marginal densities" of the TFR, $T_X(t,f)$. As a consequence, the signal energy $E_X = \int |x(t)|^2 dt = \int |X(f)|^2 df$ can be derived by integrating $T_X(t,f)$ over the entire time-frequency plane.

Many quadratic TFRs may be loosely interpreted in terms of signal energy even though they do not satisfy the marginal properties. Here, two prominent examples are the *Spectrogram* and the *Scalogram* defined as the squared magnitudes of the linear TFRs, the Short time Fourier transform and Wavelet transform, respectively. The Spectrogram is defined as

$$\mathrm{SPEC}_X^{(\gamma)}(t,f) = \left|\mathrm{STFT}_X^{(\gamma)}(t,f)\right|^2 \tag{2.6}$$

where $\mathrm{STFT}_X^{(\gamma)}(t,f)$ is defined in (2.4). The spectrogram has been extensively used to analyze speech signals [13, 19, 20] and other "nonstationary" signals. The Scalogram is defined as

$$\mathrm{SCAL}_X^{(\gamma)}(t,f) \;=\; \left|\mathrm{WT}_X^{(\gamma)}(t,f)\right|^2, \tag{2.7}$$

where $\mathrm{WT}_X^{(\gamma)}(t,f)$ is defined as

$$\mathrm{WT}_X^{(\gamma)}(t,f) \;=\; \int_{t'} x(t')\,\sqrt{|f/f_r|}\,\gamma^*\left(\frac{f}{f_r}(t'-t)\right)\,dt'. \tag{2.8}$$

Here, $\gamma(t)$ (the "mother wavelet") is a real or a complex bandpass function centered around $t=0$ in the time domain [21, 22]. Similar time-varying spectral representations are the sonagram, rayspan and spectran [16]. The scalogram [23, 22] can be considered as a "constant-Q version" of the spectrogram.

The Spectrogram of the sum of two signals, $x_1(t)+x_2(t)$, is not simply the sum of the individual spectrograms, $\mathrm{SPEC}_{X_1}^{(\gamma)}(t,f)+\mathrm{SPEC}_{X_2}^{(\gamma)}(t,f)$; hence, the linearity structure of the STFT is violated in the quadratic spectrogram. In fact, any quadratic TFR, T_X, satisfies the "quadratic superposition principle"

$x(t) \;=\; c_1x_1(t)+c_2x_2(t) \Longrightarrow$

$T_X(t,f) \;=\; |c_1|^2\,T_{X_1}(t,f)+|c_2|^2\,T_{X_2}(t,f)+c_1c_2^*\,T_{X_1X_2}(t,f)+c_2c_1^*\,T_{X_2X_1}(t,f)$

where $T_X(t,f)$ is the "auto-TFR" of the signal x(t) and $T_{X_1X_2}$ is the "cross-TFR" of the two-signals $x_1(t)$ and $x_2(t)$ with $T_{XX}(t,f)=T_X(t,f)$. Note that the cross-TFR $T_{X_1X_2}(t,f)$ is bilinear in the signals $x_1(t)$ and $x_2(t)$ [9].

The interference terms of the spectrogram and the scalogram are oscillatory structures which are restricted to those regions of the time-frequency plane where the corresponding auto representations (signal terms) overlap. Hence, if two signal components are sufficiently far apart in the time-frequency plane, then their cross representation (interference term) will be essentially zero [24-27]. This property is generally deemed desirable. On the other hand, a disadvantage of the spectrogram and the scalogram is their poor time-frequency concentration (or resolution) in some regions of the time-frequency plane. The Wigner distribution, to be discussed next, has excellent time-frequency concentration, but substantial interference terms.

2.4 Wigner distribution and Ambiguity Function

The Wigner distribution (WD) was introduced by E.P. Wigner [28] in 1932 in the context of quantum mechanics and later resurrected by J. Ville [29] in 1948 in the context of communications. The Wigner distribution of the signal $x(t)$ is defined as

$$W_X(t,f) = \int x(t+\frac{\tau}{2})\, x^*(t-\frac{\tau}{2})\, e^{-j2\pi f\tau}\, d\tau. \tag{2.9}$$

The Wigner distribution can also be equivalently represented by

$$W_X(t,f) = \int X(f+\frac{\nu}{2})\, X^*(f-\frac{\nu}{2})\, e^{j2\pi t\nu}\, d\nu, \tag{2.10}$$

where $X(f)$ represents the Fourier transform of $x(t)$ given by (2.1).

The WD satisfies a large number of desirable TFR properties and features optimal time-frequency concentration [30]. For example, $W_X(t,f)$ is always real-valued and preserves time shifts and frequency shifts of the signal $x(t)$. The real valuedness property is necessary for the interpretation $W_X(t,f)$ as an energy distribution. Unfortunately, however, the WD is not necessarily a positive function.

The Fourier dual counterpart of the WD in the *time lag/frequency lag* or "correlative" domain is the Woodward or narrowband ambiguity function (AF) which is defined as [1]

$$A_X(\tau,\nu) = \int x(t+\frac{\tau}{2})\, x^*(t-\frac{\tau}{2})\, e^{-j2\pi\nu t}\, dt \tag{2.11}$$

$$= \int X(f+\frac{\nu}{2})\, X^*(f-\frac{\nu}{2})\, e^{j2\pi\tau f}\, df. \tag{2.12}$$

The WD and the AF form a two-dimensional FT pair,

$$W_X(t,f) = \int\int A_X(\tau,\nu)\, e^{j2\pi(t\nu-f\tau)}\, d\tau\, d\nu. \tag{2.13}$$

A major drawback in the practical application of the WD is the problem of cross-terms or interference terms, especially if the WD of a multi-component signal is to be visually analyzed by a human signal analyst. Because the WD is a quadratic representation, cross-terms occur between every pair of auto-components of a multi-component signal [1].

The interference geometries of the WD and AF are illustrated in Figure 2.4 for the case of a signal composed of two time-frequency shifted Gaussian components having

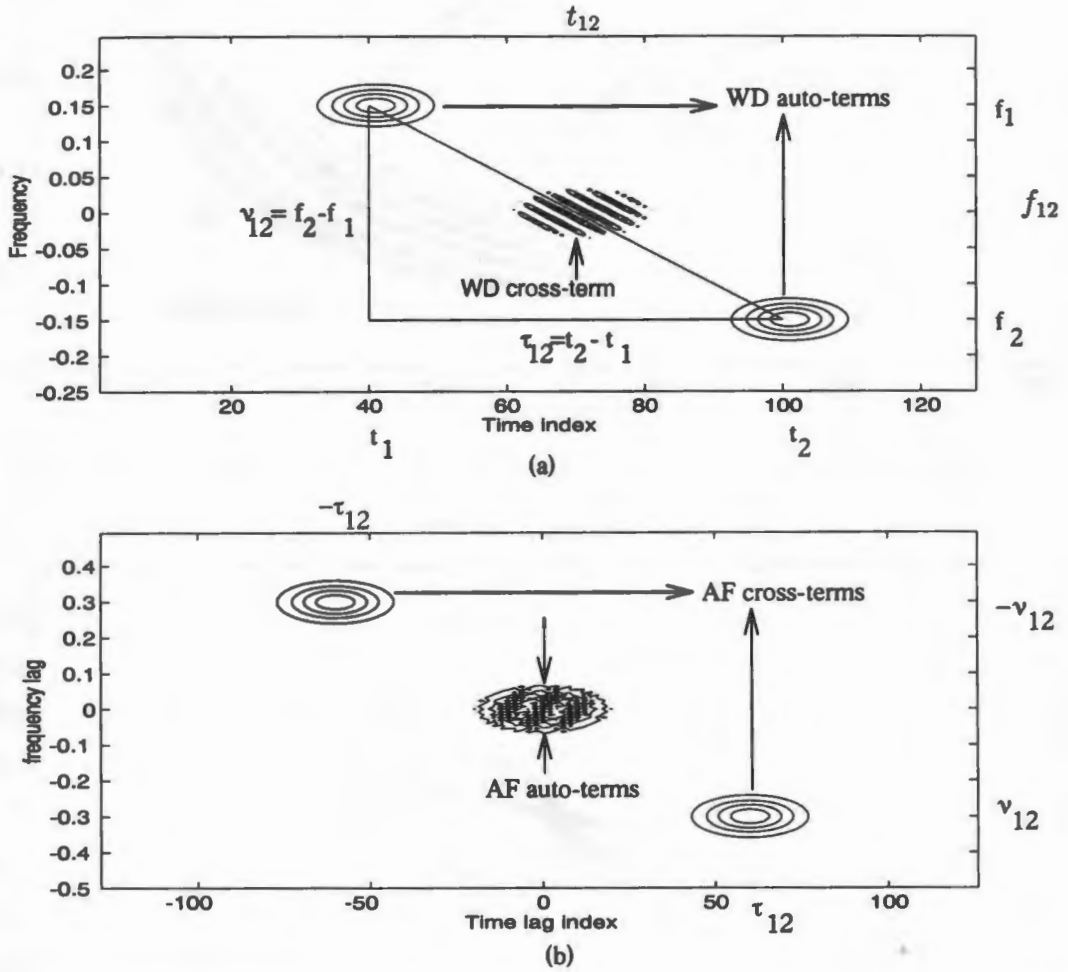

Figure 2.4: Interference geometries of the WD and the AF. (a) WD of a two-component Gaussian signal exhibiting an "outer" interference term centered at (t_{12}, f_{12}) and (b) corresponding AF with cross terms centered at (τ_{12}, ν_{12}) and $(-\tau_{12}, -\nu_{12})$. ($\tau_{12} = t_2 - t_1$, $\nu_{12} = f_2 - f_1$, $t_{12} = \frac{t_1+t_2}{2}$ and $f_{12} = \frac{f_1+f_2}{2}$)

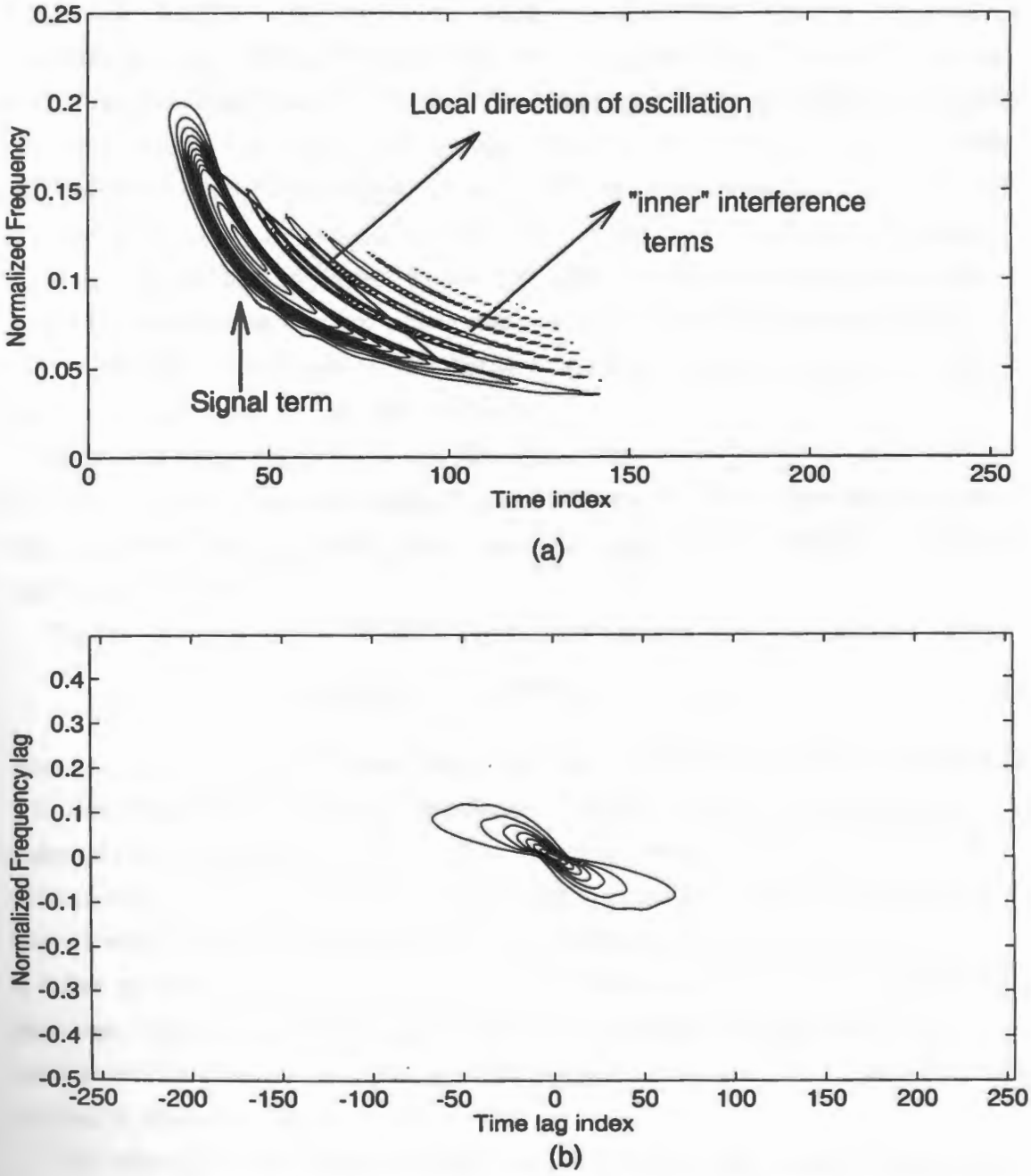

Figure 2.5: Interference geometries of the WD and the AF. (a) WD of a monocomponent Hyperbolic impulse in (2.14) (pre-tapered with a Hanning window) exhibiting "inner" interference terms and (b) corresponding AF.

equal amplitude and variance. When analyzing multicomponent signals, these geometries need to be taken into account. Figure 2.4 shows that two signal components occurring around the time-frequency points (t_1, f_1) and (t_2, f_2) produce two signal auto-term components and one cross-term component in the WD plane (see Figure 2.4(a)); there are two cross-terms components in the AF (see Figure 2.4 (b)) plane. Note that the cross-term component in the WD is located around the center point (t_{12}, f_{12}) with $t_{12} = (t_1 + t_2)/2$ and $f_{12} = (f_1 + f_2)/2$. The cross-term component is partly negative and oscillates. The overall direction of oscillation is perpendicular to the line connecting the two signal components and the frequency of this oscillation is directly proportional to the distance between the signal components in the time-frequency plane [1]. See Figure (2.4(a)).

In the ambiguity function plane, the signal terms are located around the origin of the $\tau - \nu$ plane. The cross-term components consists of two terms located around the "lag points" (τ_{12}, ν_{12}) and $(-\tau_{12}, -\nu_{12})$, where $\tau_{12} = t_2 - t_1$ and $\nu_{12} = f_2 - f_1$. See Figure (2.4(b)).

Figure 2.5(a) shows the WD of a Hyperbolic impulse signal defined as

$$H_c(f) = \frac{1}{\sqrt{f}} e^{-2j\pi c \ln\left(\frac{f}{f_r}\right)}, \; f \geq 0. \tag{2.14}$$

Here, $f_r > 0$ is a fixed reference frequency and its value is chosen to be equal to 1 in this thesis unless otherwise mentioned. The parameter $c \in \mathbb{R}$ determines the shape of the hyperbola and will be called *hyperbolic parameter* [3]. In the hyperbolic examples in this thesis, the infinite bandwidth signal in (2.14) was pretapered or filtered with a Hanning window [10] in the frequency domain and an inverse FFT is taken to obtain the corresponding signal in the time domain for computational purposes. This example illustrates the fact that the WD of a monocomponent signal can also exhibit cross-terms which are called "inner" cross-terms [1]. The AF of such a signal is shown in Figure 2.5 (b).

The bilinear time-frequency distributions are grouped into various classes depending upon the properties they exhibit. The most extensively studied and researched class of time frequency distributions is the Cohen's fixed kernel class or simply referred to as Cohen's class of time frequency distributions [1]. These Cohen's class members are invariant to time shifts and frequency shifts, as shown in equation (1.1).

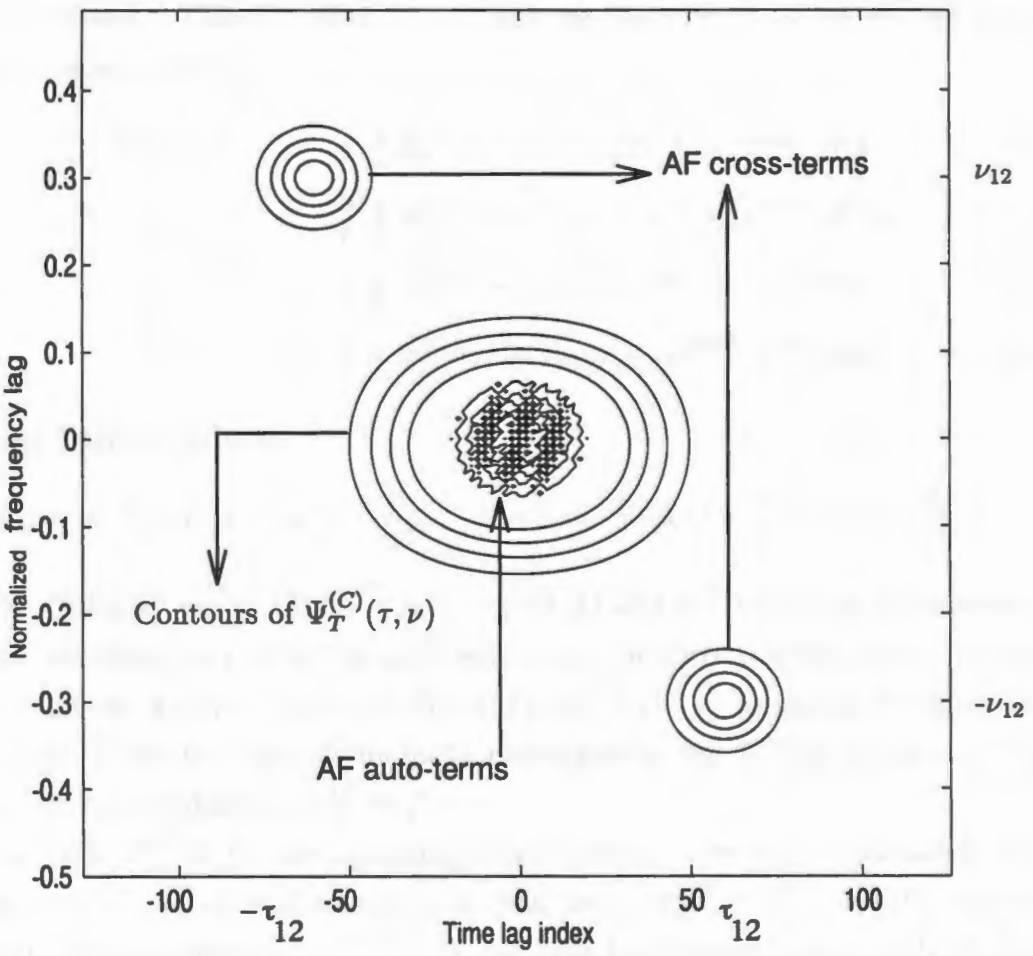

Figure 2.6: Interference geometry of the AF of a two component Gaussian signal exhibiting "outer"interference. The contours of a Cohen's class kernel, $\Psi_T^{(C)}(\tau,\nu)$, are shown superimposed on the AF of the signal in order to give more intuition into the product, $\Psi_T^{(C)} A_X$, shown in Eq. (2.18).

2.5 Cohen's Class of Time-Frequency representations

The Wigner distribution is one member of a large class of time-frequency representations, known as Cohen's class [5]. All the members of this class of distributions have the general forms

$$T_X^{(C)}(t,f) = \int\int \phi_T^{(C)}(t-t',\tau)\, u_X(t',\tau)\, e^{-j2\pi f\tau}\, dt'd\tau \quad (2.15)$$

$$= \int\int \Phi_T^{(C)}(f-f',\nu)\, U_X(f',\nu)\, e^{j2\pi t\nu}\, df'd\nu \quad (2.16)$$

$$= \int\int \psi_T^{(C)}(t-t',f-f')\, W_X(t',f')\, dt'df' \quad (2.17)$$

$$= \int\int \Psi_T^{(C)}(\tau,\nu)\, A_X(\tau,\nu)\, e^{j2\pi(t\nu-f\tau)}\, d\tau d\nu \quad (2.18)$$

with the "signal products"

$$u_X(t,\tau) \triangleq x(t+\frac{\tau}{2})\, x^*(t-\frac{\tau}{2}), \quad U_X(f,\nu) \triangleq X(f+\frac{\nu}{2})\, X^*(f-\frac{\nu}{2}).$$

The "kernels" $\phi_T^{(C)}(t,\tau)$, $\Phi_T^{(C)}(f,\nu)$, $\psi_T^{(C)}(t,f)$ and $\Psi_T^{(C)}(\tau,\nu)$ are interrelated by Fourier transforms in exactly the same way as are the corresponding quadratic signal representations $u_X(t,\tau)$, $U_X(f,\nu)$, $W_X(t,f)$ and $A_X(\tau,\nu)$ as shown in Figure (2.7) [31]. Any of the four kernels uniquely characterizes the QTFR (Quadratic Time Frequency representations) $T_X^{(C)}(t,f)$.

The TFR, $T_X^{(C)}(t,f)$, corresponding to a "sufficiently smooth", real-valued kernel function, $\psi_T^{(C)}(t,f)$, or, equivalently, a lowpass kernel $\Psi_T^{(C)}(\tau,\nu)$, is called a smoothed WD [1]. The properties of $T_X^{(C)}(t,f)$ can now be discussed very easily in terms of the shape of the kernel, $\Psi_T^{(C)}(\tau,\nu)$, in the AF plane. The required constraints on the kernel $\Psi_T^{(C)}(\tau,\nu)$ in order for $T_X^{(C)}(t,f)$ to satisfy the desirable TFR properties listed in Table 2.1 are given in Table 2.2 [1]. In the Tables and throughout this thesis, $\langle x,y\rangle = \int x(t)y^*(t)dt$ denotes the inner product between $x(t)$ and $y(t)$. Also, the inner product between $T_X^{(C)}(t,f)$ and $T_Y^{(C)}(t,f)$ is defined by $\langle T_X^{(C)}(t,f), T_Y^{(C)}(t,f)\rangle = \int\int T_X^{(C)}(t,f)T_Y^{(C)*}(t,f)dtdf$.

For example, the *time marginal* and the *time moments* properties are easily met provided that $\Psi_T^{(C)}(0,\nu) = 1$, i.e., the kernel has a value of one along the ν-axis.

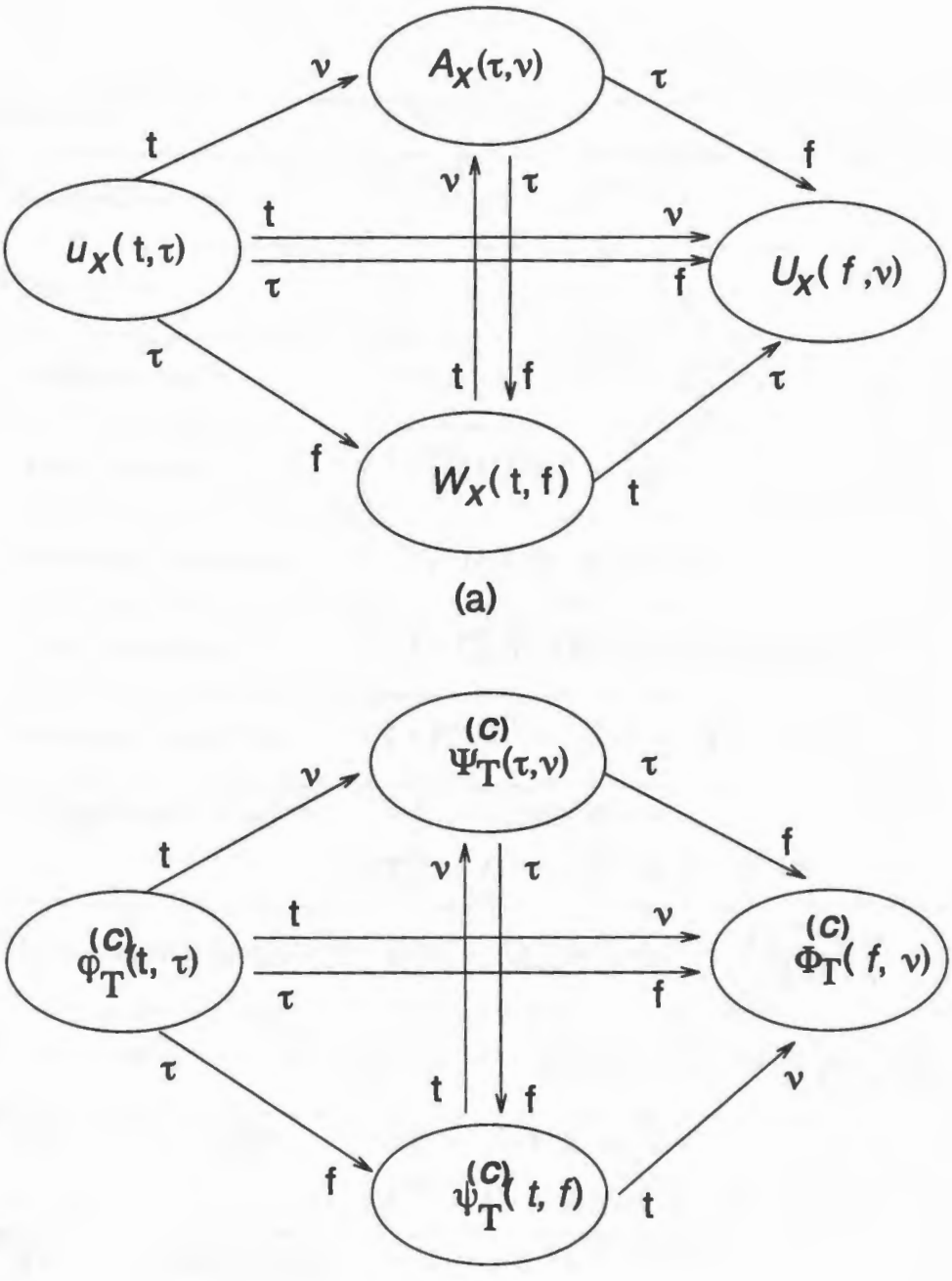

Figure 2.7: (a) The quadratic signal representations $u_X(t,\tau)$, $U_X(f,\nu)$, $A_X(\tau,\nu)$ and $W_X(t,f)$ are all interrelated by Fourier transforms; (b) identical Fourier-transform relations connect the four kernel functions $\varphi_T^{(C)}(t,\tau)$, $\Phi_T^{(C)}(f,\nu)$, $\Psi_T^{(C)}(\tau,\nu)$ and $\psi_T^{(C)}(t,f)$. Here, $\tau \rightarrow f$ indicates a Fourier transform from time lag τ to frequency f. (Figure was taken from [1]).

PROPERTY	RELATION
$P_1^{(C)}$:Real-valuedness	$T_X^{(C)}(t,f) = T_X^{(C)*}(t,f)$
$P_2^{(C)}$:Time shift	$\tilde{x}(t) = x(t-t_0) \Rightarrow T_{\tilde{X}}^{(C)}(t,f) = T_X^{(C)}(t-t_0,f)$
$P_3^{(C)}$:Frequency shift	$\tilde{x}(t) = x(t)e^{j2\pi f_0 t} \Rightarrow T_{\tilde{X}}^{(C)}(t,f) = T_X^{(C)}(t,f-f_0)$
$P_4^{(C)}$:Time marginal	$\int T_X^{(C)}(t,f)df = \lvert x(t)\rvert^2$
$P_5^{(C)}$:Frequency marginal	$\int T_X^{(C)}(t,f)dt = \lvert X(f)\rvert^2$
$P_6^{(C)}$:Time moments	$\int\int t^n T_X^{(C)}(t,f)dtdf = \int t^n \lvert x(t)\rvert^2 dt$
$P_7^{(C)}$:Frequency moments	$\int\int f^n T_X^{(C)}(t,f)dtdf = \int f^n \lvert X(f)\rvert^2 df$
$P_8^{(C)}$:Time-frequency scaling	$\tilde{x}(t) = \sqrt{\lvert a\rvert}x(at) \Rightarrow$ $T_{\tilde{X}}^{(C)}(t,f) = T_X^{(C)}(at,\frac{f}{a}), \forall a \neq 0$
$P_9^{(C)}$:Instantaneous frequency	$f_x(t) = \frac{1}{2\pi}\frac{d}{dt}arg[x(t)] = \frac{\int fT_X^{(C)}(t,f)df}{\int T_X^{(C)}(t,f)df}$
$P_{10}^{(C)}$:Group delay	$t_x(f) = -\frac{1}{2\pi}\frac{d}{df}arg[X(f)] = \frac{\int tT_X^{(C)}(t,f)dt}{\int T_X^{(C)}(t,f)dt}$
$P_{11}^{(C)}$:Finite time support	$x(t) = 0, \forall t \notin [t_1,t_2] \Rightarrow$ $T_X^{(C)}(t,f) = 0, \forall t \notin [t_1,t_2]$
$P_{12}^{(C)}$:Finite frequency support	$X(f) = 0, \forall f \notin [f_1,f_2] \Rightarrow$ $T_X^{(C)}(t,f) = 0, \forall f \notin [f_1,f_2]$

Table 2.1: Some "desirable" mathematical properties for time-frequency representations [1] (Table was taken from [2]). (Continued on next page)

PROPERTY	RELATION
$P_{13}^{(C)}$:Moyal's formula	$\left\langle T_X^{(C)}(t,f), T_Y^{(C)}(t,f)\right\rangle = \lvert\langle x,y\rangle\rvert^2$
$P_{14}^{(C)}$:Convolution in time	$\tilde{x}(t) = h(t) * x(t) \Rightarrow$ $T_{\tilde{X}}^{(C)}(t,f) = \int T_H^{(C)}(t-\beta,f) T_X^{(C)}(\beta,f) d\beta$
$P_{15}^{(C)}$:Convolution in frequency	$\tilde{X}(f) = H(f) * X(f) \Rightarrow$ $T_{\tilde{X}}^{(C)}(t,f) = \int T_H^{(C)}(t,f-\beta) T_X^{(C)}(t,\beta) d\beta$
$P_{16}^{(C)}$:Fourier transform	$\tilde{x}(t) = \sqrt{\lvert c\rvert} x(ct) \Rightarrow$ $T_{\tilde{X}}^{(C)}(t,f) = T_X^{(C)}(\frac{-f}{c}, ct), \forall c \neq 0$
$P_{17}^{(C)}$:Chirp convolution	$\tilde{x}(t) = x(t) * \sqrt{\lvert c\rvert}\exp(j2\pi\frac{c}{2}t^2) \Rightarrow$ $T_{\tilde{X}}^{(C)}(t,f) = T_X^{(C)}(t-\frac{f}{c}, f)$
$P_{18}^{(C)}$:Chirp multiplication	$\tilde{x}(t) = x(t)\exp(j2\pi\frac{c}{2}t^2) \Rightarrow$ $T_{\tilde{X}}^{(C)}(t,f) = T_X^{(C)}(t, f-ct)$
$P_{19}^{(C)}$:Positivity	$T_X^{(C)}(t,f) \geq 0$
$P_{20}^{(C)}$:Invertibility	$x(t)x^*(0) =$ $\int\int\int \Psi_T^{(-1)}(t,\nu) T_X^{(C)}(u,f) e^{j2\pi u(f+\nu)} e^{-j\pi\nu t} du df d\nu$
$P_{21}^{(C)}$:Causality	$T_X^{(C)}(t_0,f)$ depends on $x(t)$ only for $t \leq t_0$
$P_{22}^{(C)}$:Energy	$E_X = \int\int T_X^{(C)}(t,f) dt df = \langle x,x\rangle = \int \lvert x(t)\rvert^2 dt$

Table 2.1 (Continued).

The *frequency marginal* and *frequency moments* properties are satisfied by any kernel that is equal to one along the τ-axis (see Table 2.2).

In order to attenuate interference terms in Figures 2.4 and 2.6, the kernel $\Psi_T^{(C)}(\tau,\nu)$ must be close to zero around the "lag points" (τ_{12},ν_{12}) and $(-\tau_{12},-\nu_{12})$ and close to one around the origin of the $\tau-\nu$ plane. This follows from the fact that cross-terms are located away from the origin whereas signal terms are centered around the origin of the $\tau-\nu$ plane. See Figure 2.4(b). The idea is to let as much of the signal terms "pass" unchanged while "blocking" as much as possible of the cross-terms (see Figure 2.6). Quite generally, however, the filtering operation represented by (2.18) tends to produce the following effects: (1) a (desired) partial or full attenuation of cross-terms; (2) an (undesired) broadening of signal terms, i.e., a loss of time-frequency concentration; and (3) an (undesired) loss of some of the properties of the Wigner distribution. Thus, in general, the design of a "good" kernel function, $\Psi_T^{(C)}(\tau,\nu)$, is an attempt to achieve effect (1) while avoiding, as much as possible, effect (2) and, sometimes, also effect (3) [2].

2.5.1 Conventional TFRs

The Spectrogram of a signal $x(t)$, defined in (2.6) can also be written as,

$$\mathrm{SPEC}_X^{(\gamma)}(t,f) \;=\; \int\int A_\Gamma(-\tau,-\nu)\; A_X(\tau,\nu)\; e^{j2\pi(\nu t-\tau f)}\; d\nu\; d\tau, \tag{2.19}$$

which has a lowpass kernel, $\Psi_{\mathrm{SPEC}}^{(C)}(\tau,\nu) \;=\; A_\Gamma(-\tau,-\nu)$, that is essentially the ambiguity function of the analysis window, $\gamma(t)$. It suffers from a trade-off between time resolution versus frequency resolution since good time (frequency) resolution of the spectrogram requires a short (long) analysis window, $\gamma(t)$. Consequently, for lowpass windows $\gamma(t)$ and, hence, lowpass AF kernels, $\Psi_{\mathrm{SPEC}}^{(C)}(\tau,\nu)$, the spectrogram provides substantial interference attenuation but lacks good time-frequency concentration because the effective time and frequency supports of its smoothing kernel function cannot be independently controlled [1]. The spectrogram kernel corresponding to a short analysis window, $\gamma(t)$, is depicted in Figure (2.8)(a) whereas that corresponding to a longer window is shown in Figure (2.8)(b). The lack of control of the amount of smoothing along both the time and frequency axes becomes evident when Figures

PROPERTY	KERNEL CONSTRAINT
$P_1^{(C)}$:Real-valuedness	$\Psi_T^{(C)}(\tau,\nu) = \Psi_T^{(C)*}(-\tau,-\nu)$
$P_2^{(C)}$:Time shift	None
$P_3^{(C)}$:Frequency shift	None
$P_4^{(C)}$:Time marginal	$\Psi_T^{(C)}(0,\nu) = 1$
$P_5^{(C)}$:Frequency marginal	$\Psi_T^{(C)}(\tau,0) = 1$
$P_6^{(C)}$:Time moments	$\Psi_T^{(C)}(0,\nu) = 1$
$P_7^{(C)}$:Frequency moments	$\Psi_T^{(C)}(\tau,0) = 1$
$P_8^{(C)}$:Time-frequency scaling	$\Psi_T^{(C)}(\alpha\tau,\frac{\nu}{\alpha}) = \Psi_T^{(C)}(\tau,\nu), \forall\alpha \neq 0$
$P_9^{(C)}$:Instantaneous frequency	$\Psi_T^{(C)}(0,\nu) = 1$ and $\frac{\partial}{\partial\tau}\Psi_T^{(C)}(\tau,\nu)\|_{\tau=0} = 0$
$P_{10}^{(C)}$:Group Delay	$\Psi_T^{(C)}(\tau,0) = 1$ and $\frac{\partial}{\partial\nu}\Psi_T^{(C)}(\tau,\nu)\|_{\nu=0} = 0$
$P_{11}^{(C)}$:Finite time support	$\varphi_T^{(C)}(t,\tau) = 0, \|\frac{t}{\tau}\| > \frac{1}{2}$
$P_{12}^{(C)}$:Finite frequency support	$\Phi_T^{(C)}(f,\nu) = 0, \|\frac{f}{\nu}\| > \frac{1}{2}$
$P_{13}^{(C)}$:Moyal's formula	$\|\Psi_T^{(C)}(\tau,\nu)\| \equiv 1$
$P_{14}^{(C)}$:Convolution in time	$\Psi_T^{(C)}(\tau_1+\tau_2,\nu) = \Psi_T^{(C)}(\tau_1,\nu)\Psi_T^{(C)}(\tau_2,\nu)$
$P_{15}^{(C)}$:Convolution in frequency	$\Psi_T^{(C)}(\tau,\nu_1+\nu_2) = \Psi_T^{(C)}(\tau,\nu_1)\Psi_T^{(C)}(\tau,\nu_2)$
$P_{16}^{(C)}$:Fourier transform	$\Psi_T^{(C)}(-\frac{\nu}{c},c\tau) = \Psi_T^{(C)}(\tau,\nu), \forall c \neq 0$
$P_{17}^{(C)}$:Chirp convolution	$\Psi_T^{(C)}(\tau-\frac{\nu}{c},\nu) = \Psi_T^{(C)}(\tau,\nu), \forall c \neq 0$
$P_{18}^{(C)}$:Chirp multiplication	$\Psi_T^{(C)}(\tau,\nu-c\tau) = \Psi_T^{(C)}(\tau,\nu), \forall c \neq 0$
$P_{19}^{(C)}$:Positivity	$\Psi_T^{(C)}(\tau,\nu) = \sum_{k=1}^{\infty} c_k A_{H_k}^*(\tau,\nu), \sum_{k=1}^{\infty} c_k = 1$
$P_{20}^{(C)}$:Invertibility	$\Psi_T^{(C)}(\tau,\nu) \neq 0$
$P_{21}^{(C)}$:Causality	$\varphi_T^{(C)}(t,\tau) = \varphi_T^{(C)}(t,\tau)u(-t-\frac{\|\tau\|}{2})$
$P_{22}^{(C)}$:Energy	$\Psi_T^{(C)}(0,0) = 1$

Table 2.2: TFR properties and corresponding kernel constraints for Cohen's class (Table was taken from [2]). Here, $u(t) = 1, \forall\, t \geq 0$ and $u(t) = 0, \forall\, t < 0$ is a unit step function and $\{h_k(t)\}_{k=1}^{\infty}$ form an orthonormal set of square-summable functions.

(2.8)(a) and (2.8)(b) are compared.

The pseudo Wigner distribution (PWD) has the kernel function

$$\Psi^{(C)}_{\text{PWD}}(\tau,\nu) \;=\; \eta(\frac{\tau}{2})\,\eta^*(-\frac{\tau}{2}), \tag{2.20}$$

where $\eta(\tau)$ is a lowpass window function. As illustrated in Figure (2.8)(c), the PWD kernel exhibits a lack of attenuation along the frequency lag direction. Figure (2.8)(d) depicts a typical kernel for the smoothed pseudo Wigner distribution (SPWD). In contrast to the spectrogram, the SPWD has a separable kernel,

$$\Psi^{(C)}_{\text{SPWD}}(\tau,\nu) \;=\; \eta(\frac{\tau}{2})\,\eta^*(-\frac{\tau}{2})\,G(\nu), \tag{2.21}$$

which allows independent amounts of time and frequency smoothing. Moreover, with proper choices for the temporal window, $\eta(\tau)$, and the spectral window, $G(\nu)$, the SPWD is capable of performing better than the spectrogram [1].

An extensive list of TFRs can be found in [1]. The WD, with $\Psi^{(C)}_{\text{WD}}(\tau,\nu) \;=\; 1$, is considered by many to be the first TFR. Other classic or conventional Cohen's class TFRs include the Born-Jordan distribution, the Levin distribution, the Page distribution, the Rihaczek distribution, the spectrogram, the pseudo Wigner distribution and the smoothed pseudo Wigner distribution. Table 2.3 includes the kernels for all these representations as well as for the modern TFRs like the Choi-Williams distribution, the generalized exponential distribution, the Butterworth distribution, the cone-kernel distribution and the tilted Gaussian distribution [1, 32-34].

In certain cases, like in the case of a signal consisting of two or more Hyperbolic impulses (defined in (2.14)), the filtering operation represented by (2.18) becomes very challenging. Figure (2.9) shows the Ambiguity function of the sum of two Hyperbolic impulses in (2.14) with Hyperbolic parameters $c_1 \;=\; 2.5$ and $c_2 \;=\; 5$. The design of the kernel in the ambiguity function plane to filter out cross-terms is a very challenging problem in this example. For such kinds of signals, the Hyperbolic class of time frequency distributions [3], which will be discussed in later sections of the chapter, works well.

Also, the time-frequency (TF) shift invariance property underlying Cohen's class implies a type of TF analysis where the QTFRs analysis or desired resolution characteristics do not change with time t or frequency f [3]. In particular, all TF points

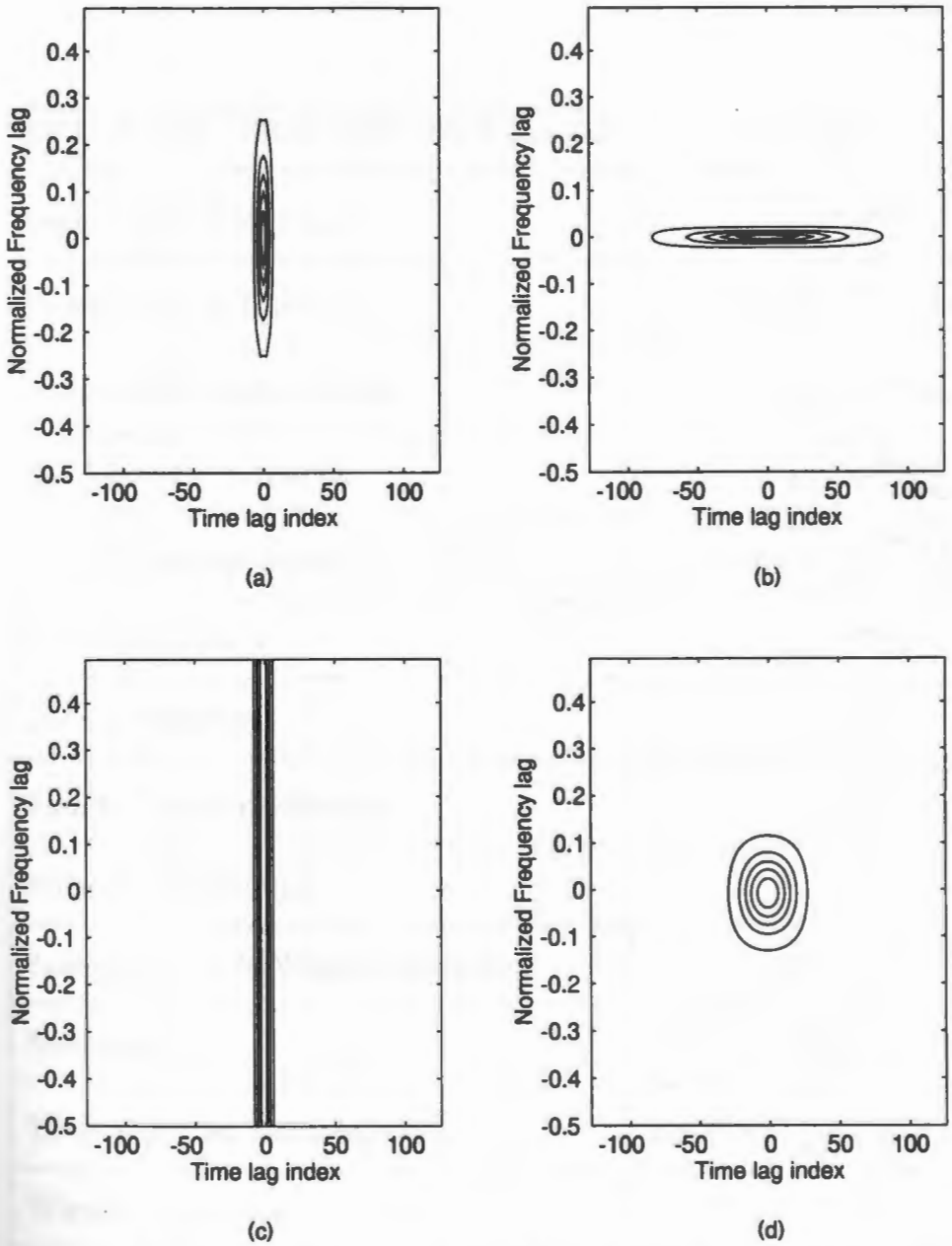

Figure 2.8: Ambiguity function domain contour plot of the kernels, $\Psi_T^{(C)}(\tau, \nu)$, for the Spectrogram, the pseudo Wigner distribution (PWD) and the smoothed pseudo Wigner distribution (SPWD). (a) Spectrogram for a short, 10-point Hamming window; (b) Spectrogram kernel for a long, 110-point Hamming window; (c) PWD kernel for a 10-point Hamming window; (d) SPWD kernel with a 40 point Hanning window for frequency smoothing and 10 point Hamming window for time smoothing.

TIME-FREQUENCY REPRESENTATION	$\Psi_T^{(C)}(\tau,\nu)$
Born-Jordan distribution	$\frac{\sin(\pi\tau\nu)}{\pi\tau\nu}$
Butterworth distribution	$\left[1+\left[\frac{\tau}{\tau_1}\right]^{2M}\left[\frac{\nu}{\nu_1}\right]^{2N}\right]^{-1}$
Choi-Williams distribution	$\exp\left[-\frac{(2\pi\tau\nu)^2}{\sigma}\right]$
Cone-kernel distribution	$g(\tau)\lvert\tau\rvert\frac{\sin(\pi\tau\nu)}{\pi\tau\nu}$
Generalized exponential distribution	$\exp\left\{-\left[\frac{\tau}{\tau_1}\right]^{2M}\left[\frac{\nu}{\nu_1}\right]^{2N}\right\}$
Levin distribution	$e^{j\pi\lvert\tau\rvert\nu}$
Page distribution	$e^{-j\pi\lvert\tau\rvert\nu}$
Pseudo Wigner distribution	$\eta(\frac{\tau}{2})\eta^*(-\frac{\tau}{2})$
Rihaczek distribution	$e^{j\pi\tau\nu}$
Smoothed pseudo Wigner distribution	$\eta(\frac{\tau}{2})\eta^*(-\frac{\tau}{2})G(\nu)$
Spectrogram	$A_\Gamma(-\tau,-\nu)$
Tilted Gaussian distribution	$\exp\left\{-\pi\left[[\frac{\tau}{\tau_0}]^2+[\frac{\nu}{\nu_0}]^2+2r[\frac{\tau\nu}{\tau_0\nu_0}]\right]\right\}$
Wigner distribution	1

Table 2.3: Definition of the Ambiguity function domain kernel $\Psi_T^{(C)}(\tau,\nu)$ for various Cohen's class time-frequency distributions. (Table was taken from [2]).

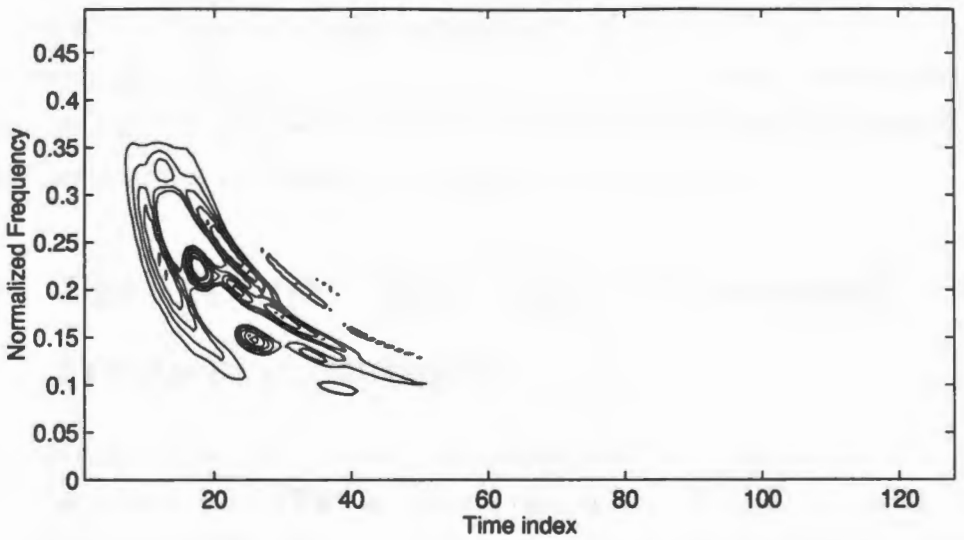

(a)

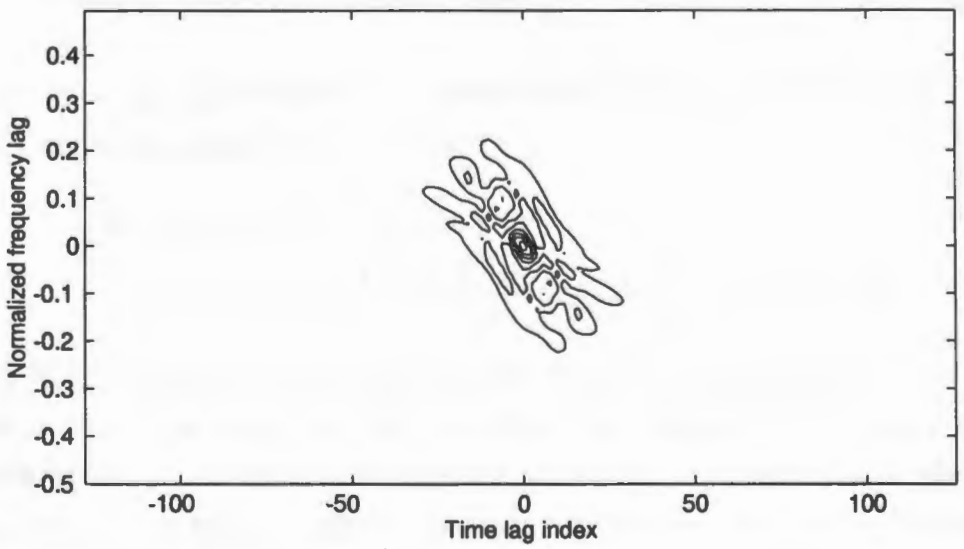

(b)

Figure 2.9: Figure showing the difficulty of Cohen's class QTFRs when dealing with Hyperbolic impulses. (a) Wigner distribution of the sum of two Hyperbolic impulses with Hyperbolic parameters $c_1 = 2.5$ and $c_2 = 5$. (b) magnitude of the Ambiguity function of the sum of two Hyperbolic impulses.

(t, f) are analyzed with the same time resolution and frequency resolution. This is similar to the *constant band-width* analysis achieved by short-time Fourier transform, where the analysis bandwidth does not depend on the analysis time or analysis frequency. In fact, the squared magnitude of the short-time Fourier transform (known as the spectrogram) is a member of Cohen's class [1, 35].

2.6 The Affine class and Constant-Q Time-Frequency Analysis

An alternative to the constant-bandwidth analysis achieved by the short-time Fourier transform and QTFRs of Cohen's class is provided by the *wavelet transform* and QTFRs of the *affine class*. For the wavelet transform defined in (2.8), the analysis bandwidth is proportional to the analysis frequency f, i.e., the quality factor (Q = center frequency $\div$ bandwidth) is independent of the analysis frequency ("constant-Q analysis").

The squared magnitude of the wavelet transform (known as the *scalogram*) [36] can be written in terms of the WD as

$$\begin{aligned} \mathrm{SCAL}_x(t,f) &= |\mathrm{WT}_x(t,f)|^2 \\ &= \int\int W_\Gamma\left(\frac{f}{f_r}(t'-t), f_r\frac{f'}{f}\right) W_x(t',f')\,dt'df' \end{aligned} \tag{2.22}$$

where $\Gamma(f)$ is the Fourier transform of the wavelet $\gamma(t)$ used in (2.8)[36]. Hence, the scalogram is a smoothed WD, for which the amounts of frequency and time smoothing are proportional and inversely proportional, respectively, to the analysis frequency f. This type of "affine smoothing" results in a constant-Q TF analysis.

The *affine class* of QTFRs is obtained by generalizing (2.22) as

$$T_x^{(A)}(t,f) = \int\int \psi_T^{(A)}\left(f(t-t'), \frac{f'}{f}\right) W_x(t',f')\,dt'df' \tag{2.23}$$

where $\psi_T^{(A)}(\alpha,\beta)$ is a two-dimensional kernel function [36-39]. If this kernel is a sufficiently smooth function concentrated about $\beta = 1$, then (2.23) results in an affine smoothing of the WD, just as in the case of the scalogram in (2.22). The affine

QTFR class can alternatively be defined as the class of all QTFRs that are covariant to time-shifts and TF scalings as defined in the first chapter.

An alternative approach to constant-Q analysis has been proposed by Altes in [40]. A specific TF warping is used to convert the WD into a "wideband WD" called the *Q-distribution*. This approach, which is also closely connected with the TF scaling operator C_a as discussed in the first chapter, will be further considered in Section 2.7.

2.7 The Hyperbolic Geometry

The scaling operator C_a discussed in chapter 1 is intimately related to a "hyperbolic TF geometry" [37]-[41], [40]-[42]. First of all, consider the *hyperbolic impulse* [43] defined in the frequency domain in (2.14). The hyperbolic impulse mentioned in (2.14) is an analytic signal with spectr al energy density $|H_c(f)|^2 = \frac{1}{f}\,\mathrm{u}(f)$ and its group delay corresponds to a hyperbola $t = c/f$ u(f) in the TF plane where $u(f)$ is the unit ste p function (see Figure 2.10). The hyperbolic impulse naturally arises in the context of TF scalings since it is an eigenfunction of the TF scaling operator C_a [44], i.e.,

$$(C_a H_c)(f) = e^{j2\pi c \ln a}\, H_c(f)\,.$$

In other words, the scaling operator does not affect the hyperbolic impulse $H_c(f)$ except for a constant phase factor. This shows that the hyperbolic impulse is a "Doppler-invariant" signal similar to the signals used by bats and dolphins for echo location [45].

2.7.1 CONSTANT-Q WARPING AND THE HYPERBOLIC CLASS

2.7.2 Constant-Q Warping

Given a Cohen's class QTFR $T_X^{(C)}(t,f)$, a new QTFR is derived, $T_X^{(H)}(t,f)$, with constant-Q characteristic, conceptually similar to the wavelet transform or its

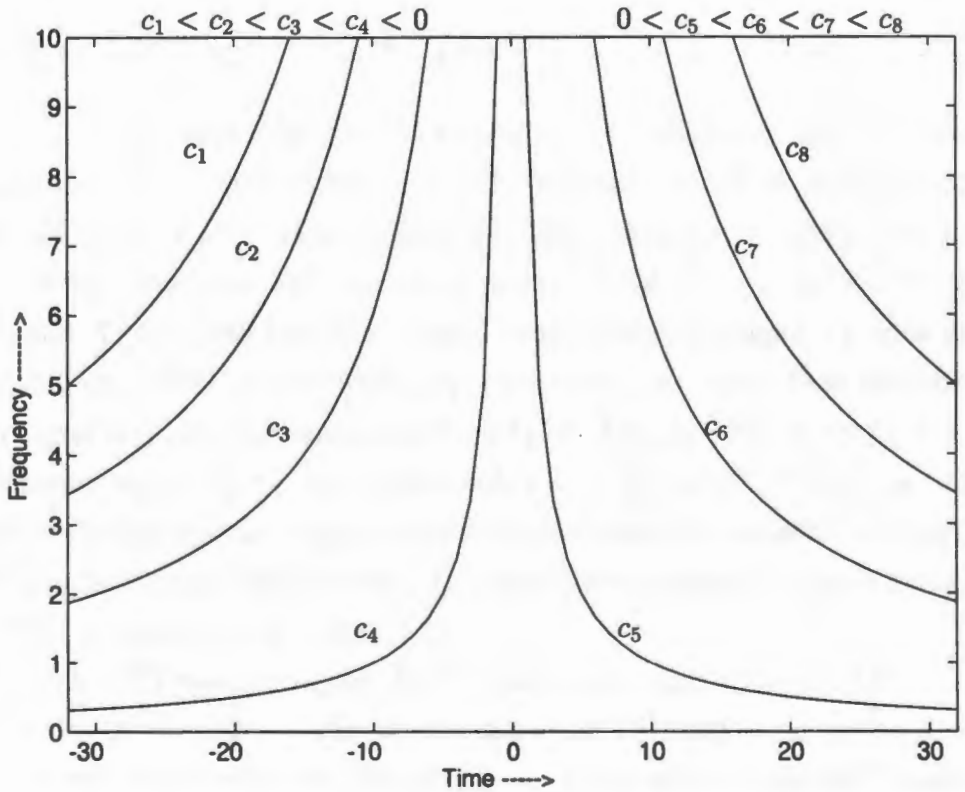

Figure 2.10: The hyperbolic time-frequency geometry. The hyperbolic impulse $H_c(f)$ and the hyperbolic time-shift operator $\mathcal{H}_c$ both correspond to a hyperbola $t = c/f$ in the TF plane. The family of hyperbolas $t = c/f$ covers the entire TF plane as the hyperbolic parameter c varies from $-\infty$ to ∞ (Figure was taken from [3]).

squared magnitude, the scalogram [3]. To this end, a "constant-Q warping" procedure [46] proposed consists of three steps which are visualized in Figure 2.11 [3]. In the following, let $x(t)$ be analytic, i.e., a signal whose Fourier transform $X(f)$ is zero for $f < 0$.

Step 1. The signal $X(f)$ is subjected to a *logarithmic frequency warping* $\mathcal{W}$ defined as

$$\tilde{X}(f) = (\mathcal{W}X)(f) \triangleq \sqrt{e^{f/f_r}}\, X\big(f_r\, e^{f/f_r}\big)\,, \qquad -\infty < f < \infty\,, \tag{2.24}$$

where $f_r > 0$ is a fixed reference (or normalization) frequency which is needed to obtain the correct physical dimensions. The warping defined in [40] is modified to include the factor $\sqrt{e^{f/f_r}}$ which makes the linear frequency warping transform $\mathcal{W}$ unitary [3, 4]. Note that the frequency-warped signal $\tilde{X}(f)$ is no longer analytic. If the signal $X(f)$ is well localized around time t_X and frequency f_X with effective duration τ_X and effective bandwidth ν_X, then it can be shown that the frequency-warped signal $\tilde{X}(f)$ is localized around time $t_{\tilde{X}} = \frac{f_X}{f_r}\, t_X$ and frequency $f_{\tilde{X}} = f_r \ln\frac{f_X}{f_r}$, with duration $\tau_{\tilde{X}} \approx \frac{f_X}{f_r}\tau_X$ and bandwidth $\nu_{\tilde{X}} \approx \frac{f_r}{f_X}\nu_X$ [3]. Thus, the mapping $\mathcal{W}$ produces a logarithmic frequency warping by which bandwidths are compressed proportional to the original frequency, f_X, and a time expansion which is proportional to f_X. This is illustrated in Figure 2.11.

Step 2. The TF-warped signal, $\tilde{X}(f)$, is analyzed using a given QTFR $T^{(C)}$ from Cohen's class. $T^{(C)}$ produces a constant-bandwidth TF analysis. However, the signal $\tilde{X}(f)$ has been subjected to the logarithmic frequency warping by which bandwidths are compressed proportional to frequency. Hence, the result of Step 2, $T^{(C)}_{\tilde{X}}(t,f)$, is actually a TF analysis where the effective analysis bandwidth is proportional to frequency f, i.e., a *constant-Q* analysis. On the other hand, due to the time expansion $t_{\tilde{X}} = \frac{f_X}{f_r}\, t_X$ and the frequency compression $f_{\tilde{X}} = f_r \ln\frac{f_X}{f_r}$ inherent in $\tilde{X}(f)$, the QTFR $T^{(C)}_{\tilde{X}}(t,f)$ will display the signal around $(t_{\tilde{X}}, f_{\tilde{X}})$ instead of the correct TF location (t_X, f_X) [3]. Thus, $T^{(C)}_{\tilde{X}}(t,f)$ shows incorrect "absolute TF localization" as shown in Figure 2.11.

Step 3. This incorrect TF localization is finally corrected by substituting $t \rightarrow \frac{f}{f_r}t$ and $f \rightarrow f_r \ln\frac{f}{f_r}$ in $T^{(C)}_{\tilde{X}}(t,f)$.

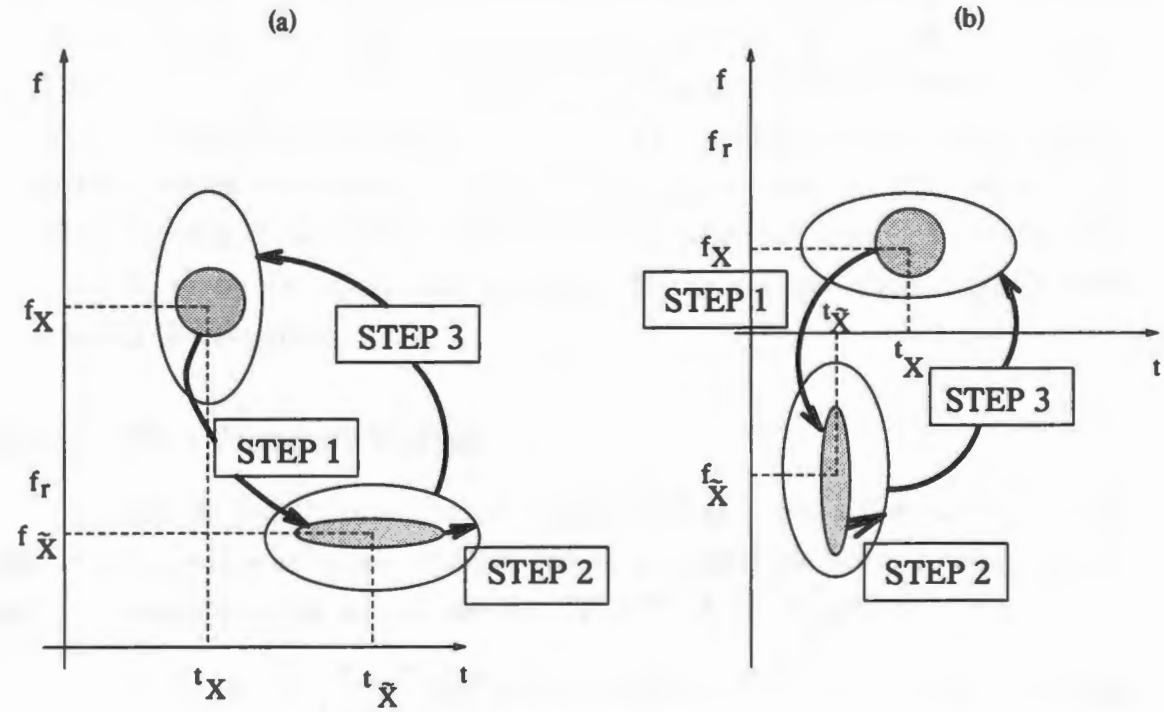

Figure 2.11: The geometry of constant-Q warping, depicted for (a) $\frac{f_X}{f_r} = 2$ and (b) $\frac{f_X}{f_r} = 1/2$. STEP 1 produces a TF displacement and a compression/dilation of duration and bandwidth. STEP 2 is a "constant-bandwidth" TF analysis with given TF concentration, resulting in a broadening that is independent of the TF location. STEP 3 produces a TF displacement and a dilation/compression of duration and bandwidth, both of which are inverse to Step 1. The final result is a TF representation that displays "high-frequency" signals with good time resolution but poor frequency resolution (see (a)) and "low-frequency" signals with poor time resolution but good frequency resolution (see (b)), i.e., a TF representation with constant-Q characteristic (Figure was taken from [3]) .

The three steps detailed above result in a new QTFR

$$T_X^{(H)}(t,f) \;\triangleq\; T_{WX}^{(C)}\Big(\frac{tf}{f_r},\, f_r \ln\frac{f}{f_r}\Big)\;, \qquad f>0\,, \tag{2.25}$$

defined for analytic signals $X(f)$. The QTFR $T_X^{(H)}(t,f)$ will produce a constant-Q TF analysis (with *correct* TF localization) provided that the original Cohen's class QTFR $T_X^{(C)}(t,f)$ can be interpreted as a constant-bandwidth TF analysis (i.e., if $T_X^{(C)}(t,f)$ is a smoothed WD [25]). Note that $T_X^{(H)}(t,f)$ is only defined for positive frequencies, which corresponds to the frequency support of the analytic signal $X(f)$.

The collection of all QTFRs $T_X^{(H)}(t,f)$ that are derived from Cohen's class QTFRs, $T_X^{(C)}(t,f)$, by the constant-Q warping (2.25) forms a new class of QTFRs with constant-Q characteristic.

2.7.3 The Normal Forms

Inserting the four "normal forms" (2.15)-(2.18) of Cohen's class into (2.25), the following four expressions are obtained (which are called the Normal Forms I, II, III and IV, respectively) for an arbitrary QTFR $T^{(H)}$ of the HC [3]:

$$T_X^{(H)}(t,f) \;=\; \int_{-\infty}^{\infty}\!\!\int_{-\infty}^{\infty} \phi_T^{(H)}(tf-c,\,\zeta)\; v_X(c,\zeta)\; e^{-j2\pi\left(\ln\frac{f}{f_r}\right)\zeta}\; dc\, d\zeta \tag{2.26}$$

$$= \int_{-\infty}^{\infty}\!\!\int_{-\infty}^{\infty} \Phi_T^{(H)}\Big(\ln\frac{f}{f_r}-b,\,\beta\Big)\; V_X(b,\beta)\; e^{j2\pi tf\beta}\; db\, d\beta \tag{2.27}$$

$$= \int_{-\infty}^{\infty}\!\!\int_{0}^{\infty} \psi_T^{(H)}\Big(tf-t'f',\,\ln\frac{f}{f'}\Big)\; Q_X(t',f')\; dt'\, df' \tag{2.28}$$

$$= \int_{-\infty}^{\infty}\!\!\int_{-\infty}^{\infty} \Psi_T^{(H)}(\zeta,\beta)\; B_X(\zeta,\beta)\; e^{j2\pi\left(tf\beta-\left(\ln\frac{f}{f_r}\right)\zeta\right)}\; d\zeta\, d\beta\,, \tag{2.29}$$

with the "hyperbolic signal products"

$$v_X(c,\zeta) \;\triangleq\; \frac{1}{f_r}\, u_{WX}\Big(\frac{c}{f_r},\frac{\zeta}{f_r}\Big)\;, \tag{2.30}$$

$$V_X(b,\beta) \;\triangleq\; f_r\, U_{WX}(f_r b, f_r\beta) \;=\; f_r e^{b}\; X\Big(f_r e^{b+\beta/2}\Big)\; X^*\Big(f_r e^{b-\beta/2}\Big)\;, \tag{2.31}$$

defined using u_X and U_X given in section 2.5, the TF version of the Q-distribution[2] (subsequently called *Altes-Marinovic distribution* (AD)) [40, 42]

$$\begin{aligned} Q_X(t,f) &= W_{WX}\left(\frac{tf}{f_r}, f_r \ln\frac{f}{f_r}\right) \qquad (2.32)\\ &= \int_{-\infty}^{\infty} v_X(tf,\zeta)\, e^{-j2\pi(\ln\frac{f}{f_r})\zeta}\, d\zeta = \int_{-\infty}^{\infty} V_X\left(\ln\frac{f}{f_r}, \beta\right) e^{j2\pi tf\beta}\, d\beta \\ &= f\int_{-\infty}^{\infty} X\left(fe^{\beta/2}\right)\, X^*\left(fe^{-\beta/2}\right)\, e^{j2\pi tf\beta}\, d\beta\,, \end{aligned}$$

and the "hyperbolic ambiguity function "[42]

$$\begin{aligned} B_X(\zeta,\beta) &= A_{WX}\left(\frac{\zeta}{f_r}, f_r\beta\right) \qquad (2.33)\\ &= \int_{-\infty}^{\infty} v_X(c,\zeta)\, e^{-j2\pi\beta c}\, dc = \int_{-\infty}^{\infty} V_X(b,\beta)\, e^{j2\pi\zeta b}\, db \\ &= \int_{0}^{\infty} X\left(fe^{\beta/2}\right)\, X^*\left(fe^{-\beta/2}\right)\, e^{j2\pi\zeta\ln\frac{f}{f_r}}\, df\,. \end{aligned}$$

The Hyperbolic Ambiguity function, $B_X(\zeta,\beta)$, is analogous to the Ambiguity function, $A_X(\tau,\nu)$, in the Cohen's class. Weighting different regions of the Hyperbolic Ambiguity function can be used to remove cross-terms similar to the way in which the Ambiguity function is used to remove cross-terms Figure 2.6. The way the Hyperbolic Ambiguity function and the normal form IV can be used to remove cross-terms will be discussed in the fifth chapter of this thesis.

One of the advantages of formulating the HC QTFRs in the specific forms given by (2.26)-(2.29), is that the kernels $\phi_T^{(H)}(c,\zeta)$, $\Phi_T^{(H)}(b,\beta)$, $\psi_T^{(H)}(c,b)$, and $\Psi_T^{(H)}(\zeta,\beta)$ are simply scaled versions of the respective kernels of the original Cohen's class QTFR $T_X^{(C)}(t,f)$:

$$\phi_T^{(H)}(c,\zeta) = \frac{1}{f_r}\,\phi_T^{(C)}\left(\frac{c}{f_r}, \frac{\zeta}{f_r}\right)\,, \qquad \Phi_T^{(H)}(b,\beta) = f_r\,\Phi_T^{(C)}(f_r b, f_r\beta)\,, \qquad (2.34)$$

$$\psi_T^{(H)}(c,b) = \psi_T^{(C)}\left(\frac{c}{f_r}, f_r b\right)\,, \qquad \Psi_T^{(H)}(\zeta,\beta) = \Psi_T^{(C)}\left(\frac{\zeta}{f_r}, f_r\beta\right)\,. \qquad (2.35)$$

[2]The original Q-distribution, $\tilde{Q}_X(c,f)=\int_{-\infty}^{\infty} X(fe^{\beta/2})\,X^*(fe^{-\beta/2})\,e^{j2\pi c\beta}\,d\beta$, introduced in [40], depends on the (dimensionless) hyperbolic parameter c and the frequency f. The TF version considered here is obtained as $Q_X(t,f) = f\,\tilde{Q}_X(c,f)|_{c=tf}$. A "time-domain" version of the Q-distribution, which is formulated using the time-domain signal $x(t)$ instead of the signal's Fourier transform $X(f)$, was proposed by Marinovic in [42].

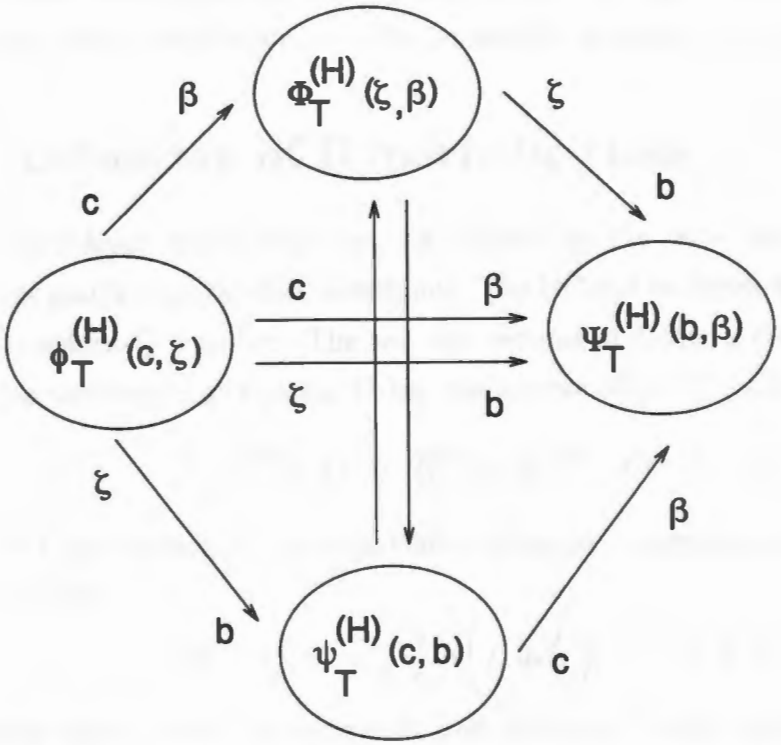

Figure 2.12: Fourier transform relations connecting the kernels of the hyperbolic class. An arrow "$a \longrightarrow b$" indicates a Fourier transform from a to b. (Figure was taken from [3]).

According to the normal forms (2.26)-(2.29), any member of the HC can be derived from the hyperbolic signal products $v_X(c,\zeta)$ and $V_X(b,\beta)$, the AD $Q_X(t,f)$ or the hyperbolic AF $B_X(\zeta,\beta)$ by some characteristic, two-dimensional transform. Also, any hyperbolic QTFR is characterized mathematically by any of the four two-dimensional kernels $\phi_T^{(H)}(c,\zeta)$, $\Phi_T^{(H)}(b,\beta)$, $\psi_T^{(H)}(c,b)$ and $\Psi_T^{(H)}(\zeta,\beta)$ [3].

Two prominent members of the HC are the AD $Q_X(t,f)$ defined in (2.32) and the *Bertrand unitary P_0-distribution* [43, 36, 38, 39] that is also a member of the affine class. Both distributions will be considered in more detail in Section 2.9.

2.8 Definition of Hyperbolic class

Cohen's fixed kernel class can be defined by the two "axioms" of time-shift covariance and frequency-shift covariance. The HC can be derived from Cohen's class via the constant-Q warping. The way the axioms of Cohen's class are transformed under this warping is as follows. Using the inverse of (2.25), one can show that

$$T_X^{(C)}(t,f) \;=\; T_{\mathcal{W}^{-1}X}^{(H)}(te^{-f/f_r}, f_r e^{f/f_r}). \tag{2.36}$$

Here, $\mathcal{W}^{-1}$, the inverse of the logarithmic-frequency-warping operator $\mathcal{W}$ in (2.24), is given by [3]

$$(\mathcal{W}^{-1}X)(f) = \sqrt{\frac{f_r}{f}}\, X\!\left(f_r \ln\frac{f}{f_r}\right), \qquad f>0\,.$$

It is easily shown that the time-shift and frequency-shift covariance properties of Cohen's class transform into the following properties of the corresponding hyperbolic class QTFR [3]:

$$T_{\mathcal{W}^{-1}\mathcal{S}_\tau\mathcal{W}X}^{(C)}(t,f) = T_X^{(C)}\!\left(t-\frac{f_r\tau}{f},\, f\right), \qquad T_{\mathcal{W}^{-1}\mathcal{M}_\nu\mathcal{W}X}^{(C)}(t,f) = T_X^{(C)}\!\left(e^{\nu/f_r}\,t,\, \frac{f}{e^{\nu/f_r}}\right).$$

The composite operators $\mathcal{W}^{-1}\mathcal{S}_\tau\mathcal{W}$ and $\mathcal{W}^{-1}\mathcal{M}_\nu\mathcal{W}$, which can be considered the images of the time-shift operator $\mathcal{S}_\tau$ and the frequency-shift operator $\mathcal{M}_\nu$ under the logarithmic frequency mapping $\mathcal{W}$, can be shown to be equal to the hyperbolic time-shift operator and the TF scaling operator, respectively, [3]

$$\mathcal{W}^{-1}\mathcal{S}_\tau\mathcal{W} = \mathcal{H}_{f_r\tau}\,, \qquad \mathcal{W}^{-1}\mathcal{M}_\nu\mathcal{W} = \mathcal{C}_{e^{\nu/f_r}}\,.$$

Setting $c = f_r\tau$ and $a = e^{\nu/f_r}$, we finally obtain the result that the HC properties corresponding to the time-shift and frequency-shift covariances of Cohen's class are the *hyperbolic time-shift covariance* (previously considered in [47]) and the *TF scale covariance*, respectively, as stated by the following theorem [3].

> *Theorem:* The HC is the class of all QTFRs which are covariant to hyperbolic time-shifts $\mathcal{H}_c$ and TF scalings $\mathcal{C}_a$ according to [3]
>
> $$T^{(H)}_{\mathcal{H}_c X}(t,f) = T_X\left(t-\frac{c}{f}, f\right), \qquad T^{(H)}_{\mathcal{C}_a X}(t,f) = T_X\left(at, \frac{f}{a}\right). \quad (2.37)$$

This means that the HC can be defined axiomatically by the above two covariance properties with respect to the operators $\mathcal{H}_c$ and $\mathcal{C}_a$, just as Cohen's fixed kernel class can be defined axiomatically by the time-shift and frequency-shift covariance properties, and just as the affine class can be defined by the time-shift and TF scale covariance properties. Note that the scale covariance property $T_{\mathcal{C}_a X}(t,f) = T_X(at, \frac{f}{a})$ is an axiom of both the affine class and the HC. In fact, the HC differs from the affine class merely by the fact that the conventional time-shift ($\mathcal{S}_\tau$) is replaced by the hyperbolic time-shift ($\mathcal{H}_c$) [3].

Since the family of hyperbolic impulses $H_c(f)$ with $-\infty < c < \infty$ covers the entire TF plane according to Figure 2.10, any finite-energy, analytic signal $X(f)$ can be written as a superposition of hyperbolic impulses,

$$X(f) = \int_{-\infty}^{\infty} \rho_X(c)\, H_c(f)\, dc = \int_{-\infty}^{\infty} \rho_X(c)\, \frac{1}{\sqrt{f}}\, e^{-j2\pi c \ln \frac{f}{f_r}}\, dc\,.$$

The *hyperbolic coefficient function* $\rho_X(c)$ is the inner product [3]

$$\rho_X(c) = \langle X, H_c \rangle = \int_0^{\infty} X(f)\, H_c^*(f)\, df = \int_0^{\infty} X(f)\, \frac{1}{\sqrt{f}}\, e^{j2\pi c \ln \frac{f}{f_r}}\, df\,. \quad (2.38)$$

It is also related to the Mellin transform of $X(f)$ [3].

The QTFR mapping (2.25) or, equivalently, the kernel mappings (2.34)-(2.35), establish a one-to-one correspondence between Cohen's class and the new HC, by which any QTFR, $T^{(C)}$, of Cohen's class is mapped into a QTFR, $T^{(H)}$, of the HC. Furthermore, any QTFR property, $\mathrm{P}^{(C)}$, of Cohen's class maps into a corresponding

QTFR property, P, in the HC and vice versa, in the sense that a Cohen's class QTFR satisfies property $P^{(C)}$ if and only if the corresponding hyperbolic QTFR satisfies the corresponding property P. Table 2.4 lists corresponding QTFR properties and the associated kernel constraints for the HC kernels [3][3]. These kernel constraints are identical to the well-known kernel constraints for Cohen's class [1] since, according to (2.34)-(2.35), the kernels of the two classes are themselves identical up to scaling by the reference frequency f_r.

The study of corresponding QTFR properties provides a means for understanding the structure of the HC, in particular, the HC's relation to the hyperbolic TF geometry. Therefore, the correspondences are summarized in Table 2.4.

2.9 Some Members of the Hyperbolic Class

Due to the one-to-one mapping between Cohen's class and the HC, any QTFR, $T^{(C)}$, of Cohen's class is mapped into a QTFR, $T^{(H)}$, of the HC. As a result, well-known Cohen's class QTFRs such as the (generalized) WD, the spectrogram, the smoothed pseudo-WD, the (generalized) Choi-Williams distribution, the Butterworth distribution etc. [1], can be converted into corresponding hyperbolic QTFRs that satisfy the hyperbolic time-shift covariance property and the scale covariance as well as other desirable properties. Conversely, using the inverse mapping in (2.36), we can also construct Cohen's class QTFRs corresponding to interesting hyperbolic QTFRs [48, 46], such as the Bertrand unitary P_0-distribution.

This section considers some specific QTFRs of the HC. We start with a discussion of the two most prominent hyperbolic QTFRs, the Altes-Marinovic distribution and the Bertrand unitary P_0-distribution. All hyperbolic QTFRs discussed are listed in Table 2.5 together with the corresponding QTFRs of Cohen's class. Table 2.6 shows the QTFR kernels and the QTFR properties satisfied.

[3]Note that the signals used in the context of QTFRs or QTFR properties of Cohen's class are not assumed analytic while they are in the HC .

COHEN'S CLASS PROPERTY	HYPERBOLIC CLASS PROPERTY	HYPERBOLIC CLASS KERNEL CONSTRAINT
$P_2^{(C)}$: time-shift covariance $(\mathcal{S}_\tau X)(f) = e^{-j2\pi\tau f} X(f) \Rightarrow$ $T^{(C)}_{\mathcal{S}_\tau X}(t,f) = T^{(C)}_X(t-\tau, f)$	P_1: hyperbolic time-shift covariance $(\mathcal{H}_c X)(f) = e^{-j2\pi c \ln \frac{f}{f_r}} X(f) \Rightarrow$ $T^{(H)}_{\mathcal{H}_c X}(t,f) = T^{(H)}_X(t-\frac{c}{f}, f)$	always satisfied
$P_3^{(C)}$: frequency-shift covariance $(\mathcal{M}_\nu X)(f) = X(f-\nu) \Rightarrow$ $T^{(C)}_{\mathcal{M}_\nu X}(t,f) = T^{(C)}_X(t, f-\nu)$	P_2: scale covariance $(\mathcal{C}_a X)(f) = \frac{1}{\sqrt{a}} X(\frac{f}{a}) \Rightarrow$ $T^{(H)}_{\mathcal{C}_a X}(t,f) = T^{(H)}_X(at, \frac{f}{a})$	always satisfied
$P_1^{(C)}$: real-valuedness $T^{(C)}_X(t,f) = T^{(C)*}_X(t,f)$	P_3: real-valuedness $T^{(H)}_X(t,f) = T^*_X(t,f)$	$\Psi^{(H)*}_T(-\zeta,-\beta) = \Psi^{(H)}_T(\zeta,\beta)$
$P_{22}^{(C)}$: energy distribution $\int_{-\infty}^{\infty}\int_{-\infty}^{\infty} T^{(C)}_X(t,f)\,dtdf = \int_{-\infty}^{\infty} \lvert X(f)\rvert^2\,df$	P_4: energy distribution $\int_{-\infty}^{\infty}\int_{0}^{\infty} T^{(H)}_X(t,f)\,dt\,df = \int_{0}^{\infty} \lvert X(f)\rvert^2\,df$	$\Psi^{(H)}_T(0,0) = 1$
$P_5^{(C)}$: frequency marginal $\int_{-\infty}^{\infty} T^{(C)}_X(t,f)\,dt = \lvert X(f)\rvert^2$	P_5: frequency marginal $\int_{-\infty}^{\infty} T^{(H)}_X(t,f)\,dt = \lvert X(f)\rvert^2$	$\Psi^{(H)}_T(\zeta,0) = 1$
$P_{13}^{(C)}$: Moyal's formula/unitarity $\left\langle T^{(C)}_{X_1}, T^{(C)}_{X_2}\right\rangle = \lvert\langle X_1, X_2\rangle\rvert^2$	P_6: Moyal's formula/unitarity $\left\langle T^{(H)}_{X_1}, T^{(H)}_{X_2}\right\rangle = \lvert\langle X_1, X_2\rangle\rvert^2$	$\lvert\Psi^{(H)}_T(\zeta,\beta)\rvert = 1$

Table 2.4: Corresponding properties of Cohen's class $P_i^{(C)}$ defined in Table 2.1 and the P_j of hyperbolic class. Here, $\rho_X(c)$ is defined in (2.38). (Table was taken from [3] and [4]) (Continued on next four pages)

COHEN'S CLASS PROPERTY	HYPERBOLIC CLASS PROPERTY	HYPERBOLIC CLASS KERNEL CONSTRAINT
$P_{10}^{(C)}$: group delay $\frac{\int_{-\infty}^{\infty} t\, T_X^{(C)}(t,f)\, dt}{\int_{-\infty}^{\infty} T_X^{(C)}(t,f)\, dt} = -\frac{1}{2\pi}\frac{d}{df}\arg X(f)$	P_7: group delay $\frac{\int_{-\infty}^{\infty} t\, T_X^{(H)}(t,f)\, dt}{\int_{-\infty}^{\infty} T_X^{(H)}(t,f)\, dt} = -\frac{1}{2\pi}\frac{d}{df}\arg X(f)$	$\Psi_T^{(H)}(\zeta,0) = 1$ and $\frac{\partial}{\partial\beta}\Psi_T^{(H)}(\zeta,\beta)\Big\vert_{\beta=0} = 0$
$P_{12}^{(C)}$: finite frequency support $X(f) = 0$ for $f \notin [f_1, f_2] \Rightarrow$ $T_X^{(C)}(t,f) = 0$ for $f \notin [f_1, f_2]$	P_8: finite frequency support $X(f) = 0$ for $f \notin [f_1, f_2] \Rightarrow$ $T_X^{(H)}(t,f) = 0$ for $f \notin [f_1, f_2]$	$\Phi_T^{(H)}(b,\beta) = 0$ for $\vert\frac{b}{\beta}\vert > \frac{1}{2}$
$P^{(C)}$: Dirac frequency localization $X(f) = \delta(f-f_0) \Rightarrow$ $T_X^{(C)}(t,f) = \delta(f-f_0)$	P_9: Dirac frequency localization $X(f) = \delta(f-f_0)$, $f_0 > 0 \Rightarrow$ $T_X^{(H)}(t,f) = \delta(f-f_0)$	$\Psi_T^{(H)}(\zeta,0) = 1$
$P_4^{(C)}$: time marginal $\int_{-\infty}^{\infty} T_X^{(C)}(t,f)\, df = \vert x(t)\vert^2$	P_{10}: hyperbolic marginal $\int_0^{\infty} T_X^{(H)}(\frac{c}{f},f)\frac{df}{f} = \vert\rho_X(c)\vert^2$	$\Psi_T^{(H)}(0,\beta) = 1$
$P^{(C)}$: Dirac time localization $X(f) = e^{-j2\pi t_0 f} \Rightarrow$ $T_X^{(C)}(t,f) = \delta(t-t_0)$	P_{11}: hyperbolic localization $H_c(f) = \frac{1}{\sqrt{f}}\, e^{-j2\pi c \ln\frac{f}{f_r}}\, u(f) \Rightarrow$ $T_{H_c}^{(H)}(t,f) = \frac{1}{f}\,\delta(t-\frac{c}{f})$, $f > 0$	$\Psi_T^{(H)}(0,\beta) = 1$

Table 2.4 (continued).

COHEN'S CLASS PROPERTY	HYPERBOLIC CLASS PROPERTY	HYPERBOLIC CLASS KERNEL CONSTRAINT
$\mathrm{P}_{11}^{(C)}$: finite time support $x(t)=0$ for $t \notin [t_1,t_2] \Rightarrow$ $T_X^{(C)}(t,f)=0$ for $t \notin [t_1,t_2]$	P_{12}: finite hyperbolic support $\rho_X(c)=0$ for $c \notin [c_1,c_2] \Rightarrow$ $T_X^{(H)}(\frac{c}{f},f)=0$ for $c \notin [c_1,c_2]$	$\phi_T^{(H)}(c,\zeta)=0$ for $\lvert\frac{c}{\zeta}\rvert > \frac{1}{2}$
$\mathrm{P}_{6}^{(C)}$: time moments $\int_{-\infty}^{\infty}\int_{-\infty}^{\infty} t^n T_X^{(C)}(t,f)\,dt\,df =$ $\int_{-\infty}^{\infty} t^n \lvert x(t)\rvert^2\,dt$	P_{13}: hyperbolic moments $\int_{-\infty}^{\infty}\int_{0}^{\infty} c^n T_X^{(H)}(\frac{c}{f},f)\,dc\,\frac{df}{f} =$ $\int_{-\infty}^{\infty} c^n \lvert\rho_X(c)\rvert^2\,dc$	$\Psi_T^{(H)}(0,\beta)=1$
$\mathrm{P}_{8}^{(C)}$: scale covariance $(\mathcal{C}_a X)(f)=\frac{1}{\sqrt{a}}X(\frac{f}{a}) \Rightarrow$ $T_{\mathcal{C}_a X}^{(C)}(t,f)=T_X^{(C)}(at,\frac{f}{a})$	P_{14}: power-warp covariance $(\mathcal{P}_a X)(f)=\sqrt{\frac{1}{a}(\frac{f}{f_r})^{\frac{1}{a}-1}}X\big(f_r(\frac{f}{f_r})^{\frac{1}{a}}\big) \Rightarrow$ $T_{\mathcal{P}_a X}^{(H)}(t,f)=T_X^{(H)}\big(\frac{at}{(\frac{f}{f_r})^{\frac{1}{a}-1}},f_r(\frac{f}{f_r})^{\frac{1}{a}}\big)$	$\Psi_T^{(H)}(\zeta,\beta)=S_T(\zeta\beta)$ with $S_T(\xi)$ arbitrary
$\mathrm{P}^{(C)}$: exponential time-shift covariance $(\mathcal{E}_\tau X)(f)=e^{-j2\pi\tau f_r e^{f/f_r}}X(f) \Rightarrow$ $T_{\mathcal{E}_\tau X}^{(C)}(t,f)=T_X^{(C)}\big(t-\tau e^{f/f_r},f\big)$	P_{15}: time-shift covariance $(\mathcal{S}_\tau X)(f)=e^{-j2\pi\tau f}X(f) \Rightarrow$ $T_{\mathcal{S}_\tau X}^{(H)}(t,f)=T_X^{(H)}(t-\tau,f)$	$\Psi_T^{(H)}(\zeta,\beta)=B_T(\beta)e^{-j2\pi\zeta\ln G(\beta)}$ with $G(\beta)=\frac{\beta/2}{\sinh(\beta/2)}$ and $B_T(\beta)$ arbitrary
$\mathrm{P}^{(C)}$: axis reversal $\tilde{x}(t)=x(-t)$, $\tilde{X}(f)=X(-f) \Rightarrow$ $T_{\tilde{X}}^{(C)}(t,f)=T_X^{(C)}(-t,-f)$	P_{16}: hyperbolic axis reversal $\rho_{\tilde{X}}(c)=\rho_X(-c)$, $\tilde{X}(f)=\frac{f_r}{f}X(\frac{f_r^2}{f}) \Rightarrow$ $T_{\tilde{X}}^{(H)}(t,f)=T_X^{(H)}(-\frac{f_r^2}{f_r^2}t,\frac{f_r^2}{f})$	$\Psi_T^{(H)}(-\zeta,-\beta)=\Psi_T^{(H)}(\zeta,\beta)$

Table 2.4 (continued).

COHEN'S CLASS PROPERTY	HYPERBOLIC CLASS PROPERTY	HYPERBOLIC CLASS KERNEL CONSTRAINT
$P_7^{(C)}$: frequency moments $\int_{-\infty}^{\infty}\int_{-\infty}^{\infty} f^n T_X^{(C)}(t,f)\,dt\,df =$ $\int_{-\infty}^{\infty} f^n \lvert X(f)\rvert^2\,df$	P_{17}: hyperbolic frequency moments $\int_{-\infty}^{\infty}\int_{0}^{\infty} (f_r \ln\frac{f}{f_r})^n T_X^{(H)}(t,f)\,dt\,df =$ $\int_{0}^{\infty} (f_r \ln\frac{f}{f_r})^n \lvert X(f)\rvert^2\,df$	$\Psi_T^{(H)}(\zeta,0) = 1$
$P_9^{(C)}$: instantaneous frequency $\frac{\int_{-\infty}^{\infty} f\, T_X^{(C)}(t,f)\,df}{\int_{-\infty}^{\infty} T_X^{(C)}(t,f)\,df} = \frac{1}{2\pi}\frac{d}{dt}\arg x(t)$	P_{18}: hyperbolic instantan. frequency $\frac{\int_0^{\infty}(\ln\frac{f}{f_r})\, T_X^{(H)}(\frac{c}{f},f)\,\frac{df}{f}}{\int_0^{\infty} T_X^{(H)}(\frac{c}{f},f)\,\frac{df}{f}} = \frac{1}{2\pi}\frac{d}{dc}\arg\rho_X(c)$	$\Psi_T^{(H)}(0,\beta) = 1$ and $\frac{\partial}{\partial\zeta}\Psi_T^{(H)}(\zeta,\beta)\Big\rvert_{\zeta=0} = 0$
$P_{14}^{(C)}$: convolution in time $\tilde{x}(t) = (g * x)(t)\,,$ $\tilde{X}(f) = G(f)\,X(f) \;\Rightarrow\; T_{\tilde{X}}^{(C)}(t,f)$ $= \int_{-\infty}^{\infty} T_G^{(C)}(t-t',f)\,T_X^{(C)}(t',f)\,dt'$	P_{19}: hyperbolic convolution $\rho_{\tilde{X}}(c) = (\rho_G * \rho_X)(c)\,,$ $\tilde{X}(f) = \sqrt{f}\,G(f)\,X(f) \;\Rightarrow$ $T_{\tilde{X}}^{(H)}(t,f) = \int_{-\infty}^{\infty} T_G^{(H)}(t-\frac{c}{f},f)\,T_X^{(H)}(\frac{c}{f},f)dc$	$\Psi_T^{(H)}(\zeta,\beta) = e^{\zeta C_T(\beta)}$ with $C_T(\beta)$ arbitrary
$P_{15}^{(C)}$: convolution in frequency $\tilde{x}(t) = g(t)\,x(t)\,,$ $\tilde{X}(f) = (G * X)(f) \;\Rightarrow\; T_{\tilde{X}}^{(C)}(t,f)$ $= \int_{-\infty}^{\infty} T_G^{(C)}(t,f-f')\,T_X^{(C)}(t,f')\,df'$	P_{20}: hyperbolic multiplication $\rho_{\tilde{X}}(c) = \rho_G(c)\,\rho_X(c)\,,$ $\tilde{X}(f) = \sqrt{f_r}\int_0^{\infty} G(f_r\frac{f}{f'})X(f')\,df' \;\Rightarrow$ $T_{\tilde{X}}^{(H)}(t,f) = \int_0^{\infty} T_G^{(H)}(\frac{tf'}{f_r}, f_r\frac{f}{f'})\,T_X^{(H)}\left(\frac{tf}{f'},f'\right)\frac{df'}{f}$	$\Psi_T^{(H)}(\zeta,\beta) = e^{\beta C_T(\zeta)}$ with $C_T(\beta)$ arbitrary

Table 2.4 (continued).

COHEN'S CLASS PROPERTY	HYPERBOLIC CLASS PROPERTY	HYPERBOLIC CLASS KERNEL CONSTRAINT
$\mathrm{P}^{(C)}$: weighted convolution $\tilde{X}(f)=\sqrt{e^{-f/f_r}}G(f)X(f) \Rightarrow T_{\tilde{X}}^{(C)}(t,f)$ $= e^{-f/f_r}\int_{-\infty}^{\infty} T_G^{(C)}(t-t',f)\,T_X^{(C)}(t',f)\,dt'$	P_{21}: convolution $\tilde{X}(f) = G(f)\,X(f) \Rightarrow$ $T_{\tilde{X}}^{(H)}(t,f) = \int_{-\infty}^{\infty} T_G^{(H)}(t-t',f)\,T_X^{(H)}(t',f)\,dt'$	$\Phi_T^{(H)}(b_1,\beta)\,\Phi_T^{(H)}(b_2,\beta) =$ $e^{b_1}\,\Phi_T^{(H)}(b_1,\beta)\,\delta(b_1-b_2)$
$\mathrm{P}^{(C)}$: chirp localization $X(f) = e^{-j\pi a f^2} \Rightarrow$ $T_X^{(C)}(t,f) = \delta(t-af)$	P_{22}: hyperbolic chirp localization $X(f) = \frac{1}{\sqrt{f}}\,e^{-j\pi b\left(\ln\frac{f}{f_r}\right)^2}\,\mathrm{u}(f) \Rightarrow$ $T_X^{(H)}(t,f) = \frac{1}{f}\,\delta(t-\frac{b}{f}\ln\frac{f}{f_r}),\ \ f>0$	$\Psi_T^{(H)}(\zeta,\beta) = 1$ (i.e., $T^{(H)}$ is the AD)

Table 2.4 .

2.9.1 The Altes-Marinovic Distribution

The Altes-Marinovic distribution (AD) [40, 42, 46]

$$\begin{aligned} Q_X(t,f) &= \int_{-\infty}^{\infty} v_X(tf,\zeta)\, e^{-j2\pi(\ln\frac{f}{f_r})\zeta}\, d\zeta = \int_{-\infty}^{\infty} V_X\Big(\ln\frac{f}{f_r},\, \beta\Big)\, e^{j2\pi tf\beta}\, d\beta \\ &= f\int_{-\infty}^{\infty} X\big(fe^{\beta/2}\big)\, X^*\big(fe^{-\beta/2}\big)\, e^{j2\pi tf\beta}\, d\beta \end{aligned}$$

is the hyperbolic counterpart of the WD [49, 25, 1] in Cohen's class with v_X and V_X defined in (2.30) and (2.31). The AD's kernels are particularly simple,

$$\phi_Q^{(H)}(c,\zeta) = \delta(c)\,, \qquad \Phi_Q^{(H)}(b,\beta) = \delta(b)\,, \qquad \psi_Q^{(H)}(c,b) = \delta(c)\,\delta(b)\,, \qquad \Psi_Q^{(H)}(\zeta,\beta) = 1\,.$$

According to Table 2.6, the AD satisfies all QTFR properties listed in Table 2.4 except for the conventional time-shift covariance property, P_{15}. Since P_{15} is not satisfied, the AD is not a member of the affine QTFR class. The AD is the only member of the HC that satisfies the hyperbolic chirp localization property P_{22}. Several sets of other QTFR properties can, alternatively, be used to uniquely define the AD inside the HC, in the sense that the AD is the only member of the HC that satisfies these properties. One such property set consists of the marginal properties P_5 and P_{10}, the finite-support properties P_8 and P_{12}, unitarity P_6 and real-valuedness P_3 [50]. An alternative property set consists of the hyperbolic convolution property P_{19} and the hyperbolic multiplication property P_{20}, unitarity P_6 and real-valuedness P_3 [3, 51].

The AD is perfectly adapted to the hyperbolic TF geometry and indeed it can be considered as the "central" QTFR in the HC. Specifically, the hyperbolic properties P_{10}–P_{13} can be generalized to modified versions of the hyperbolic impulse defined as $\bar{H}_c(f) = f^a H_c(f)$, with some power parameter a [38]. The AD satisfies the corresponding generalized hyperbolic properties for any power a. A second indication of the AD's desirability is the result for the cross-AD of two hyperbolic impulses, which is

$$Q_{H_{c_1},H_{c_2}}(t,f) = \frac{1}{f}\,\delta\Big(t-\frac{c_{12}}{f}\Big)\, e^{-j2\pi\zeta_{12}\ln\frac{f}{f_r}} \qquad (2.39)$$

$$\text{where} \quad c_{12} = \frac{c_1+c_2}{2} \quad \text{and} \quad \zeta_{12} = c_1 - c_2\,,$$

COHEN'S CLASS QTFR $T_X^{(C)}(t,f)$	HYPERBOLIC CLASS QTFR $T_X^{(H)}(t,f)$
Wigner distribution $W_X(t,f) = \int_{-\infty}^{\infty} u_X(t,\tau)\, e^{-j2\pi f\tau}\, d\tau$ $= \int_{-\infty}^{\infty} U_X(f,\nu)\, e^{j2\pi t\nu}\, d\nu$ $= \int_{-\infty}^{\infty} X(f+\frac{\nu}{2})\, X^*(f-\frac{\nu}{2})\, e^{j2\pi t\nu}\, d\nu$	Altes-Marinovic distribution $Q_X(t,f) = \int_{-\infty}^{\infty} v_X(tf,\zeta)\, e^{-j2\pi(\ln\frac{f}{f_r})\zeta}\, d\zeta$ $= \int_{-\infty}^{\infty} V_X(\ln\frac{f}{f_r},\, \beta)\, e^{j2\pi tf\beta}\, d\beta$ $= f\int_{-\infty}^{\infty} X(fe^{\beta/2})\, X^*(fe^{-\beta/2})\, e^{j2\pi tf\beta}\, d\beta$
Generalized Wigner distribution $W_X^{(\alpha)}(t,f) = \int_{-\infty}^{\infty} u_X(t+\alpha\tau,\tau)\, e^{-j2\pi f\tau}\, d\tau$ $= \int_{-\infty}^{\infty} U_X(f-\alpha\nu,\nu)\, e^{j2\pi t\nu}\, d\nu$	Generalized Altes-Marinovic distribution $Q_X^{(\alpha)}(t,f) = \int_{-\infty}^{\infty} v_X(tf+\alpha\zeta,\zeta)\, e^{-j2\pi(\ln\frac{f}{f_r})\zeta}\, d\zeta$ $= \int_{-\infty}^{\infty} V_X(\ln\frac{f}{f_r}-\alpha\beta,\, \beta)\, e^{j2\pi tf\beta}\, d\beta$
Cohen-Bertrand P_0 distribution $P_X^{(C)}(t,f) = \int_{-\infty}^{\infty} U_X(f+f_r\ln G(\frac{\nu}{f_r}),\, \nu)\, e^{j2\pi t\nu} d\nu$ with $G(\beta) = \frac{\beta/2}{\sinh(\beta/2)}$	Bertrand unitary P_0 distribution $P_X(t,f) = \int_{-\infty}^{\infty} V_X\Big(\ln(\frac{f}{f_r}G(\beta)),\, \beta\Big)\, e^{j2\pi tf\beta}\, d\beta$ with $G(\beta) = \frac{\beta/2}{\sinh(\beta/2)}$

Table 2.5: Corresponding QTFRs of Cohen's class and the hyperbolic class. Note that $u_X(t,\tau) = x(t+\tau/2)\, x^*(t-\tau/2)$, $U_X(f,\nu) = X(f+\nu/2)\, X^*(f-\nu/2)$, and, $v_X(c,\zeta)$, $V_X(b,\beta)$ and $\rho_X(c)$ are given by (2.30), (2.31), and (2.38), respectively. (Table was taken from [3] and [4]). (Continued on next page)

COHEN'S CLASS QTFR $T_X^{(C)}(t,f)$	HYPERBOLIC CLASS QTFR $T_X^{(H)}(t,f)$
Spectrogram $S_X(t,f) = \left\| \int_{-\infty}^{\infty} X(f')\,\Gamma^*(f'-f)\,e^{j2\pi tf'}\,df' \right\|^2$ $= \int_{-\infty}^{\infty}\int_{-\infty}^{\infty} W_\Gamma(t'-t,f'-f)\,W_X(t',f')\,dt'df'$	Hyperbologram $Y_X(t,f) = \frac{f_r}{f}\left\| \int_0^{\infty} X(f')\,\tilde{\Gamma}^*\left(\frac{f_r}{f}f'\right) e^{j2\pi tf\ln\frac{f'}{f_r}}\,df' \right\|^2$ $= \int_{-\infty}^{\infty}\int_0^{\infty} Q_{\tilde{\Gamma}}^*(\frac{1}{f_r}\frac{f}{f'}(t'f'-tf),\, f_r\frac{f'}{f})\,Q_X(t',f')\,dt'\,df'$ with $\tilde{\Gamma}(f) = \sqrt{\frac{f_r}{f}}\,\Gamma(f_r\ln\frac{f}{f_r})$
Pseudo Wigner distribution $\mathrm{PWD}_X(t,f) =$ $= \int_{-\infty}^{\infty} u_\Gamma(0,\tau)\,u_X(t,\tau)\,e^{-j2\pi f\tau}\,d\tau$ $= \int_{-\infty}^{\infty} W_\Gamma(0,f-f')\,W_X(t,f')\,df'$	Pseudo Altes-Marinovic distribution $\mathrm{PAD}_X(t,f) =$ $= f_r\int_{-\infty}^{\infty} v_{\tilde{\Gamma}}(0,\zeta)\,v_X(tf,\zeta)\,e^{-j2\pi(\ln\frac{f}{f_r})\zeta}\,d\zeta$ $= f_r\int_0^{\infty} Q_{\tilde{\Gamma}}(0,f_r\frac{f}{f'})\,Q_X(\frac{tf}{f'},f')\,\frac{df'}{f'}$ with $\tilde{\Gamma}(f) = \sqrt{\frac{f_r}{f}}\,\Gamma(f_r\ln\frac{f}{f_r})$
Smoothed Pseudo Wigner distribution $\mathrm{SPWD}_X(t,f) =$ $= \int_{-\infty}^{\infty} s(t-t')\,\mathrm{PWD}_X(t',f)\,dt'$ $= \int_{-\infty}^{\infty}\int_{-\infty}^{\infty} s(t-t')\,u_\Gamma(0,\tau)\,u_X(t',\tau)\,e^{-j2\pi f\tau}\,dt'd\tau$ $= \int_{-\infty}^{\infty}\int_{-\infty}^{\infty} s(t-t')\,W_\Gamma(0,f-f')\,W_X(t',f')\,dt'df'$	Smoothed Pseudo Altes-Marinovic distribution $\mathrm{SPAD}_X(t,f) =$ $= \int_{-\infty}^{\infty} \hat{s}(tf-c)\,\mathrm{PAD}_X(\frac{c}{f},f)\,dc$ $= f_r\int_{-\infty}^{\infty}\int_{-\infty}^{\infty} \hat{s}(tf-c)\,v_{\tilde{\Gamma}}(0,\zeta)\,v_X(c,\zeta)\,e^{-j2\pi(\ln\frac{f}{f_r})\zeta}\,dcd\zeta$ $= f_r\int_{-\infty}^{\infty}\int_0^{\infty} \hat{s}(tf-c)\,Q_{\tilde{\Gamma}}(0,f_r\frac{f}{f'})\,Q_X(\frac{c}{f'},f')\,dc\frac{df'}{f'}$ with $\hat{s}(t)=\frac{1}{f_r}s(\frac{t}{f_r})$, $\tilde{\Gamma}(f)=\sqrt{\frac{f_r}{f}}\,\Gamma(f_r\ln\frac{f}{f_r})$

Table 2.5 (continued).

HYPERBOLIC QTFR	KERNELS	PROPERTIES SATISFIED
Altes-Marinovic distribution Q	$\phi_Q^{(H)}(c,\zeta) = \delta(c)$ $\Phi_Q^{(H)}(b,\beta) = \delta(b)$ $\psi_Q^{(H)}(c,b) = \delta(c)\delta(b)$ $\Psi_Q^{(H)}(\zeta,\beta) = 1$	P_1–P_{14}, P_{16}–P_{22}
Generalized Altes–Marinovic distribution $Q^{(\alpha)}$	$\phi_{Q^{(\alpha)}}^{(H)}(c,\zeta) = \delta(c+\alpha\zeta)$ $\Phi_{Q^{(\alpha)}}^{(H)}(b,\beta) = \delta(b-\alpha\beta)$ $\psi_{Q^{(\alpha)}}^{(H)}(c,b) = \frac{1}{\lvert\alpha\rvert}\, e^{j2\pi\frac{cb}{\alpha}}$ $\Psi_{Q^{(\alpha)}}^{(H)}(\zeta,\beta) = e^{j2\pi\alpha\zeta\beta}$	P_1, P_2, P_4–P_6, P_9–P_{11}, P_{13}, P_{14}, P_{16}, P_{17}, P_{19}, P_{20}; P_8 and P_{12} if $\lvert\alpha\rvert < \frac{1}{2}$
Bertrand distribution P	$\phi_P^{(H)}(c,\zeta) = \int_{-\infty}^{\infty} e^{j2\pi(c\beta-\zeta \ln G(\beta))}\, d\beta$ $\Phi_P^{(H)}(b,\beta) = \delta(b+\ln G(\beta))$ $\psi_P^{(H)}(c,b) = \int_{-\infty}^{\infty} \delta(b+\ln G(\beta))\, e^{j2\pi c\beta}\, d\beta$ $\Psi_P^{(H)}(\zeta,\beta) = e^{-j2\pi\zeta \ln G(\beta)}$ with $G(\beta) = \frac{\beta/2}{\sinh(\beta/2)}$	P_1–P_{11}, P_{12}??*, P_{13}, P_{15}, P_{17}, P_{19}

Table 2.6: Kernels and properties of some QTFRs of the hyperbolic class. The distributions are defined in Table 2.5 and the properties are defined in Table 2.4. (Table was taken from [3]). $\rho_X(c)$, $v_X(c,\zeta)$ and $V_X(b,\beta)$ are defined in (2.38), (2.30) and (2.31) respectively. Also, $\hat{s}(c)$ and $\hat{S}(\beta)$ are Fourier transform pairs. (*It is still unknown whether property P_{12} is satisfied by the BD.) (Continued on next page)

HYPERBOLIC QTFR	KERNELS	PROPERTIES SATISFIED
Hyperbologram Y	$\phi_Y^{(H)}(c,\zeta) = v_{\tilde{\Gamma}}(-c,-\zeta)$ $\Phi_Y^{(H)}(b,\beta) = V_{\tilde{\Gamma}}(-b,-\beta)$ $\psi_Y^{(H)}(c,b) = Q_{\tilde{\Gamma}}\left(\frac{-c}{f_r e^{-b}}, f_r e^{-b}\right)$ $\Psi_Y^{(H)}(\zeta,\beta) = B_{\tilde{\Gamma}}(-\zeta,-\beta)$	P_1–P_3; P_4 if $\int_0^\infty \lvert\tilde{\Gamma}(f)\rvert^2\, df = 1$ P_{16} if $\tilde{\Gamma}(-f) = \pm\tilde{\Gamma}(f)$
Pseudo Altes-Marinovic distribution PAD	$\phi_{\text{PAD}}^{(H)}(c,\zeta) = f_r\,\delta(c)\,v_{\tilde{\Gamma}}(0,\zeta)$ $\Phi_{\text{PAD}}^{(H)}(b,\beta) = f_r\,Q_{\tilde{\Gamma}}(0, f_r e^b)$ $\psi_{\text{PAD}}^{(H)}(c,b) = f_r\,\delta(c)\,Q_{\tilde{\Gamma}}(0, f_r e^b)$ $\Psi_{\text{PAD}}^{(H)}(\zeta,\beta) = f_r\,v_{\tilde{\Gamma}}(0,\zeta)$	P_1–P_3, P_{12}; P_4, P_{10}, P_{11}, and P_{13} if $\lvert\rho_{\tilde{\Gamma}}(0)\rvert^2 = \frac{1}{f_r}$, P_{16} if $v_{\tilde{\Gamma}}(0,-\zeta) = v_{\tilde{\Gamma}}(0,\zeta)$, P_{18} if $\text{Im}\{\frac{d}{dc}\rho_{\tilde{\Gamma}}(c)\lvert_{c=0}\,\rho_{\tilde{\Gamma}}^*(0)\} = 0$
Smoothed pseudo Altes-Marinovic distribution SPAD	$\phi_{\text{SPAD}}^{(H)}(c,\zeta) = f_r\,\hat{s}(c)\,v_{\tilde{\Gamma}}(0,\zeta)$ $\Phi_{\text{SPAD}}^{(H)}(b,\beta) = f_r\,\hat{S}(\beta)\,Q_{\tilde{\Gamma}}(0, f_r e^b)$ $\psi_{\text{SPAD}}^{(H)}(c,b) = f_r\,\hat{s}(c)\,Q_{\tilde{\Gamma}}(0, f_r e^b)$ $\Psi_{\text{SPAD}}^{(H)}(\zeta,\beta) = f_r\,\hat{S}(\beta)\,v_{\tilde{\Gamma}}(0,\zeta)$	P_1, P_2; P_3 if $\hat{s}(c) \in \mathrm{R}$, P_4 if $\hat{S}(0)\,\lvert\rho_{\tilde{\Gamma}}(0)\rvert^2 = \frac{1}{f_r}$, P_{16} if $\hat{S}(-f) = \hat{S}(f)$ and $v_{\tilde{\Gamma}}(0,-\zeta) = v_{\tilde{\Gamma}}(0,\zeta)$

Table 2.6 (Continued).

where the cross-AD of two signals $X(f)$ and $Y(f)$ is defined as

$$Q_{X,Y}(t,f) \;=\; f\int X(fe^{\beta/2})\,Y^*(fe^{-\beta/2})\,e^{j2\pi tf\beta}\,d\beta. \tag{2.40}$$

The result for the cross-AD $Q_{H_{c_1},H_{c_2}}(t,f)$ is a "cross-version" of the hyperbolic localization property P_{11} and the result states that the cross or interference term of two different hyperbolic impulses with hyperbolic parameters c_1 and c_2 is perfectly concentrated along the "mean hyperbola" $t = c_{12}/f$, along which it is oscillatory [3]. A similar result is,

$$\begin{aligned} Q_{L_{f_1},L_{f_2}}(t,f) \;&=\; \delta(f-f_{12})\,e^{j2\pi\nu_{12}t} \\ \text{where}\quad f_{12} \;&=\; \sqrt{f_1f_2}\quad\text{and}\quad \nu_{12}=\sqrt{f_1f_2}\,\ln\frac{f_1}{f_2}\,, \end{aligned} \tag{2.41}$$

which states that the cross-AD of two spectral lines, $L_{f_1}(f)=\delta(f-f_1)$ and $L_{f_2}(f)=\delta(f-f_2)$, is an oscillatory Dirac ridge at the geometric-mean frequency $f_{12}=\sqrt{f_1f_2}$ [3].

Since the WD is known to feature perfect concentration in the case of linear FM signals (chirp signals) $X(f)=e^{-j\pi af^2}$, an analogous result must hold for the AD [9]. The frequency-warped version $(\mathcal{W}^{-1}X)(f)$ of the linear-FM chirp signal can be shown to be (up to a constant factor) the "hyperbolic chirp signal" $R_b(f)=\frac{1}{\sqrt{f}}\,e^{-j\pi b(\ln\frac{f}{f_r})^2}\,\mathrm{u}(f)$ (where $b=af_r^2$ is a "hyperbolic chirp rate" and $\mathrm{u}(f)$ is the unit step), whose group delay is $\tau(f)=\frac{b}{f}\ln\frac{f}{f_r}$. The AD of the hyperbolic chirp signal defined above is, indeed, a Dirac ridge along the group delay curve $t=\tau(f)$,

$$Q_{R_b}(t,f)=\frac{1}{f}\,\delta\!\left(t-\frac{b}{f}\,\ln\frac{f}{f_r}\right)\,,\quad f>0\,.$$

This property suffices to uniquely define the AD inside the HC.

2.9.2 The Generalized Altes-Marinovic Distribution

Many of the properties of the AD can be extended to the family of hyperbolic QTFRs depending on a real-valued parameter α [46]

$$Q_X^{(\alpha)}(t,f) \;=\; \int_{-\infty}^{\infty} v_X(tf+\alpha\zeta,\,\zeta)\,e^{-j2\pi(\ln\frac{f}{f_r})\zeta}\,d\zeta$$

$$= \int_{-\infty}^{\infty} V_X\Big(\ln\frac{f}{f_r} - \alpha\beta,\, \beta\Big)\, e^{j2\pi t f\beta}\, d\beta$$
$$= f\int_{-\infty}^{\infty} e^{-\alpha\beta}\, X\Big(fe^{(\frac{1}{2}-\alpha)\beta}\Big)\; X^*\Big(fe^{-(\frac{1}{2}+\alpha)\beta}\Big)\; e^{j2\pi t f\beta} d\beta$$

which we call *generalized Altes-Marinovic distribution* (GAD). The GAD is the hyperbolic counterpart of the *generalized Wigner distribution* [31, 25, 50, 52] of Cohen's class. Note that the AD is a special case for $\alpha = 0$ and is the only GAD which is real-valued. The interference term concentration properties of the AD, shown in Eqs. (2.39) and (2.41), can be extended to the GAD, but with an α-dependent displacement of the interference term location [3].

2.9.3 The Bertrand Distribution

Another prominent member of the HC is the *Bertrand unitary P_0-distribution* [38, 43, 36, 39, 46, 53], briefly called Bertrand distribution (BD) in the following.

$$\begin{aligned} P_X(t,f) &= \int_{-\infty}^{\infty} U_X\Big(fF\big(\tfrac{\nu}{f}\big),\, \nu\Big)\, G\big(\tfrac{\nu}{f}\big)\, e^{j2\pi t\nu}\, d\nu \\ &= \int_{-\infty}^{\infty} X\Big(fF\big(\tfrac{\nu}{f}\big)+\tfrac{\nu}{2}\Big)\, X^*\Big(fF\big(\tfrac{\nu}{f}\big)-\tfrac{\nu}{2}\Big)\, G\big(\tfrac{\nu}{f}\big)\, e^{j2\pi t\nu} d\nu \\ &= \int_{-\infty}^{\infty} V_X\Big(\ln\big(\tfrac{f}{f_r}G(\beta)\big),\, \beta\Big)\, e^{j2\pi t f\beta}\, d\beta \\ &= f\int_{-\infty}^{\infty} X\big(fG(\beta)\, e^{\frac{\beta}{2}}\big)\, X^*\big(fG(\beta)\, e^{-\frac{\beta}{2}}\big) G(\beta)\, e^{j2\pi t f\beta}\, d\beta \end{aligned}$$

where[4]

$$F(\beta) = \frac{\beta}{2}\coth\frac{\beta}{2} = \frac{\beta}{2}\,\frac{e^{\beta/2}+e^{-\beta/2}}{e^{\beta/2}-e^{-\beta/2}}, \qquad G(\beta) = \frac{\beta/2}{\sinh(\beta/2)} = \frac{\beta}{e^{\beta/2}-e^{-\beta/2}}.$$

Two of the kernels of the BD are simple functions,

$$\Phi_P^{(H)}(b,\beta) = \delta\big(b + \ln G(\beta)\big), \qquad \Psi_P^{(H)}(\zeta,\beta) = e^{-j2\pi\zeta \ln G(\beta)}.$$

The BD satisfies many of the desirable properties listed in Table 2.4. The main feature of the BD (from a HC viewpoint) is that the BD satisfies the conventional

[4]Note that $F(\beta) = \frac{1}{2}(\lambda_0(\beta)+\lambda_0(-\beta))$ and $G(\beta) = \mu_0(\beta) = \lambda_0(\beta)\, e^{-\beta/2}$, where $\lambda_0(\beta)$ and $\mu_0(\beta)$ are the functions used in [38].

time-shift covariance property P_{15}. Thus, it is also a member of the affine QTFR class; indeed, it may be considered as the central QTFR inside the hyperbolic subclass that forms the intersection between the HC and the affine class [48, 54]. Inside the HC, the BD is uniquely defined by the time-shift covariance property, P_{15}, the real-valuedness property P_3 and the hyperbolic marginal property P_{10} (or, equivalently, the hyperbolic localization property P_{11}) [3].

From the viewpoint of the *affine QTFR class*, the BD is unique because of the hyperbolic properties it satisfies. Indeed, inside the affine class, the BD is uniquely defined by the real-valuedness property P_3, the hyperbolic time-shift covariance property P_1 and the hyperbolic marginal property P_{10} (or, equivalently, the hyperbolic localization property P_{11}) [3]. Other property sets defining the BD are discussed in [38, 36].

Since the BD is a prominent member of the HC, it is interesting to see to which member of Cohen's class the BD corresponds. Using the relation (2.36), the Cohen's class counterpart of the BD (abbreviated CBD in the following) is obtained as [46]

$$\begin{aligned} \mathrm{CBD}_X^{(C)}(t,f) &= \int_{-\infty}^{\infty} U_X\Big(f+f_r \ln G\big(\frac{\nu}{f_r}\big),\, \nu\Big)\, e^{j2\pi t\nu}\, d\nu \\ &= \int_{-\infty}^{\infty} X\Big(f+f_r \ln G\big(\frac{\nu}{f_r}\big)+\frac{\nu}{2}\Big)\, X^*\Big(f+f_r \ln G\big(\frac{\nu}{f_r}\big)-\frac{\nu}{2}\Big)\, e^{j2\pi t\nu}\, d\nu\,. \end{aligned}$$

where $G(\beta) = \frac{\beta/2}{\sinh \beta/2}$ as defined before. The main feature of the CBD is the exponential time-shift covariance property which is the Cohen's class counterpart of the time-shift covariance property in the HC. Indeed, inside Cohen's class, the CBD is uniquely defined by the real-valuedness property $P_1^{(C)}$, the exponential time-shift covariance property and the time-domain marginal property, $P_4^{(C)}$ (or, equivalently, the time localization property) [3].

2.9.4 The Hyperbologram

As a basis for a further hyperbolic QTFR, we first define the *hyperbolic wavelet transform* as the inner product of the signal $X(f)$ and a TF-scaled and hyperbolically

time-shifted analysis wavelet $\tilde{\Gamma}(f)$,

$$\mathrm{HWT}_X(c,a) \triangleq \left\langle X, \mathcal{H}_c \mathcal{C}_a \tilde{\Gamma} \right\rangle = \frac{1}{\sqrt{a}} \int_0^\infty X(f') \, \tilde{\Gamma}^*\left(\frac{f'}{a}\right) e^{j2\pi c \ln \frac{f'}{f_r}} \, df' \, .$$

where $\tilde{\Gamma}(f)$ is defined as

$$\tilde{\Gamma}(f) = (\mathcal{W}^{-1}\Gamma)(f) = \sqrt{\frac{f_r}{f}} \, \Gamma\left(f_r \ln \frac{f}{f_r}\right) \, , \qquad f > 0 \, ,$$

and $\Gamma(f)$ is a smooth, lowpass function [3]. The analysis wavelet, $\tilde{\Gamma}(f)$, is assumed to be an analytic bandpass signal concentrated around the positive reference frequency f_r. Note that $\mathrm{HWT}_X(c,a)$ is a linear signal representation which is analogous to the wavelet transform in (2.8), the difference being that the time-shift used in the wavelet transform is replaced by a hyperbolic time-shift. A TF version of the hyperbolic wavelet transform can easily be obtained through the substitution $c = tf$ and $a = f/f_r$.

The *hyperbologram*, $Y_X(t,f)$, is now defined as the squared magnitude of the TF version of the hyperbolic wavelet transform [46],

$$\begin{aligned} Y_X(t,f) &\triangleq \left| \mathrm{HWT}_X\left(tf, \frac{f}{f_r}\right) \right|^2 \\ &= \left| \left\langle X, \mathcal{H}_{tf} \mathcal{C}_{f/f_r} \tilde{\Gamma} \right\rangle \right|^2 = \frac{f_r}{f} \left| \int_0^\infty X(f') \, \tilde{\Gamma}^*\left(\frac{f_r}{f} f'\right) e^{j2\pi t f \ln \frac{f'}{f_r}} \, df' \right|^2 . \end{aligned}$$

The hyperbologram is a (nonnegative) member of the HC. It can be shown that the hyperbologram can be written in terms of any *unitary* [55, 56] hyperbolic QTFR $T_X^{(H)}(t,f)$ (e.g., the AD or BD) as

$$Y_X(t,f) = \int_{-\infty}^\infty \int_0^\infty T_{\tilde{\Gamma}}^{(H)*}\left(\frac{1}{f_r}\frac{f}{f'}(t'f' - tf), \, f_r \frac{f'}{f}\right) T_X^{(H)}(t',f') \, dt' \, df' \, ,$$

where $T_{\tilde{\Gamma}}^{(H)}(t,f)$ is the HC QTFR of the analysis wavelet.

2.9.5 The Pseudo Altes-Marinovic Distribution

The hyperbolic counterpart of the pseudo Wigner distribution in Cohen's class [49] is the *pseudo Altes-Marinovic distribution* (PAD) defined as

$$\mathrm{PAD}_X(t,f) \triangleq f_r \int_{-\infty}^\infty \left[\rho_X\left(tf + \frac{\zeta}{2}\right) \rho_\Gamma\left(\frac{\zeta}{2}\right)\right] \left[\rho_X\left(tf - \frac{\zeta}{2}\right) \rho_\Gamma\left(-\frac{\zeta}{2}\right)\right]^* e^{-j2\pi(\ln \frac{f}{f_r})\zeta} d\zeta$$

$$= f_r \int_{-\infty}^{\infty} v_{\tilde{\Gamma}}(0,\zeta)\, v_X(tf,\zeta)\, e^{-j2\pi(\ln \frac{f}{f_r})\zeta}\, d\zeta\,,$$

where $\tilde{\Gamma}(f)$ is an analysis wavelet and v_X and ρ_X were defined in (2.30) and (2.38), respectively. The PAD can be formally derived from the AD, $Q_X(t,f) = \int_{-\infty}^{\infty} \rho_X\left(tf+\frac{\zeta}{2}\right) \rho_X^*\left(tf-\frac{\zeta}{2}\right) e^{-j2\pi(\ln \frac{f}{f_r})\zeta}\, d\zeta$, by replacing $\rho_X(c)$ with the locally windowed version $\rho_X(c)\,\rho_{\tilde{\Gamma}}(c-tf)$ (i.e., $\rho_X(c)$ is multiplied by the "window" $\rho_{\tilde{\Gamma}}(c)$ shifted to the respective analysis parameter $c = tf$ that is induced by the analysis TF point (t,f)). It is easily shown that the PAD is a smoothed version of the AD, where the smoothing occurs along hyperbolas $t' = c/f'$ with $c = tf$ [3],

$$\mathrm{PAD}_X(t,f) = f_r \int_0^{\infty} Q_{\tilde{\Gamma}}\left(0, f_r \frac{f}{f'}\right) Q_X\left(\frac{tf}{f'}, f'\right) \frac{df'}{f'}\,.$$

2.9.6 The Smoothed Pseudo Altes-Marinovic Distribution

In order to incorporate an additional smoothing component in the vertical direction to the hyperbolas, the PAD is extended by defining the *smoothed pseudo Altes-Marinovic distribution* (SPAD) as [3, 4]

$$\begin{aligned}
\mathrm{SPAD}_X(t,f) &\triangleq \int_{-\infty}^{\infty} \hat{s}(tf-c)\, \mathrm{PAD}_X\left(\frac{c}{f}, f\right)\, dc \\
&= f_r \int_{-\infty}^{\infty}\int_{-\infty}^{\infty} \hat{s}(tf-c)\, v_{\tilde{\Gamma}}(0,\zeta)\, v_X(c,\zeta)\, e^{-j2\pi(\ln \frac{f}{f_r})\zeta}\, dc\, d\zeta \\
&= f_r \int_{-\infty}^{\infty}\int_{0}^{\infty} \hat{s}(tf-c)\, Q_{\tilde{\Gamma}}\left(0, f_r \frac{f}{f'}\right) Q_X\left(\frac{c}{f'}, f'\right)\, dc\, \frac{df'}{f'}\,,
\end{aligned}$$

where $\hat{s}(c)$ is a smoothing (i.e., lowpass) function, v_X is defined in (2.30), and Q is the Altes distribution. Note that the SPAD reduces to the PAD when $\hat{s}(c) = \delta(c)$. The SPAD is the hyperbolic counterpart of the smoothed pseudo Wigner distribution in Cohen's class [57, 25, 1]. Analogous to the spectrogram/hyperbologram correspondence, the analysis wavelet, $\tilde{\Gamma}(f)$, of the corresponding smoothed pseudo Altes-Marinovic distribution is the frequency-warped version of the window $\Gamma(f)$. Note that the kernels of the SPAD are separable functions (cf. Table 2.6). This entails a type of AD smoothing which allows both an efficient computation and a flexible and simple choice of the smoothing characteristics. If the computation of

HC representations is based on the hyperbolic coefficient function $\rho_X(c)$ (which permits the application of the fast Mellin transform [6]), then the (smoothed) pseudo AD will have similar computational advantages as the (smoothed) pseudo WD in Cohen's class.

2.10 Conclusions

An overview of three classes of time-frequency distributions was presented. In one example, it has been shown that cross-term removal using the Cohen's class of time-frequency techniques is very challenging (see Figure (2.9)). In the case of Hyperbolic impulses, the Hyperbolic class of time-frequency representations works well; this will be discussed in the next chapter. Also in the next chapter, previous work done on the implementation of the Hyperbolic class will be discussed.

Chapter 3

Previous Work on the Implementation of the Hyperbolic class

3.1 Introduction

In this chapter, the Discrete Mellin Transform which connects the geometrically spaced samples of a signal to arithmetically, i.e. uniformly, spaced samples of its Mellin Transform, is described [44]. Next, the computation or implementation of the Affine class of Time-Frequency distributions using the Discrete Mellin Transform is discussed. This implementation is of interest because it can be used to implement the Bertrand unitary P_0 distribution which is also a member of the Hyperbolic class [6].

The warping technique for implementing the Hyperbolic class of Time-Frequency distributions is the one proposed by Canfield and Jones [7]. This technique will be discussed in the section (3.4) of this chapter.

3.2 Discrete Mellin Transform for Signal Analysis

In this section, properties and time-frequency interpretation of the Mellin transform relevant to the computation of the Affine class of time-frequency distributions are discussed [44]. Later, the discretization of the Mellin Transform into a form which can be computed using any Fast Fourier Transform (FFT) algorithm is discussed.

This technique is used for computing broad-band radar ambiguity functions and the Affine class of time-frequency representations [6].

3.2.1 Time-Frequency interpretation of MT

The introduction of the Mellin Transform in signal analysis corresponds generally to the search for a transformation with scale invariant properties [58, 59]. In this chapter, we consider the Mellin Transform as an interesting technique for the computation of functionals containing dilations.

The Mellin Transform is defined on the analytical signal $X(f)$, i.e., $X(f) = 0$ for $f < 0$, by the relation:

$$\mathcal{M}_X(\beta) = \int_0^\infty X(f)\, f^{2j\pi\beta - 1/2}\, df \tag{3.1}$$

and by its inverse form:

$$X(f) = \int_{-\infty}^\infty \mathcal{M}_X(\beta)\, f^{-2j\pi\beta - 1/2}\, d\beta \tag{3.2}$$

Hence, we will talk about the relationships between the signal's "f-space" referring to the frequency domain representation of the signal, and the Mellin transform's "β-space" referring to the signal's forward Mellin transform.

The transformation is unitary, i.e., it preserves inner products.

$$\int_0^\infty X_1(f)\, X_2^*(f)\, df = \int_{-\infty}^\infty \mathcal{M}_{X_1}(\beta)\, \mathcal{M}_{X_2}^*(\beta)\, d\beta \tag{3.3}$$

Our main interest of the transformation in (3.1)–(3.2) appears when considering the operation:

$$X(f) \longrightarrow X'(f) = a^{1/2}\, X(af) \tag{3.4}$$

which corresponds to a dilation of the signal by the coefficient $a > 0$. In the Mellin Transform β-space, the transformation in (3.4) is simply expressed by:

$$\mathcal{M}_{X'}(\beta) = a^{-2j\pi\beta}\, \mathcal{M}_X(\beta) \tag{3.5}$$

Basically, this latter relation comes from the fact that (3.2) represents a decomposition of the signal onto the following basis of signals:

$$Z(f, \beta) = f^{-2j\pi\beta - 1/2}. \tag{3.6}$$

which are eigen functions of the transformation operation in (3.4).

3.2.2 Some properties of the transform

In the signal's frequency-space, a product can be introduced by:

$$(X_1 \, o \, X_2)(f) \;=\; f^{1/2} \, X_1(f) \, X_2(f). \tag{3.7}$$

The Mellin Transform of this product is given by:

$$\mathcal{M}_{(X_1 \, o \, X_2)}(\beta) \;=\; \mathcal{M}_{X_1}(\beta) * \mathcal{M}_{X_2}(\beta) \;=\; \int_{-\infty}^{\infty} \mathcal{M}_{X_1}(\alpha) \, \mathcal{M}_{X_2}(\beta - \alpha) \, d\alpha \tag{3.8}$$

where the $*$ operation is the linear convolution of functions.

A multiplicative or scale convolution of functions is defined as

$$(X_1 \; ** \; X_2)(f) \;=\; \int_0^{\infty} X_1(f/\alpha) \, X_2(\alpha) \, \alpha^{-1} \, d\alpha. \tag{3.9}$$

For a given $X_1(f)$ (or $X_2(f)$), this is an important linear operation, since the Mellin Transform of (3.9) yields the relation:

$$\mathcal{M}_{(X_1 \; ** \; X_2)}(\beta) \;=\; \mathcal{M}_{X_1}(\beta) \, \mathcal{M}_{X_2}(\beta) \tag{3.10}$$

where the r.h.s. operation is the product of Mellin transforms in the β-space. Thus, scale convolution in frequency in (3.9) results in multiplication in the Mellin transform β-space in (3.10).

For discretization of the Mellin Transform, it is useful to define the geometric sampling function:

$$\Delta_Q(f) \;=\; \sum_{n=-\infty}^{\infty} Q^{n/2} \, \delta(f - Q^n), \;\; f, \; Q \in R \tag{3.11}$$

whose Mellin Transform is the distribution:

$$\mathcal{M}_{\Delta_Q}(\beta) \;=\; \frac{1}{\ln Q} \sum_{p=-\infty}^{\infty} \delta(\beta - p/\ln Q) \tag{3.12}$$

Here, $\delta(f)$ is a Dirac function. Expressions (3.11) and (3.12) are the counterparts of the "Dirac comb" function $w_A(t) \;=\; \sum_{m=-\infty}^{\infty} \delta(t - mA)$ and its Fourier transform (FT), $W_A(f) \;=\; \frac{1}{A} \sum_{p=-\infty}^{\infty} \delta(f - \frac{p}{A})$ used to represent the effects of uniform sampling on a signal and its Fourier transform. As defined in equation (3.11), the geometric sampling function is the sum of Dirac functions which repeat geometrically, i.e., like in a geometric progression, contrary to other sampling functions like the one in (3.12), $w_A(t)$ or $W_A(f)$, wherein the Dirac functions repeat arithmetically, i.e., like in an arithmetic progression.

3.2.3 Discrete Mellin Transform

We focus now on signals located in a bounded domain of the time-frequency half-plane ($f > 0$). The signal $X(f)$ is assumed to be limited to the frequency band $f \in (f_1, f_2)$ as shown in figure (3.1(a)). The support of the Mellin transform of the signal $X(f)$ is assumed to be $\beta \in (\beta_1, \beta_2)$ as shown in figure (3.1(b)). The objective is to discretize the Mellin transform so that digital computers can be used to compute it. The discretization used in this thesis was proposed in [44]. It is derived from samples in both the frequency domain and in the β-domain in a manner that ensures that aliasing errors do not occur in the Mellin transform domain. The Discrete Mellin Transform relates N geometrically spaced samples of the signal's spectrum to N uniformly spaced samples of its Mellin transform.

Initially, the beta domain is discretized by the following equation

$$\begin{aligned} \mathcal{M}_{\overline{X}}(\beta) &= \mathcal{M}_{\Delta_Q}(\beta)\mathcal{M}_X(\beta) \\ &= \frac{1}{\ln Q}\sum_p \mathcal{M}_X(\frac{p}{\ln Q})\,\delta(\beta - \frac{p}{\ln Q}) \end{aligned} \tag{3.13}$$

where $\mathcal{M}_{\Delta_Q}(\beta)$, given by (3.12), effectively uniformly samples the continuous Mellin transform of the signal in the beta domain. The effect of the above equation is shown in figure (3.1(d)). Since multiplication in the beta domain corresponds to scale/multiplicative convolution in frequency-space, the effect of the above operation on the signal $X(f)$ is shown below,

$$\overline{X}(f) = \Delta_Q(f) ** X(f)\,, \tag{3.14}$$

where $**$ is defined in (3.9). The signal $\overline{X}(f)$, called the dilatocycled form of $X(f)$, can be written as

$$\overline{X}(f) = \sum_{n=-\infty}^{\infty} Q^{n/2}\, X(Q^n f)\,,\ Q \in R\,. \tag{3.15}$$

The effect of dilatocycling on the signal $X(f)$ is shown in figure (3.1(c)).

Next, $\mathcal{M}_{\overline{X}}(\beta)$, is made periodic by the operation:

$$\begin{aligned} \mathcal{M}_{\underline{\overline{X}}}(\beta) &= \mathcal{M}_{\Delta_q}(\beta) * \mathcal{M}_{\overline{X}}(\beta) \\ &= \frac{1}{\ln q}\sum_l \mathcal{M}_{\overline{X}}(\beta - \frac{l}{\ln q}) \end{aligned} \tag{3.16}$$

Convolution with $\mathcal{M}_{\Delta_q}(\beta)$, which in (3.12) is a sum of periodically repeated Dirac delta functions spaced every $(\frac{1}{\ln q})$ units, results in periodic repetition of the Mellin transform of the signal $\overline{X}(f)$. The repetition due to the convolution in (3.16) is shown in figure (3.1(f)). In order to avoid aliasing, the sampling period, $\frac{1}{\ln q}$, of the function, $\mathcal{M}_{\Delta_q}(\beta)$ should satisfy the following condition:

$$1/\ln q \;\geq\; |\beta_2 - \beta_1| \tag{3.17}$$

where β_1 and β_2 are defined to be the boundary points of the support $\mathcal{M}_X(\beta)$, i.e., $\mathcal{M}_X(\beta) = 0$, for $\beta < \beta_1$ and $\beta > \beta_2$.

Convolution in the beta domain results in scaled multiplication in frequency domain. So, the inverse Mellin transform of (3.16) is obtained by using equations (3.2) and (3.8). The result is

$$\begin{aligned} \underline{\overline{X}}(f) &= \left(\Delta_q(f) \; o \; \overline{X}(f)\right) \\ &= \sum_n q^n \; \overline{X}(q^n) \; \delta(f - q^n) \end{aligned} \tag{3.18}$$

If the real numbers Q and q appearing, respectively, in (3.13) and (3.16) are connected by the relation:

$$Q \;=\; q^N \tag{3.19}$$

where N is a positive integer, then $\underline{\overline{X}}(f)$ is a sampled, periodic function. In the same way, condition (3.19) ensures that the geometric sampling in (3.16) does not destroy the dilatocycled structure of the function $\overline{X}(f)$ defined in (3.14). The Discrete Mellin transform is then readily obtained by writing (3.13) and (3.16) explicitly. The result is :

$$\mathcal{M}_{\underline{\overline{X}}}(p/\ln Q) \;=\; \ln Q \; (N)^{-1} \sum_{k=P}^{P+N-1} q^{k/2} \; e^{2j\pi kp/N} \; \overline{X}(q^k) \tag{3.20}$$

In (3.20), the integer P is obtained by looking at the support of $X(f)$, i.e., $q^P \cong f_1$ and $q^{P+N-1} \cong f_2$ where $X(f) = 0$, $f \notin (f_1, f_2)$. P is usually proportional to the logarithm of the minimum frequency at which $X(f)$ is non-zero, i.e., $P \cong \ln f_1 / \ln q$. The sequence of operations leading to (3.20) are listed in Table 3.1.

A pictorial synopsis of the operations leading to (3.20) is given in figure (3.1).

Figure (3.1) consists of six subplots where the right column of the subplots shows the Mellin transform of the left column of the subplots. Initially, in figure (3.1(a)),

Signal	Mellin Transform
$X(f) = \int_{-\infty}^{\infty} x(t)\, e^{-j2\pi ft}\, dt$	$\mathcal{M}_X(\beta) = \int_0^{\infty} X(f) f^{j2\pi\beta - 1/2}\, df$
$\overline{X}(f) = \sum_{n=-\infty}^{\infty} Q^{n/2}\, X(Q^n f)$	$\mathcal{M}_{\overline{X}}(\beta) = \mathcal{M}_{\Delta_Q}(\beta)\, \mathcal{M}_X(\beta)$ $= \frac{1}{\ln Q} \sum_{p=-\infty}^{\infty} \mathcal{M}_X(\frac{p}{\ln Q})\, \delta(\beta - \frac{p}{\ln Q})$
$\underline{X}(f) = \sum_{m=-\infty}^{\infty} q^m\, \overline{X}(q^m)\, \delta(f - q^m)$	$\mathcal{M}_{\underline{X}}(\beta) = \frac{1}{\ln q} \sum_{p'=-\infty}^{\infty} \mathcal{M}_{\overline{X}}(\beta - \frac{p'}{\ln q})$ $\mathcal{M}_{\underline{X}}(\frac{p}{\ln Q}) = \left[\ln q \sum_{k=P}^{P+N-1} q^{k/2}\, \overline{X}(q^k)\, e^{j\frac{2\pi kp}{N}}\right]$

Table 3.1: Discretization of the Mellin transform, assuming $Q = q^N$.

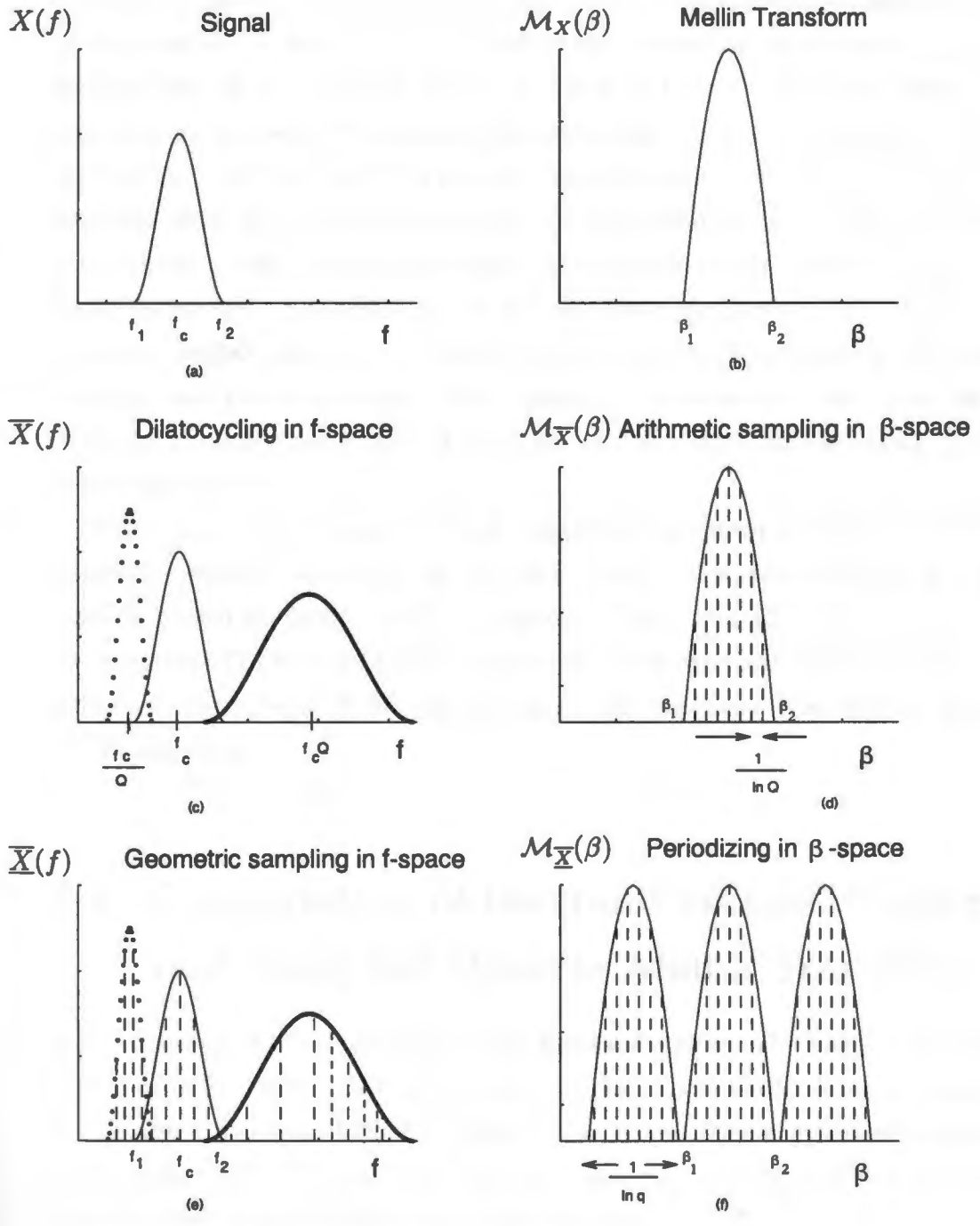

Figure 3.1: Graphical development of the Discrete Mellin Transform.

a signal with finite frequency support is shown. The signal's continuous Mellin transform is shown in figure (3.1(b)). Now, due to the arithmetic sampling in beta-space, as shown in figure (3.1(d)), dilatocycling occurs in the frequency space. The dilatocycling of the signal is shown in figure (3.1(c)). The dilatocycling can be explained as follows. During signal analysis using Fourier transforms, sampling in the frequency domain results in periodic repetition of the signal in the time domain. Similarly, when the Mellin transform is uniformly sampled in the beta domain, there is repetition in the frequency domain together with compression or dilation of the signal depending on the location of the repetition in the frequency space. In the frequency domain, the repeated waveform of the signal gets dilated as the frequency increases and gets compressed as the frequency decreases, as seen from the figure (3.1(c)). Figures (3.1(c)) and (3.1(d)) are the results of the equations (3.14) and (3.13), respectively.

Now the frequency space is being discretized as shown in figure (3.1(e)) which results in periodic repetition in the beta space. The discretization in the beta space is shown in figure (3.1(f)). Figures (3.1(e)) and (3.1(f)) are the result of the equations (3.18) and (3.16), respectively. The practical implementation of the discretized formula in (3.20) can be carried out with any Fast Fourier Transform (FFT) algorithm.

3.3 Computation of Bertrand unitary P_0 distribution using the Discrete Mellin Transform

In this section, the computation of the Bertrand unitary P_0 distribution using the Discrete Mellin Transform is discussed since the Bertrand distribution is of interest as it is also a member of the Hyperbolic class of time-frequency distributions. Also, it was shown that this computational technique can be generalized to compute any time-frequency distribution of the Affine class [6].

The unitary form of the Bertrand P_0 distribution is given by [37][1]

$$P_X(t,f) = f \int_{-\infty}^{\infty} e^{2j\pi tfu}\, X\left(f\frac{ue^{u/2}}{2\sinh(u/2)}\right)\, X^*\left(f\frac{ue^{-u/2}}{2\sinh(u/2)}\right) \left(\frac{u}{2\sinh(u/2)}\right)\, du. \tag{3.21}$$

From a computational point of view, this formula may look formidable. However, the use of an appropriate Mellin transform reduces the task of its implementation to just a few Fast Fourier Transforms (FFT). Initially, the sampling conditions of the Discrete Mellin transform will be discussed. In the next section, the main principle for the computation of the Bertrand unitary P_0 distribution is discussed. In later sections, an algorithm for the computation of the P_0 distribution is discussed, and then, some examples of applications to synthetic signals are presented and discussed.

The Discrete Mellin transform (DMT) can be used on signals with limited support in both the frequency, f, and Mellin transform, β, variables. In a general manner, the DMT relates N geometrically spaced samples of the signal in frequency to N arithmetically spaced samples of its Mellin transform. If a signal $X(f)$ is limited to the band $f \in (f_1, f_2)$, i.e., $X(f) = 0, f \notin (f_1, f_2)$, and if the support of its Mellin transform is $\beta \in (\beta_1, \beta_2)$, i.e., $\mathcal{M}_X(\beta) = 0, \beta \notin (\beta_1, \beta_2)$,
then the DMT is given by [2] :

$$\mathcal{M}_{\overline{X}}(\frac{p}{N \ln q}) = \sum_{k=0}^{N-1} \left[q^{k/2}\, \overline{X}(f_1 q^k)\, \ln\, q\right]\, e^{2j\pi kp/N}. \tag{3.22}$$

Since $\ln Q = N \ln q$, this transformation can be thought of as the output of a linear system characterized by a ratio factor q and an integer, N, which must satisfy the two conditions:

$$Q = q^N > f_2/f_1 \qquad \text{and} \qquad (\ln\, q)^{-1} > |\beta_2 - \beta_1| \tag{3.23}$$

[1]We note that in the paper [37], the Bertrand unitary P_0 distribution was defined with two parameters $r \in R$ and $q \in R$. We used the standard choices of $r = -1/2$ and $q = 0$ through out this thesis [37]. Note that the q in [37] is not equal to the parameter q used in this thesis in (3.18)-(3.41).

[2]We note that DMT given in (3.22), which was taken from [6], has to be multiplied by $q^{P/2}e^{\frac{2j\pi Pp}{N}}$ to be consistent with Equation (3.20).

in order to avoid aliasing. As a consequence, the number, N, of complex samples of the DMT to deal with must be no less than:

$$N = |\beta_2 - \beta_1| \ln (\frac{f_2}{f_1}) \tag{3.24}$$

As seen in formula (3.22), the efficient computation of a DMT can be performed by using any FFT algorithm on the function $\left[q^{k/2}\, \overline{X}(f_1 q^k)\, \ln\, q\right]$.

There is, in general, no a priori knowledge of the support of the Mellin transform of a signal. However, as noted in [44], it can be asserted that the Mellin transform of any approximately bandlimited signal of finite duration has a bounded support which can be determined directly. For example, if the signal has the approximate temporal support $(-T/2, +T/2)$ and approximate spectral support (f_1, f_2), then its P_0 distribution will be located in the time-frequency half-plane approximately between the two hyperbolas:

$$t = \pm\frac{\beta_0}{f}\ ,\ \beta_0 = \frac{T}{2}\, f_2 \tag{3.25}$$

Such a simple geometrical analysis is sufficient to assert that, in this case, the approximate support of the Mellin transform of the signal will be the interval $\beta \in (-\beta_0, \beta_0)$.

3.3.1 Principle of the computation of the Bertrand P_0 distribution

Equation (3.21) does not involve crossterms between positive and negative frequency parts of the signal. This property, combined with the fact that the P_0 distribution associated with real signals $x(t)$ is an even function of the f variable, permits to consider the implementation of (3.21) for analytic signals only [6]. In the computation of the Bertrand P_0 distribution, one first reparameterizes the half-plane $(f > 0)$ by setting $\gamma = ft$ and using the notation $\tilde{P}_X$:

$$\tilde{P}_X(\gamma, f) = P_X(t, f) \qquad , \gamma = tf \tag{3.26}$$

The P_0 distribution in (3.21) is rewritten as :

$$\tilde{P}_X(\gamma, f) = f^{1/2} \int_{-\infty}^{\infty} [\lambda_0(u)\ \lambda_0(-u)]^{1/2}\ f^{1/2} X(f\lambda_0(u))\ X^*(f\lambda_0(-u))\ e^{2j\pi\gamma u}\ du \quad (3.27)$$

with

$$\lambda_0(u) = \frac{ue^{u/2}}{2\ \sinh(u/2)} \quad (3.28)$$

After multiplying both l.h.s and r.h.s of the equation (3.27) by $f^{-1/2}$, a Mellin transform with respect to f is performed. Since the variable of integration in (3.27) is u, multiplication of the l.h.s and the r.h.s of the equation (3.27) with $f^{-1/2}$ is not going to alter the equation. Thanks to the relations (3.4)-(3.5) and (3.7)-(3.8) the result becomes:

$$\mathcal{M}_{[f^{-1/2}\ \tilde{P}_X]}(\beta) = \int_{-\infty}^{\infty} e^{2j\pi\gamma u} \left[\int_{-\infty}^{\infty} D_{\overline{X}}(\beta', u)\ D^*_{\overline{X}}(\beta' - \beta, -u)\ d\beta'\right] du \quad (3.29)$$

where

$$D_{\overline{X}}(\beta, u) = (\lambda_0(u))^{-2j\pi\beta}\ \mathcal{M}_{\overline{X}}(\beta) \quad (3.30)$$

The expression inside the brackets in (3.29) is a cross-correlation which can be computed using the Fourier transform. The Fourier transform of the function $D_{\overline{X}}(\beta, \pm u)$ along the β-axis is defined as

$$F_{\pm}(\theta, u) = \int_{-\infty}^{\infty} D_{\overline{X}}(\beta, \pm u) e^{-2j\pi\beta\theta} d\beta \quad (3.31)$$

The result leads to a new form of (3.29) which can be written as:

$$\mathcal{M}_{[f^{-1/2}\ \tilde{P}_X]}(\beta) = \int_{-\infty}^{\infty} e^{2j\pi\gamma u} \left[\int_{-\infty}^{\infty} F_+(\theta, u)\ F^*_-(\theta, u)\ e^{2j\pi\beta\theta}\ d\theta\right] du \quad (3.32)$$

Finally, inverting the Mellin transform using (3.2) and using $\gamma = tf$ to switch back to the time variable, yields the formula to be discretized:

$$P_X(t, f) = 2\mathcal{R}\left[\int_0^{\infty} F_+(\ln\ f, u)\ F^*_-(\ln\ f, u)\ e^{2j\pi tfu}\ du\right] \quad (3.33)$$

where $\mathcal{R}$ denotes the real part operation.

3.3.2 Algorithm

There are three main steps in the discretization of (3.33), namely the computation of the Mellin transform of the signal, the computation of $F_{\pm}(\theta,\ u)$ and the inverse Fourier transform with respect to u. The limit u_0 is chosen such that in the domain $u \in (0, u_0)$, both $\lambda_0(u)$ and $\lambda_0(-u)$ stay within the interval $\lambda_0(\pm u) \in (f_1/f_2,\ f_2/f_1)$. Once u_0 is determined, the number of samples M in the u space is chosen such that:

$$M \ \geq \ BT\frac{a}{a-1}\,u_0\ ,\ a \ = \ f_2/f_1, B \ = \ f_2 - f_1. \tag{3.34}$$

where $X(f) \cong 0$ for $f \notin (f_1, f_2)$ and $x(t) \cong 0$, $t \ncong (-T/2, T/2)$ and T is the time duration of the signal. The constraint on N comes from the Mellin transformation and is identical with (3.24) which reads here:

$$N \ \geq \ BT\frac{a\ \ln a}{a-1} \tag{3.35}$$

which comes from the relation (3.24) with $B = f_2 - f_1$ and $a \ = \ f_2/f_1$.

The three main steps in the algorithm are described as follows. We will use square brackets to indicate the sampled version of a function, evaluated along the set of integers.

1. Suppose we start with a signal $X(f)$ geometrically sampled on the interval (f_1, f_2) with the ratio $q \ = \ (f_2/f_1)^{1/N}$, where N is the number of frequency samples.

$$\begin{aligned} X[p] \ &= \ X(f_1 q^p), \qquad 0 \leq p \leq N-1 \\ &= \ 0, \qquad\quad N \leq p \leq 2N-1 \end{aligned} \tag{3.36}$$

Since (3.29) involves the correlation of $D_{\overline{X}}(\beta, u)$ and $D_{\overline{X}}(\beta, -u)$, the number of samples in β-space must be doubled to avoid aliasing since the correlation is being implemented indirectly using an FFT. This is achieved in (3.36) by padding the signal with N zeros in the frequency-space. The Discrete Mellin transform of the geometrically sampled signal $\overline{X}[p]$ is calculated as follows where it is assumed that $\overline{X}(f) \cong X(f)$, for $f_1 < f < f_2$.

$$M_{\overline{X}}[k] \ = \ \sum_{p=0}^{2N-1} q^{p/2}\ \ln q\ X[p]\ e^{2j\pi\frac{kp}{2N}}, \qquad 0 \leq k \leq 2N-1$$

$$= \mathcal{M}_{\overline{X}}(\beta_k), \qquad \text{where } \beta_k = \frac{k}{2N \ln q} \tag{3.37}$$

2. $D_{\pm}[k,n]$, which is the discrete version of the function $D_{\overline{X}}(\beta, \pm u)$, is calculated as follows.

$$D_{\pm}[k,n] = M_{\overline{X}}[k]\ \lambda_0(\pm u_n)^{-2j\pi\beta_k} \tag{3.38}$$

where $0 \leq k \leq 2N-1$, $0 \leq n \leq M-1$ and

$$D_{\pm}[k,n] = \begin{cases} D_{\overline{X}}(\beta_k, \pm u_n), & \beta_k = \frac{-1}{2\ln q} + \frac{k}{2N\ln q},\ u_n = nu_0/M \\ 0, & \text{otherwise} \end{cases}$$

where M is the length of the signal in time domain. The functions $F_{\pm}[p,n]$, which are discrete forms of $F_{\pm}(\theta,u)$ are then obtained by performing a FFT on $D_{\pm}[k,n]$ as shown below.

$$F_{+}[p,n] = \sum_{k=0}^{2N-1} D_{+}[k,n]\, e^{-2j\pi\frac{kp}{2N}}, \quad 0 \leq p \leq 2N-1,\ 0 \leq n \leq M-1 \tag{3.39}$$

$$F_{-}[p,n] = \sum_{k=0}^{2N-1} D_{-}[k,n]\, e^{-2j\pi\frac{kp}{2N}}, \quad 0 \leq p \leq 2N-1,\ 0 \leq n \leq M-1 \tag{3.40}$$

$$\text{where } F_{\pm}[p,n] = \begin{cases} F_{\pm}(\theta_p, u_n), & \theta_p = p\ln q,\ u_n = nu_0/M \\ 0, & \text{otherwise} \end{cases}$$

Here, we note that only N samples of $D_{\pm}[k,n]$ will be non-zero.

3. Perform an equivalent Discrete inverse u-Fourier transform of the continuous inverse u-Fourier transform in (3.33) which is expressed by the discrete formula:

$$P[k,p] = \frac{1}{M} \sum_{n=0}^{M-1} F_{+}[p,n]\ F_{-}^{*}[p,n] e^{2j\pi kn/(M*\text{exp\_factor}_p)} \tag{3.41}$$

where $0 \leq k \leq M-1$, $0 \leq p \leq N-1$ and

$$P[k,p] = \begin{cases} P_X(t_k, f_p), & \text{for } t_k = k\Delta T,\ f_p = f_1 q^p \\ 0, & \text{otherwise} \end{cases}$$

The term exp_factor_p in (3.41) is the ratio of the highest frequency to the frequency component being calculated, i.e, f_2/f_p.

The approximate complexity of this algorithm can be expressed in terms of the number of FFTs being performed. If the time-frequency representation $P_X(t,f)$ is characterized by (M,N) points in time and frequency, respectively, then we have to deal with (2M+1) FFT of 2N points and (N) FFT of $(M\frac{f_2}{2f_1})$ points.

In the limit of narrow-band signals, formulas (3.34) and (3.35) are reduced to $M \geq 2BT$ and $N \geq BT$, respectively. The above procedure has been applied to several signals described by closed form functions of frequency [6]. In this case, the geometric sampling of the signal spectrum in (3.36) is easy to obtain and the Mellin transform implementation of the Bertrand unitary P_0 distribution can be applied directly.

For example, one such closed form function of frequency is the Hyperbolic impulse, defined as:

$$H_c(f) = \frac{1}{\sqrt{f}}\, e^{-2j\pi c \ln f}\ ,\ f \geq 0. \tag{3.42}$$

The Bertrand unitary P_0 representation for a rectangularly windowed form of the Hyperbolic impulse is shown in figure (3.2).

The Bertrand unitary P_0 representation of this signal is mathematically localized in the time-frequency half-plane about the hyperbola $t = \frac{c}{f}$, where c is the hyperbolic parameter. The Bertrand unitary P_0 representation of a narrow-band signal is very close to its Wigner-Ville representation. This property is demonstrated in figure (3.3) which gives the P_0 representation of a chirp (linear group delay modulation) which is defined as:

$$E_{\gamma,\alpha}(f) = \sqrt{\frac{\pi}{\gamma - i\alpha\pi}}\, e^{-\frac{\pi^2(f-f_0)^2}{\gamma - i\alpha\pi}}. \tag{3.43}$$

3.4 Implementation of any Hyperbolic class Time-frequency representation by warping technique

An infinite number of new signal analysis and processing tools are obtained by simply prewarping the signal via a unitary transformation, performing standard processing

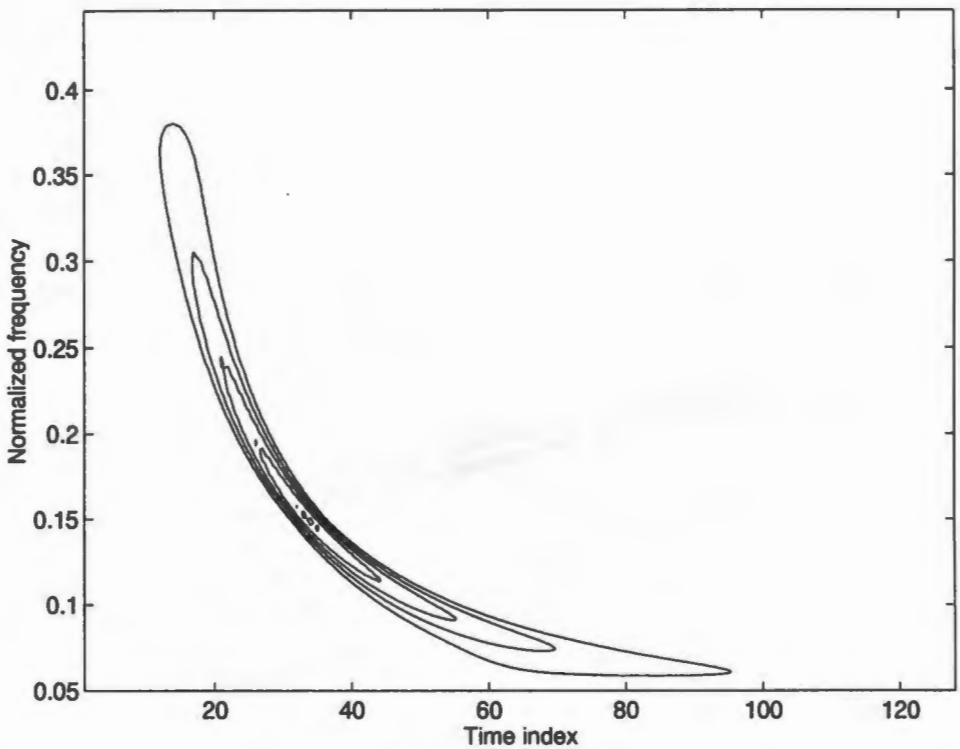

Figure 3.2: Bertrand unitary P_0 representation of the rectangularly windowed hyperbolic impulse with c=5.0 and $f_2/f_1 = 9$.

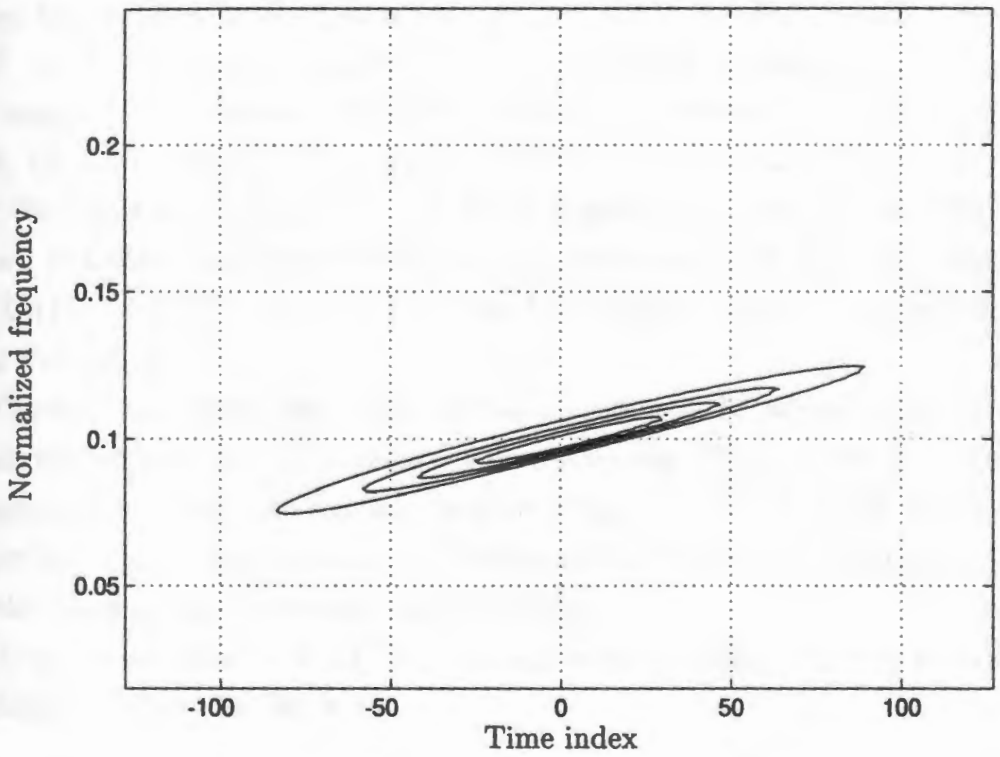

Figure 3.3: P_0 representation of a linear FM chirp with Gaussian amplitude modulation with f_0=0.1, $f_2/f_1 = 10$, γ= 0.00028 and α=0.00039.

techniques on the warped signal, and then (in some cases) unwarping the resultant output [60, 61]. The unitary transformation is obtained by applying a unitary operator U. Unitary operators and their applications have been discussed in the second chapter of this thesis.

Let us briefly discuss unitary operators before we discuss the implementation of the Hyperbolic class. The concepts of time, frequency, and scale can be associated with operators on the Hilbert space of square-integrable functions L^2. This space has an inner product $< g, h > = \int g(\tau)\ h^*(\tau) d\tau$ for $g, h \in L^2$ and norm $\|h\|^2 = < h, h >$. An operator $\mathcal{A}$ on L^2 is simply a mapping $\mathcal{A} : L^2 \rightarrow L^2$. For signals in L^2, the time, frequency and scale operators are defined as the time shift, $(S_\tau X)(f) = e^{-2j\pi\tau f}\ X(f)$, the frequency shift, $(\mathcal{M}_\nu X)(f) = X(f - \nu)$, and the dilation, $(C_a X)(f) = \sqrt{\frac{1}{a}}\ X(\frac{f}{a})$, respectively. The unitary operator $\mathcal{W}$, known as Logarithmic frequency warping operator on a signal $X(f)$ [3], is defined as $(\mathcal{W}X)(f) = \sqrt{e^{f/f_r}}\ X(f_r\ e^{f/f_r})$ and has been used to obtain the Hyperbolic class from Cohen's class.

Canfield and Jones have proposed an algorithm in [7] which efficiently implements any warped class Time-frequency representation (TFR) warped by any unitary transformation. Only the warping function $W(f) = f_r\ e^{f/f_r}$ which results in the Hyperbolic class from Cohen's class, is discussed in this thesis. The implementation for this warping function is also discussed below.

A hyperbolic-class TFR $T_X^{(H)}(t, f)$ of any arbitrary signal $x(t)$ may be generated by doing the following [46, 3, 4]:

1. Let $\tilde{X}(f) = X(f_r e^{\frac{f}{f_r}})\ \sqrt{e^{\frac{f}{f_r}}}$, where $X(f)$ is the Fourier Transform (FT) of the signal $x(t)$.

2. Compute a Cohen's-class TFR, $T_{\tilde{X}}^{(C)}(t, f)$, of $\tilde{X}(f)$.

3. Let $T_X^{(H)}(t, f) = T_{\tilde{X}}^{(C)}(\frac{f}{f_r}t, f_r\ \ln(\frac{f}{f_r}))$

The implementation is discussed in the next section.

3.4.1 A Hyperbolic-Class implementation

In the case of the hyperbolic-class TFR, warping $X(f)$ into $\tilde{X}(f)$ can be accomplished by executing the following steps:

1. Scale $X(f)$: $X_A(f) = X(f_r f)$.
2. High-pass filter the result: $X_B(f) = \sqrt{f}\, X_A(f)$.
3. Logarithmically warp the result: $X_C(f) = X_B(e^f)$.
4. Unscale $X_C(f)$: $\tilde{X}(f) = X_C(\frac{f}{f_r}) = \sqrt{e^{f/f_r}} X(f_r e^{f/f_r})$

Steps #1, #2, and #4 are straightforward to implement. Step #3 requires more consideration before implementing. The signal $x_C(t)$ should not be aliased when samples of $X_C(f)$ are computed. Also, $X_C(f)$ should be sufficiently bandlimited to one fourth the sampling rate to prevent aliasing when a Cohen's-class TFR of $\tilde{X}(f)$ is calculated [7].

Before samples of $\tilde{X}(f)$ are calculated from $X(f)$, $X(f)$ is upsampled by a factor of g to allow closely spaced samples of $\tilde{X}(f)$ to be calculated. Samples of $X(f)$ are expressed as $X_B(\frac{n\Delta f}{g})$, where $\frac{\Delta f}{g}$ is the sample spacing. Samples of $\tilde{X}(f)$ are expressed as $X_B(e^{m\Delta v}) = X_C(m\Delta v)$, where Δv is the sample spacing. A given sample, m, of $X_C(f)$ can be mapped to the nth sample of $X_B(f)$ using the following equation:

$$n = \frac{g e^{m\Delta v}}{\Delta f} \tag{3.44}$$

Aliasing in $x_C(t)$ (and, thus, in $\tilde{x}(t)$), is reduced by the following scheme. If $X_B(f)$ contains N frequency samples, and $X_C(f)$ contains R frequency samples, then the following equations can be applied to ensure that no aliasing occurs [7]:

$$\frac{N}{2g}\Delta f = e^{R\Delta v} \tag{3.45}$$

$$\frac{\frac{N}{2} - g}{g}\Delta f = e^{R-1}\Delta v \tag{3.46}$$

Solving for Δv and Δf gives:

$$\Delta v = \ln\left(\frac{\frac{N}{2}}{\frac{N}{2}-g}\right) \tag{3.47}$$

$$\Delta f = \left(\frac{\frac{N}{2}}{\frac{N}{2}-g}\right)^{R} - \left(\frac{\frac{N}{2}}{\frac{N}{2}-g}\right)^{R-1} \tag{3.48}$$

To avoid aliasing in calculating a Cohen's class TFR of $\tilde{X}(f)$, $\tilde{X}(f)$ should be bandlimited to one fourth the sampling rate, which can be accomplished by interpolation if the signal has not been aliased already.

In the case of the hyperbolic class, unwarping $T_{\tilde{X}}^{(C)}(t,f)$ into $T_{X}^{(H)}(t,f)$ can be accomplished by executing the following steps:

1. Scale the frequency axis $T_{\tilde{X}}^{(C)}(t,f) : T_{X_A}(t,f) = T_{\tilde{X}}^{(C)}(t, f_r f)$.
2. Unwarp the frequency axis: $T_{X_B}(t,f) = T_{X_A}(t, \ln(f))$.
3. Unwarp the time axis: $T_{X_C}(t,f) = T_{X_B}(ft, f)$.
4. Unscale the axes of $T_{X_C}(t,f) : T_{X}^{(H)}(t,f) = T_{X_C}(t, \frac{f}{f_r}) = T_{\tilde{X}}^{(C)}\left(\frac{f}{f_r} f, f_r \ln(\frac{f}{f_r})\right)$.

Steps #1 and #4 are straightforward to implement, but the other steps require more consideration.

The operation in step #2 is performed to unwarp the frequency axis of $T_{\tilde{X}}^{(C)}(t,f)$. This unwarping undoes the mapping that warps $X(f)$ into $\tilde{X}(f)$. Solving (3.44) for m yields:

$$m = \frac{\ln(\frac{n\Delta f}{g})}{\Delta v} \tag{3.49}$$

The indices m and n reference frequency samples in $T_{X_A}(t,f)$ and $T_{X_B}(t,f)$, respectively. In step # 3, the time axis of $T_{X_B}(t,f)$ is unwarped as follows. Consider the situation in which time-frequency distribution $T_{X_B}(t,f)$ is calculated as a matrix with rows indicating the frequency locations and columns indicating the time locations. Then $T_{X_B}(t,f)$ is expanded by the mapping explained below. Each time location in the row corresponding to a particular frequency is multiplied by an amount proportional to the frequency and is mapped to a different time location. Experimental results show that the discrete-time techniques used to find $\tilde{X}(f)$ and

$T_X^{(H)}(t,f)$ result in components in $T_{X_B}(t,f)$ at frequency $\frac{f_h}{l}$ (where f_h is the highest frequency in $T_{X_B}(t,f)$) having to be multiplied by a factor of l to be at the correct time location in $T_X^{(H)}(t,f)$.

The steps taken in the above technique can be graphically explained as follows. Consider a Hyperbolic impulse signal defined in the equation (2.14). A Hamming windowed version of the Hyperbolic impulse in frequency domain, $H_c(f)$, is shown in fig. 3.4.

The signal is computed with normalized frequency going from 0 to 0.5 with the step size being equal to $\Delta f = 0.5/N$ when $(2N)$ is the size of the signal required. In this example, $N = 128$. Later, the resultant signal is then zero padded with N zeroes and then the Inverse Fast Fourier Transform is taken to calculate the signal in time domain.

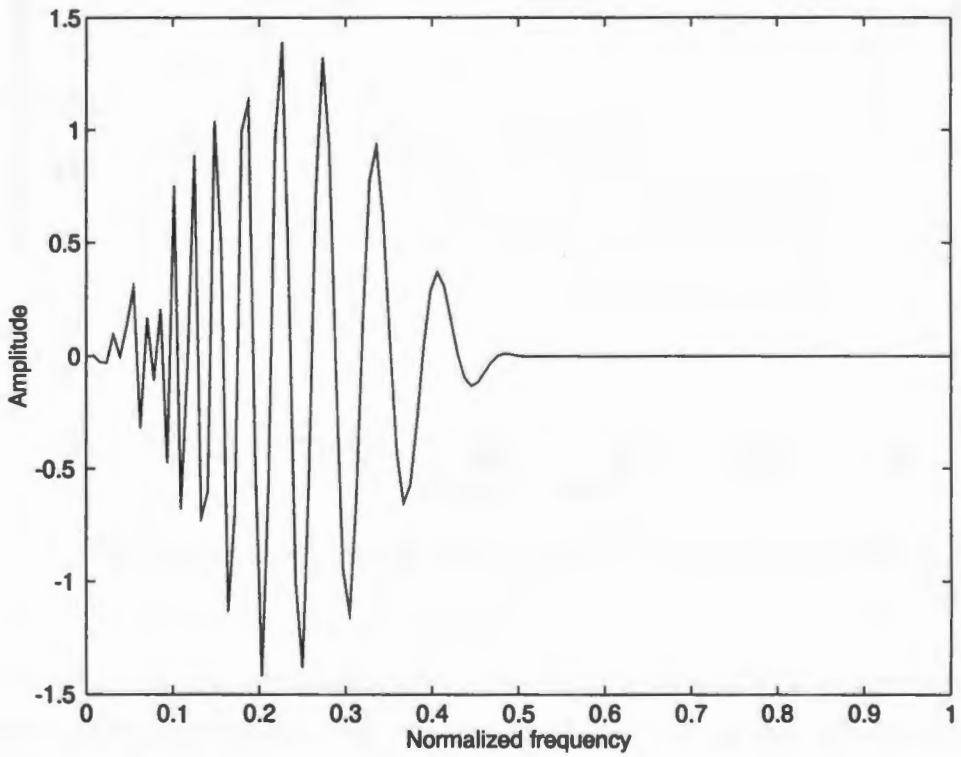

Figure 3.4: The real part of a windowed Hyperbolic impulse (c=5) computed in the the frequency domain.

The spectral energy density of $H_c(f)$ is $|H_c(f)|^2 = \frac{1}{f}$, $f \geq 0$. A TFR of the hyperbolic impulse should re-enforce the fact that its group delay corresponds to a hyperbola ($t = \frac{c}{f}$) in the time-frequency plane. The time-frequency plot of the warped signal in Figure (3.5) shows a vertical ridge whose horizontal position depends on c when "warped" time is plotted on the horizontal axis and "warped" frequency is plotted in the vertical axis. The Wigner distribution of the warped signal is shown in Figure 3.5.

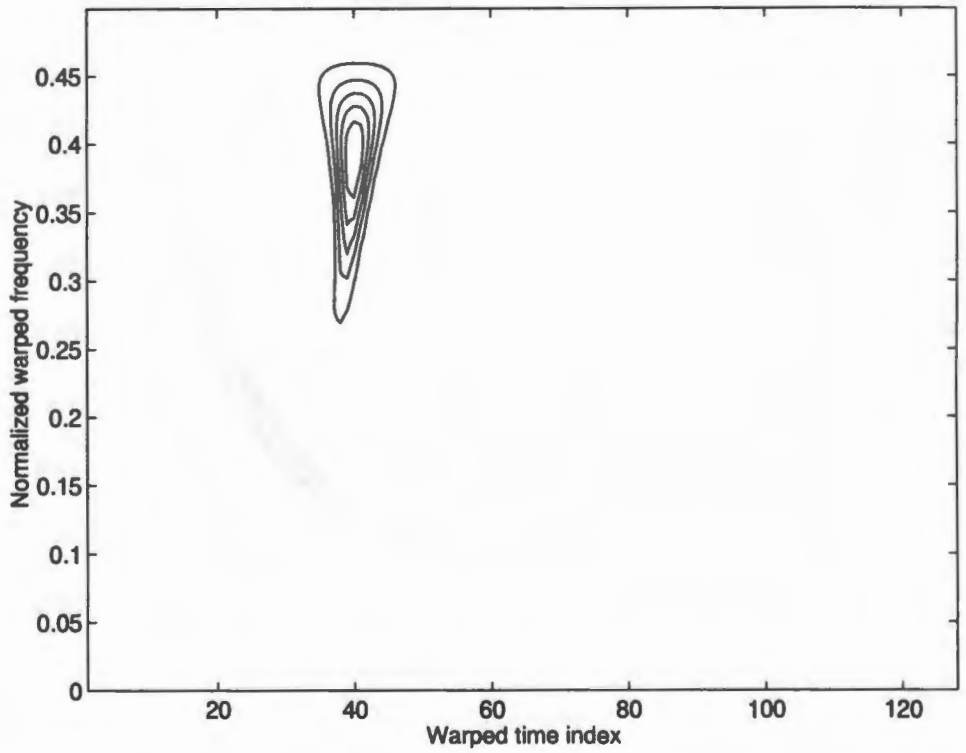

Figure 3.5: The Wigner distribution of the warped, windowed Hyperbolic impulse (c=5).

Unwarping this time-frequency plot (according to step #3 in section 3.5) maps the vertical line of support in Fig. 3.5 into the hyperbolic region of support in Fig. 3.6. Furthermore, the time-frequency representation in Fig. 3.6 corresponds to the well known Altes-Marinovic distribution, since the calculations started with the WD in Cohen's class, which maps to the Altes-Marinovic distribution in the Hyperbolic class.

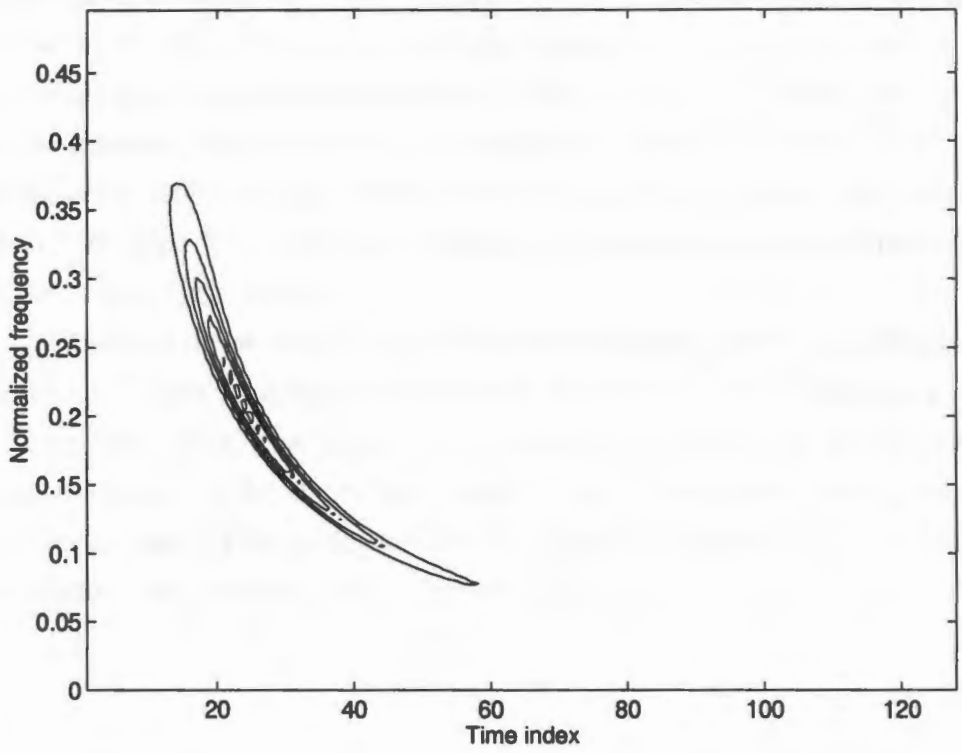

Figure 3.6: The Altes-Marinovic distribution of a windowed Hyperbolic impulse (c=5).

3.5 Conclusions

In the previous sections of this chapter, the previous work done on implementation of the Hyperbolic class of time-frequency distributions has been discussed. The implementation of the Hyperbolic class proposed by Canfield and Jones [7] is a "brute-force" technique. The warping technique used zero padding of the signal by $g = 8$ times the length of the signal for warping the signal. The warped signal is four times the length of the signal; Cohen's class TFR of the warped signal is taken. Thus, for calculating the Hyperbolic class of discrete time-frequency distributions of the size (M,M), the program requires calculation of Cohen's class TFR of size (4M,4M). This makes the memory requirements very demanding. Also, the computation is done using first order interpolation which introduces error in the computed values. This constitutes the need for an efficient technique for implementing the Hyperbolic class of time-frequency distributions.

As discussed in the section 3.3, an efficient computation of the P_0 distribution is done using the Mellin transform of the signal. Since the P_0 distribution is a member of the Hyperbolic class, this opens up the possibility of using the Mellin transform for the computation of the Hyperbolic class TFRs. In this thesis, implementation of the Hyperbolic class TFRs using the Mellin transform is proposed and this proposed implementation will be discussed in the next chapter.

Chapter 4

Implementation of the members of the Hyperbolic class using a Fast Mellin transform

4.1 Introduction

In the previous chapter, the implementation of the Bertrand unitary P_0 distribution using a Fast Mellin transform was discussed. We extend this technique to implement the Altes-Marinovic distribution using a Fast Mellin transform. Later, a new technique to implement other members of the Hyperbolic class of time-frequency distributions is proposed and discussed.

4.2 Computation of Altes-Marinovic distribution

For convenience, the Bertrand unitary P_0 distribution of an analytical signal $X(f)$ is repeated below.

$$P_X(t,f) = f \int_{-\infty}^{\infty} e^{2j\pi tfu} X\left(f\frac{ue^{u/2}}{2\sinh(u/2)}\right) X^*\left(f\frac{ue^{-u/2}}{2\sinh(u/2)}\right) \left(\frac{u}{2\sinh(u/2)}\right) du \tag{4.1}$$

The Bertrand unitary P_0 distribution can also be written as

$$P_X(t,f) \;=\; f^{1/2} \int_{-\infty}^{\infty} [\lambda_0(u)\;\lambda_0(-u)]^{1/2}\; f^{1/2} X(f\lambda_0(u))\; X^*(f\lambda_0(-u))\; e^{2j\pi tfu}\; du \tag{4.2}$$

with

$$\lambda_0(u) \;=\; \frac{ue^{u/2}}{2\,\sinh(u/2)}.$$

The Altes-Marinovic distribution is given by [40, 42] [1]

$$Q_X(t,f) \;=\; f \int_{-\infty}^{\infty} X(fe^{u/2})\; X^*(fe^{-u/2})\; e^{j2\pi tfu}\; du, \tag{4.3}$$

which also can be written as

$$Q_X(t,f) \;=\; f^{1/2} \int_{-\infty}^{\infty} \left[\tilde{\lambda}(u)\;\tilde{\lambda}(-u)\right]^{1/2}\; f^{1/2}\; X(f\tilde{\lambda}(u))\; X^*(f\tilde{\lambda}(-u))\; e^{j2\pi tfu}\; du, \tag{4.4}$$

where

$$\tilde{\lambda}(u) \;=\; e^{u/2}.$$

One can observe that equation (4.4) for the Altes-Marinovic distribution is very similar in structure to equation (4.2) which defines the Bertrand unitary P_0 distribution except for the function $\tilde{\lambda}(u)$. We propose in this thesis that the Altes distribution can also be computed using the Fast Mellin transform similar to the way in which the Bertrand P_0 distribution is computed using the Fast Mellin transform. By substituting $\tilde{\lambda}(u)$ instead of $\lambda_0(u)$ in equation (3.30), we propose that the Altes-Marinovic distribution can be computed by using the same algorithm used for the Bertrand unitary P_0 distribution (see section 3.3).

Let us consider the computation of the Altes-Marinovic distribution of a linear FM chirp with Gaussian amplitude modulation which is defined in (3.43). The steps taken for the computation of the Altes-Marinovic distribution of the linear FM chirp is shown in a series of figures given below. Figure 4.1 is the frequency domain representation of the linear FM chirp with Gaussian amplitude modulation. The program which computes the Altes-Marinovic distribution asks the signal analyst to choose the following frequencies: minimum frequency f_1, and maximum frequency f_2. The chosen minimum and maximum frequencies are superimposed on the signal spectrum

[1] Note that the dummy variable of integration used in (4.3)-(4.4) is u instead of β used in (2.32).

with dotted lines as shown in Figure 4.2. The program then computes geometrically spaced samples of the signal spectrum using the Discrete Fourier transform of the signal. The geometrically spaced samples of the signal spectrum are shown in Figure 4.3. The Discrete Mellin transform of the signal is then computed and is plotted in Figure 4.4. Finally, the Altes-Marinovic distribution is computed using the Discrete Mellin transform and is shown in Figure 4.5.

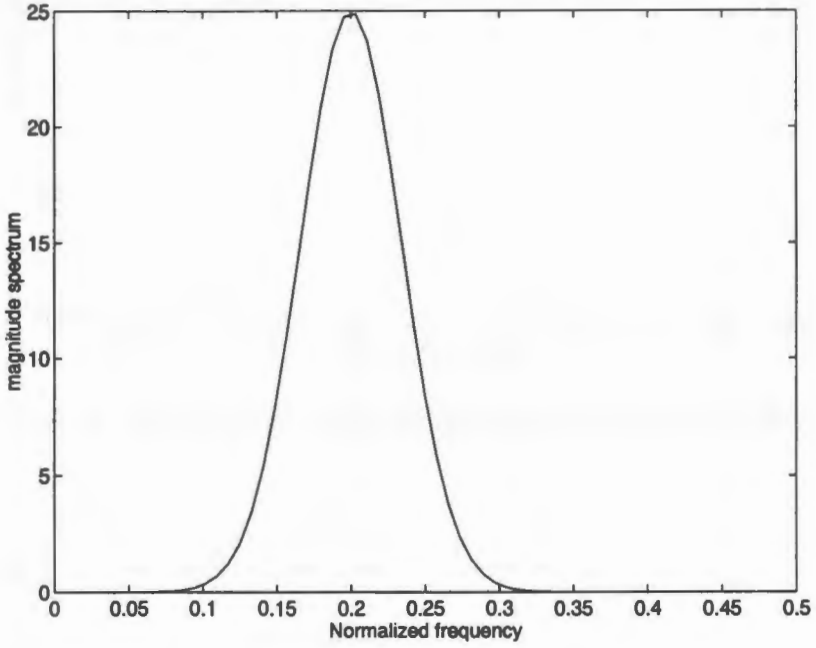

Figure 4.1: Signal Spectrum.

Let us consider a windowed version of the Hyperbolic impulse signal defined in (2.14). Figure 4.6 shows the Discrete Mellin transform of a windowed hyperbolic impulse with $c = 10$. One can observe that the Discrete Mellin transform of this windowed hyperbolic impulse is approximately an impulse in the β domain whose location on the beta axis depends on c (hyperbolic chirp parameter). Figure 4.7 shows the Altes-Marinovic distribution of the signal.

The Altes-Marinovic distribution of a multicomponent signal exhibits cross terms or interference terms which were discussed in the second chapter. The cross term or interference term of two different hyperbolic impulses with hyperbolic parameters c_1 and c_2 is concentrated along the "mean hyperbola", $t = c_{12}/f$, along which

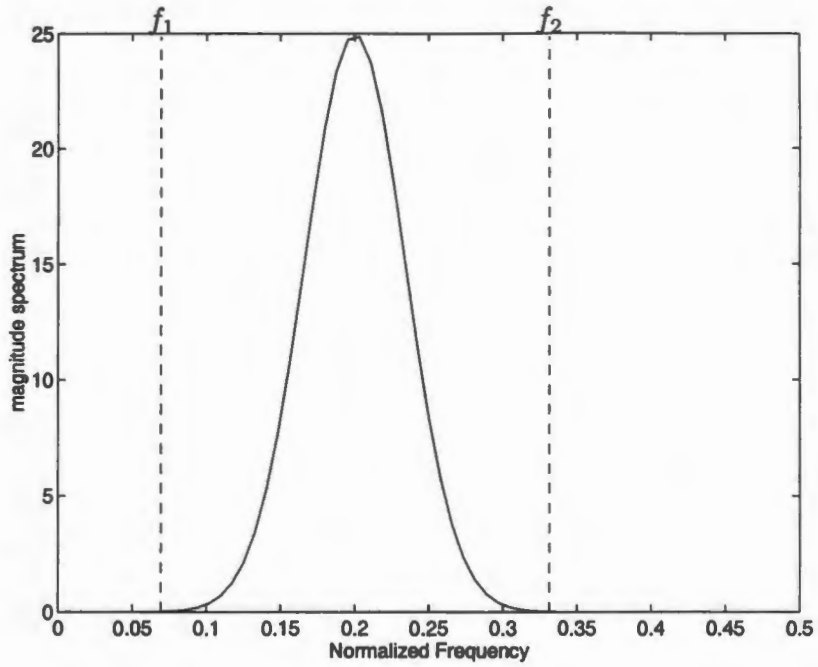

Figure 4.2: f_2 and f_1 superimposed with dotted lines on the Signal spectrum, $f_2/f_1 = 4.375$.

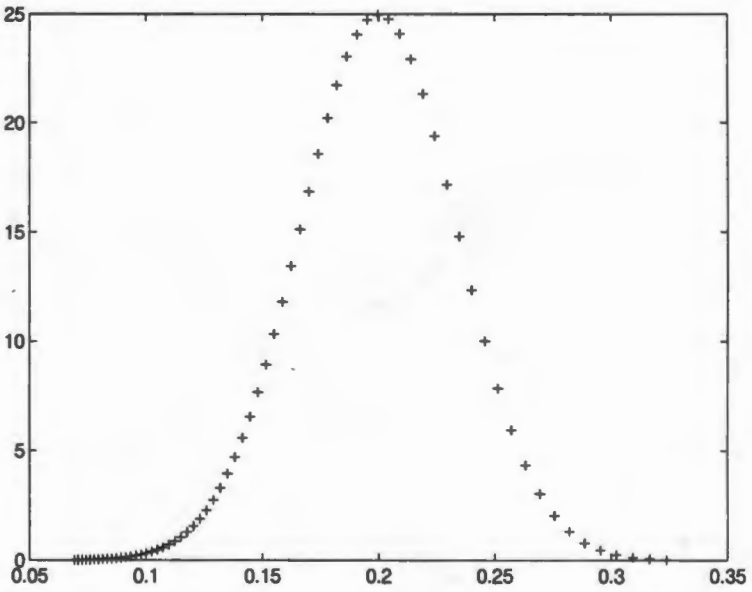

Figure 4.3: Geometrically sampled signal spectrum.

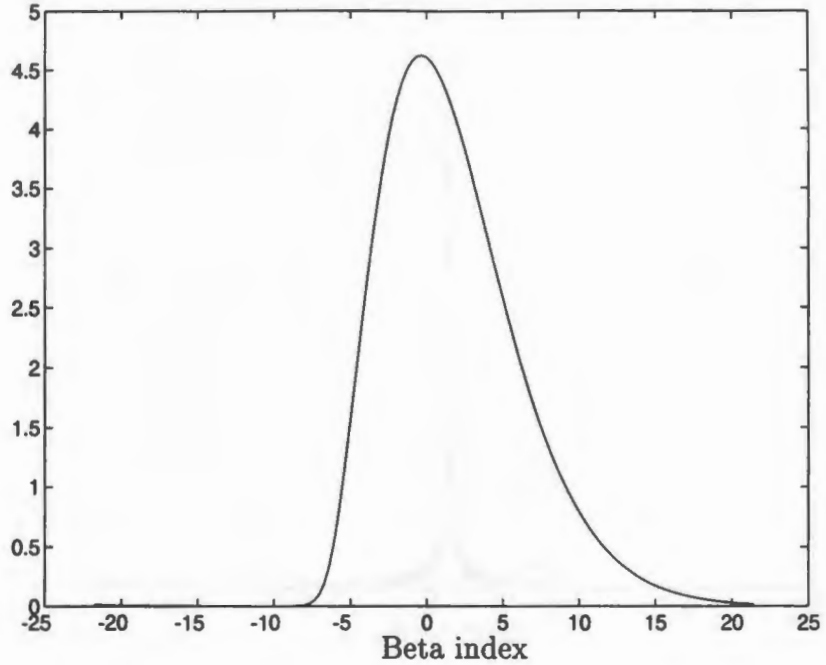

Figure 4.4: Mellin transform of the signal spectrum with $\Delta\beta = 0.3263$.

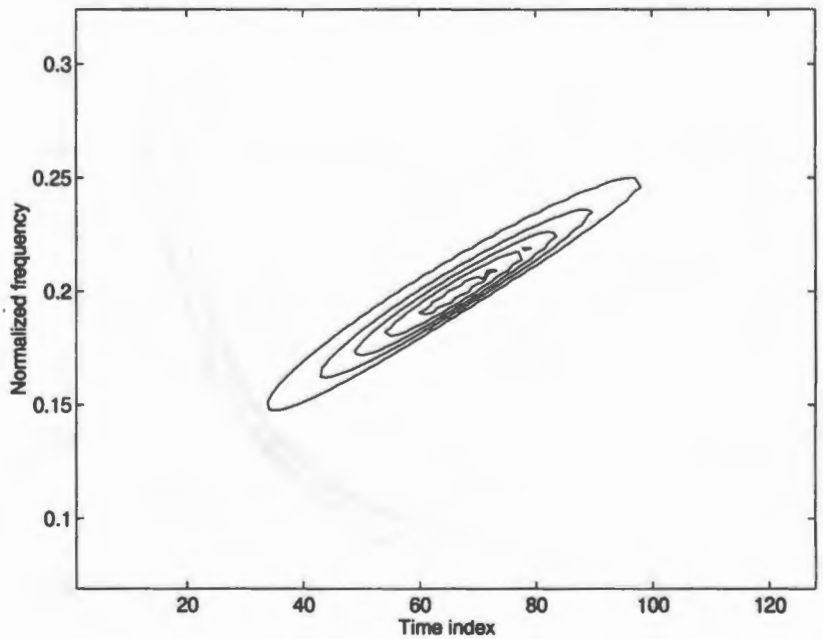

Figure 4.5: Altes-Marinovic distribution of the signal.

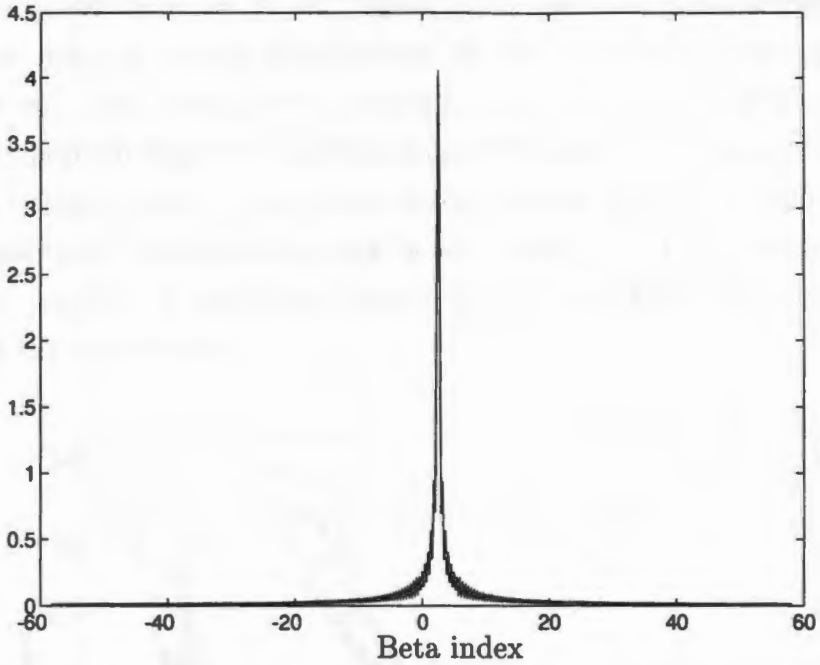

Figure 4.6: Mellin Transform of the windowed Hyperbolic impulse (c=5) with $\Delta\beta = 0.2276$.

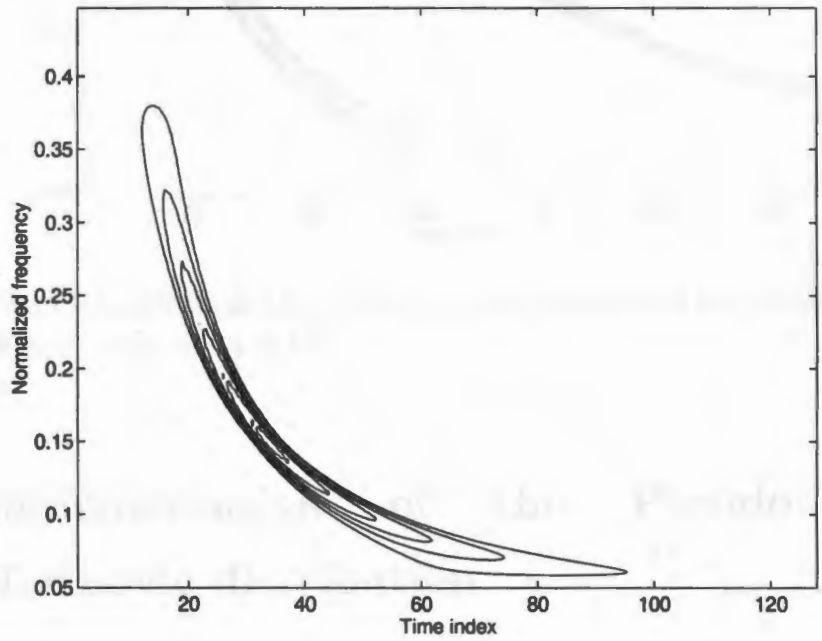

Figure 4.7: Altes-Marinovic distribution of the windowed Hyperbolic impulse (c=5).

it is oscillatory, where $c_{12} = \frac{c_1+c_2}{2}$. Figure 4.8 is the ideal case; it shows the sum of individual Altes-Marinovic distributions of two windowed Hyperbolic impulses ($c_1 = 5$ and $c_2 = 15$). The actual Altes-Marinovic distribution of the sum of two windowed Hyperbolic impulses (c_1=5 and c_2=15) is shown in Figure 4.9. The cross terms or interference terms cause serious interpretation problems as discussed in the second chapter and constitute the need for smoothing. The Pseudo Altes-Marinovic distribution, which is a smoothed version of the Altes-Marinovic distribution, is discussed in the next section.

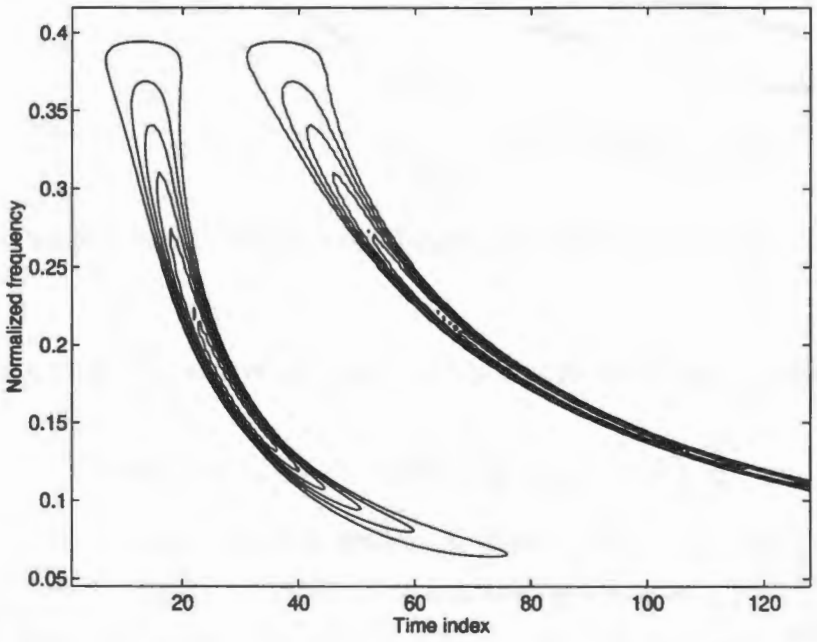

Figure 4.8: Sum of individual Altes-Marinovic distributions of two windowed Hyperbolic impulses ($c_1 = 5$ and $c_2 = 15$).

4.3 Implementation of the Pseudo Altes-Marinovic distribution

The Pseudo Altes-Marinovic distribution, a member of the Hyperbolic class, is a smoothed version of the Altes-Marinovic distribution. It is defined in section 2.9.5

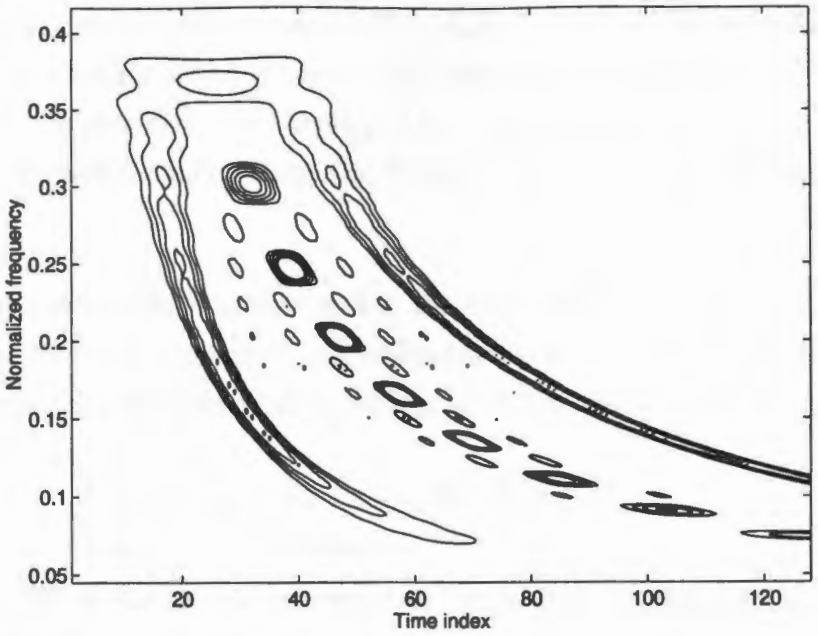

Figure 4.9: Altes-Marinovic distribution of sum of two windowed Hyperbolic impulses ($c_1 = 5$ and $c_2 = 15$).

and, for convenience, the expression which we are implementing is repeated here.

$$\mathrm{PAD}_X(t,f) \;=\; f_r \int_0^\infty Q_{\tilde{\Gamma}}(0, f_r \frac{f}{f'})\, Q_X(\frac{tf}{f'}, f')\, \frac{df'}{f'} \tag{4.5}$$

Here $\Gamma(f)$ is an analysis window which is exponentially frequency warped as $\tilde{\Gamma}(f) \;=\; \sqrt{\frac{f}{f_r}}\, \Gamma(f_r \ln \frac{f}{f_r}), \quad f > 0$. The smoothing function $Q_{\tilde{\Gamma}}(0, f_r \frac{f}{f'})$ in (4.5) is related to the Wigner distribution as follows. A Cohen's class TFR, $T_X^{(C)}$, is obtained from the corresponding Hyperbolic class TFR, $T_X^{(H)}$, as

$$T_{\tilde{\Gamma}}^{(H)}(t,f) \;=\; T_{\Gamma}^{(C)}(\frac{tf}{f_r}, f_r \ln \frac{f}{f_r}). \tag{4.6}$$

From the above equation, $Q_{\tilde{\Gamma}}(0, f_r \frac{f}{f'})$ in equation (4.5) is equal to $W_{\Gamma}(0, f_r \ln \frac{f}{f'})$. Equation (4.5) can be rewritten as

$$\mathrm{PAD}_X(t,f) \;=\; f_r \int_0^\infty W_{\Gamma}(0, f_r \ln \frac{f}{f'})\, Q_X(\frac{tf}{f'}, f')\, \frac{df'}{f'}. \tag{4.7}$$

In this section, we use equation (4.7) to implement the Pseudo Altes-Marinovic

distribution, since the computation of $Q_{\tilde{\Gamma}}(0, f_r \frac{f}{f'})$ is difficult because of the exponential frequency warping of the window. The computation of $W_\Gamma(0, f_r \ln \frac{f}{f'})$ instead of $Q_{\tilde{\Gamma}}(0, f_r \frac{f}{f'})$ is simpler since no warping of the window is involved.

The steps used for computing the Pseudo Altes-Marinovic distribution are as follows.

1. Initially, as discussed in section 4.2, the Altes-Marinovic distribution of the signal is calculated using the Fast Mellin transform. Let us denote the calculated, sampled Altes-Marinovic distribution as $Q[k,p]$ where for $0 \leq k \leq M-1$ and $0 \leq p \leq N-1$,

$$Q[k,p] = \begin{cases} Q_X(t_k, f_p), & \text{for } t_k = k\Delta T,\ f_p = f_1 q^p, \\ 0, & \text{otherwise.} \end{cases}$$

Here, ΔT is the sampling period in time, and q is the geometric sampling period in frequency (See step 1 in section 3.3.2), f_1 is the minimum frequency of the support region of $X(f)$, M is the length of the signal, and N is given by (3.35).

2. The Wigner distribution of a window, $\Gamma(f)$, of suitable length is taken. A slice of the sampled Wigner distribution at time $t = 0$ is taken. Let us denote this slice by $\hat{W}[l]$ where

$$\hat{W}[l] = \begin{cases} W_\Gamma(0, f_l), & \text{for } f_l = l\Delta f, \text{ for } 0 \leq l \leq (L-1)/2, \\ 0, & \text{otherwise.} \end{cases}$$

Here, Δf is the sample spacing in frequency, and L is the length of the window in frequency [2]. The Wigner distribution of the window is usually computed for positive and negative frequencies. The negative frequencies are truncated since we are interested in smoothing an analytic signal, and hence only values of the Wigner distribution of the window at time $t = 0$ and $f \geq 0$ are considered.

3. In equation (4.7), the integration is done with respect to a dummy variable f' which corresponds to frequency. A vector of values $f'[m]$ is evaluated by uniformly distributing them between the minimum frequency, f_1, and the maximum frequency, f_2. Hence, $f'[m] = m\Delta f'$ where $\Delta f' = \frac{f_2 - f_1}{K}$. Here, K

[2] L is assumed to be odd for simplicity.

determines the length of the vector $f'[m]$ and partly the accuracy of the result of the numerical integration in (4.7).

4. For an output point in the time frequency plane corresponding to time t_k and frequency f_p, the integration in (4.7) is calculated as follows. Using the vector of f', the vectors $lr[m] = \ln \frac{f_p}{f'[m]}$ and $tfr[m] = \frac{t_k f_p}{f'[m]}$ are calculated. Only the values of $f'[m]$ are chosen which satisfy the constraints $f_1 \leq lr[m] \leq f_2$ and $T_{\min} \leq tfr[m] \leq T_{\max}$ where T_{min} and T_{max} are the minimum and maximum times during which the signal is essentially non-zero.

5. The values of $f'[m]$ which do not satisfy the above specified constraints are eliminated from the vector $f'[m]$. Also, the elements in the vectors $lr[m]$ and $tfr[m]$ which correspond to the eliminated elements in vector $f'[m]$ are also eliminated (see definitions of $lr[m]$ and $tfr[m]$ in step 4). Since the elements of these vectors are the result of operations like natural logarithm and division of integers, they may not be integers. So, evaluation of the Wigner distribution and the Altes-Marinovic distribution at these time and frequency instances is done using first order linear interpolation [62] [63]. Using the values of $\hat{W}[l]$ and first order linear interpolation, the new vector $\tilde{W}[m]$ is evaluated whose elements are the values of the Wigner distribution of the smoothing window at time $t = 0$ and frequencies $lr[m]$. Here, $\tilde{W}[m] \cong W_\Gamma(0, lr[m]) = W_\Gamma(0, \ln \frac{f_p}{f'[m]})$. Also, using the values of $Q_X[k,p]$ and first order interpolation, the new vector $\tilde{Q}_X[m]$ is evaluated whose elements are the values of the Altes-Marinovic distribution at times $tfr[m]$ and frequency $f'[m]$. Here,
$\tilde{Q}_X[m] \cong Q_X(tfr[m], f'[m]) = Q_X(\frac{t_k f_p}{f'[m]}, f'[m])$.

6. Once the vectors $\tilde{W}[m]$ and $\tilde{Q}_X[m]$ are evaluated, they are multiplied together and are divided by $f'[m]$. The resulting vector is used as input to perform Simpson's method of numerical integration [62] [63], which results in an approximation to $\mathrm{PAD}_X(t_k, f_p)$.

7. For each required output time and frequency point in the time frequency plane, steps 3 - 6 are repeated to calculate the Pseudo Altes-Marinovic distribution.

The Pseudo Altes-Marinovic distribution of a signal (See Figure 4.8) which is the sum of two windowed Hyperbolic impulses ($c_1 = 5$ and $c_2 = 15$) is shown in Figure 4.11. A Hanning window of length 7 is used for smoothing. The slice of the Wigner distribution of the window at time $t = 0$ is shown in Figure 4.10.

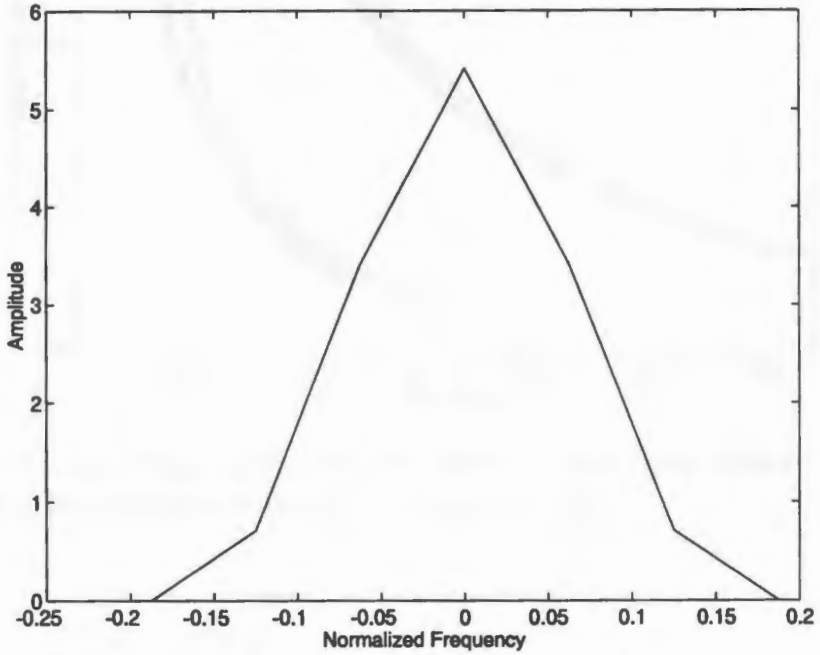

Figure 4.10: Slice at time $t = 0$ of the Wigner distribution of a Hanning window of length 7.

When compared with figure 4.9, figure 4.11 demonstrates the capability of the Pseudo Altes-Marinovic distribution to remove the cross term occurring between the Hyperbolic impulses. But, the Pseudo Altes distribution computed using the Fast Mellin transform does not remove the cross term entirely when the two hyperbolic impulses come closer together. Let us consider a signal which is the sum of two windowed hyperbolic impulses with $c_1 = 5$ and $c_2 = 10$. Figure 4.12 shows the ideal case, which is the sum of the Altes distribution of the individual hyperbolic impulses. Figure 4.13 shows the actual case, which is the Altes distribution of the sum of two hyperbolic impulses ($c_1 = 5$ and $c_2 = 10$). Figure 4.14 shows the Pseudo Altes-Marinovic distribution of the signal; a Hanning window of length 7 was used

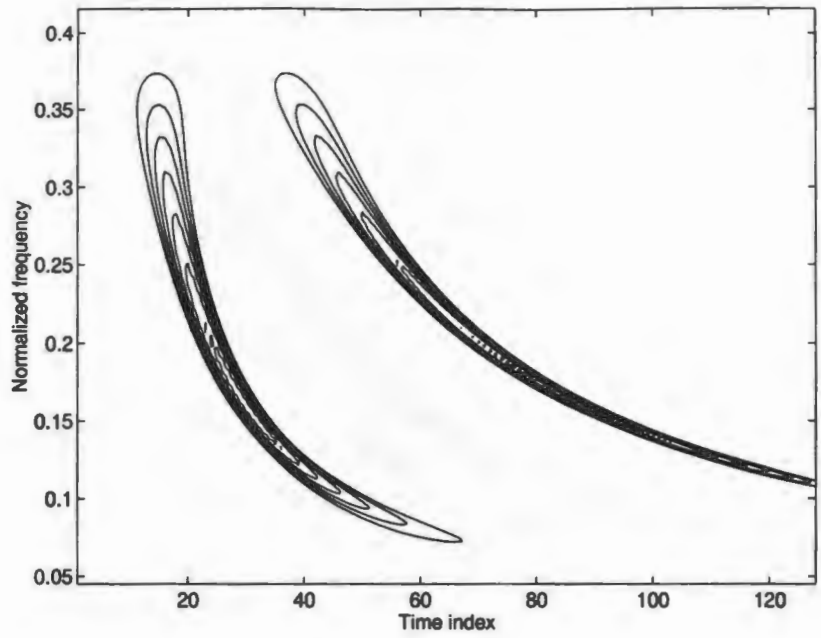

Figure 4.11: Pseudo Altes-Marinovic distribution of the signal which is the sum of two windowed Hyperbolic impulses ($c_1 = 5$ and $c_2 = 15$).

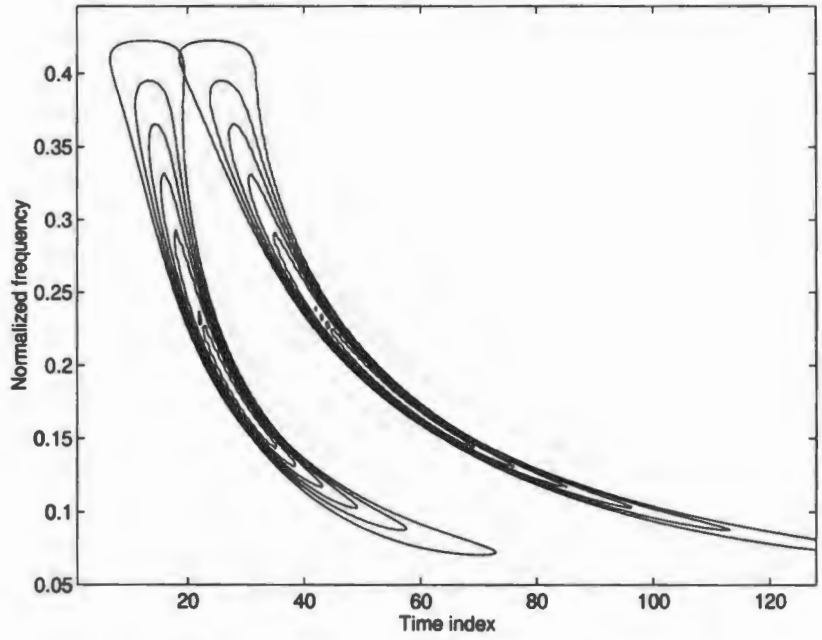

Figure 4.12: Sum of individual Altes-Marinovic distributions of two windowed Hyperbolic impulses ($c_1 = 5$ and $c_2 = 10$).

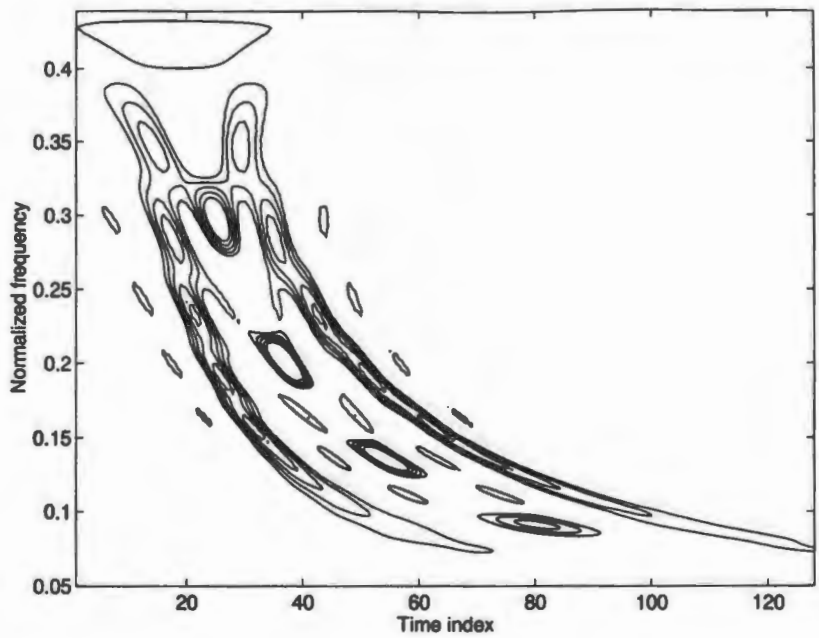

Figure 4.13: Altes-Marinovic distribution of sum of two windowed Hyperbolic impulses ($c_1 = 5$ and $c_2 = 10$).

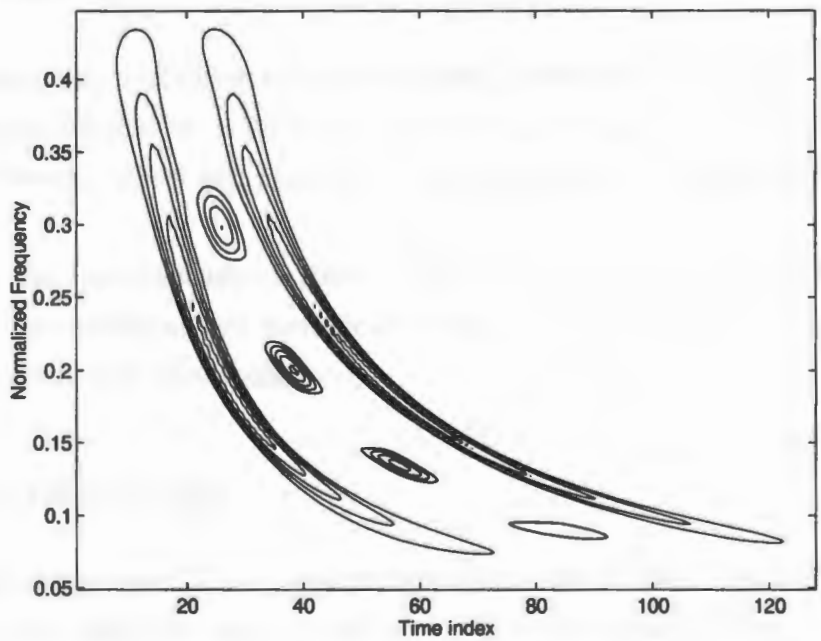

Figure 4.14: Pseudo Altes-Marinovic distribution of the signal which is the sum of two windowed Hyperbolic impulses ($c_1 = 5$ and $c_2 = 10$) computed using a Hanning window of length 7.

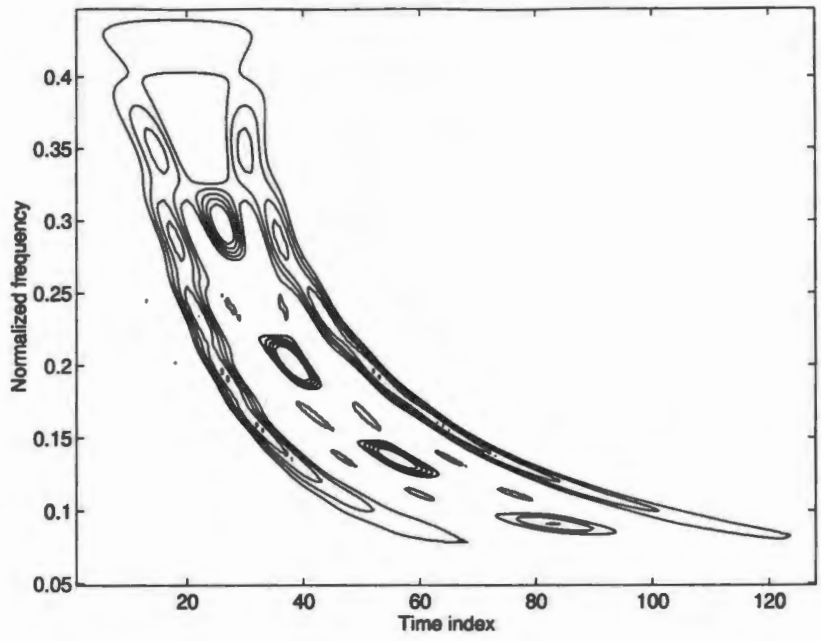

Figure 4.15: Pseudo Altes-Marinovic distribution of the signal which is the sum of two windowed Hyperbolic impulses ($c_1 = 5$ and $c_2 = 10$) computed using a Blackman window of length 31.

for smoothing. One can observe that smoothing takes place with the Pseudo Altes-Marinovic distribution but it does not entirely smooth out or remove the cross term as in the previous case of two hyperbolic impulses with c_1=5 and c_2=15 (see Figure 4.11).

The way the Pseudo Altes-Marinovic distribution is implemented in this chapter, using linear interpolation and numerical integration, can also be used to implement other members of the Hyperbolic class.

4.4 Conclusions

In this chapter, we have shown a way to implement the Altes-Marinovic distribution and the Pseudo Altes-Marinovic distribution. The Altes-Marinovic distribution was implemented using the Fast Mellin transform by extending the technique used to implement the Bertrand P_0 distribution. The Pseudo Altes-Marinovic distribution

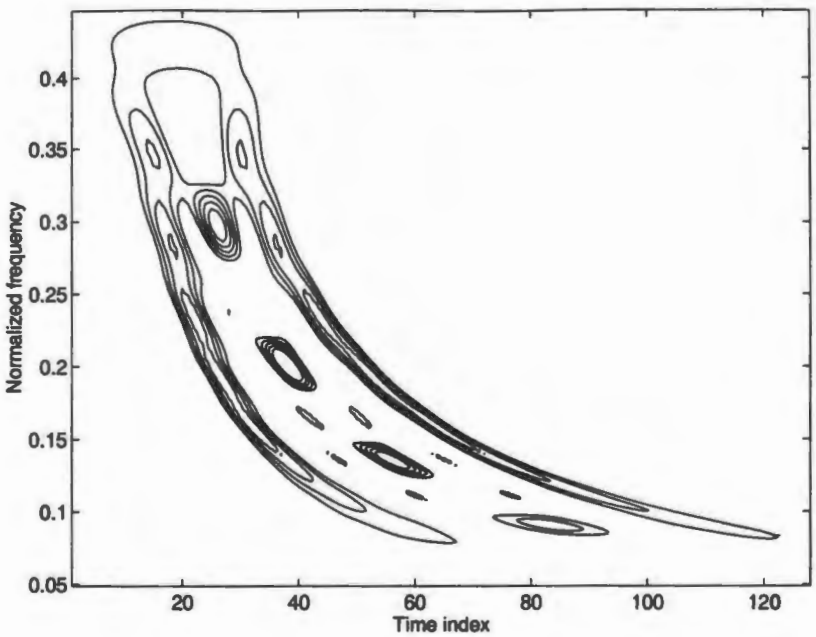

Figure 4.16: Pseudo Altes-Marinovic distribution of the signal which is the sum of two windowed Hyperbolic impulses ($c_1 = 5$ and $c_2 = 10$) computed using a Hanning window of length 15.

is implemented by smoothing the Altes-Marinovic distribution using linear interpolation and numerical integration. Other members of the Hyperbolic class, which are smoothed versions of the Altes-Marinovic distribution, can be implemented in a similar manner.

The memory requirements for this technique depend upon the time-bandwidth product (BT) of the signal where $B = f_2 - f_1$ and T is the time duration of the signal. If the length of the signal in time is M points, then the sampled Altes-Marinovic distribution is characterized by M points in time and N points in frequency where N is given by equation (3.35). The memory requirements for computation of the Altes-Marinovic distribution using the Fast Mellin transform are less compared to that of the warping technique, in general, requiring only (1/32) to (1/8) the memory required for the warping technique for the length 128 examples in this thesis. But, for the computation of Pseudo Altes-Marinovic distribution and other Smoothed Altes-Marinovic distributions, the proposed technique takes more time. (In general, the new technique takes around three hours compared to the warping technique which

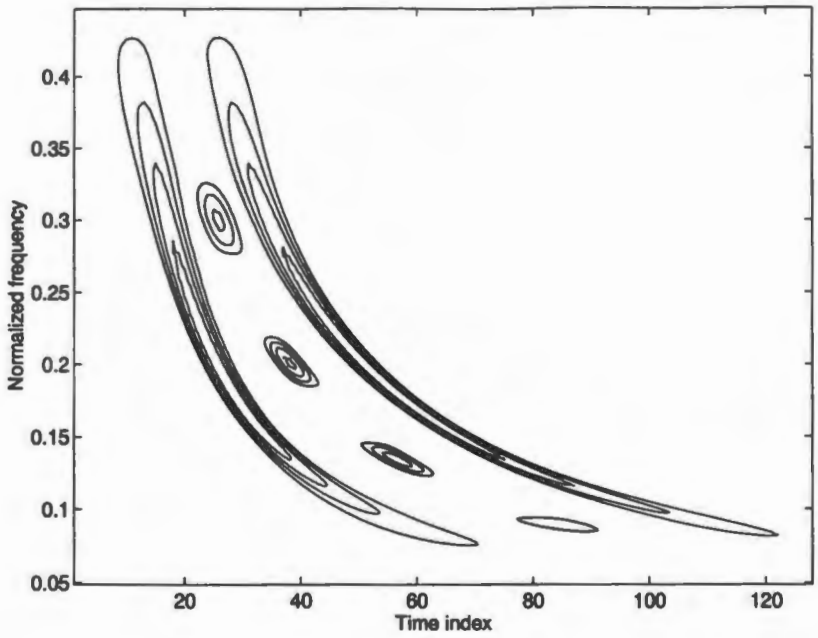

Figure 4.17: Pseudo Altes-Marinovic distribution of the signal which is the sum of two windowed Hyperbolic impulses ($c_1 = 5$ and $c_2 = 10$) computed using a Hanning window of length 5.

takes 3 minutes). Also, since the computation involves first order interpolation and numerical integration, there is an error between the actual value and the calculated value.

For smoothing the cross-terms of the Altes-Marinovic distribution, the way of determining the type and the length of the window is a trial and error procedure which is quite frustrating for a signal analyst. To illustrate that point, consider Figures 4.15, 4.16, 4.17 and 4.18. Figure 4.15 shows the Pseudo Altes-Marinovic distribution of the sum of two windowed Hyperbolic impulses ($c_1 = 5$ and $c_2 = 10$) computed using a Blackman window of length 31. Figure 4.16 shows the Pseudo Altes-Marinovic distribution of the same signal computed using a Hanning window of length 15. Figure 4.17 shows the Pseudo Altes-Marinovic distribution of the sum of two windowed Hyperbolic impulses ($c_1 = 5$ and $c_2 = 10$) computed using a Hanning window of length 5. Figure 4.18 shows the Pseudo Altes-Marinovic distribution of the sum of two windowed Hyperbolic impulses ($c_1 = 5$ and $c_2 = 10$) computed

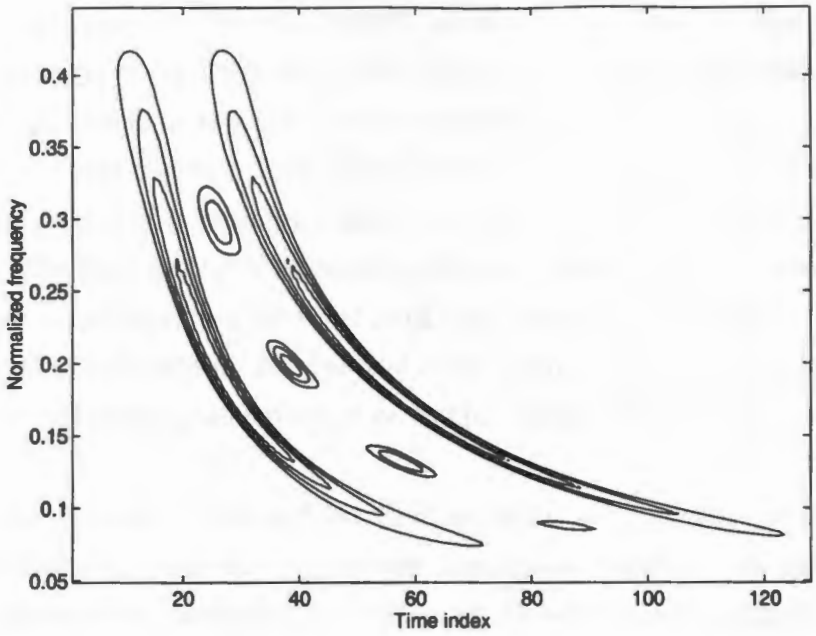

Figure 4.18: Pseudo Altes-Marinovic distribution of the signal which is the sum of two windowed Hyperbolic impulses ($c_1 = 5$ and $c_2 = 10$) computed using a Hanning window of length 3.

using a Hanning window of length 3. These can be compared to the Pseudo Altes-Marinovic distribution of the same signal, in Figures 4.13-4.14 which were computed using no window and a length 7 Hanning window, respectively. One can see that as the window length decreases the degree of smoothing increases; cross terms get smoothed and decrease in their amplitude (compare Figure 4.17 which shows Pseudo Altes-Marinovic distribution computed using a Hanning window of length 5 with Figure 4.16 which shows the Pseudo Altes-Marinovic distribution computed using a Hanning window of length 15). Figure 4.18 uses a Hanning window of length 3 and it has the best performance of smoothing the cross terms without distorting the auto terms among the examples which show Pseudo Altes-Marinovic distribution of the sum of two windowed Hyperbolic impulses ($c_1 = 5$ and $c_2 = 10$) computed using various window lengths.

One can observe from the figures, that as the window length decreases, the smoothing improves but this in no way gives the analyst the value of the window length which does the best smoothing possible. In the example where the Hyperbolic

impulses are far apart ($c_1 = 5$ and c_2=15), a Hanning window of length 7 was used for entirely smoothing the cross term (see Figure 4.11) but the trial and error procedure was used to arrive at the value of the window length. But, when the hyperbolic impulses come closer together, (see Figure 4.14) the Pseudo Altes-Marinovic distribution computed using a Hanning window of length 7 does not entirely remove the cross terms. The best available smoothing through this technique among the examples that were considered was obtained with Hanning window of length 3 (see Figure 4.18) but it does not entirely remove the cross term. All this provides motivation for a better smoothing implementation technique which will be discussed in the next chapter.

In the next chapter, we show that the implementation of the various members of the Hyperbolic class via the Hyperbolic Ambiguity function will give the signal analyst an opportunity to decide the length of the window and also more intuition as to how cross terms and auto terms map in the Hyperbolic class.

Chapter 5

Implementation of Hyperbolic ambiguity function and use of it for removal of cross terms

5.1 Introduction

In this chapter, an extensive analysis of the warping technique proposed by Canfield and Jones [7] is done. Canfield and Jones [8] have used a warping technique to implement a Data Adaptive Radially-Gaussian Hyperbolic-class representation; but it does not work well for the removal of cross terms in the case of a signal which is the sum of two or more linear FM chirps closer to each other in the time-frequency plane. We have used the warping technique to implement several members of the hyperbolic class, like the Pseudo Altes distribution and Smoothed Pseudo Altes distribution. In our approach of the warping technique, the Hyperbolic ambiguity function is calculated. Later, in section 5.2, we use weighting of the HAF to smooth cross terms and to implement any arbitrary member of the Hyperbolic class.

There is a need for new members of the Hyperbolic class of TFRs. As discussed in the third chapter of this thesis, Canfield and Jones [8] have used a warping technique to implement a Data Adaptive Radially-Gaussian Hyperbolic-class representation; but it does not work well for the removal of cross terms in the case of a signal which is the sum of two or more linear FM chirps. Also, the Pseudo Altes-Marinovic distribution and the Smoothed Pseudo Altes-Marinovic distribution don't work very

well either for multi-component linear FM signals.

In this chapter, we propose a new member of the Hyperbolic class which is called the MTEK (Multiform, Tiltable Exponential Kernel) smoothed Altes-Marinovic distribution which works well both for Hyperbolic impulses and linear FM chirps. The MTEK smoothed Altes-Marinovic distribution uses the MTED kernel [2, 64] to weight the Hyperbolic ambiguity function of the signal in order to remove cross terms. The MTED kernel is discussed in detail in the third section of this chapter. Also, cross term removal in various time frequency scenarios involving Hyperbolic impulses and other signals like Gaussian signals or linear FM chirps is shown in this chapter.

5.2 Definition and Implementation of the Hyperbolic ambiguity function

As defined in the second chapter of this thesis, the Hyperbolic Ambiguity function [42, 3, 4] is

$$\begin{aligned} B_X(\zeta,\beta) &= A_{\mathcal{W}X}\Big(\frac{\zeta}{f_r}, f_r\beta\Big) \\ &= \int_0^\infty X\big(fe^{\beta/2}\big)\; X^*\big(fe^{-\beta/2}\big)\; e^{j2\pi\zeta \ln\frac{f}{f_r}}\, df\,. \end{aligned} \tag{5.1}$$

As can be seen from the above equation, the Hyperbolic ambiguity function is the narrowband Ambiguity function $A_X(\tau,\nu)$, defined in (2.12), of a logarithmically warped signal $(\mathcal{W}X)(f) = \sqrt{e^{f/f_r}}X\big(f_r\, e^{f/f_r}\big)\,, \quad -\infty < f < \infty$. Any Hyperbolic class TFR can be expressed in terms of the Hyperbolic ambiguity function $B_X(\zeta,\beta)$ as (Normal form IV in equation (2.29))

$$T_X^{(H)}(t,f) = \int_{-\infty}^{\infty}\int_{-\infty}^{\infty} \Psi_T^{(H)}(\zeta,\beta)\; B_X(\zeta,\beta)\; e^{j2\pi(tf\beta-(\ln\frac{f}{f_r})\zeta)}\, d\zeta\, d\beta\,. \tag{5.2}$$

All of the members of the Hyperbolic class can be understood by investigating their kernel, $\Psi_T^{(H)}(\zeta,\beta)$, which is a scaled version of the corresponding Cohen's class kernel, $\Psi_T^{(C)}(\zeta,\beta)$, as shown below.

$$\Psi_T^{(H)}(\zeta,\beta) = \Psi_T^{(C)}(\frac{\zeta}{f_r}, f_r\beta) \tag{5.3}$$

Assuming $f_r = 1$, we can use the same kernels for HC TFRs that were used in Cohen's class. Thus, each member of Cohen's class has an equivalent Hyperbolic class member. The equivalent Hyperbolic class QTFR of the Wigner distribution, which has the kernel $\Psi_{\text{WD}}^{(C)}(\zeta,\beta) = 1$, is the Altes-Marinovic distribution, with kernel $\Psi_{Q}^{(H)}(\zeta,\beta) = 1$. The equivalent QTFRs in the Hyperbolic class of the Pseudo Wigner distribution, the Smoothed Pseudo Wigner distribution, and the Spectrogram in the are the Pseudo Altes-Marinovic distribution, the Smoothed Pseudo Altes-Marinovic distribution, and the Hyperbologram, respectively [3, 4]. We propose in this thesis a new distribution, called the "Multiform Tiltable Exponential kernel smoothed Altes-Marinovic distribution" whose kernel $\Psi_{\text{MTEK-AD}}^{(H)}(\zeta,\beta)$, is the MTED (Multiform Tiltable Exponential distribution) kernel proposed in [2]. We will discuss this kernel in more detail in section 5.3.

5.2.1 Implementation of the Hyperbolic class via the Hyperbolic Ambiguity function

The normal form IV formulation in (5.2) completely defines any arbitrary, quadratic Hyperbolic class Time-frequency representation. One implementation of the normal form IV can be explained in the following five steps.

Step 1. The input signal $X(f)$, is subjected to a *logarithmic frequency warping* $\mathcal{W}$ [3, 4]. The signal warping is defined in the second chapter of this thesis. The warping is implemented using Canfield's technique as discussed in section 3.4 of this thesis [7].

Step 2. The narrowband or Woodward Ambiguity function of the warped signal is calculated. Equation (5.1) states that this is equivalent to calculating the Hyperbolic ambiguity function $B_X(\zeta,\beta)$ of the signal whenever $f_r = 1$. The Hyperbolic ambiguity function (HAF) of a signal maps the auto terms to the origin and the cross terms away from the origin of the (ζ,β) plane. This property enables one to sometimes distinguish between cross terms and auto terms. Note that if we let $\tilde{T}_X(\gamma,\nu)$ be the 2D FT of $\Psi_T^{(H)}(\zeta,\beta)\ B_X(\zeta,\beta)$, i.e.,

$$\tilde{T}_X(\gamma,\eta) \quad = \quad \int\int \Psi_T^{(H)}(\zeta,\beta)\ B_X(\zeta,\beta)\ e^{j2\pi(\gamma\beta-\eta\zeta)}\ d\zeta\ d\beta$$

$$= \quad T_X^{(H)}(\gamma\eta,\ f_r e^{\eta})$$

then $\tilde{T}_X(\gamma,\eta)$ is equal to an axis-warped version of the desired HC TFR, $T_X^{(H)}(t,f)$.

Step 3. After identifying auto terms and cross terms in the Hyperbolic ambiguity function domain, i.e. the (ζ,β) plane, the proper kernel is chosen to "pass" much of the auto terms unchanged and to "block" as much as possible of the cross-terms. In this step, the proper kernel, $\Psi_T^{(H)}(\zeta,\beta)$, in (5.2) is calculated so as to achieve the objectives of "cross term filtering" described in section 2.5.

Step 4. After multiplying the Hyperbolic ambiguity function with a suitable kernel, a two dimensional FFT is taken (one is a Fast Fourier transform and other an inverse Fast Fourier transform) to get the signal into the $t-f$ domain from the $\zeta-\beta$ domain.

Step 5. After Step 4, the time-frequency localization is corrected by changing $t \rightarrow \frac{f}{f_r}t$ and $f \rightarrow f_r \ln \frac{f}{f_r}$. This time frequency localization correction is done using Canfield's technique discussed in the section 3.4.1.

This way of implementing the Hyperbolic class of time frequency distributions gives one the opportunity to look at the Hyperbolic Ambiguity function of the signal and the opportunity to design a proper kernel. Also, the Hyperbolic Ambiguity function of a signal gives one the opportunity to learn the mapping of various signal terms due to the warping used in (2.24). Without knowledge of the mapping, designing a proper kernel for smoothing becomes a very difficult task. The implementation of a few members of the Hyperbolic class of TFRs via the Hyperbolic Ambiguity function is shown below.

The Hyperbolic Ambiguity function of a windowed version of the Hyperbolic impulse defined in (2.14) with c=2.5 is shown in Figure 5.1 (a) [1]. The kernel for the Altes-Marinovic distribution is $\Psi_Q^{(H)}(\zeta,\beta) = 1$. The resulting Altes-Marinovic distribution is shown in Figure 5.1 (b). In Figure 5.2, the signal being considered is the sum of two windowed Hyperbolic impulses (c_1=2.5 and c_2=5.0). In Figure 5.2 (a), the ideal case consisting of the sum of the Altes-Marinovic distributions of the individual Hyperbolic impulses is shown. In Figure 5.2 (b), the Altes-Marinovic

[1] In this thesis, in all the examples considered the sampling period $\Delta\zeta = 0.5073$ unless otherwise mentioned

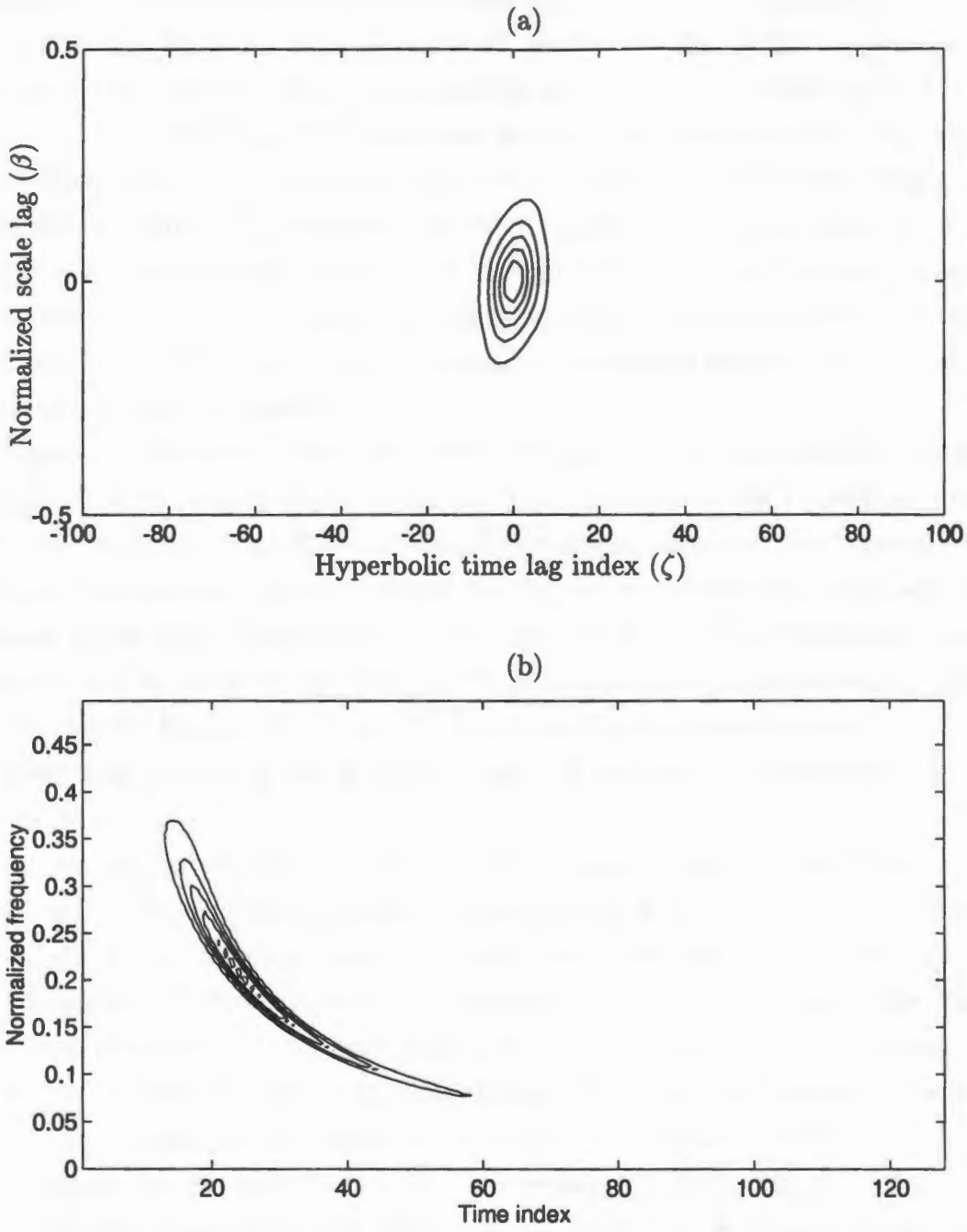

Figure 5.1: Contour plots for the simulation involving one windowed Hyperbolic impulse (c=2.5) with $\Delta\zeta = 0.5073$. (a) Hyperbolic Ambiguity function magnitude, (b) Altes-Marinovic distribution.

distribution of the sum of the two windowed Hyperbolic impulses is shown.

Figure 5.3 (a) shows the magnitude of the Hyperbolic Ambiguity function of the individual windowed Hyperbolic impulses superimposed upon one another. One can observe that the Hyperbolic impulses map to linear regions in the HAF plane. Hyperbolic impulses with different hyperbolic parameter c map to the origin, but with different tilt. The magnitude of the Hyperbolic Ambiguity function of the sum of the two windowed chirps, shown in Figure 5.3 (b), shows the auto terms at the origin and the cross terms slightly away from the origin. Since the auto terms add together with different phase, they appear to oscillate around the origin of the Hyperbolic Ambiguity function.

Figure 5.4 (a) shows the Pseudo Altes-Marinovic distribution kernel defined as $\Psi^{(H)}_{\text{PAD}}(\zeta,\beta) = \eta(\frac{\zeta}{2})\eta^*(-\frac{\zeta}{2})$ superimposed on the magnitude of the Hyperbolic Ambiguity function of the sum of two windowed Hyperbolic impulses. The Pseudo Altes-Marinovic distribution, shown in Figure 5.4 (b), gets rid of the cross terms very well without significantly distorting the auto terms. The Pseudo Altes-Marinovic distribution kernel is similar to the Pseudo Wigner distribution kernel shown in Figure 2.8 (c). All the kernels, $\Psi^{(C)}_T(\tau,\nu)$, which are used in the Cohen's class can be used for cross term removal in the Hyperbolic class by making a simple variable change of $\tau \rightarrow \frac{\zeta}{f_r}, \nu \rightarrow \beta f_r$.

Let us consider another example where the Pseudo Altes-Marinovic distribution works well. The simulation involves a signal which is the sum of four windowed Hyperbolic impulses (c_1=2, c_2=5, c_3=8 and c_4=11). Figure 5.5 (a) shows the sum of the individual Altes-Marinovic distributions. Figure 5.5 (b) shows the Altes-Marinovic distribution of the sum of the windowed Hyperbolic impulses. Since the cross terms map on top of auto terms in this example, there is distortion of the auto terms, too. Figure 5.6 (a) shows the Pseudo Altes-Marinovic distribution kernel superimposed on the magnitude of the Hyperbolic ambiguity function of the sum of the Hyperbolic impulses and Figure 5.6 (b) shows the resulting Pseudo Altes-Marinovic distribution which gets rid of the cross terms very well without significantly distorting the auto terms.

However, the Pseudo Altes-Marinovic kernel lacks the ability to attenuate along

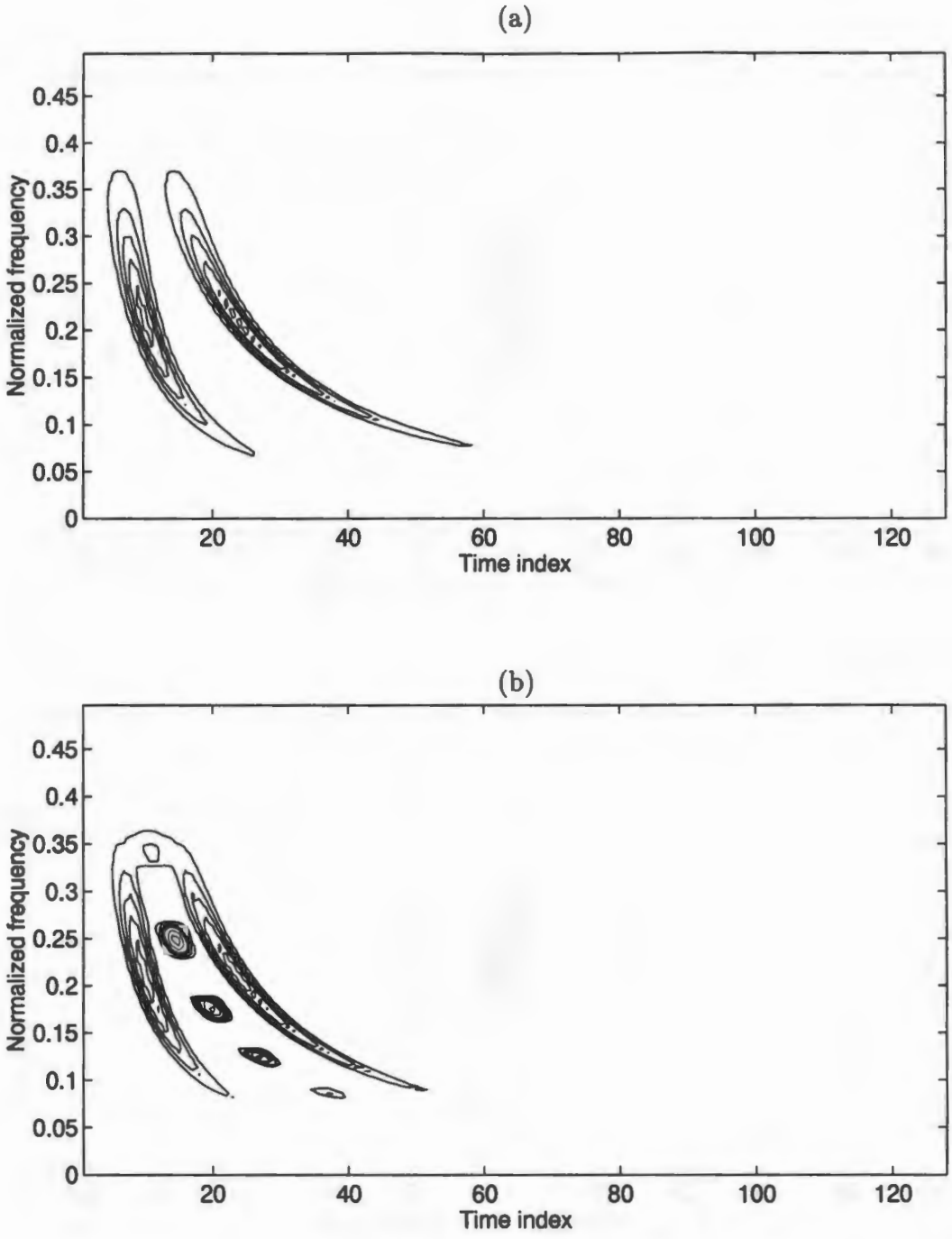

Figure 5.2: Contour plots for the simulation involving two windowed Hyperbolic impulses ($c_1 = 2$ and $c_2 = 5.0$). (a) individual Altes-Marinovic distributions of the Hyperbolic impulses superimposed on each other, (b) Altes-Marinovic distribution of the sum of the two impulses.

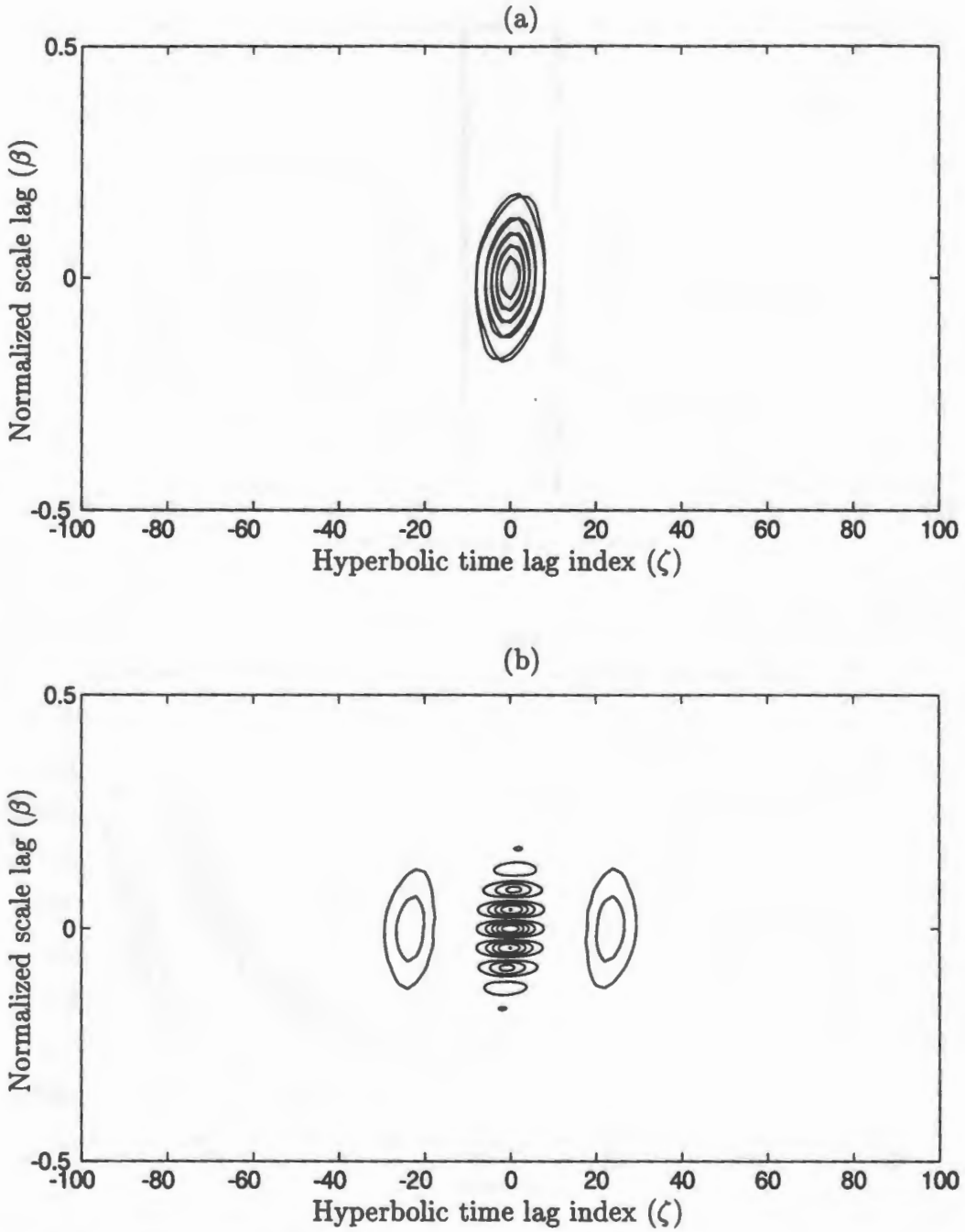

Figure 5.3: Contour plots for the simulation involving two Hyperbolic impulses (c_1=2 and c_2=5.0). (a) Absolute value of individual Hyperbolic Ambiguity functions superimposed upon each other, (b) Hyperbolic Ambiguity function magnitude of the sum of the two impulses.

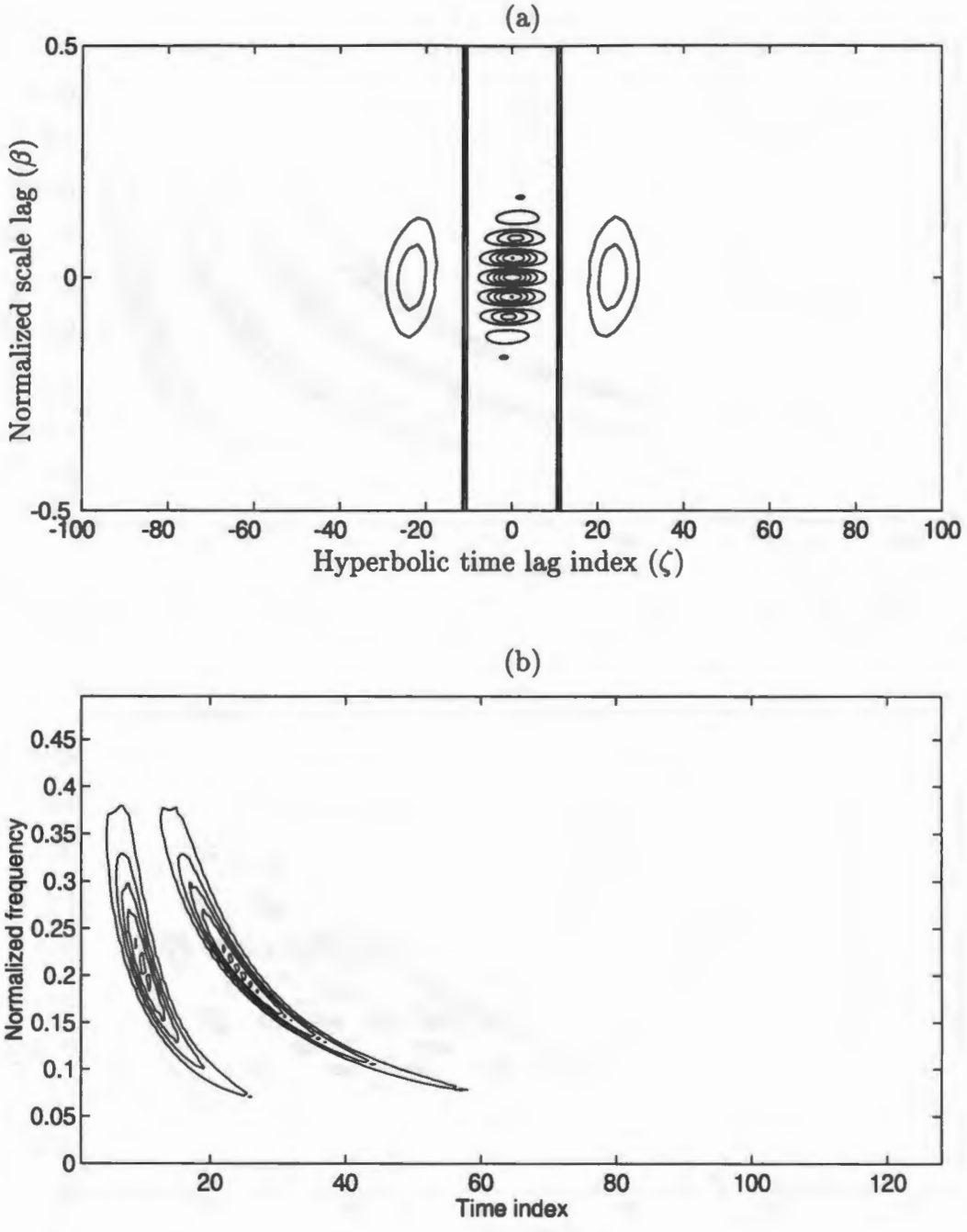

Figure 5.4: Contour plots for the simulation involving a signal equal to the sum of two windowed Hyperbolic impulses (c_1=2.5 and c_2=5.0). (a) Pseudo Altes-Marinovic distribution kernel (computed using a rectangular window of length 12) superimposed on the Hyperbolic Ambiguity function magnitude of the sum of the two Hyperbolic impulses; (b) resulting Pseudo Altes-Marinovic distribution of the signal.

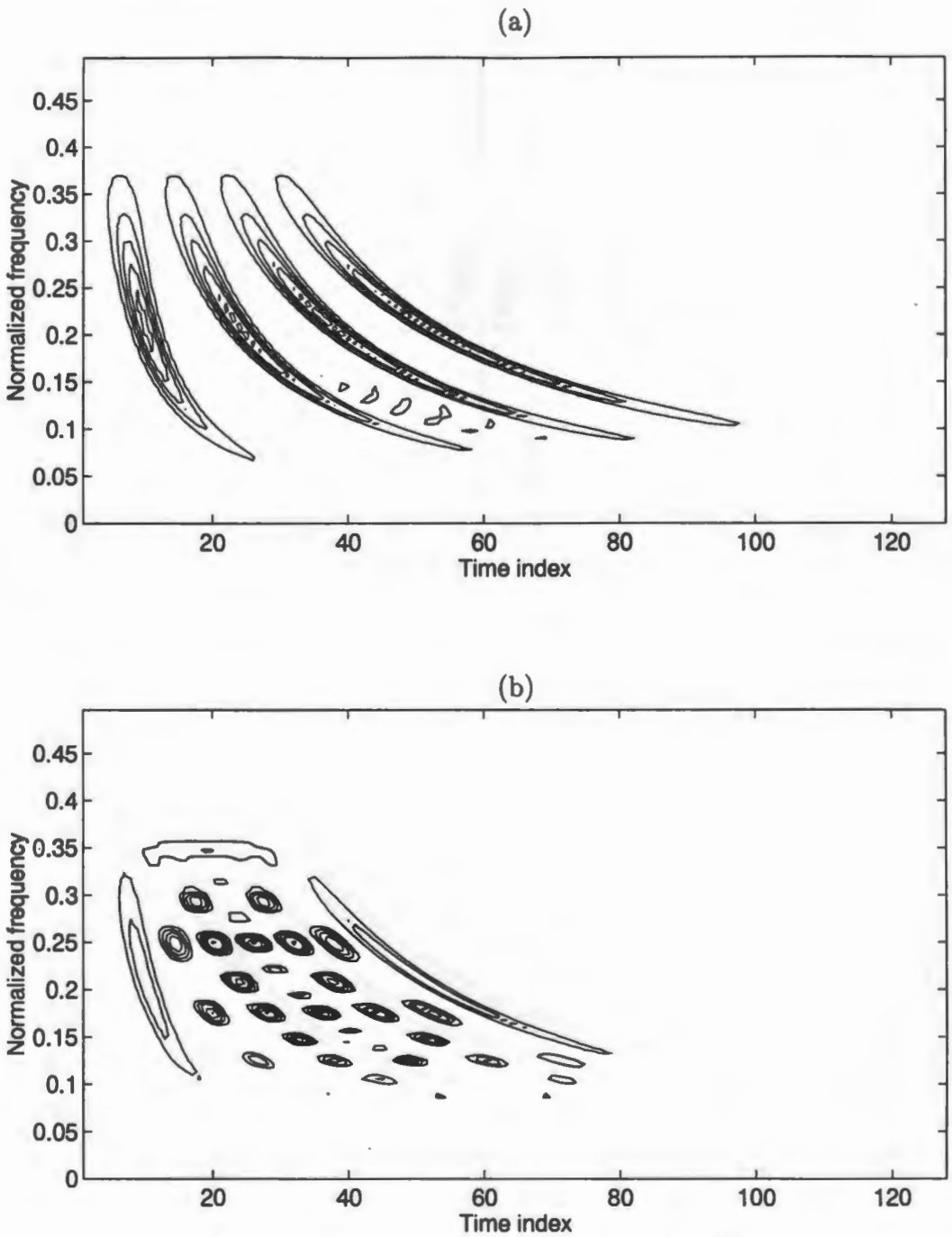

Figure 5.5: Contour plots for the simulation involving the signal equal to the sum of four windowed Hyperbolic impulses (c_1=2, c_2=5, c_3=8 and c_4=11). (a) individual Altes-Marinovic distributions of the signal components; (b) the resulting Altes-Marinovic distribution of the sum of the components.

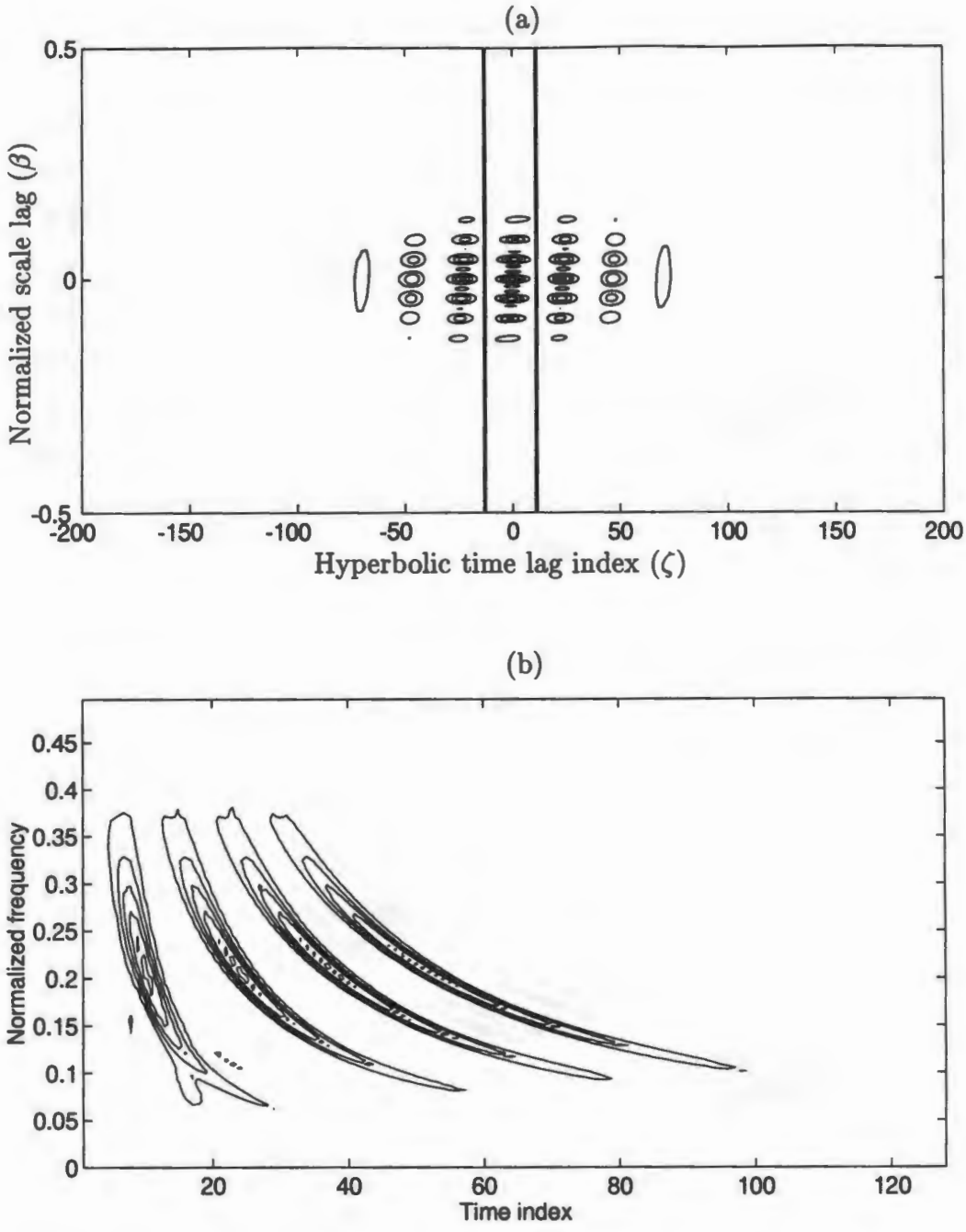

Figure 5.6: Contour plots for the simulation involving the signal equal to the sum of four windowed Hyperbolic impulses (c_1=2, c_2=5, c_3=8 and c_4=11). (a) Pseudo Altes-Marinovic distribution (computed using a rectangular window of size 12) kernel is superimposed on the Hyperbolic Ambiguity function magnitude of the signal; (b) the resulting Pseudo Altes-Marinovic distribution.

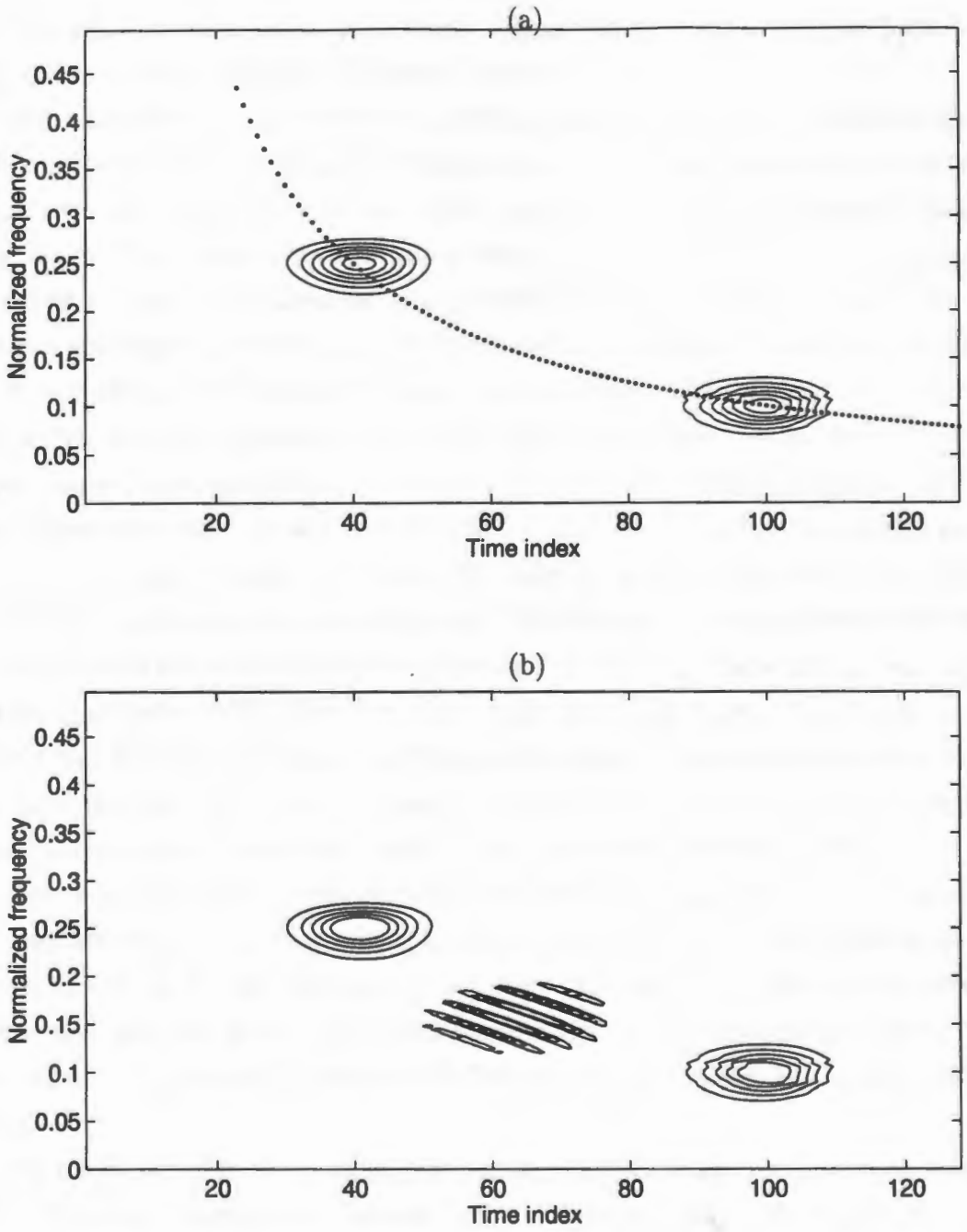

Figure 5.7: Contour plots for the simulation involving the signal which is the sum of two Gaussian components which are centered at different times and different frequencies, but both are centered along the hyperbolic curve, $t = \frac{10}{f}$ indicated by a dotted curve. (a) individual Altes-Marinovic distributions of the signal components superimposed upon each other, (b) Altes-Marinovic distribution of the signal.

the β axis[2]; this is similar to the Pseudo Wigner distribution kernel (see Figure 2.8 (c)) which lacks the ability to attenuate along the ν axis.

For example, the next simulation involves a signal which is the sum of two Gaussian signals which are centered at different frequencies but have approximately zero hyperbolic time lag. The way two signals can have approximately zero hyperbolic time lag is if their instantaneous group delay lies along the same hyperbola corresponding to one particular value of c (hyperbolic chirp parameter). Figure 5.7 (a) involves this signal, which is sum of two Gaussian components centered at different times and different frequencies but who have zero Hyperbolic time lag. Figure 5.7 (a) shows the individual Altes-Marinovic distribution of the two Gaussian components superimposed upon each other. In Figure 5.7 (a), the two Gaussian components have zero Hyperbolic time lag and this is demonstrated by the dotted line which corresponds to the group delay of an hyperbolic impulse with a particular c ($c = 10$) on which both signals are centered. Figure 5.7 (b) shows the Altes-Marinovic distribution of the sum of these two Gaussian signals. Figure 5.8 (a) shows the superposition of the magnitudes of the individual Hyperbolic ambiguity functions of the Gaussian signals and Figure 5.8 (b) shows the Hyperbolic ambiguity function of the sum of two Gaussian signals. Note that the support region of one of the HAF of the Gaussian signal is centered along the horizontal ζ axis, while the other one is tilted.

Figure 5.9 (a) shows the Hyperbolic ambiguity function of the sum of two Gaussian signals with the contour plot of the Pseudo Altes-Marinovic distribution kernel superimposed on it. One can observe that the cross terms lie in the kernel passband region and that the pseudo Altes-Marinovic distribution kernel passes most of the cross terms. Figure 5.9 (b) shows the Pseudo Altes-Marinovic distribution of the signal.

The cross terms in these examples can be removed using the Smoothed Pseudo Altes-Marinovic distribution, defined in [3]. Figure 5.10 (a) shows the Hyperbolic Ambiguity function magnitude of the same signal as in Figure 5.7, but with the Smoothed Pseudo Altes-Marinovic distribution kernel (computed using Hanning window of length 100 for smoothing in the ζ direction and a Hamming window of length

[2]Note that in the Hyperbolic Ambiguity function plots, the horizontal axis corresponds to the ζ axis and the vertical axis corresponds to the β axis for $B_X(\zeta, \beta)$ in (5.1)

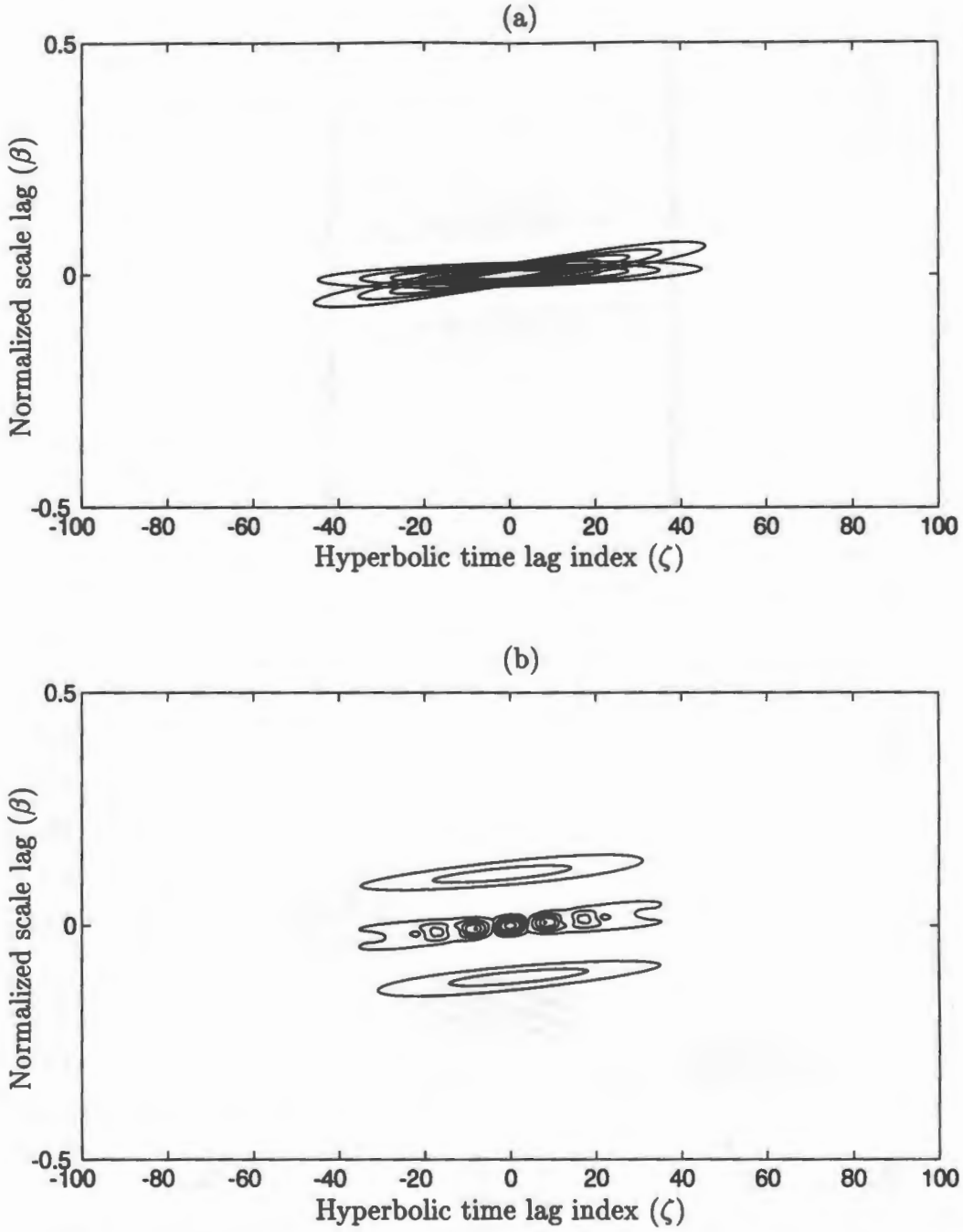

Figure 5.8: Contour plots for the simulation involving a signal described in Figure 5.7. (a) magnitude of the individual Hyperbolic ambiguity functions superimposed upon each other, (b) magnitude of the Hyperbolic ambiguity function of the sum of the two components.

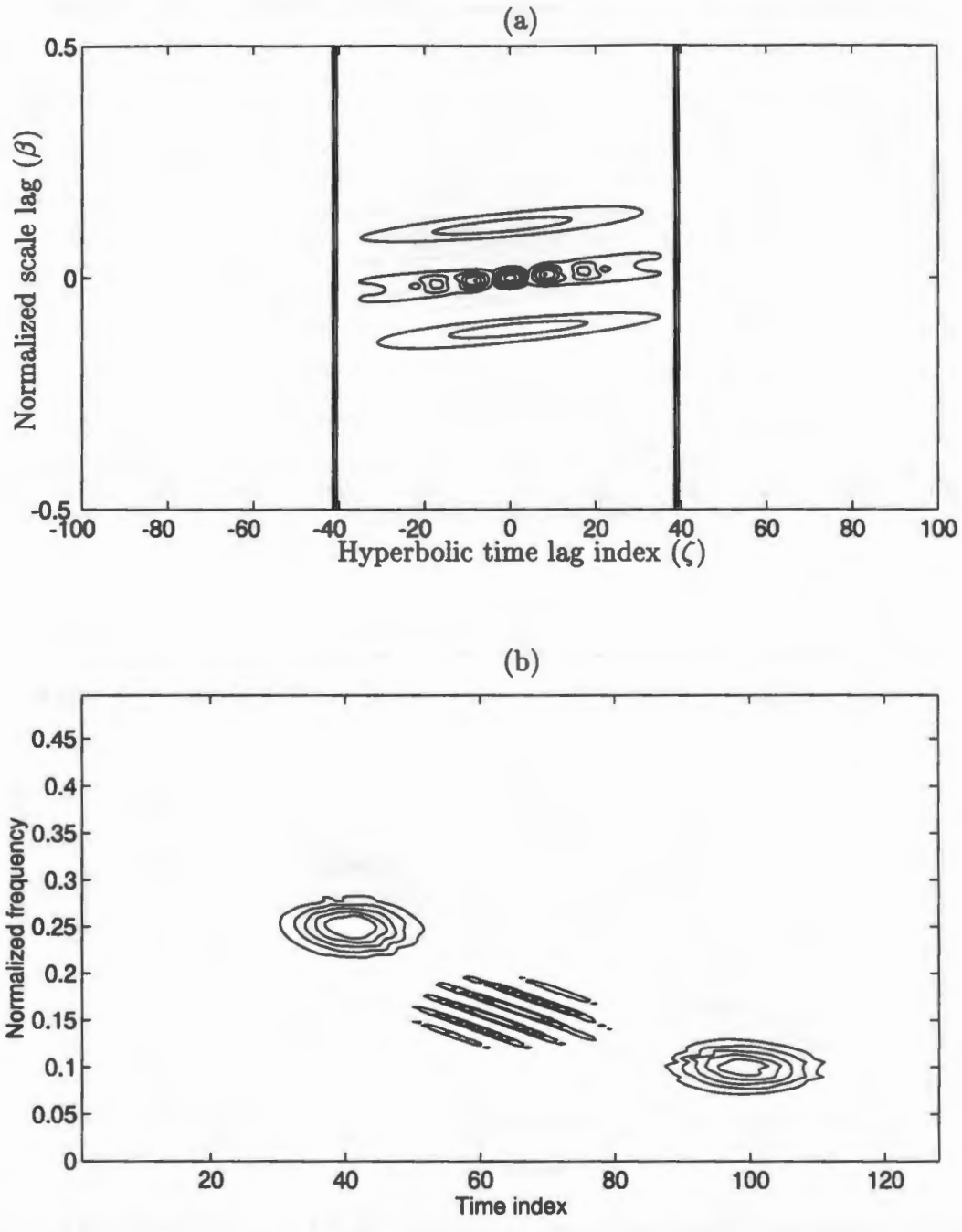

Figure 5.9: Contour plots for the simulation involving a signal described in Figure 5.7. (a) Pseudo Altes-Marinovic distribution kernel (computed using a rectangular window of size 40) superimposed on the magnitude of the Hyperbolic ambiguity function of the signal, (b) resulting Pseudo Altes-Marinovic distribution of the signal.

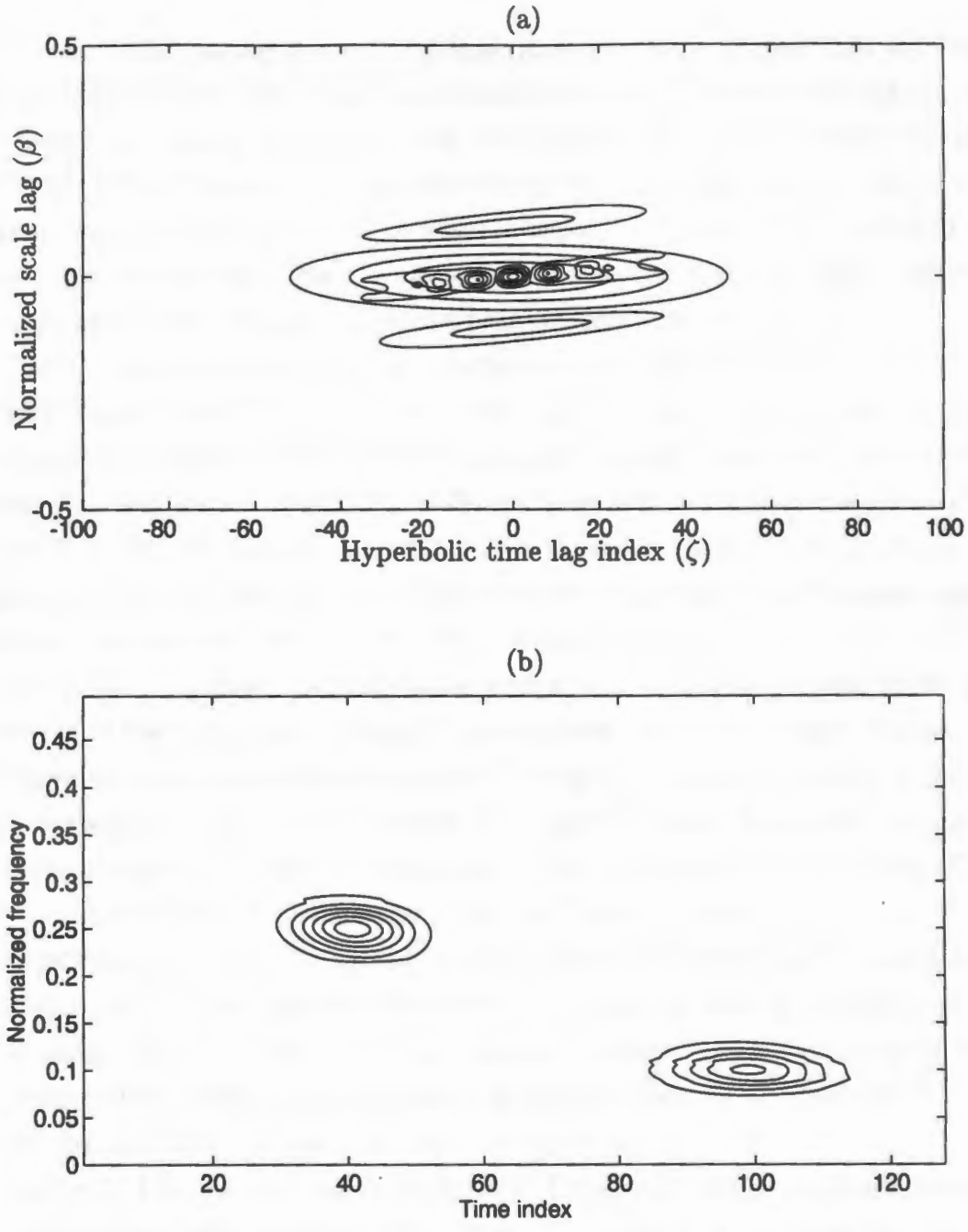

Figure 5.10: Contour plots for the simulation involving a signal described in Figure 5.7. (a) Smoothed Pseudo Altes-Marinovic distribution kernel (computed using a Hanning window of length 100 for smoothing in ζ direction and a Hamming window of length 20 for smoothing in β direction) superimposed on the magnitude of the Hyperbolic ambiguity function of the signal, (b) resulting Smoothed Pseudo Altes-Marinovic distribution of the signal.

20 for smoothing in the β direction) superimposed on it. Figure 5.10 (b) shows the Smoothed Pseudo Altes-Marinovic distribution of the signal. One can see that the Smoothed Pseudo Altes-Marinovic distribution kernel does a better job than the Pseudo Altes-Marinovic distribution kernel of suppressing the cross terms while passing most of the auto terms. However, comparing Figures 5.7 (a) and 5.10 (b), we see that the Smoothed Pseudo Altes-Marinovic distribution has slightly distorted the first auto-term making it tilt in the time-frequency plane.

The Pseudo Altes-Marinovic distribution doesn't work well in the case of two Gaussian signals which are centered at the same frequency but at different times as shown in the following plots. The simulation involves a signal which is the sum of two Gaussian signals centered at different times but at the same frequencies. In Figure 5.11 (a), the sum of individual Altes-Marinovic distributions is shown. In Figure 5.11 (b), the Altes-Marinovic distribution of the sum of the Gaussian signals is shown. One can observe the cross terms in Figure 5.11 (b).

Figure 5.12 (a) shows the individual magnitudes of the Hyperbolic Ambiguity functions of the two Gaussian signals superimposed upon one another. Figure 5.12 (b) shows the magnitude of the Hyperbolic Ambiguity function of the sum of the two Gaussian signals. Figure 5.13 (a) shows the magnitude of the Hyperbolic Ambiguity function of the sum of the two Gaussian signals; also shown is the kernel of the Pseudo Altes-Marinovic distribution (computed using a rectangular window of size 35) superimposed on it. One can see that the Hyperbolic Ambiguity function maps the auto terms of the Gaussian signals to tilted regions around the origin in the (ζ, β) plane. Also, the cross terms are mapped to tilted curves slightly away from the origin. The Pseudo Altes-Marinovic distribution fails to perform well since its kernel does not have the ability to tilt in the (ζ, β) plane.

Figure 5.14 (a) shows the magnitude of the Hyperbolic Ambiguity function of the sum of the two Gaussian signals; also shown is the kernel of the Smoothed Pseudo Altes-Marinovic distribution (computed using a Hamming window of length 40 for smoothing along ζ direction and a Blackman window of length 40 for smoothing along β direction) superimposed on it. The Smoothed Pseudo Altes-Marinovic distribution smooths out the cross terms but ends up distorting the auto terms such that they

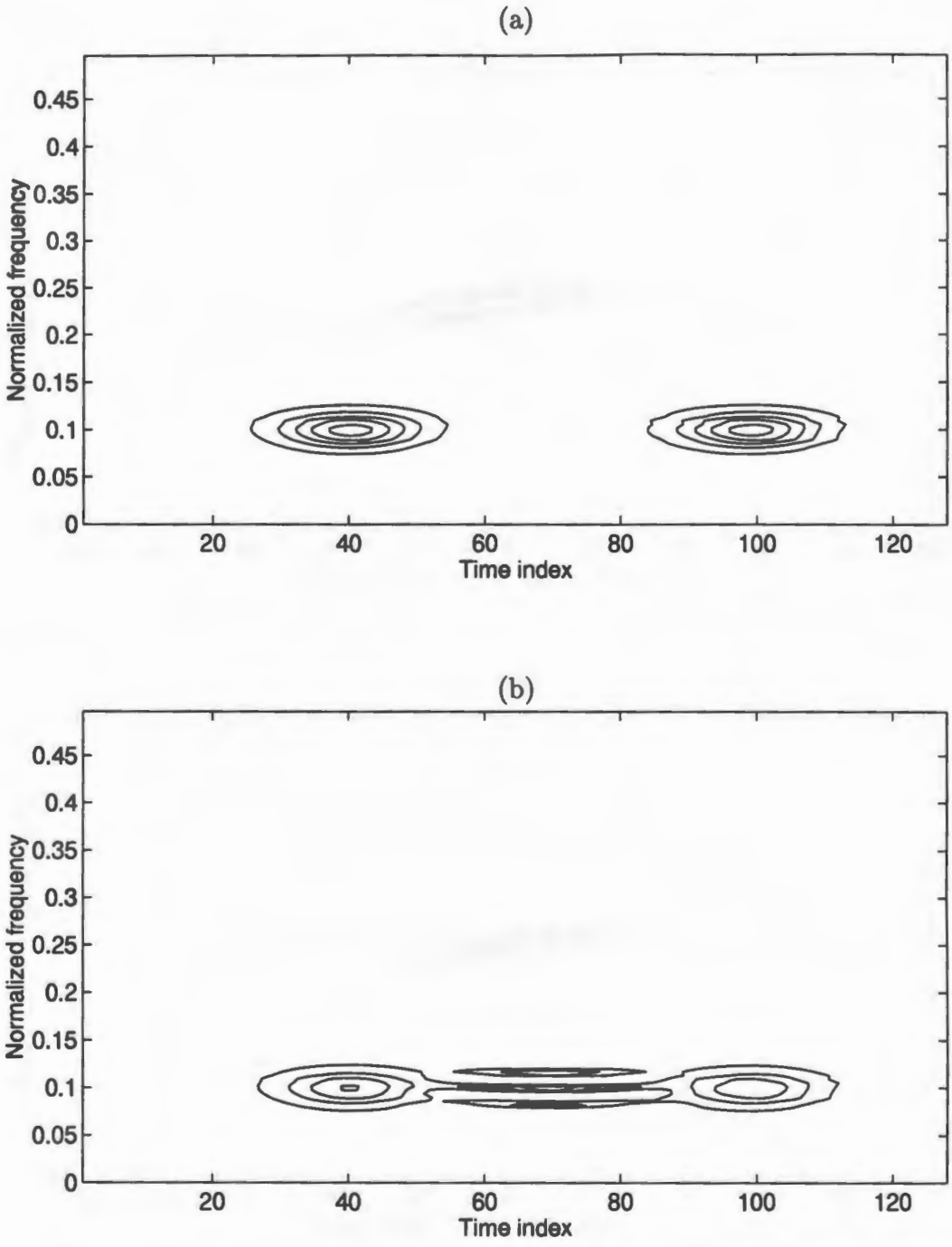

Figure 5.11: Contour plots for the simulation involving a signal which is the sum of two Gaussian components centered at different times but at the same frequency (a) individual Altes-Marinovic distributions of the components superimposed upon each other, (b) Altes-Marinovic distribution of the sum of components.

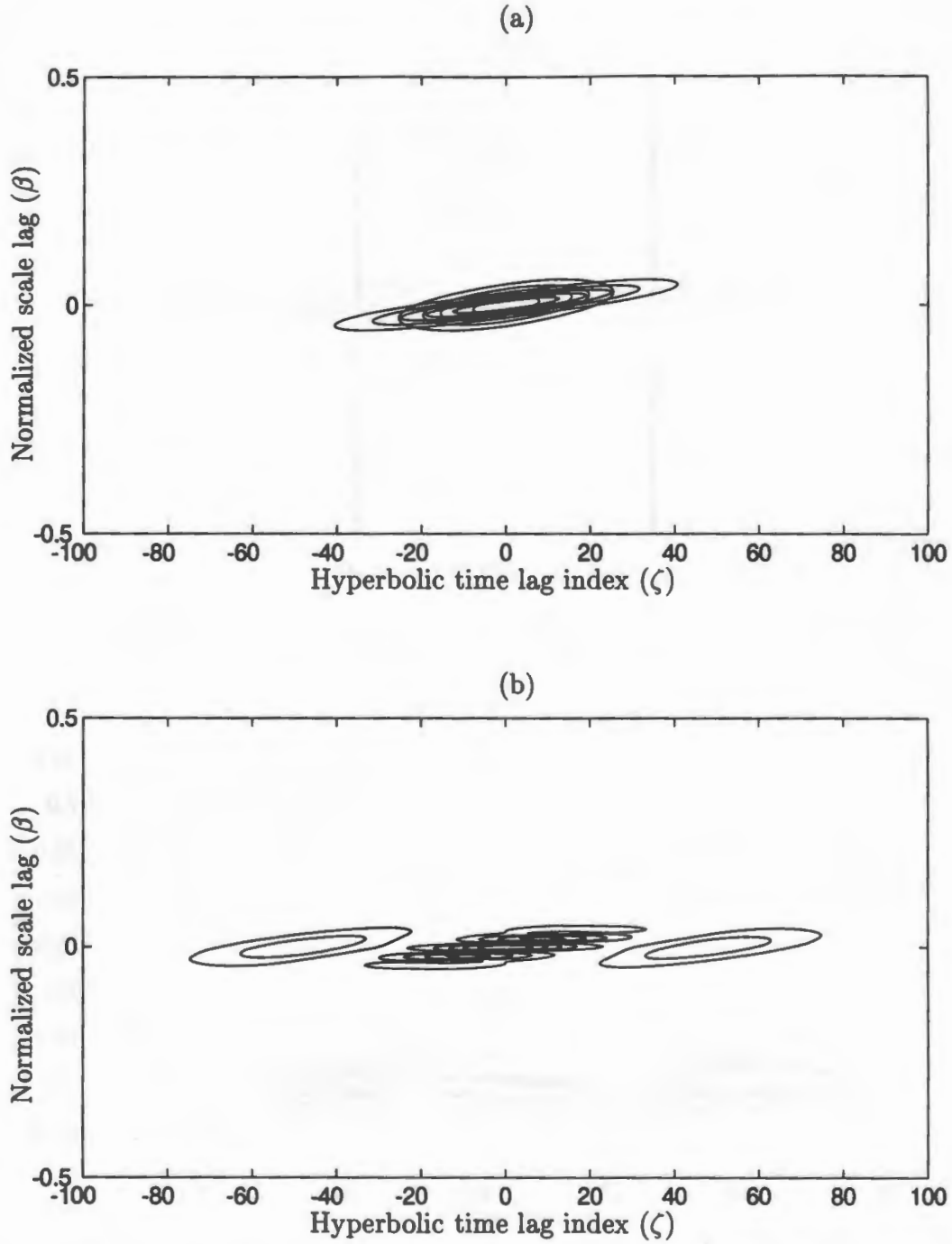

Figure 5.12: Contour plots for the simulation involving a signal described in Figure 5.11. (a) Absolute value of the individual Hyperbolic Ambiguity functions superimposed upon each other, (b) Hyperbolic Ambiguity function magnitude of the sum of the two impulses.

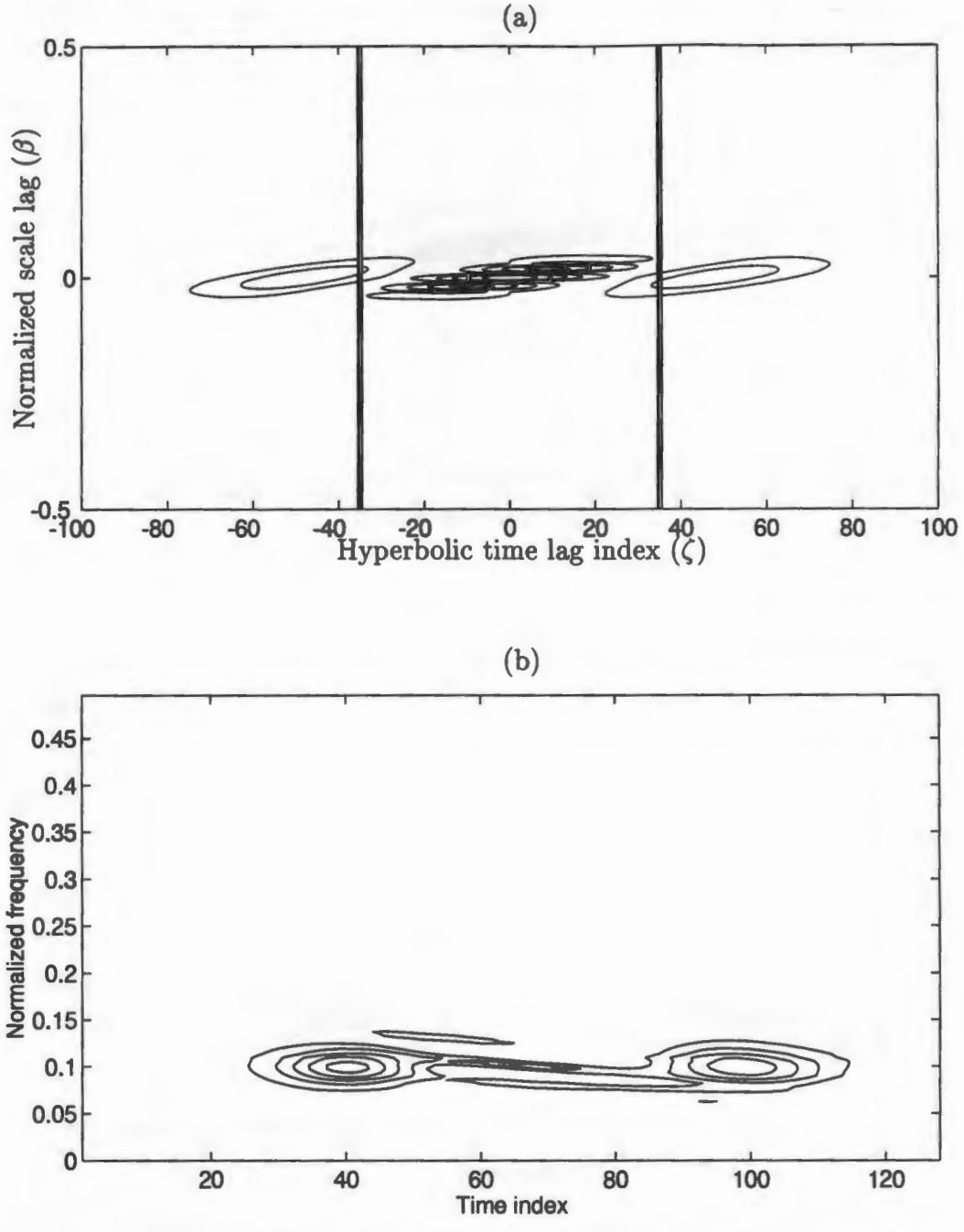

Figure 5.13: Contour plots for the simulation involving a signal described in Figure 5.11. (a) Pseudo Altes-Marinovic distribution kernel (computed using a rectangular window of size 35) superimposed on the magnitude of the Hyperbolic ambiguity function of the signal, (b) Pseudo Altes-Marinovic distribution of the signal.

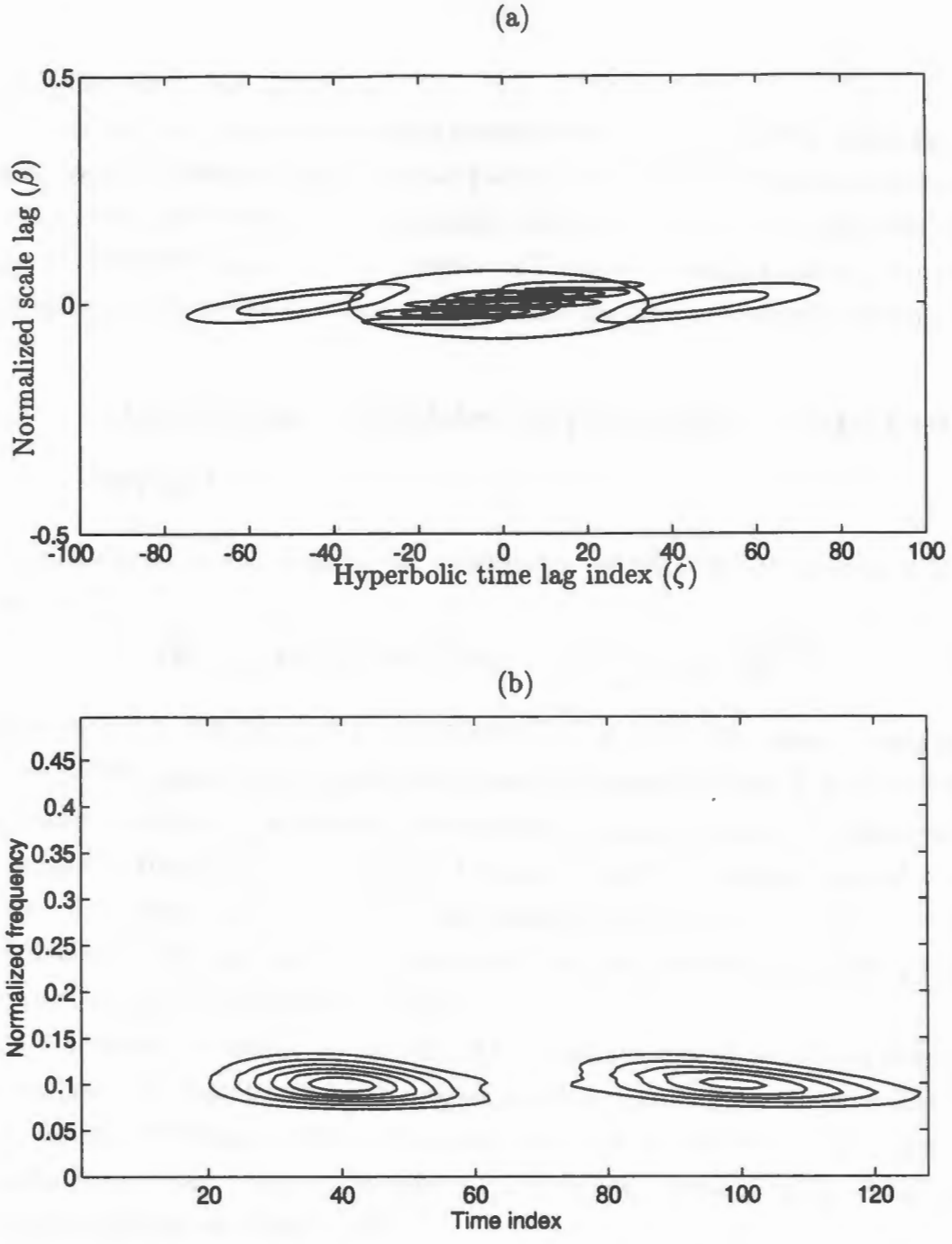

Figure 5.14: Contour plots for the simulation involving a signal described in Figure 5.11. (a) Smoothed Pseudo Altes-Marinovic distribution kernel (computed using a Hamming window of length 40 for smoothing in ζ direction and a Blackman window of size 40 for smoothing in β direction) superimposed on the magnitude of the Hyperbolic ambiguity function of the signal, (b) resulting Smoothed Pseudo Altes-Marinovic distribution of the signal.

tilt in the time-frequency plane.

This provides the motivation for a kernel which has tilt capability, but at the same time, has the ability to perform as well as the Pseudo Altes-Marinovic distribution or the Smoothed Pseudo Altes-Marinovic distribution which are very useful in the case of Hyperbolic impulses. The Multiform Tiltable Exponential distribution kernel, which will be discussed in the next section, has the above required properties.

5.3 Multiform Tiltable Exponential distribution kernel

The multiform, tiltable exponential distribution (MTED) kernel function is defined as [2, 64]

$$\Psi^{(C)}_{MTED}(\tau,\nu) \;=\; \exp\left\{-\pi\left[\mu^2\left(\frac{\tau}{\tau_0},\frac{\nu}{\nu_0};\alpha,r,\beta,\gamma\right)\right]^{\lambda}\right\}, \tag{5.4}$$

where $\mu(\tilde{\tau},\tilde{\nu};\alpha,r,\beta,\gamma) \;=\; \tilde{\tau}^2(\tilde{\nu}^2)^{\alpha}+(\tilde{\tau}^2)^{\alpha}\tilde{\nu}^2+2r\left[(\tilde{\tau}\tilde{\nu})^{\beta}\right]^{\gamma}$. The "design" parameters of the MTED kernel are a non-negative power α, a positive power λ, a positive time-lag scaling constant τ_0, a positive frequency-lag scaling constant ν_0, a tilt parameter r usually in the range $r \in [-1,1]$, and β and γ which are powers coupled in such a way that either $(\beta,\gamma) \;=\; (1,1)$, for causing no change, or $(\beta,\gamma) \;=\; (2,1/2)$, for producing the magnitude of the product term $\tilde{\tau}\tilde{\nu}$. Altogether, there are seven parameters in the MTED kernel function.

By properly choosing combinations of these parameters, it is possible to get kernel iso-contours (and, hence, passband/stopband shapes) in the ambiguity plane that look like parallel lines at arbitrary angles, crosses of parallel lines, rectangles, diamonds, hyperbolas, ellipses, and many other shapes. Some of the possible kernel shapes are plotted in Figure 5.15.

We like to point out that many more shapes can be obtained from the MTED kernel and we have listed only some of them which were useful to us. The interested reader can refer to these publications [2, 64] for more detail. Figure 5.15 (a) shows the effect of varying α while keeping the remaining parameters in (5.4) fixed. Notice that the HAF plane basic iso-contour shapes in Fig. 5.15 (a) (ellipse, diamond,

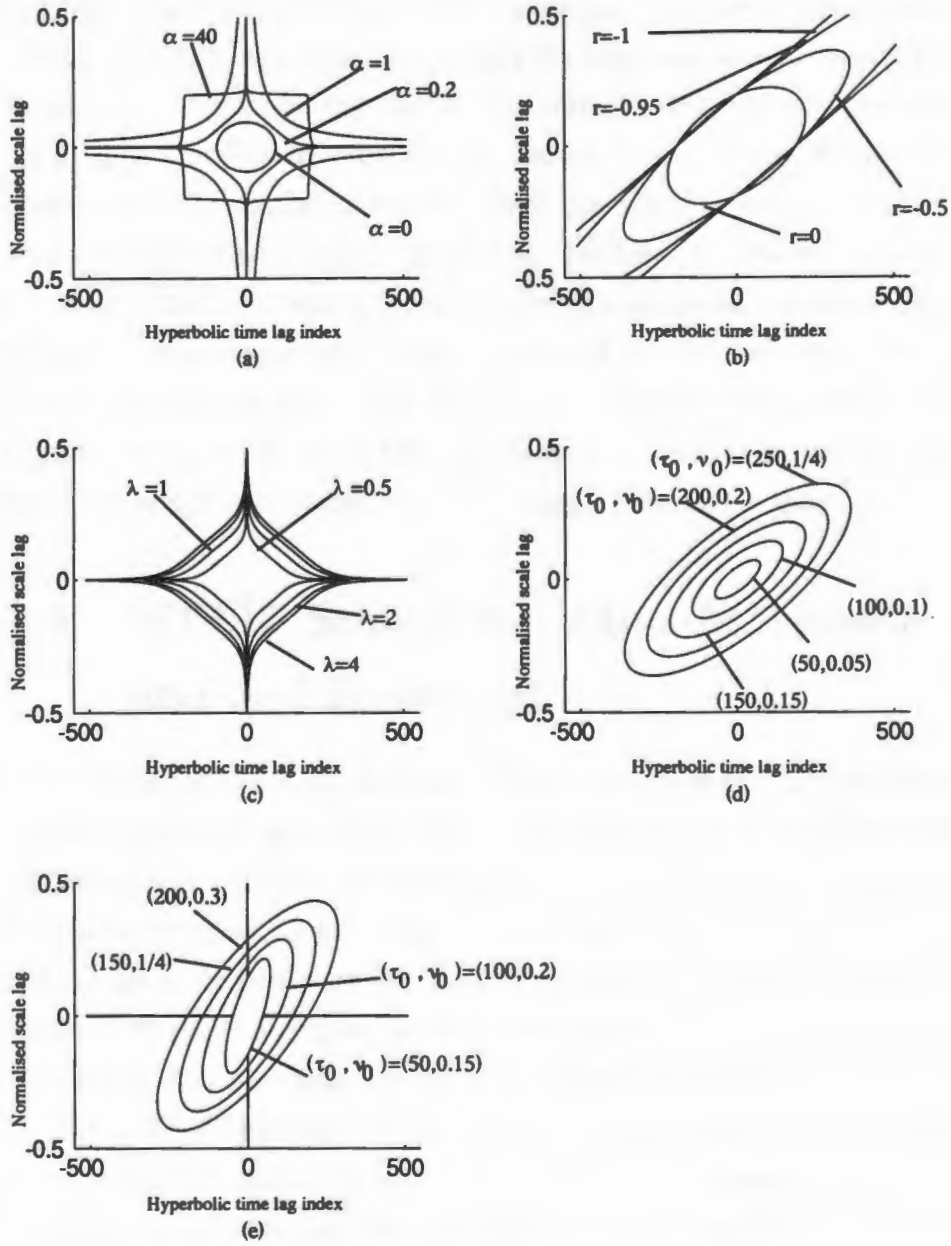

Figure 5.15: $\Psi^{(C)}_{\text{MTED}}(\tau,\nu) = 1/2$ iso-contours for several combinations of the parameters of the MTED kernel function. In Figs. 5.1(a)-5.1(c) only one parameter is allowed to change, while in Figs. 5.1(d)-5.1(f) two parameters are allowed to change. (a) $\tau_0 = 200$, $\nu_0 = 0.2$, $r = 0$ and $\lambda = 1/2$; (b) $\tau_0 = 200$, $\nu_0 = 0.2$, $\alpha = 0$, $\beta = \gamma = 1$ and $\lambda = 8$; (c) $\tau_0 = 200$, $\nu_0 = 0.2$, $r = 0$, $\alpha = 0.2$; (d) $r = -0.75$, $\alpha = 0$, $\beta = \gamma = 1$ and $\lambda = 8$; (e) $r = -0.75$, $\alpha = 0.001$, $\beta = \gamma = 1$ and $\lambda = 8$. (Figure was taken from [64]).

rectangle, and hyperbola) are easily obtained by properly constraining α. The effect of varying r while the other parameters are kept constant, is depicted in Fig. 5.15 (b). When $r = -1$ (not shown), the MTED kernel would, instead, produce parallel strips oriented in the NW-SE direction of the ambiguity plane. Either case is useful for scenarios where parallel, linear FM chirps are present. In Fig. 5.15 (c), λ is allowed to vary while the other parameters are kept constant. In practice, increasing λ produces narrower transition regions between the passband and stopband iso-contours. The effective scaling capability of varying τ_0 and ν_0 while keeping their ratio $\frac{\tau_0}{\nu_0} = 1000$ fixed is depicted in Fig. 5.15 (d). Notice that the tilt angle of the different-sized ellipses in Fig. 5.15 (d) is kept constant by maintaining the ratio $\frac{\tau_0}{\nu_0}$ fixed. When this ratio is not kept constant, the tilt angle changes as shown in Fig. 5.15 (e).

5.4 MTEK Smoothed Altes-Marinovic distribution and Examples

Let us consider the example of two Gaussian components at different time-frequency scenarios (see Figures 5.9 and 5.10 or Figures 5.13 and 5.14) where the Pseudo Altes-Marinovic distribution and Smoothed Pseudo Altes-Marinovic distribution either fail to remove the cross terms or end up distorting the auto terms. In Figure 5.16 (a), the MTED kernel is superimposed on the Hyperbolic ambiguity function of the signal. Figure 5.16 (b) shows that the MTEK smoothed Altes-Marinovic distribution does a good job of suppressing the cross terms while preserving the auto terms.

The MTEK smoothed Altes-Marinovic distribution does as well as the Pseudo Altes-Marinovic distribution in the case of two windowed Hyperbolic impulses (see Figure 5.4), as demonstrated by Figure 5.17. Figure 5.17 (a) shows the MTED kernel superimposed on the magnitude of the Hyperbolic ambiguity function of the signal and Figure 5.17 (b) shows the corresponding MTEK smoothed Altes-Marinovic distribution.

Figure 5.18 shows a simulation involving a signal which is the sum of two Gaussian components centered at the same time but at different frequencies. Figure

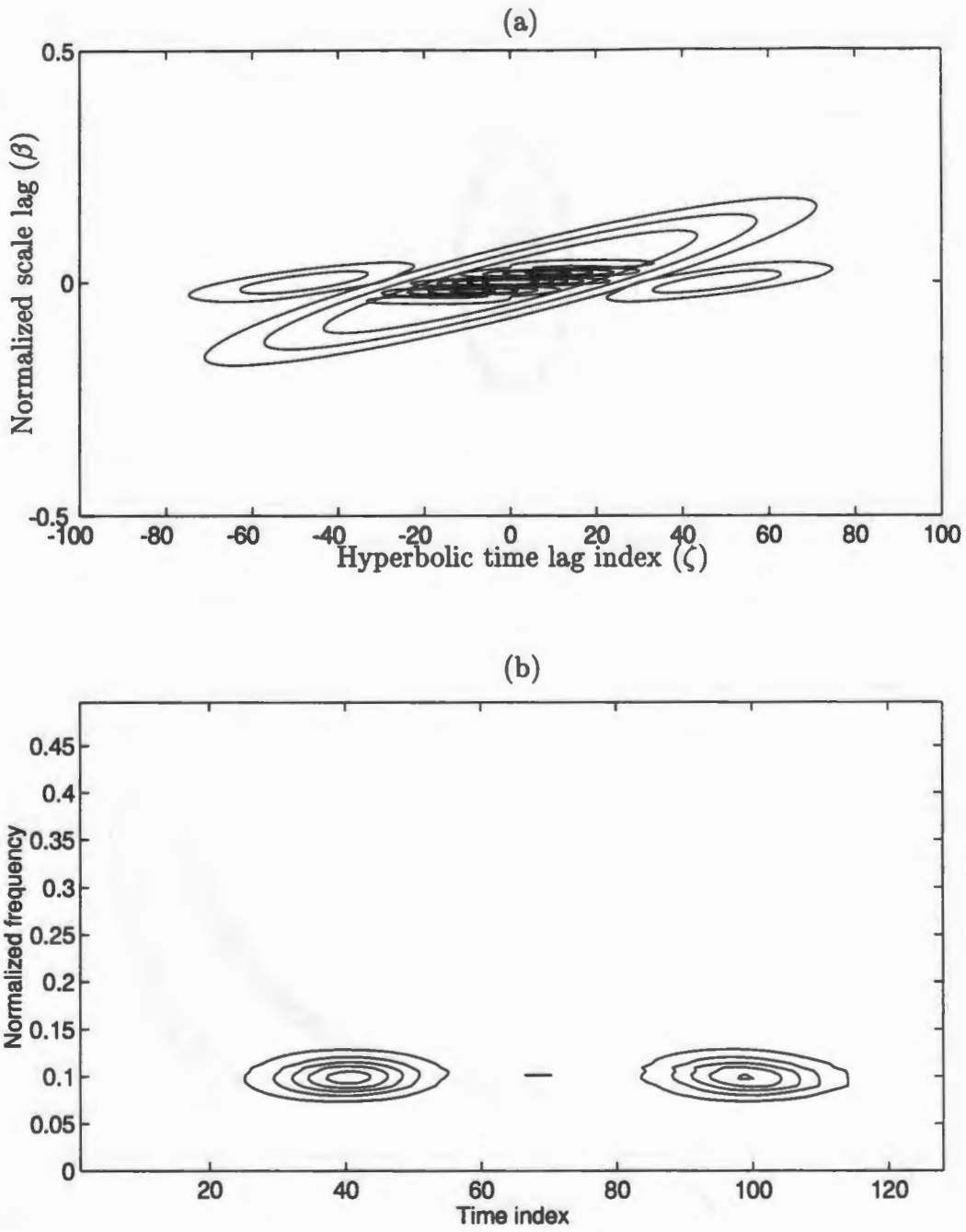

Figure 5.16: Contour plots for the simulation involving a signal which is described in Figure (5.11). (a) MTED kernel with $\tau_0 = 27.2844$, $\nu_0 = 0.0455$, $r = -1$, $\beta = 1$, $\gamma = 1$, $\alpha = 0$ and $\lambda = 2$ superimposed on the magnitude of the Hyperbolic Ambiguity function of the signal, (b) resulting MTEK smoothed Altes-Marinovic distribution.

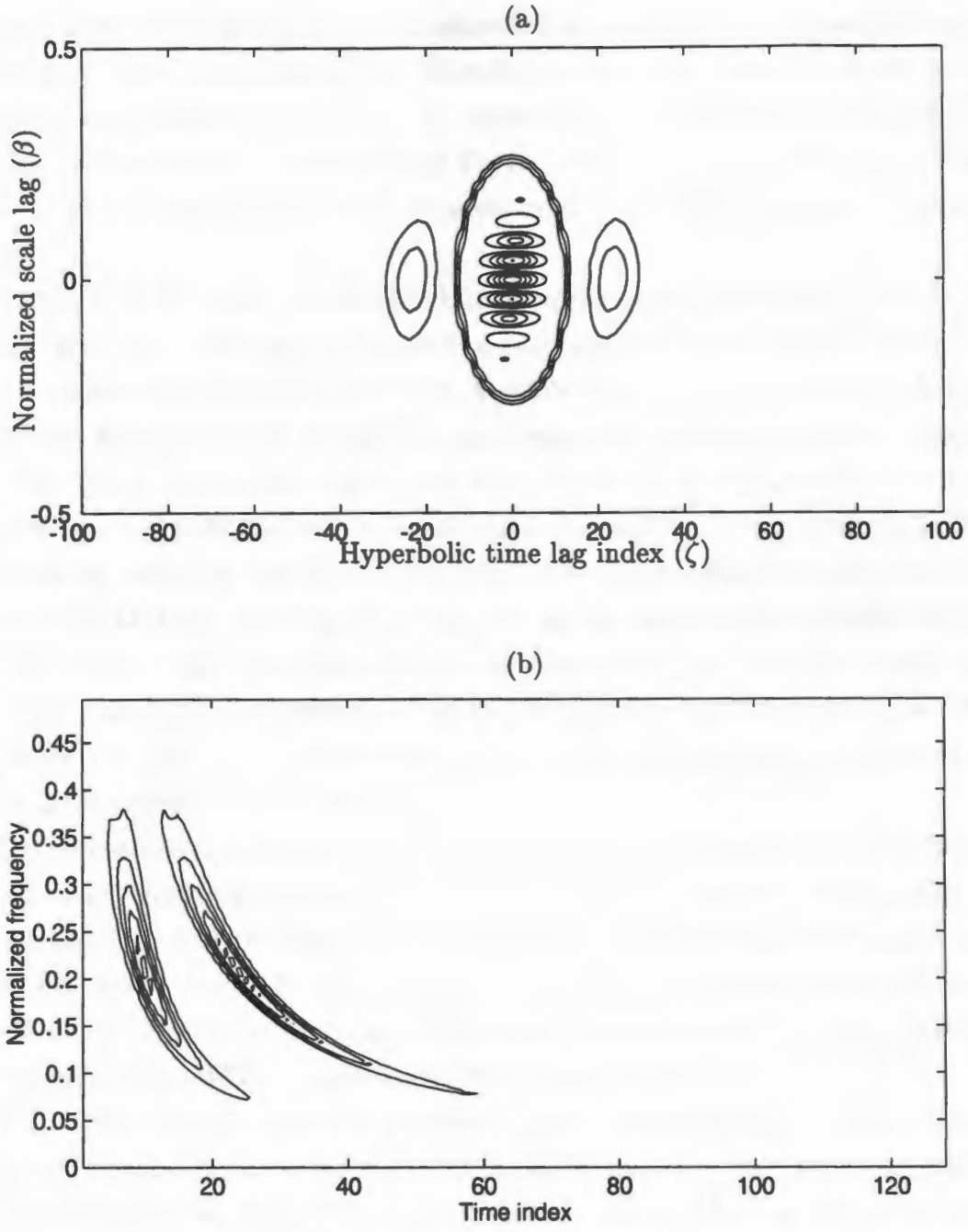

Figure 5.17: Contour plots for the simulation involving two Hyperbolic impulses (c_1=2 and c_2=5.0). (a) MTED kernel with $\tau_0 = 10.7668$, $\nu_0 = 0.2774$, $\tau = 0$, $\lambda = 6.1260$, $\beta = 1$, $\gamma = 1$ and $\alpha = 0$ superimposed on the magnitude of the Hyperbolic Ambiguity function of the signal, (b) resulting MTEK smoothed Altes-Marinovic distribution.

5.18 (a) shows the individual Altes-Marinovic distributions of the Gaussian components and Figure 5.18 (b) shows the Altes-Marinovic distribution of the sum of two Gaussian components. Figure 5.19 (a) shows the MTED kernel superimposed on the Hyperbolic Ambiguity function and Figure 5.19 (b) shows the MTEK smoothed Altes-Marinovic distribution which removes cross terms while preserving the auto terms.

Figure 5.20 (a) shows the MTED kernel superimposed on the Hyperbolic Ambiguity function of the signal composed of two Gaussian components in Figure 5.7 centered along the hyperbolic curve $t = \frac{10}{f}$ while Figure 5.20 (b) shows the MTEK smoothed Altes-Marinovic distribution preserving the auto terms while removing the cross terms. Comparing Figure 5.20 with Figure 5.9, which shows Pseudo Altes distribution, and with Figure 5.10, which shows the smoothed Pseudo Altes distribution, one can conclude that the MTED kernel does well compared to either the PAD kernel or SPAD kernel. In Figure 5.9 (b), one can see that Pseudo Altes distribution fails to attenuate the cross terms whereas in Figure 5.10 (b), the SPAD kernel gets rid of the cross terms but ends up distorting the auto terms. Also, one can see that in Figure 5.10 (b) the auto terms are slightly tilted which is due to the smoothing along the hyperbolic $t' = \frac{c}{f'}$ direction.

Let us consider the signal which is the sum of two windowed Linear FM chirps. Fig. 5.21 (a) shows the sum of the Altes-Marinovic distributions of the individual signals and Fig. 5.21 (b) shows the Altes-Marinovic distribution of the sum of two linear FM chirps. Fig. 5.22 (a) shows the MTED kernel superimposed on the magnitude of the Hyperbolic Ambiguity function of the signal and Fig. 5.22 (b) shows the corresponding MTEK smoothed Altes-Marinovic distribution.

Fig. 5.23 (a) shows the sum of the Altes-Marinovic distributions of two different individual linear FM chirps and Fig. 5.23 (b) shows the Altes-Marinovic distribution of the sum of the two linear FM chirps. These two linear FM chirps are much closer to each other compared to the previous example. Fig. 5.24 (a) shows the MTED kernel superimposed on the Hyperbolic Ambiguity function of the sum. One can observe that the cross terms and auto terms slightly overlap with each other in this example and that the MTED kernel does a good job of removing cross terms (see

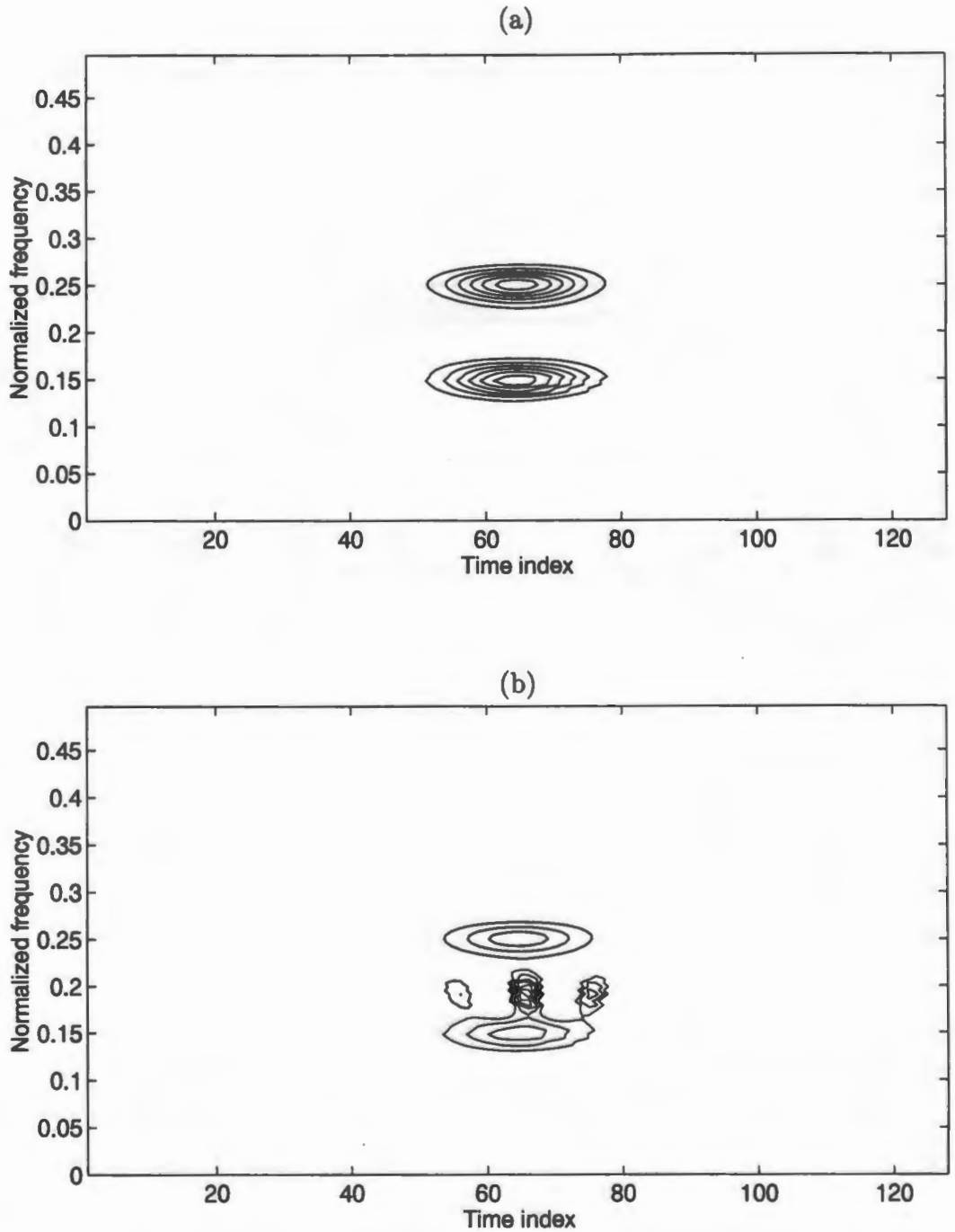

Figure 5.18: Contour plots for the simulation involving a signal which is the sum of two Gaussian components centered at the same time but at different frequencies. (a) individual Altes-Marinovic distributions of the signal components superimposed on each other, (b) Altes-Marinovic distribution of the sum of the components.

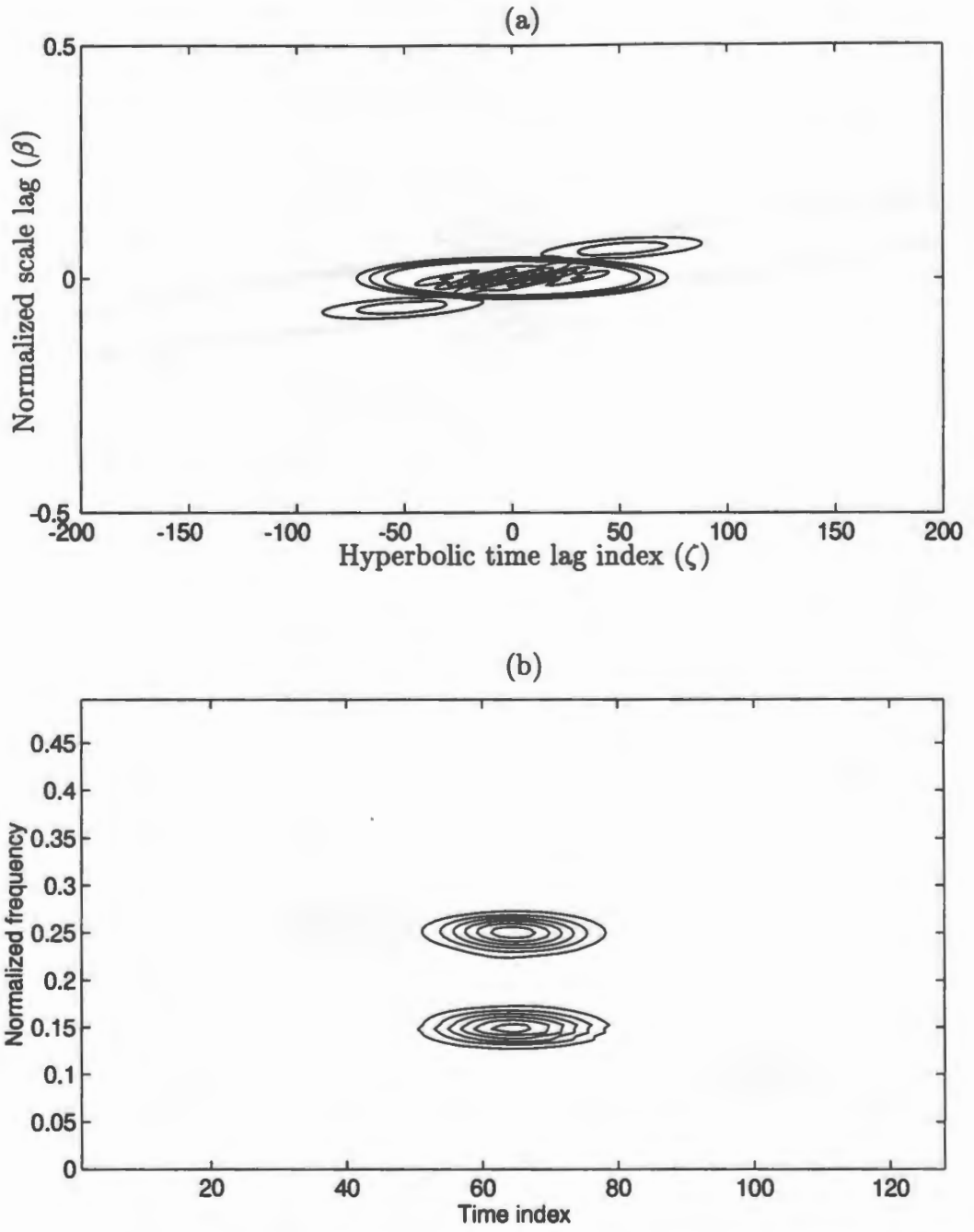

Figure 5.19: Contour plots for the simulation involving the signal mentioned in Figure (5.18). (a) MTED kernel with $\tau_0 = 40$, $\nu_0 = 0.05$, $r = 0$, $\alpha = 0$, $\beta = 1$, $\gamma = 1$ and $\lambda = 2$ superimposed on the magnitude of the Hyperbolic ambiguity function of the signal, (b) resulting MTEK smoothed Altes-Marinovic distribution.

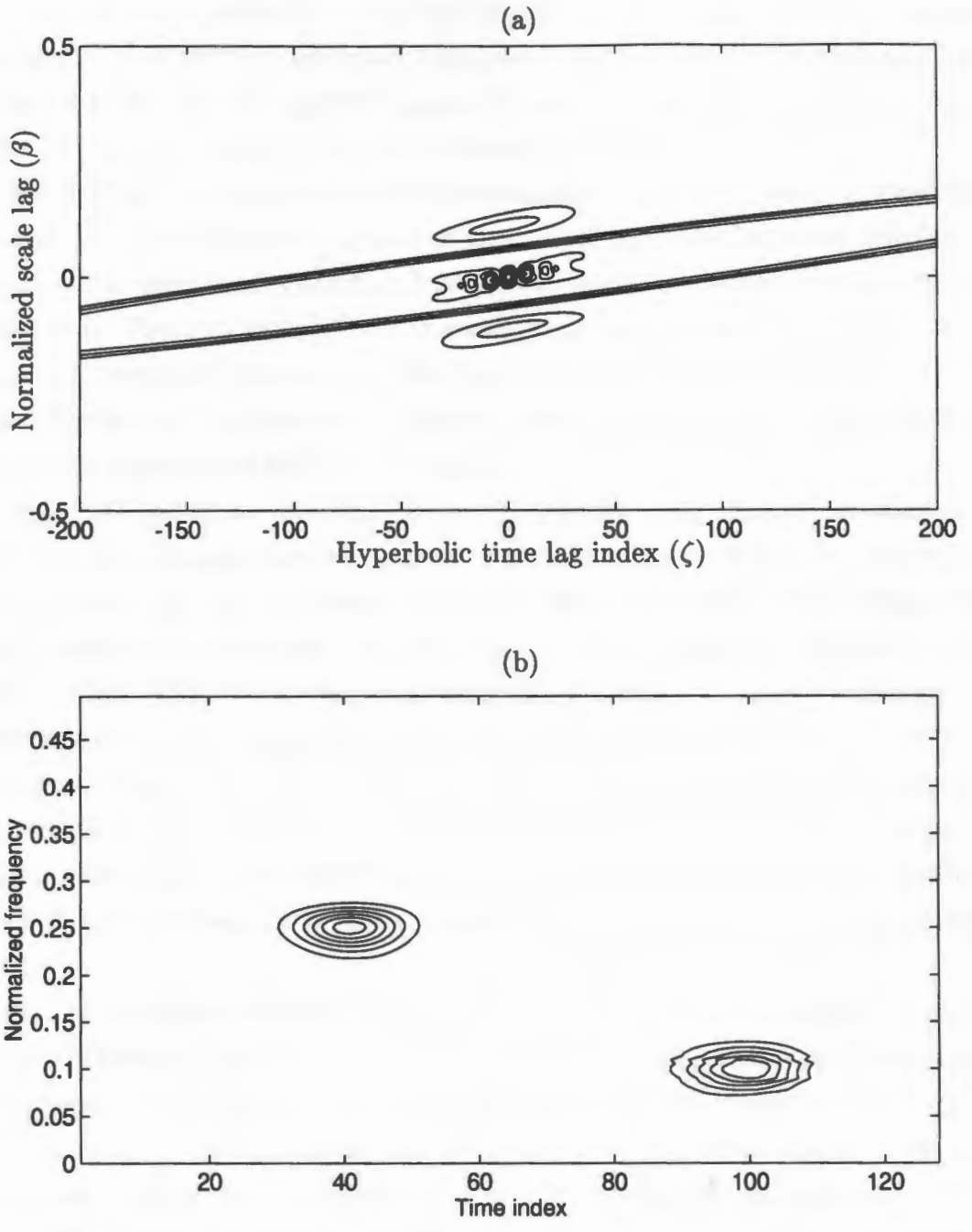

Figure 5.20: Contour plots for the simulation involving the signal mentioned in Figure (5.7). (a) MTED kernel with $\tau_0 = 60$, $\nu_0 = 0.1$, $r = -0.95$, $\alpha = 0$, $\beta = 1$, $\gamma = 1$ and $\lambda = 2$ superimposed on the magnitude of the Hyperbolic ambiguity function of the signal, (b) MTEK smoothed Altes-Marinovic distribution.

Fig. 5.24 (b)) but ends up smoothing one of the auto terms. This demonstrates the capability of MTEK smoothed Altes distribution to remove cross terms when the signal is the sum of linear FM signals. However, as the signal components come closer together, the task of filtering becomes more difficult.

Fig. 5.25 involves a signal which is the sum of a Gaussian signal and a Hyperbolic impulse. Fig. 5.25 (a) shows the sum of the individual Altes-Marinovic distribution of each of the components and Fig. 5.25 (b) shows the Altes-Marinovic distribution of the sum. Figure 5.26 (a) shows the individual magnitudes of the HAFs of the windowed Hyperbolic impulse and the Gaussian signal superimposed upon one another. Figure 5.26 (b) shows the magnitude of the HAF of the sum of the windowed Hyperbolic impulse and the Gaussian signal.

Fig. 5.27 (a) shows the PAD kernel (computed using rectangular window of length 25) superimposed on the magnitude of the Hyperbolic Ambiguity function of the signal and Fig. 5.27 (b) shows the Pseudo Altes distribution of the signal. The PAD kernel fails to attenuate the cross terms in order to pass the auto terms. Fig. 5.28 (a) shows the PAD kernel (computed using rectangular window of length 10) superimposed on the magnitude of the HAF of the signal and Fig. 5.28 (b) shows the Pseudo Altes distribution of the signal. In this example, all the cross terms were removed at the expense of the auto terms and one can see that in Fig. 5.28 (b) the Gaussian signal gets attenuated badly and due to the smoothing in the hyperbolic $t' = \frac{c}{f'}$ direction, it tends to look like a time-frequency representation of a Hyperbolic impulse.

Fig. 5.29 (a) shows the SPAD kernel superimposed on the Hyperbolic Ambiguity function of the signal and Fig. 5.29 (b) shows the Smoothed Pseudo Altes distribution of the signal. One can see that the SPAD kernel fails to smooth the cross terms and also ends up slightly tilting the Gaussian component of the signal. This kind of problem requires the tilt capability of the MTED kernel, demonstrated in Fig. 5.30. Fig. 5.30 (a) shows the MTED kernel superimposed on the magnitude of the Hyperbolic Ambiguity function of the sum and Fig. 5.30 (b) shows the MTEK smoothed Altes-Marinovic distribution. The MTEK smoothed Altes-Marinovic does much better than either the PAD or the SPAD kernel in cross term removal without

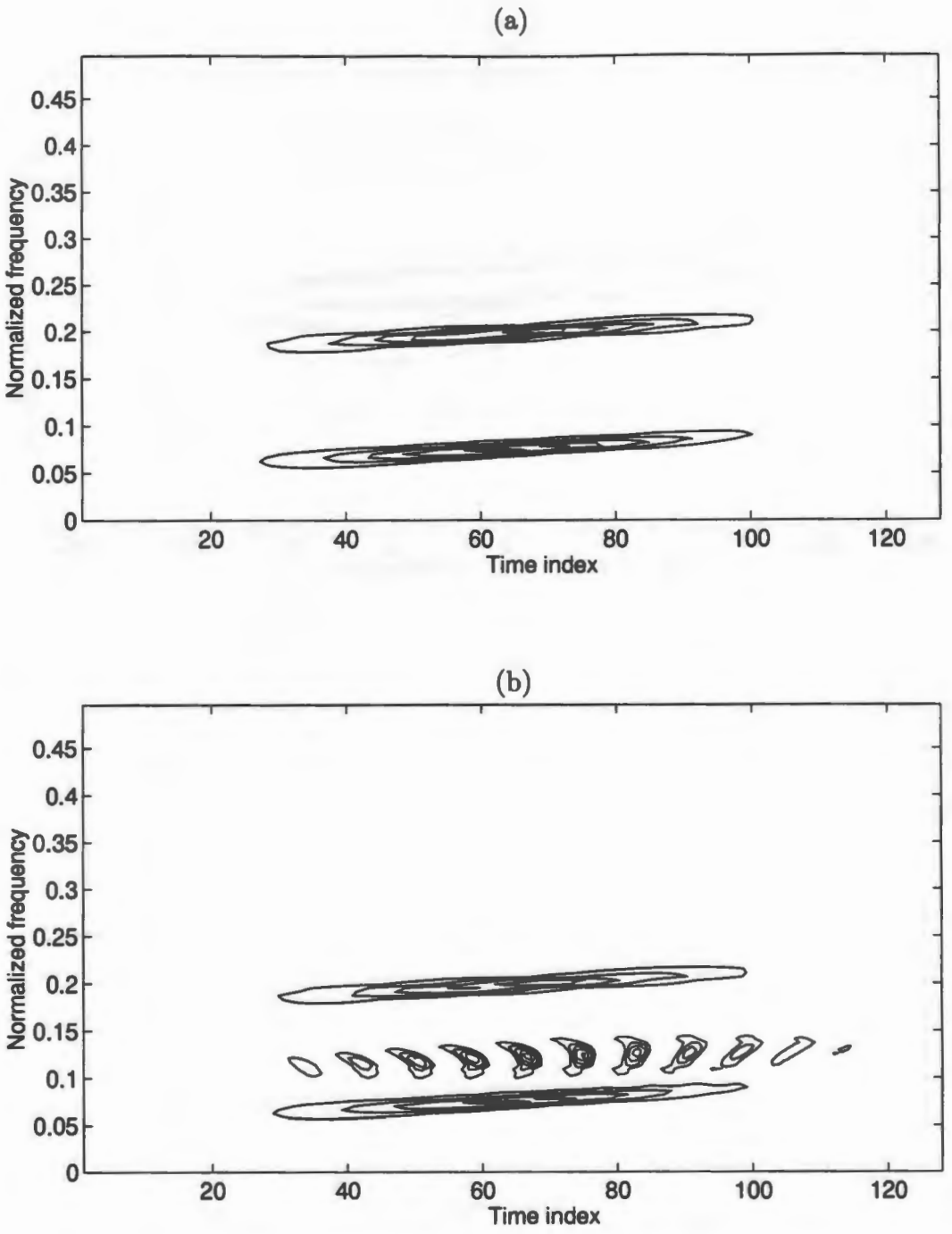

Figure 5.21: Contour plots for the simulation involving a signal which is the sum of two linear FM chirps individually tapered by a Hanning window. (a) individual Altes-Marinovic distributions of the components superimposed upon each other, (b) Altes-Marinovic distribution of the sum of the components.

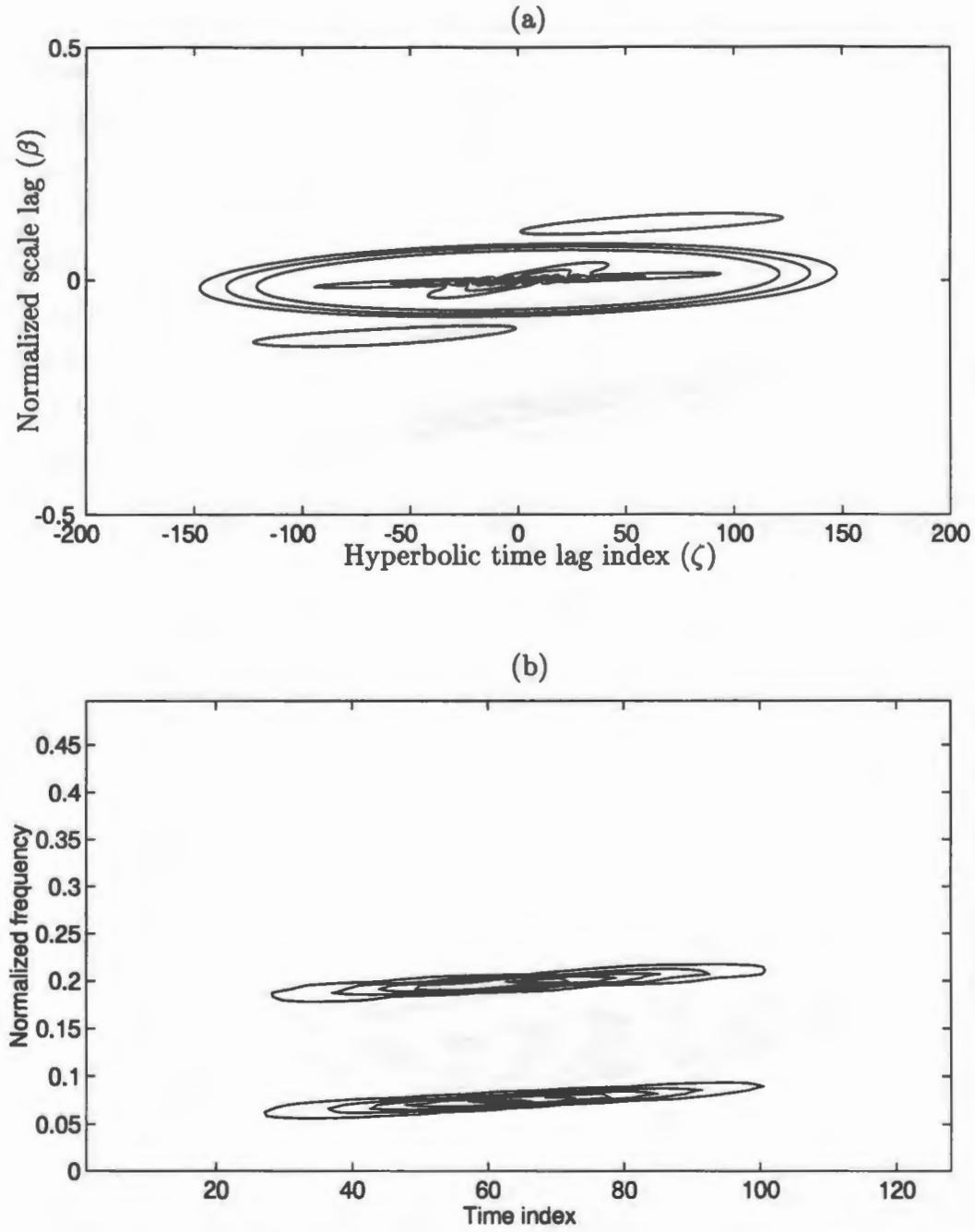

Figure 5.22: Contour plots for the simulation involving a signal which is mentioned in Figure (5.21). (a) MTED kernel with $\tau_0 = 80$, $\nu_0 = 0.085$, $r = -0.2$, $\alpha = 0$, $\beta = 1$, $\gamma = 1$ and $\lambda = 2$ superimposed on the magnitude of the Hyperbolic ambiguity function of the signal, (b) resulting MTEK smoothed Altes-Marinovic distribution.

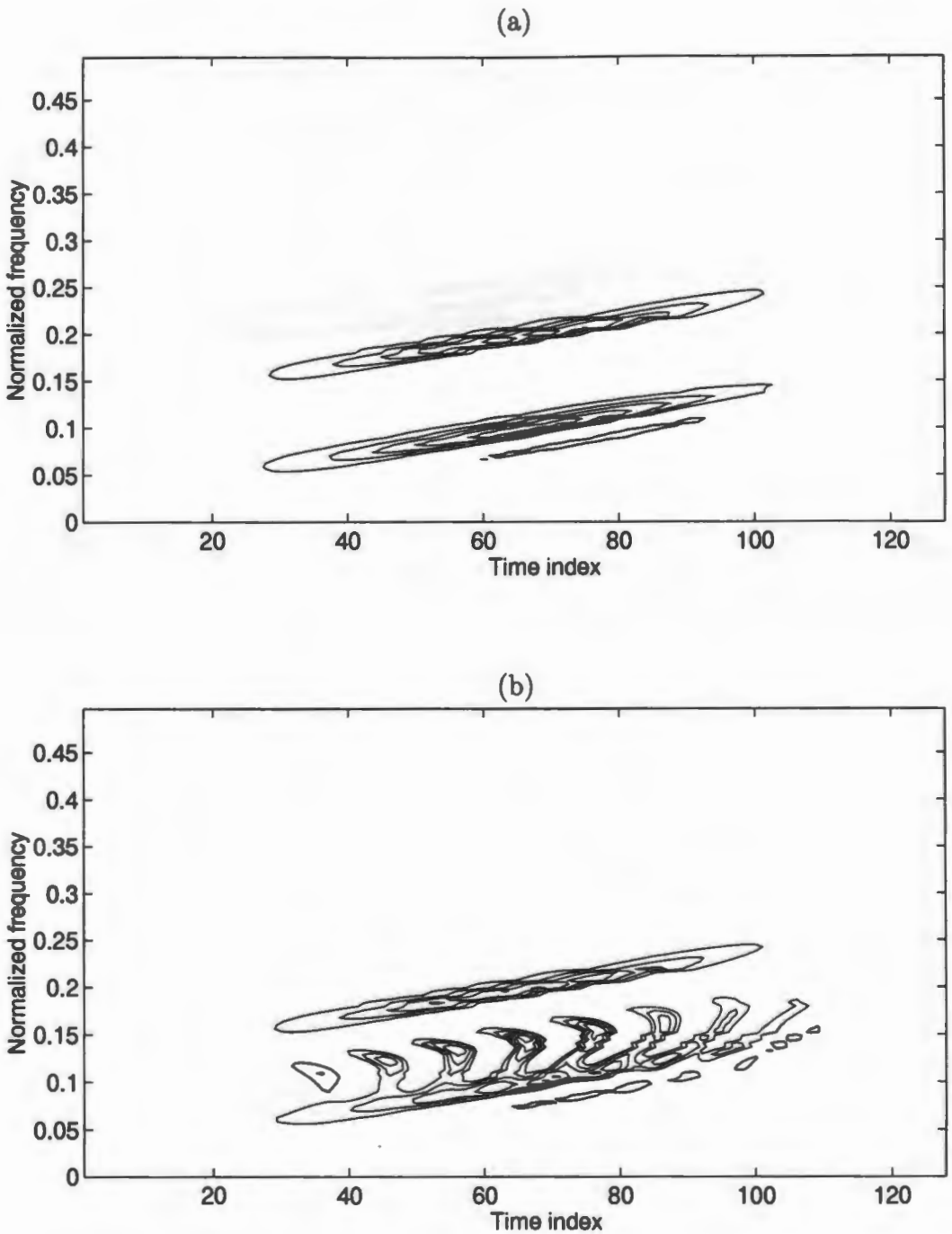

Figure 5.23: Contour plots for the simulation involving a signal which is the sum of two linear FM chirps individually tapered by a Hanning window. (a) individual Altes-Marinovic distributions of the signal components superimposed on each other, (b) Altes-Marinovic distribution of the sum of the components.

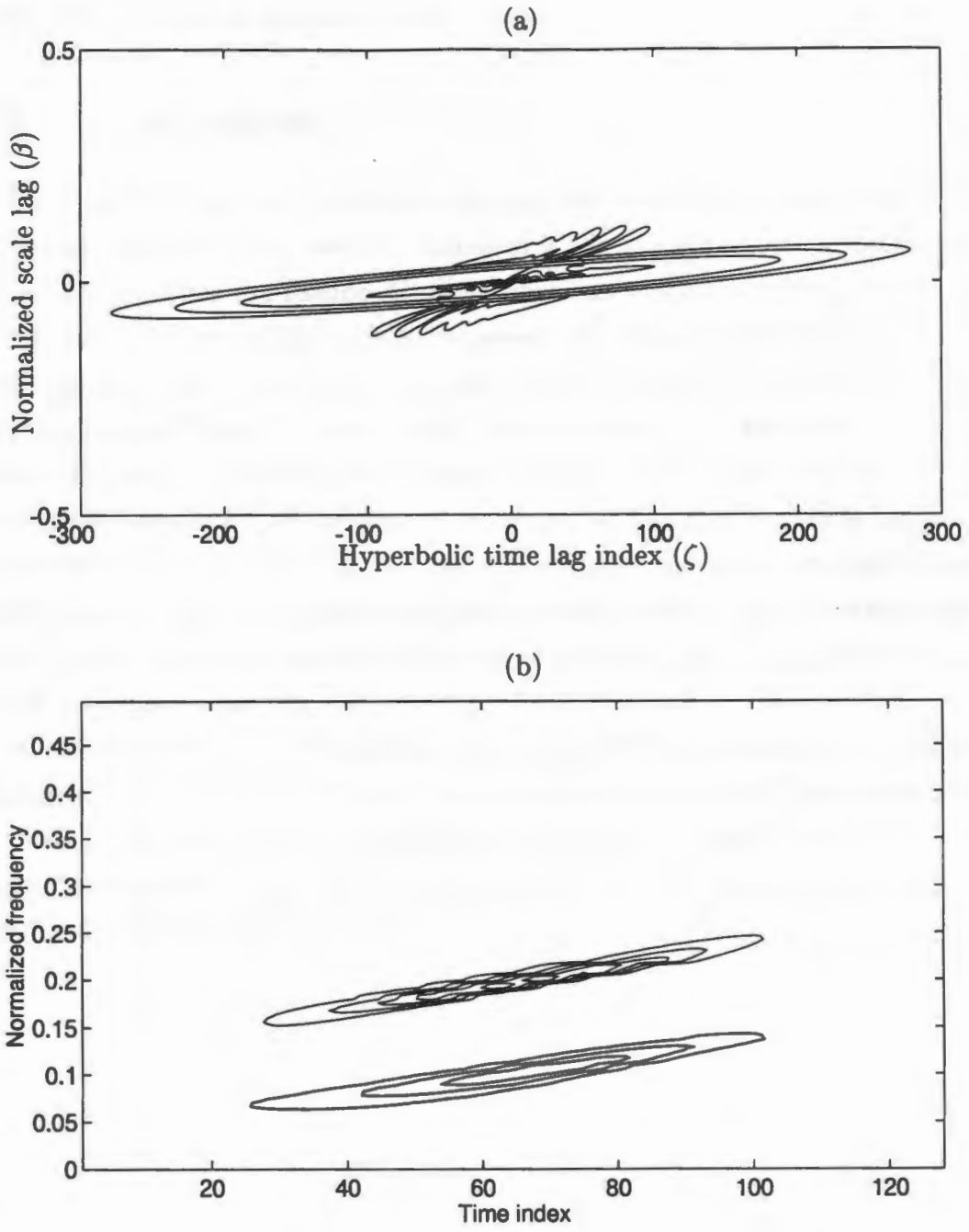

Figure 5.24: Contour plots for the simulation involving a signal which is mentioned in Figure (5.23). (a) MTED kernel with $\tau_0 = 90$, $\nu_0 = 0.05$, $r = -0.85$, $\alpha = 0$, $\beta = 1$, $\gamma = 1$ and $\lambda = 1$ superimposed on the magnitude of the Hyperbolic ambiguity function of the signal, (b) resulting MTEK smoothed Altes-Marinovic distribution.

significantly distorting the auto terms.

5.5 Conclusions

In this chapter, extensive analysis of the warping technique proposed by Canfield and Jones was done. The warping approach is used to implement members of the Hyperbolic class like the Pseudo Altes distribution and the Smoothed Pseudo Altes distribution. This technique initially implements the Hyperbolic Ambiguity function of the signal by calculating the Woodward Ambiguity function of the warped signal. Later, a suitable kernel is chosen and multiplied with the Hyperbolic Ambiguity function so that the cross terms are removed without distorting the auto terms. Then, a two dimensional FFT of the product is taken and the time-frequency localization is corrected (see section 5.2) to calculate a particular time-frequency distribution of the Hyperbolic class. This technique gives a better understanding of what warping does to each signal component and gives more flexibility and insight when designing kernels to remove cross terms.

A new member of the Hyperbolic class, the MTEK smoothed Altes-Marinovic distribution, was proposed. It uses the multiform tiltable kernel developed by [64, 2]. The MTEK smoothed Altes-Marinovic distribution works as well as or better than other hyperbolic class TFDs in most of the time-frequency scenarios that were investigated in this thesis.

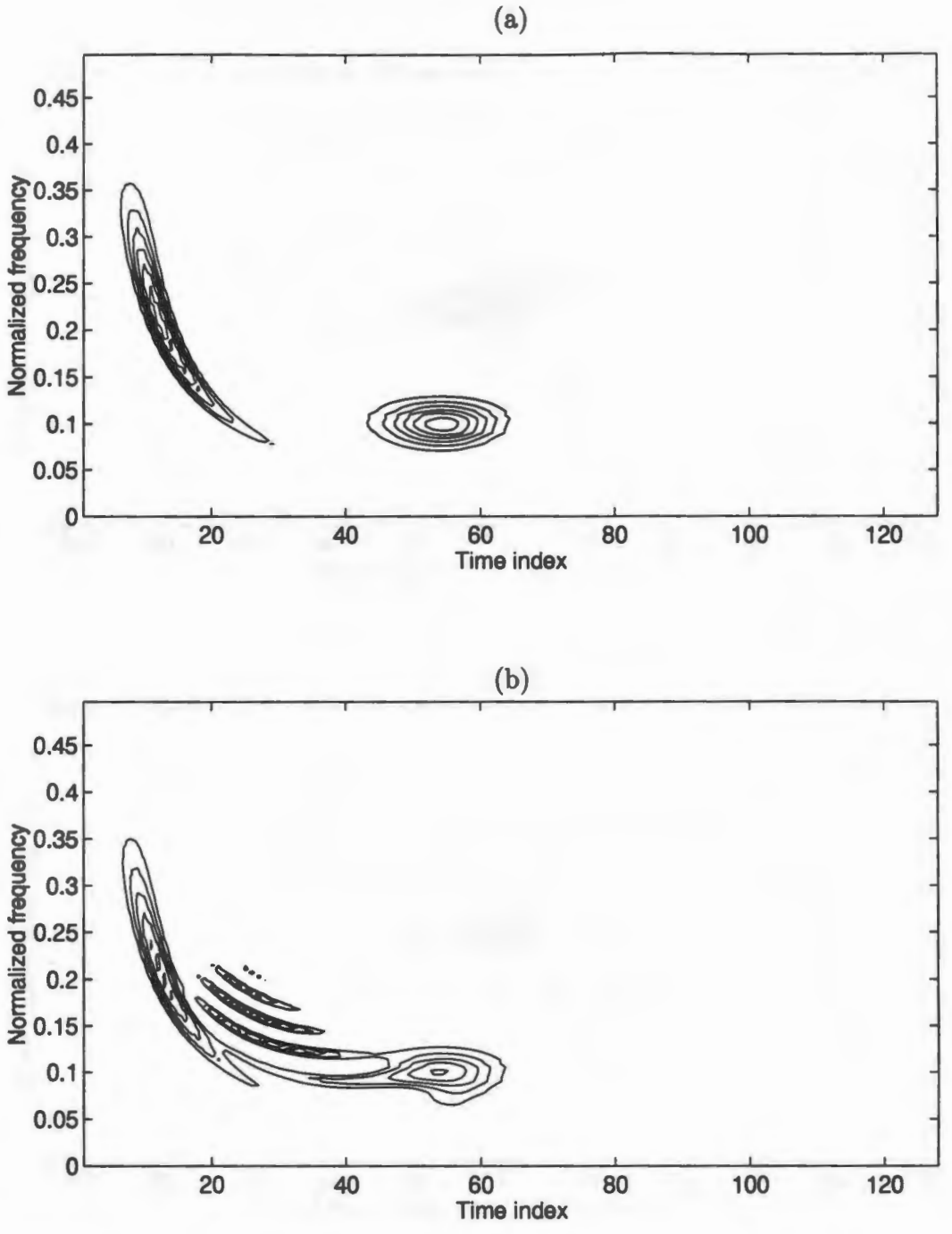

Figure 5.25: Contour plots for the simulation involving a signal which is the sum of a windowed Hyperbolic impulse and a Gaussian signal. (a) individual Altes-Marinovic distributions of the components superimposed upon one another, (b) Altes-Marinovic distribution of the sum of the two components.

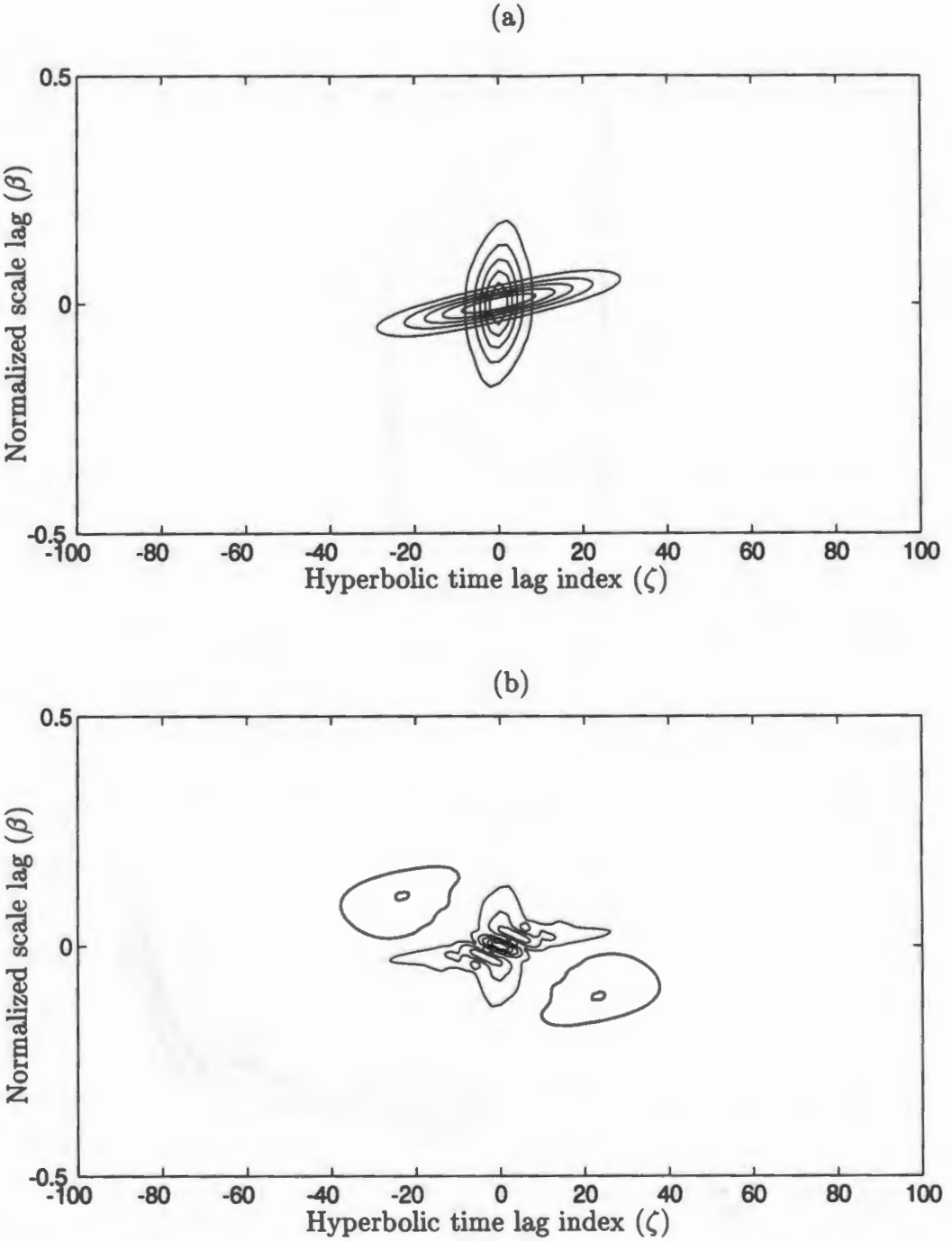

Figure 5.26: Contour plots for the simulation involving a signal which is the sum of a windowed Hyperbolic impulse and a Gaussian signal. (a) magnitude of the individual Hyperbolic ambiguity functions superimposed upon each other, (b) magnitude of the Hyperbolic ambiguity function of the sum of the two components.

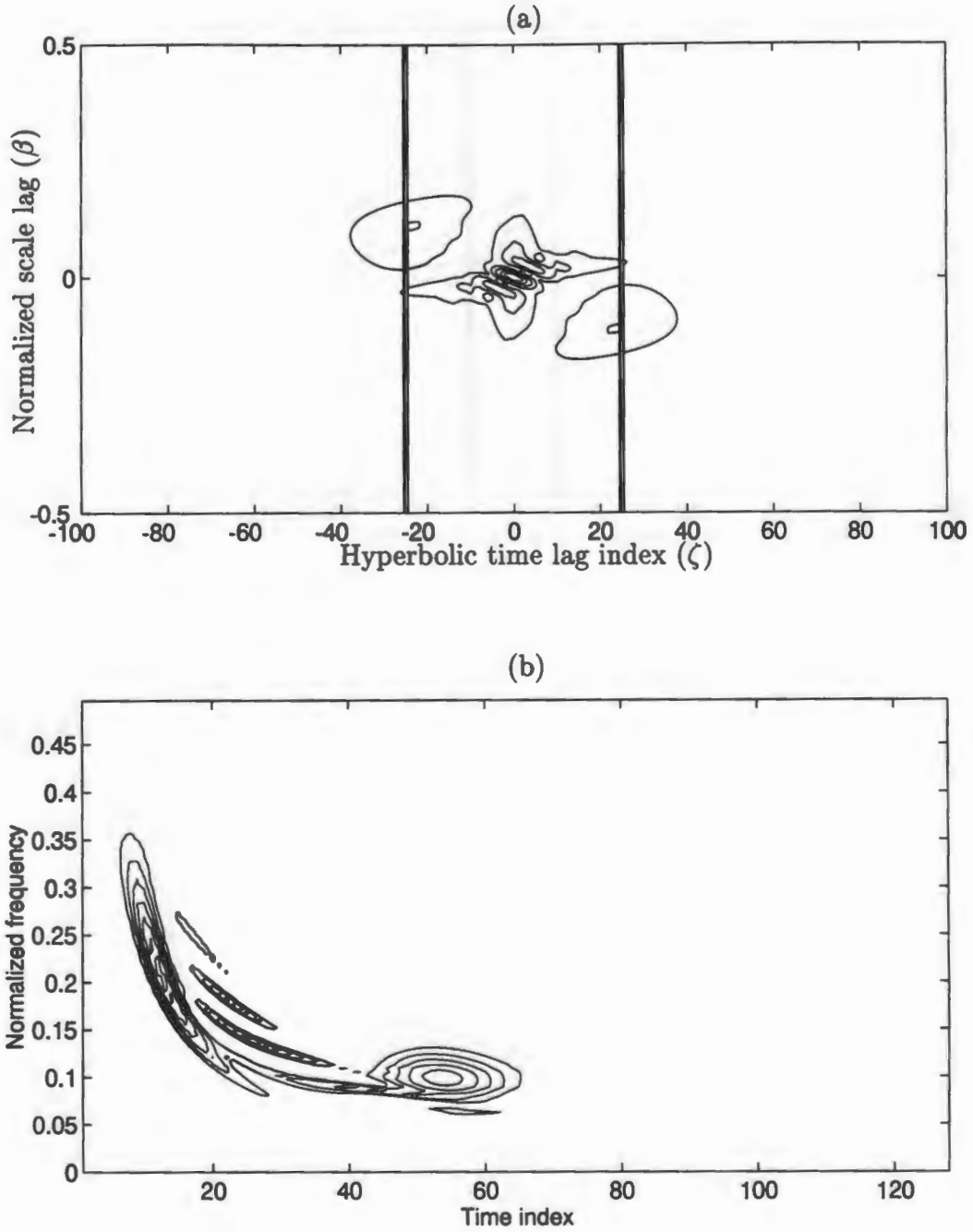

Figure 5.27: Contour plots for the simulation involving a signal which is mentioned in Figure (5.25). (a) PAD kernel with rectangular window of length 25 for smoothing in the ζ direction. (b) Pseudo Altes distribution.

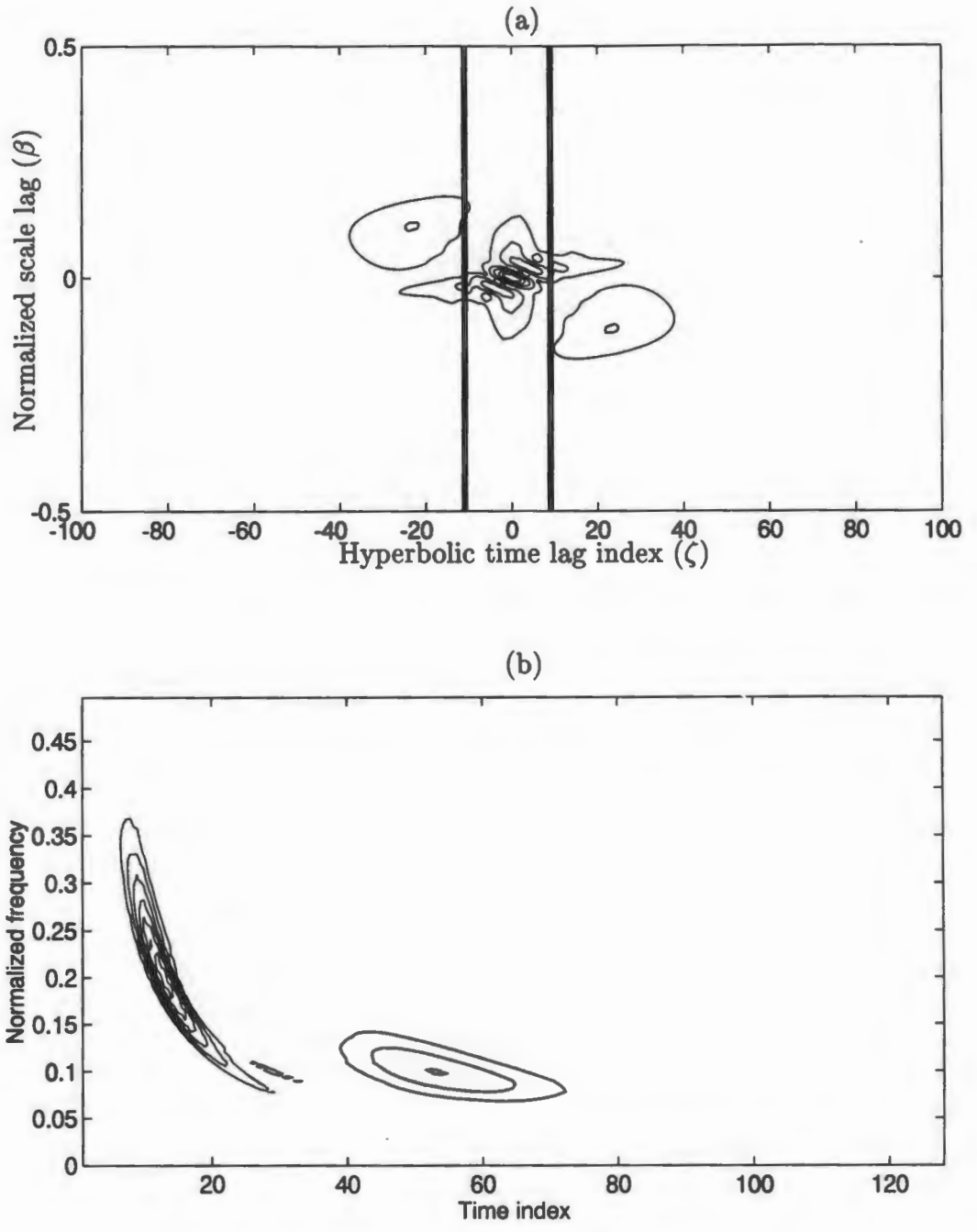

Figure 5.28: Contour plots for the simulation involving a signal which is mentioned in Figure (5.25). (a) PAD kernel with rectangular window of length 10 for smoothing in the ζ direction superimposed on the magnitude of the HAF of the signal, (b) resulting Pseudo Altes-Marinovic distribution.

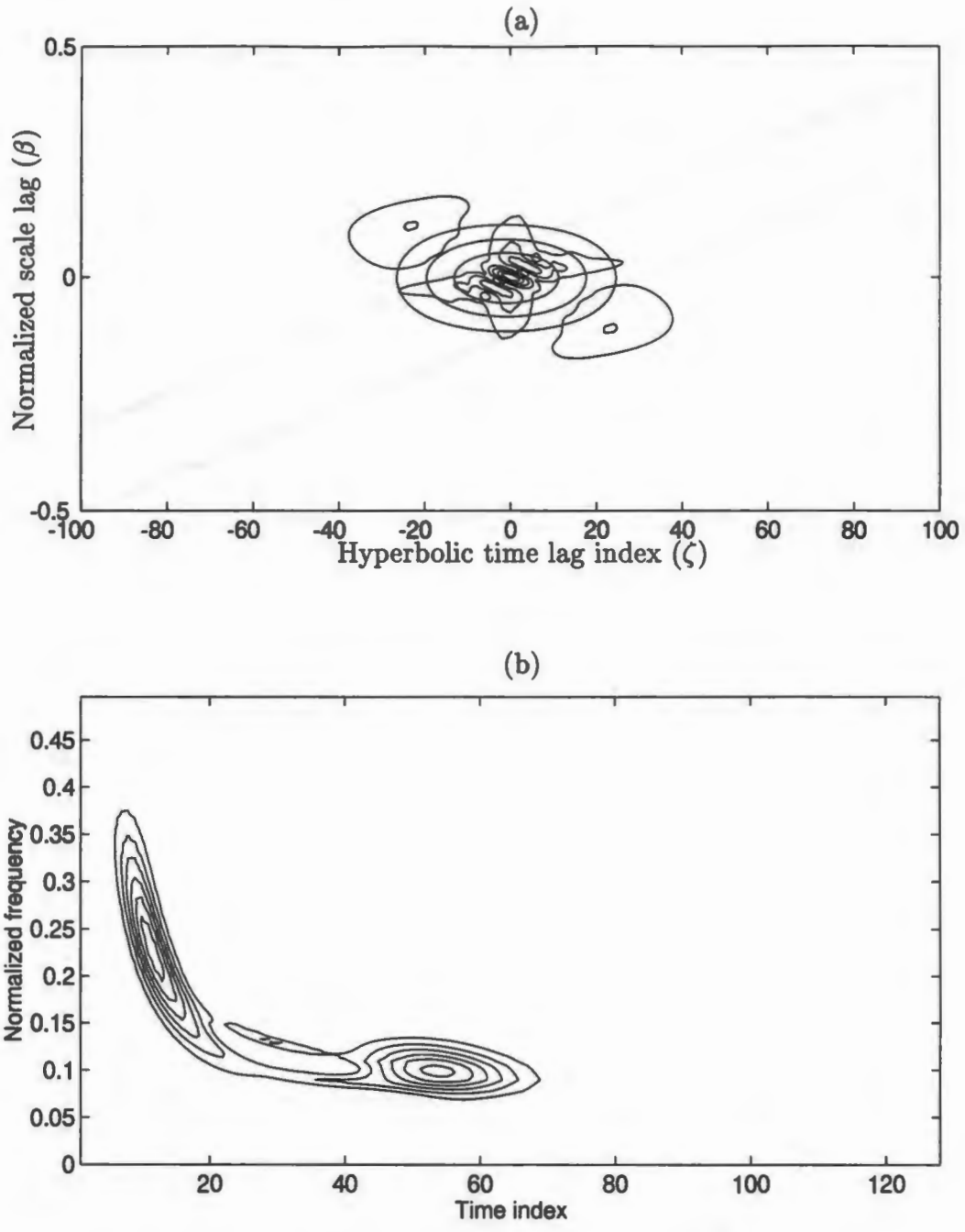

Figure 5.29: Contour plots for the simulation involving a signal which is mentioned in Figure (5.25). (a) SPAD kernel with a Hamming window of length 50 for smoothing in the ζ direction and a Blackman window of length 15 for smoothing in the β direction superimposed on the magnitude of the HAF of the signal, (b) resulting Smoothed Pseudo Altes distribution.

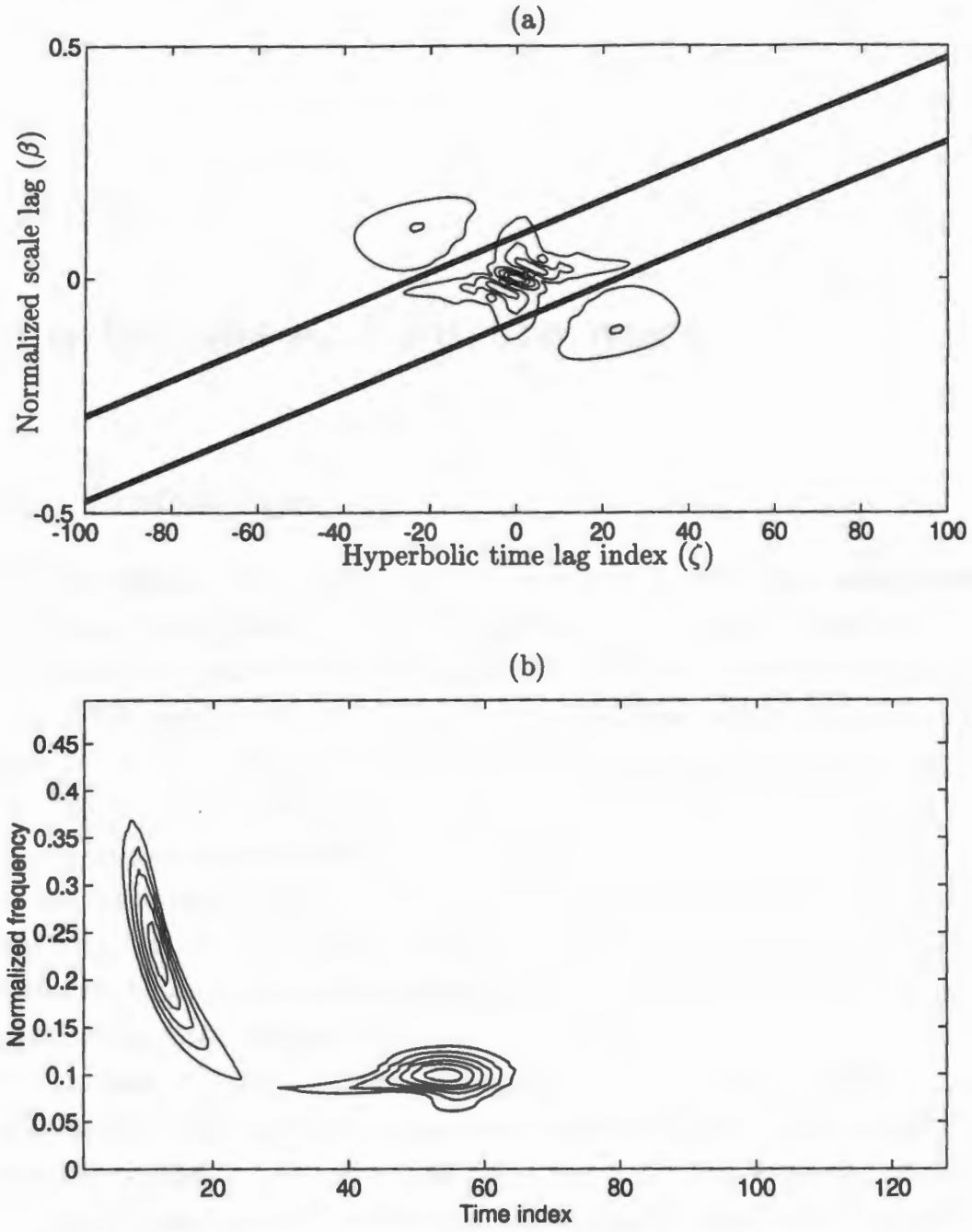

Figure 5.30: Contour plots for the simulation involving a signal which is mentioned in Figure (5.25). (a) MTED kernel with $\tau_0 = 16$, $\nu_0 = 0.16$, $r = -1$, $\beta = 1$, $\alpha = 0$, $\gamma = 1$ and $\lambda = 10$ superimposed on the magnitude of the Hyperbolic Ambiguity function of the signal, (b) resulting MTEK smoothed Altes-Marinovic distribution.

Chapter 6

Conclusions and Future work

6.1 Conclusions

In the first chapter, the introduction and motivation for this thesis were discussed. In the second and third chapters, introduction to time-frequency analysis and a review of existing work on the implementation of Hyperbolic class were discussed. In the fourth chapter of this thesis, we proposed a new way of implementing the Altes-Marinovic distribution using the Fast Mellin transform. This implementation is quicker and is more efficient in terms of memory requirements compared to the warping technique proposed by Canfield and Jones [7]. Also, a new technique was proposed which implements the Pseudo Altes-Marinovic distribution using first order linear interpolation and Simpson's method of numerical integration. Other smoothed versions of the Altes-Marinovic distribution could be implemented in a similar way as the Pseudo Altes-Marinovic distribution.

In the case of a signal which is the sum of two windowed hyperbolic impulses, the Altes-Marinovic distribution exhibits a cross term or interference term. If the hyperbolic impulses are far apart from each other in the time-frequency plane, then the Pseudo Altes-Marinovic distribution implemented using the Fast Mellin transform and numerical integration removes the cross term; however, the Pseudo Altes-Marinovic distribution does not smooth the cross term out entirely if the hyperbolic impulses are too close to each other.

In the fifth chapter, we did an extensive analysis of the Warping technique proposed by Canfield and Jones [7]. Canfield and Jones have proposed and implemented a Hyperbolic class TFR which optimally selects a radially-Gaussian kernel to weight the Hyperbolic ambiguity function of the signal. The algorithm uses volume constraints on the kernel and optimization theory to automatically estimate the approximate regions of support of the cross terms and the auto terms in the Hyperbolic ambiguity function domain. We also use the Hyperbolic Ambiguity function of a signal, since it provides intuition as to what happens to signal components due to warping and gives the user the information needed to design a kernel to remove the cross-terms without significantly distorting the auto-terms.

But, we use a variety of different kernels. In the case of a signal which is the sum of two windowed hyperbolic impulses, this method removes the cross term or interference term even when the hyperbolic impulses are close to each other; however, designing a Cohen's class kernel for smoothing the Wigner distribution in this case is challenging. Hyperbolic class kernel design for is straightforward for many signal types. The Hyperbolic Ambiguity function maps a hyperbolic impulse to a straight line and the Hyperbolic class kernel design for smoothing interference terms becomes easy. In contrast, the Woodward Ambiguity function maps a hyperbolic impulse to a non-linear region which makes the design of a Cohen's class kernel challenging.

Also, we have proposed a new member of the Hyperbolic class, the Multiform, tiltable exponential kernel (MTEK) smoothed Altes-Marinovic distribution, which does a good job of smoothing the cross terms or interference terms in the various time-frequency scenarios that were considered in the fifth chapter. The MTEK smoothed Altes-Marinovic distribution does as good a job as the Pseudo Altes-Marinovic distribution when smoothing cross terms caused by hyperbolic impulses. Also, in the case of a signal which is the involving sum of two Gaussian components, the MTEK smoothed Altes-Marinovic distribution does a great job of smoothing the interference term whereas the Pseudo Altes-Marinovic distribution and the Smoothed Pseudo Altes-Marinovic distribution fail to either completely remove the cross term or end up distorting the auto terms.

Two issues, i.e., memory requirement and speed, were considered when comparing the two implementation techniques used to implement the Hyperbolic class of time-frequency distributions. The first technique used the Fast Mellin transform to compute the Altes distribution or the Bertrand P_0 distribution. The second technique for Smoothed Altes distributions was implemented using numerical integration and interpolation. The third technique was the warping method proposed by Canfield and Jones [7], but using different kernels. All the implementation techniques mentioned in this thesis use MATLAB4.2a programming language for computation of time-frequency distributions. The following comparison was done on a SPARC5 work station running the SOLARIS2.3 operating system.

Let us consider the memory requirement issue. For a sampled signal, with M sample points in the time domain, the warping method proposed by Canfield and Jones requires the memory size of (8*4M*4M) bytes during the course of the implementation. For the smoothed Altes distribution implementation proposed in this thesis, which uses the Fast Mellin transform and Numerical integration, the required memory size is (8*M*N) bytes where N is given by

$$N \geq BT\frac{a \ln a}{a-1} \tag{6.1}$$

where $B = f_2 - f_1$ and $a = f_2/f_1$. Here, f_2 and f_1 are maximum and minimum frequencies, respectively, of the approximate frequency support region of the signal spectrum $X(f)$. Although N varies depending on the time-bandwidth product of the signal and on the ratio of f_2 and f_1, in the examples in this thesis, it varied from M/2 to 2M. Hence, the memory requirements for this technique ranged from (1/32) to (1/8) of the memory requirements required for the Canfield and Jones [7] warping technique.

Let us consider the issue of the computational speed of each technique. Usually in signal processing algorithms, FFTs are the most time consuming operations which take up a large chunk of the computation time and they are usually used as a standard for comparisons. Since techniques which we are comparing involve other time consuming operations like numerical integration and linear interpolation, it is unfair to compare the speed of the program in terms of how many FFTs are being taken. We compare the speed of computation of each technique by taking a typical example

signal. For a signal of length $M = 128$ samples in time, the computation of the Altes-Marinovic distribution using the warping technique took approximately 157 seconds. The computation of the Altes-Marinovic distribution using the Fast Mellin transform took around 63 seconds. The computation of various smoothed Altes-Marinovic distributions, like the Pseudo Altes-Marinovic distribution, smoothed Pseudo Altes-Marinovic distribution, and MTEK smoothed Altes-Marinovic distribution using the warping technique also took around 157 - 450 seconds depending on the computational complexity of the kernel. However, the computation of various smoothed Altes-Marinovic distribution using the Fast Mellin transform followed by numerical integration depends upon the distribution being computed. The time taken for the computation of the pseudo Altes-Marinovic distribution using the Fast Mellin transform plus with numerical integration algorithm partly depended on the number of points used for computing the numerical integral. The larger the number of points used, the more the accuracy; but, the time taken for the computation is also more. The time taken for computing the Pseudo Altes-Marinovic distribution with 150 points between the maximum and minimum frequencies used in Simpson's method of numerical integration was around 4 hours.

6.2 Future work

The following are ideas for future work.

1. Implement other members of the Hyperbolic class which can be formulated as smoothed Altes distributions, e.g., the smoothed Pseudo Altes-Marinovic distribution, Hyperbologram, or Generalized Altes-Marinovic distribution, etc., using the Fast Mellin transform technique followed by numerical integration algorithm described in the Fourth chapter.

2. Investigate the program which computes the Bertrand unitary P_0 distribution and the Altes-Marinovic distribution using the Fast Mellin transform. It is experiencing some degree of time-localization problems and fixing this problem will be an interesting future work.

3. Any arbitrary time-frequency distribution of the Hyperbolic class can be implemented by implementing Equation (2.29) using the Fast Mellin transform. The implementation can be done as follows. Initially, the discrete Mellin transform of the signal spectrum should be calculated. The Woodward ambiguity function of the Mellin transform of the signal spectrum is equal to the Hyperbolic Ambiguity function of the signal. Hence, the Hyperbolic Ambiguity function, $B_X(\zeta, \beta)$, of the signal can be calculated by taking the Ambiguity function of the Mellin transform of the signal spectrum. Later, the kernel, $\Psi_T^{(H)}(\zeta, \beta)$, of interest should be chosen and multiplied with the Hyperbolic Ambiguity function. Then, the inverse Mellin transform of the product should be calculated. The algorithm for Fast inverse Mellin transform is proposed and discussed in [38]. The inverse Fourier transform of that product should be calculated and unwarped (see equation 3.41) to finally calculate the time-frequency distribution. This approach might be advantageous since it does not run into memory problems because of the zero padding that the warping technique used (see Section 3.4 and 3.5). The above mentioned approach might be quicker when computing smoothed Altes-Marinovic distributions than the technique proposed in this thesis since it does not require interpolation and numerical integration needed for computation of smoothed Altes-Marinovic distributions (see Section 4.3).

4. Recently, some new classes of time-frequency distributions called the Power classes were proposed [65] [66]. These classes were obtained by warping the Affine class. The Power classes of time-frequency distributions can be implemented as follows. Initially, the signal should be warped depending on the corresponding warping function for a particular distribution. The Affine time-frequency distribution of the warped signal should calculated. The result should then be unwarped to implement any time-frequency distribution of the Power classes. The warping and unwarping can be implemented using the Canfield and Jones [7] technique and the Affine class of TFRs could be implemented using Fast Mellin transform [6].

References

[1] F. Hlawatsch and G. F. Boudreaux-Bartels, "Linear and quadratic time-frequency signal representations," *IEEE Signal Processing Magazine*, vol. 9, pp. 21–67, April 1992.

[2] A. H. Costa, *Multiform, Tiltable time-frequency representations and masked Auto Wigner distribution Synthesis.* PhD thesis, University of Rhode Island, Kingston, Rhode Island, 1994.

[3] A. Papandreou, F. Hlawatsch, and G. F. Boudreaux-Bartels, "The hyperbolic class of quadratic time-frequency representations Part I: Constant-Q warping and the hyperbolic paradigm, members and properties, and the correlative domain," *IEEE Transactions on Signal Processing*, vol. 41, pp. 3425–3444, December 1993.

[4] A. Papandreou-Suppappola, *New classes of Quadratic time-frequency representations with scale covariance and generalized time-shift covariance: Analysis, Detection, and Estimation.* PhD thesis, University of Rhode Island, Kingston, Rhode Island, 1994.

[5] L. Cohen, "Generalized phase-space distribution functions," *Journal of Mathematics and Physics*, vol. 7, pp. 781–786, 1966.

[6] J. P. Ovarlez, J. Bertrand, and P. Bertrand, "Computation of affine time-frequency distributions using the fast Mellin transform," in *Proceedings IEEE International Conference in Acoustics, Speech, and Signal Processing*, vol. 5, (San Francisco, CA), pp. 117–120, 1992.

[7] K. G. Canfield and D. L. Jones, "Implementing time frequency representations for non-Cohen classes," in *Proceedings 27th Asilomar Conference*, (Pacific Grove, CA), pp. 1464–1468, November 1993.

[8] K. G. Canfield, "An adaptive, hyperbolic-class time-frequency representation," Master's thesis, University of Illinois at Urbana-Champaign, 1993.

[9] F. Hlawatsch, "Time-frequency methods for signal processing," Tech. Rep. 1291–0001, University of Rhode Island, Department of Electrical Engineering, Kingston, RI, December 1991.

[10] L. B. Jackson, *Digital filters and Signal Processing.* Kluwer Academic Publishers, 1992.

[11] D. Gabor, "Theory of communication," *Journal of the IEE*, vol. 93(III), pp. 429–457, November 1946.

[12] P. M. Woodward, *Probability and Information Theory with Application to Radar.* London, England: Pergamon, 1953.

[13] R. Koenig, H. K. Dunn, and L. Y. Lacy, "The sound spectrograph," *J. Acoust. Soc. Am.*, vol. 18, pp. 19–49, 1946.

[14] J. B. Allen and L. R. Rabiner, "A unified approach to STFT analysis and synthesis," *Proceedings IEEE*, vol. 65, pp. 1558–1564, November 1977.

[15] R. A. Altes, "Detection, estimation, and classification with spectrograms," *Journal of the Acoustical Society of America*, vol. 67, pp. 1232–1246, April 1980.

[16] K. Kodera, R. Gendrin, and C. de Villedary, "Analysis of time-varying signals with small BT values," *IEEE Transactions on Acoustics, Speech and Signal Proceesing*, vol. ASSP 26, pp. 64–76, 1978.

[17] A. V. Oppenheim, "Speech spectrograms using the Fast Fourier transform," *IEEE Spectrogram*, vol. 7, pp. 57–62, 1970.

[18] M. R. Portnoff, "Time-frequency representations of digital signals and systems based on short-time Fourier analysis," *IEEE Transactions on Acoustics, Speech, and Signal Processing*, vol. 28, pp. 55–69, February 1980.

[19] R. K. Potter, G. A. Kopp, and H. C. Green, *Visible Speech.* New York: D. Van Nostrand CO., 1947.

[20] L. R. Rabiner and R. W. Schafer, *Digital Processing of Speech Signals.* Englewood Cliffs, New Jersey: Prentice Hall, Inc., 1978.

[21] Y. Meyer, "Orthonormal wavelets," in *Wavelets, Time-Frequency Methods and Phase Space* (J. M. Combes, J. M. Grossman, and P. Tchamitchian, eds.), pp. 21–37, Berlin: Springer-Verlag, 1989. Proceedings of the International conference on Wavelets, Time-Frequency Methods and Phase Space: Inverse Problems and Theoretical Imaging, (Marseille, France), December 14–18, 1987.

[22] O. Rioul and M. Vetterli, "Wavelets and signal processing," *IEEE Signal Processing Magazine*, pp. 14–38, 1991.

[23] P. Flandrin and O. Rioul, "Affine smoothing of the Wigner-Ville distribution," in *Proceedings IEEE International Conference in Acoustics, Speech, and Signal Processing*, (Albuquerque, NM), pp. 2455–2458, April 1990.

[24] S. Kadambe and G. F. Boudreaux-Bartels, "A comparison of the existence of cross terms in the Wigner distribution and the squared magnitude of the Wavelet transform and the short time Fourier transform," *IEEE Transactions on Signal Processing*, vol. 40, pp. 2498–2517, October 1992.

[25] F. Hlawatsch and P. Flandrin, "The interference structure of the Wigner distribution and related time-frequency signal representations," in *The Wigner Distribution — Theory and Applications in Signal Processing* (W. Mecklenbräuker, ed.), Elsevier Science Publishers, 1995.

[26] M. Riley, *Speech Time-Frequency Representations.* Kluwer Academic Publ., 1989.

[27] J. Jeong and W. J. Williams, "On the cross-terms in spectrograms," *Proceedings of the IEEE International Symposium on Circuits and Systems*, pp. 1565–1568, 1990.

[28] E. P. Wigner, "On the quantum correction for thermo-dynamic equilibrium," *Physics Review*, vol. 40, pp. 749–759, 1932.

[29] J. Ville, "Théorie et applications de la notion de signal analytique," *Câbles et Transmission*, vol. 2A, pp. 61–74, 1948. Translated into English by I. Selin, RAND Corporation Report T–92, Santa Monica, CA, August 1958.

[30] D. L. Jones and T. W. Parks, "A resolution comparison of several time-frequency representations," *IEEE Transactions on Signal Processing*, vol. 40, pp. 413–420, February 1992.

[31] F. Hlawatsch, "Duality and classification of bilinear time-frequency signal representations," *IEEE Transactions on Signal Processing*, vol. 39, pp. 1564–1574, July 1991.

[32] P. Flandrin, *Temps-fréquence*. Paris: Hermès, 1993.

[33] A. Papandreou and G. F. Boudreaux-Bartels, "Generalization of the Choi-Williams distribution and the Butterworth distribution for time-frequency analysis," *IEEE Transactions on Signal Processing*, vol. 41, pp. 463–472, January 1993.

[34] E. J. Diethorn, "The generalized exponential time-frequency distribution," *IEEE Transactions on Signal Processing*, vol. 42, pp. 1028–1037, May 1994.

[35] T. Claasen and W. Mecklenbräuker, "The Wigner distribution — A tool for time-frequency signal analysis, Part III: Relations with other time-frequency signal transformations," *Philips Journal of Research*, vol. 35, pp. 372–389, 1980.

[36] O. Rioul and P. Flandrin, "Time-scale energy distributions: A general class extending wavelet transforms," *IEEE Transactions on Signal Processing*, vol. 40, pp. 1746–1757, July 1992.

[37] J. Bertrand and P. Bertrand, "Time-frequency representations of broad-band signals," in *Proceedings IEEE International Conference in Acoustics, Speech, and Signal Processing*, (New York), pp. 2196–2199, 1988.

[38] J. Bertrand and P. Bertrand, "Affine time-frequency distributions," in *Time-Frequency Signal Analysis – Methods and Applications* (B. Boashash, ed.), ch. 5, pp. 118–140, Melbourne, Australia: Longman-Cheshire, 1991.

[39] P. Flandrin, "Sur une classe générale d'extensions affines de la distribution de Wigner-Ville," in *13ème Coll. GRETSI*, (Juan-les-Pins, France), September 1991.

[40] R. A. Altes, "Wide-band, proportional-bandwidth Wigner-Ville analysis," *IEEE Transactions on Acoustics, Speech, and Signal Processing*, vol. 38, pp. 1005–1012, June 1990.

[41] P. Flandrin, "Scale-invariant Wigner spectra and self-similarity," in *Proceedings EUSIPCO–90*, (Barcelona, Spain), pp. 149–152, September 1990.

[42] N. M. Marinovic, *The Wigner distribution and the ambiguity function: Generalizations, enhancement, compression and some applications.* PhD thesis, The City University of New York, 1986.

[43] J. Bertrand and P. Bertrand, "Représentations temps-fréquence des signaux," in *C.R. Acad. Sci. Paris*, vol. 299, pp. 635–638, 1984.

[44] J. Bertrand, P. Bertrand, and J. P. Ovarlez, "Discrete Mellin transform for signal analysis," in *Proceedings IEEE International Conference in Acoustics, Speech, and Signal Processing*, (Albuquerque, NM), pp. 1603–1606, 1990.

[45] R. A. Altes and E. L. Titlebaum, "Bat signals as optimally Doppler tolerant waveforms," *Journal of the Acoustical Society of America*, vol. 48, pp. 1014–1020, October 1970.

[46] A. Papandreou, F. Hlawatsch, and G. F. Boudreaux-Bartels, "A unified framework for the Bertrand distribution and the Altes distribution: The new hyperbolic class of quadratic time-frequency distributions," in *Proceedings IEEE*

Symposium on Time-Frequency and Time-Scale Analysis, (Victoria, Canada), pp. 27–30, October 1992.

[47] J. Bertrand and P. Bertrand, "A class of affine Wigner functions with extended covariance properties," *Journal of Mathematics and Physics*, vol. 33, pp. 2515–2527, 1992.

[48] A. Papandreou, F. Hlawatsch, and G. F. Boudreaux-Bartels, "Quadratic time-frequency distributions: The new hyperbolic class and its intersection with the affine class," in *Sixth SP Workshop on Statistical Signal and Array Processing*, (Victoria, Canada), pp. 26–29, October 1992.

[49] T. Claasen and W. Mecklenbräuker, "The Wigner distribution — A tool for time-frequency signal analysis, Part I: Continuous-time signals," *Philips Journal of Research*, vol. 35, pp. 217–250, 1980.

[50] A. J. E. M. Janssen, "On the locus and spread of pseudo-density functions in the time-frequency plane," *Philips Journal of Research*, vol. 37, no. 3, pp. 79–110, 1982.

[51] P. Flandrin and W. Martin, "Sur les conditions physiques assurant l'unicité de la représentation de Wigner-Ville comme représentation temps-fréquence," in *Neuvième Coll. sur le Traitement du Signal et ses Applications (GRETSI-83)*, (Nice, France), May 1983.

[52] F. Hlawatsch and R. L. Urbanke, "Bilinear time-frequency representations of signals: The shift-scale invariant class," *IEEE Transactions on Signal Processing*, vol. 42, pp. 357–366, February 1994.

[53] R. G. Shenoy and T. W. Parks, "Affine Wigner distributions," in *Proceedings IEEE International Conference in Acoustics, Speech, and Signal Processing*, vol. 5, (San Francisco, CA), pp. 185–188, March 1992.

[54] F. Hlawatsch, A. Papandreou, and G. F. Boudreaux-Bartels, "The hyperbolic class of quadratic time-frequency representations, Part II: Subclasses, intersection with the affine and power classes, regularity, and unitarity," *submitted to IEEE Transactions on Signal Processing.*

[55] F. Hlawatsch, "Regularity and unitarity of bilinear time-frequency signal representations," *IEEE Transactions on Information Theory*, vol. 38, pp. 82–94, January 1992.

[56] F. Hlawatsch, A. Papandreou, and G. F. Boudreaux-Bartels, "Regularity and unitarity of affine and hyperbolic time-frequency representations," in *Proceedings IEEE International Conference in Acoustics, Speech, and Signal Processing*, vol. 3, (Minneapolis, MN), pp. 245–248, April 1993.

[57] P. Flandrin, "Some features of time-frequency representations of multicomponent signals," in *Proceedings IEEE International Conference in Acoustics, Speech, and Signal Processing*, (San Diego, CA), pp. 41B.4.1–4, March 1984.

[58] R. A. Altes, "The Fourier-Mellin transform and mammalian hearing," *Journal of Acoustical Society of America*, vol. 63, pp. 174–183, January 1978.

[59] P. E. Zwicke and J. I. Kiss, "A new implementation of the Mellin transform and its application to Radar classification of ships," *IEEE Transactions on Pattern Analysis and Machine Intelligence*, vol. PAMI-5, March 1983.

[60] R. G. Baraniuk and D. L. Jones, "Warped wavelet bases: unitary equivalence and signal processing," in *Proceedings IEEE International Conference in Acoustics, Speech, and Signal Processing*, vol. 3, (Minneapolis, MN), pp. 320–323, April 1993.

[61] R. Baraniuk and D. Jones, "Unitary equivalence: A new twist on signal processing," *submitted to IEEE Transactions on Signal Processing.*

[62] W. H. Press, B. P. Flannery, S. A. Teukolsky, and W. T. Vetterling, *Numerical Recipes The Art of Scientific Computing (FORTRAN Version).* Cambridge University Press, 1989.

[63] P. J. Davis, *Interpolation & Approximation.* New York: Dover Publications, Inc., 1963.

[64] A. H. Costa and G. F. Boudreaux-Bartels, "Multiform, Tiltable, time-frequency representations using a Multiform, Tiltable Exponential kernel," in *Proceedings IEEE-SP International Symposium on Time-Frequency and Time-Scale Analysis*, (Philadelphia, Pennsylvania), pp. 205–208, October 1994.

[65] F. Hlawatsch, A. Papandreou, and G. F. Boudreaux-Bartels, "The power classes of quadratic time-frequency representations: A generalization of the affine and hyperbolic classes," in *Proceedings 27th Asilomar Conference*, (Pacific Grove, CA), pp. 1265–1270, November 1993.

[66] A. Papandreou, F. Hlawatsch, and G. F. Boudreaux-Bartels, "Quadratic time-frequency representations with scale covariance and generalized time-shift covariance: A unified framework for the affine, hyperbolic, and power classes," *in preparation for Digital Signal Processing Journal.*

Bibliography

Allen, J. B. and Rabiner, L. R., "A unified approach to STFT analysis and synthesis," *Proceedings IEEE*, vol. 65, pp. 1558–1564, November 1977.

Altes, R. A., "Detection, estimation, and classification with spectrograms," *Journal of the Acoustical Society of America*, vol. 67, pp. 1232–1246, April 1980.

Altes, R. A., "The Fourier-Mellin transform and mammalian hearing," *Journal of Acoustical Society of America*, vol. 63, pp. 174–183, January 1978.

Altes, R. A., "Wide-band, proportional-bandwidth Wigner-Ville analysis," *IEEE Transactions on Acoustics, Speech, and Signal Processing*, vol. 38, pp. 1005–1012, June 1990.

Altes, R. A. and Titlebaum, E. L., "Bat signals as optimally Doppler tolerant waveforms," *Journal of the Acoustical Society of America*, vol. 48, pp. 1014–1020, October 1970.

Baraniuk, R. G. and Jones, D. L., "Warped wavelet bases: unitary equivalence and signal processing," in *Proceedings IEEE International Conference in Acoustics, Speech, and Signal Processing*, (Minneapolis, MN), pp. 320–323, April 1993.

Baraniuk, R. and Jones, D., "Unitary equivalence: A new twist on signal processing," *submitted to IEEE Transactions on Signal Processing.*

Bertrand, J. and Bertrand, P., "Affine time-frequency distributions," in *Time-Frequency Signal Analysis – Methods and Applications*, (Boashash, B., ed.), ch. 5, pp. 118–140, Melbourne, Australia: Longman-Cheshire, 1991.

Bertrand, J. and Bertrand, P., "A class of affine Wigner functions with extended covariance properties," *Journal of Mathematics and Physics*, vol. 33, pp. 2515–2527, 1992.

Bertrand, J. and Bertrand, P., "Représentations temps-fréquence des signaux," in *C.R. Acad. Sci. Paris*, pp. 635–638, 1984.

Bertrand, J. and Bertrand, P., "Time-frequency representations of broad-band signals," in *Proceedings IEEE International Conference in Acoustics, Speech, and Signal Processing*, (New York), pp. 2196–2199, 1988.

Bertrand, J., Bertrand, P., and Ovarlez, J. P., "Discrete Mellin transform for signal analysis," in *Proceedings IEEE International Conference in Acoustics, Speech, and Signal Processing*, (Albuquerque, NM), pp. 1603–1606, 1990.

Canfield, K. G., *An Adaptive, Hyperbolic-Class Time-Frequency Representation.* Master's thesis, University of Illinois at Urbana-Champaign, 1993.

Canfield, K. G. and Jones, D. L., "Implementing time frequency representations for non-Cohen classes," in *Proceedings 27th Asilomar Conference*, (Pacific Grove, CA), pp. 1464–1468, November 1993.

Claasen, T. and Mecklenbräuker, W., "The Wigner distribution — A tool for time-frequency signal analysis, Part III: Relations with other time-frequency signal transformations," *Philips Journal of Research*, vol. 35, pp. 372–389, 1980.

Claasen, T. and Mecklenbräuker, W., "The Wigner distribution — A tool for time-frequency signal analysis, Part I: Continuous-time signals," *Philips Journal of Research*, vol. 35, pp. 217–250, 1980.

Cohen, L., "Generalized phase-space distribution functions," *Journal of Mathematics and Physics*, vol. 7, pp. 781–786, 1966.

Costa, A. H., *Multiform, Tiltable time-frequency representations and masked Auto Wigner distribution Synthesis.* PhD thesis, University of Rhode Island, Kingston, Rhode Island, 1994.

Costa, A. H. and Boudreaux-Bartels, G. F., "Multiform, Tiltable, time-frequency representations using a Multiform, Tiltable Exponential kernel," in *Proceedings*

IEEE-SP International Symposium on Time-Frequency and Time-Scale Analysis, (Philadelphia, Pennsylvania), pp. 205–208, October 1994.

Davis, P. J., *Interpolation & Approximation*. New York: Dover Publications, Inc., 1963.

Diethorn, E. J., "The generalized exponential time-frequency distribution," *IEEE Transactions on Signal Processing*, vol. 42, pp. 1028–1037, May 1994.

Flandrin, P., "Scale-invariant Wigner spectra and self-similarity," in *Proceedings EUSIPCO–90*, (Barcelona, Spain), pp. 149–152, September 1990.

Flandrin, P., "Some features of time-frequency representations of multicomponent signals," in *Proceedings IEEE International Conference in Acoustics, Speech, and Signal Processing*, (San Diego, CA), pp. 41B.4.1–4, March 1984.

Flandrin, P., "Sur une classe générale d'extensions affines de la distribution de Wigner-Ville," in *13ème Coll. GRETSI*, (Juan-les-Pins, France), September 1991.

Flandrin, P., *Temps-fréquence*. Paris: Hermès, 1993.

Flandrin, P. and Martin, W., "Sur les conditions physiques assurant l'unicité de la représentation de Wigner-Ville comme représentation temps-fréquence," in *Neuvième Coll. sur le Traitement du Signal et ses Applications (GRETSI-83)*, (Nice, France), May 1983.

Flandrin, P. and Rioul, O., "Affine smoothing of the Wigner-Ville distribution," in *Proceedings IEEE International Conference in Acoustics, Speech, and Signal Processing*, (Albuquerque, NM), pp. 2455–2458, April 1990.

Gabor, D., "Theory of communication," *Journal of the IEE*, vol. 93(III), pp. 429–457, November 1946.

Hlawatsch, F., "Duality and classification of bilinear time-frequency signal representations," *IEEE Transactions on Signal Processing*, vol. 39, pp. 1564–1574, July 1991.

Hlawatsch, F., "Regularity and unitarity of bilinear time-frequency signal representations," *IEEE Transactions on Information Theory*, vol. 38, pp. 82–94, January 1992.

Hlawatsch, F., "Time-frequency methods for signal processing," Technical Report 1291–0001, University of Rhode Island, Department of Electrical Engineering, Kingston, RI, December 1991.

Hlawatsch, F. and Boudreaux-Bartels, G. F., "Linear and quadratic time-frequency signal representations," *IEEE Signal Processing Magazine*, vol. 9, pp. 21–67, April 1992.

Hlawatsch, F. and Flandrin, P., "The interference structure of the Wigner distribution and related time-frequency signal representations," in *The Wigner Distribution — Theory and Applications in Signal Processing*, (Mecklenbräuker, W., ed.): Elsevier Science Publishers, 1995.

Hlawatsch, F., Papandreou, A., and Boudreaux-Bartels, G. F., "The hyperbolic class of quadratic time-frequency representations, Part II: Subclasses, intersection with the affine and power classes, regularity, and unitarity," *submitted to IEEE Transactions on Signal Processing.*

Hlawatsch, F., Papandreou, A., and Boudreaux-Bartels, G. F., "The power classes of quadratic time-frequency representations: A generalization of the affine and hyperbolic classes," in *Proceedings 27th Asilomar Conference*, (Pacific Grove, CA), pp. 1265–1270, November 1993.

Hlawatsch, F., Papandreou, A., and Boudreaux-Bartels, G. F., "Regularity and unitarity of affine and hyperbolic time-frequency representations," in *Proceedings IEEE International Conference in Acoustics, Speech, and Signal Processing*, (Minneapolis, MN), pp. 245–248, April 1993.

Hlawatsch, F. and Urbanke, R. L., "Bilinear time-frequency representations of signals: The shift-scale invariant class," *IEEE Transactions on Signal Processing*, vol. 42, pp. 357–366, February 1994.

Jackson, L. B., *Digital filters and Signal Processing.* Kluwer Academic Publishers, 1992.

Janssen, A. J. E. M., "On the locus and spread of pseudo-density functions in the time-frequency plane," *Philips Journal of Research*, vol. 37, pp. 79–110, 1982.

Jeong, J. and Williams, W. J., "On the cross-terms in spectrograms," *Proceedings of the IEEE International Symposium on Circuits and Systems*, pp. 1565–1568, 1990.

Jones, D. L. and Parks, T. W., "A resolution comparison of several time-frequency representations," *IEEE Transactions on Signal Processing*, vol. 40, pp. 413–420, February 1992.

Kadambe, S. and Boudreaux-Bartels, G. F., "A comparison of the existence of cross terms in the Wigner distribution and the squared magnitude of the Wavelet transform and the short time Fourier transform," *IEEE Transactions on Signal Processing*, vol. 40, pp. 2498–2517, October 1992.

Kodera, K., Gendrin, R., and de Villedary, C., "Analysis of time-varying signals with small BT values," *IEEE Transactions on Acoustics, Speech and Signal Proceesing*, vol. ASSP 26, pp. 64–76, 1978.

Koenig, R., Dunn, H. K., and Lacy, L. Y., "The sound spectrograph," *J. Acoust. Soc. Am.*, vol. 18, pp. 19–49, 1946.

Marinovic, N. M., *The Wigner distribution and the ambiguity function: Generalizations, enhancement, compression and some applications.* PhD thesis, The City University of New York, 1986.

Meyer, Y., "Orthonormal wavelets," in *Wavelets, Time-Frequency Methods and Phase Space*, (Combes, J. M., Grossman, J. M., and Tchamitchian, P., eds.), pp. 21–37, Berlin: Springer-Verlag, 1989. Proceedings of the International conference on Wavelets, Time-Frequency Methods and Phase Space: Inverse Problems and Theoretical Imaging, (Marseille, France), December 14–18, 1987.

Oppenheim, A. V., "Speech spectrograms using the Fast Fourier transform," *IEEE Spectrogram*, vol. 7, pp. 57–62, 1970.

Ovarlez, J. P., Bertrand, J., and Bertrand, P., "Computation of affine time-frequency distributions using the fast Mellin transform," in *Proceedings IEEE International Conference in Acoustics, Speech, and Signal Processing*, (San Francisco, CA), pp. 117–120, 1992.

Papandreou, A. and Boudreaux-Bartels, G. F., "Generalization of the Choi-Williams distribution and the Butterworth distribution for time-frequency analysis," *IEEE Transactions on Signal Processing*, vol. 41, pp. 463–472, January 1993.

Papandreou, A., Hlawatsch, F., and Boudreaux-Bartels, G. F., "The hyperbolic class of quadratic time-frequency representations Part I: Constant-Q warping and the hyperbolic paradigm, members and properties, and the correlative domain," *IEEE Transactions on Signal Processing*, vol. 41, pp. 3425–3444, December 1993.

Papandreou, A., Hlawatsch, F., and Boudreaux-Bartels, G. F., "Quadratic time-frequency distributions: The new hyperbolic class and its intersection with the affine class," in *Sixth SP Workshop on Statistical Signal and Array Processing*, (Victoria, Canada), pp. 26–29, October 1992.

Papandreou, A., Hlawatsch, F., and Boudreaux-Bartels, G. F., "Quadratic time-frequency representations with scale covariance and generalized time-shift covariance: A unified framework for the affine, hyperbolic, and power classes," *in preparation for Digital Signal Processing Journal.*

Papandreou, A., Hlawatsch, F., and Boudreaux-Bartels, G. F., "A unified framework for the Bertrand distribution and the Altes distribution: The new hyperbolic class of quadratic time-frequency distributions," in *Proceedings IEEE Symposium on Time-Frequency and Time-Scale Analysis*, (Victoria, Canada), pp. 27–30, October 1992.

Papandreou-Suppappola, A., *New classes of Quadratic time-frequency representations with scale covariance and generalized time-shift covariance: Analysis, Detection, and Estimation.* PhD thesis, University of Rhode Island, Kingston, Rhode Island, 1994.

Portnoff, M. R., "Time-frequency representations of digital signals and systems based on short-time Fourier analysis," *IEEE Transactions on Acoustics, Speech, and Signal Processing*, vol. 28, pp. 55–69, February 1980.

Potter, R. K., Kopp, G. A., and Green, H. C., *Visible Speech.* New York: D. Van Nostrand CO., 1947.

Press, W. H., Flannery, B. P., Teukolsky, S. A., and Vetterling, W. T., *Numerical Recipes The Art of Scientific Computing (FORTRAN Version).* Cambridge University Press, 1989.

Rabiner, L. R. and Schafer, R. W., *Digital Processing of Speech Signals.* Englewood Cliffs, New Jersey: Prentice Hall, Inc., 1978.

Riley, M., *Speech Time-Frequency Representations.* Kluwer Academic Publ., 1989.

Rioul, O. and Flandrin, P., "Time-scale energy distributions: A general class extending wavelet transforms," *IEEE Transactions on Signal Processing*, vol. 40, pp. 1746–1757, July 1992.

Rioul, O. and Vetterli, M., "Wavelets and signal processing," *IEEE Signal Processing Magazine*, pp. 14–38, 1991.

Shenoy, R. G. and Parks, T. W., "Affine Wigner distributions," in *Proceedings IEEE International Conference in Acoustics, Speech, and Signal Processing*, (San Francisco, CA), pp. 185–188, March 1992.

Ville, J., "Théorie et applications de la notion de signal analytique," *Câbles et Transmission*, vol. 2A, pp. 61–74, 1948. Translated into English by I. Selin, RAND Corporation Report T–92, Santa Monica, CA, August 1958.

Wigner, E. P., "On the quantum correction for thermo-dynamic equilibrium," *Physics Review*, vol. 40, pp. 749–759, 1932.

Woodward, P. M., *Probability and Information Theory with Application to Radar.* London, England: Pergamon, 1953.

Zwicke, P. E. and I. Kiss, J., "A new implementation of the Mellin transform and its application to Radar classification of ships," *IEEE Transactions on Pattern Analysis and Machine Intelligence*, vol. PAMI-5, March 1983.